

# MAGNETOM Flash

The Magazine of MR

Issue Number 1/2012

ISMRM Edition

Not for distribution in the US.

**SIEMENS**

## Clinical

**Clinical Experience with  
MR-PET Acquisition**  
Page 6

**MR Elastography**  
Page 20

**Understanding  
the Whiplash Condition  
at 3T**  
Page 44

**Myocardial T1-Mapping**  
Page 96

## Technology

**Cerebral TOF  
Angiography at 7T**  
Page 126

**CAIPIRINHA**  
Page 135

## How I do it

**The SNR Indicator**  
Page 144



49

Matthias Lichy, M.D.  
Editor-in-Chief



## Dear MAGNETOM Flash reader,

During the preparation of this issue of MAGNETOM Flash magazine I was faced with the realisation that each of my previous editorials had covered exactly the same ground: how innovations and new products drive better patient care. Of course, there have been different focuses for this observation, such as the introduction of the world's first simultaneous MR/PET system for clinical application, or the steering of ultra-high field MRI towards clinical usability. But what actually do I – or we within the MRI community – mean by 'innovation' in MRI? Does it require the introduction of a new revolutionary technology like simultaneous MR/PET, or the first application for parallel transmit with *syngo ZOOMit* as announced at the last RSNA in 2011?

During the early years of my specialisation I took the opportunity to be scanned in one of the very first 3Tesla installations. I already had some idea of what to expect from a good MRI scan and what not. But all I knew about 3T was that it had huge potential according to MR community hype and that, as far as I understood the theory, a lot of things ought simply to look better. To be honest, after more than an hour of scan time I found the results disappointing (and not just because of the problems with dielectric shading).

And how do I feel about 3T nowadays? Now I can examine the finest structures of cartilage acquired in the shortest scan times, or assess the smallest iron deposits in the brain, or see

the feeding vessels of a tumor in the finest detail. These amazing developments must surely be regarded as 'innovation'.

At this year's ECR, Siemens MR introduced our newest 3T scanner – MAGNETOM Spectra. If you read the specifications and take a look at the first images, and then compare them with what was possible just a few years ago, I am convinced that you will be as amazed as I am. Clearly there have been innovations to this scanner, such as the B<sub>1</sub> shimming technology, which have turned 3T from an interesting field of research into an invaluable clinical tool. However, there is also another innovation associated with this new scanner – just as important as image quality. The fact that this technology is affordable and that we can bring the advantages of imaging at 3T into wide scale clinical usage is in itself a huge innovation.

Well, I have yet again written about innovation and how this translates into better patient care. But now I realise that this is a message I am happy and proud to repeat with each new issue of MAGNETOM Flash. You won't be surprised to know, therefore that this ISMRM issue of Flash is again full of information about the latest innovations and developments. On behalf of all the editorial team I hope you will enjoy reading it as much as we did!

Matthias Lichy, M.D.

## Editorial Board

We appreciate your comments.

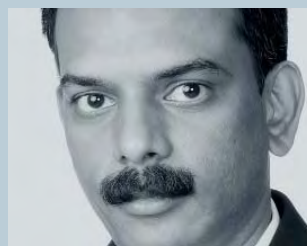
Please contact us at [magnetomworld.med@siemens.com](mailto:magnetomworld.med@siemens.com)



Antje Hellwich  
Associate Editor



Wellesley Were  
MR Business Development  
Manager Australia and New  
Zealand



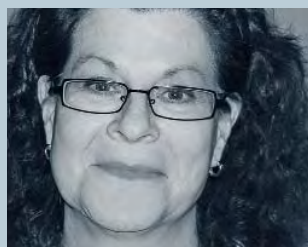
Dr. Sunil Kumar S.L.  
Senior Manager Applications,  
Canada



Christiane Bernhardt  
Head Outbound Marketing  
Erlangen, Germany



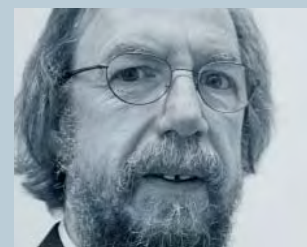
Milind Dhamankar, M.D.  
Sr. Director, MR Product  
Marketing, Malvern, PA, USA



Michelle Kessler  
US Installed Base Manager  
Malvern, PA, USA



Gary R. McNeal, MS (BME)  
Advanced Application Specialist,  
Cardiovascular MR Imaging  
Hoffman Estates, IL, USA



Peter Kreisler, Ph.D.  
Collaborations & Applications,  
Erlangen, Germany

## Review Board

Lisa **Chua**, Ph.D., Clinical Collaboration Manager

Okan **Ekinci**, M.D, Center of Clinical Competence – Cardiology

Jens-Christoph **Georgi**, Ph.D., Global Marketing Manager Biograph mMR

Wilhelm **Horger**, Application Development Oncology

Jürgen **Kampmeier**, Ph.D., MR/PET

Berthold **Kiefer**, Ph.D., Oncological and Interventional Applications

Heiko **Meyer**, Ph.D., Neuro Applications

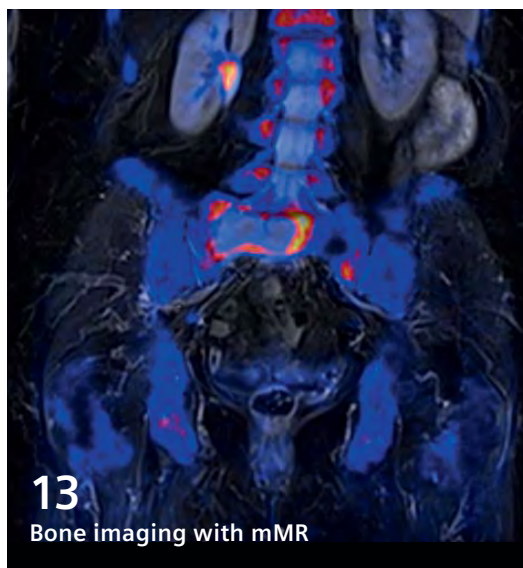
Edgar **Müller**, Cardiovascular Applications

Silke **Quick**, Global Marketing Manager Women's Health

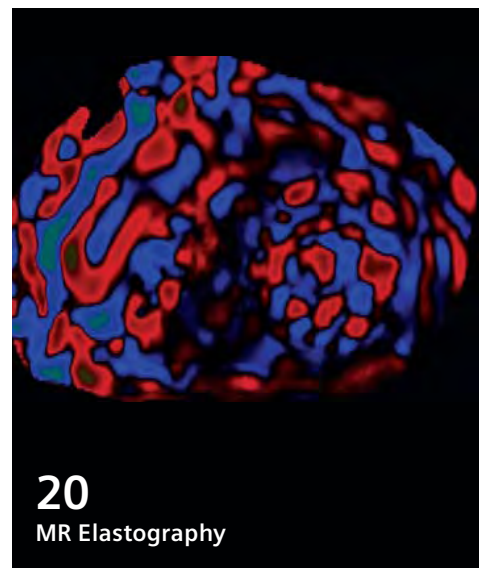
Ignacio **Vallines**, Ph.D., Global Marketing Manager Neurology and Orthopedics

Heike **Weh**, Clinical Data Manager

# Content



**13**  
Bone imaging with mMR



**20**  
MR Elastography

## Cover



T1w image of the hand acquired with a 16-channel hand/wrist coil utilizing 3T MAGNETOM Spectra. Using a high parallel imaging factor, the whole hand (30 slices) was scanned within 1:31 min at an effective resolution of  $(0.35 \times 0.35 \times 2.0) \text{ mm}^3$ .

The information presented in MAGNETOM Flash is for illustration only and is not intended to be relied upon by the reader for instruction as to the practice of medicine. Any health care practitioner reading this information is reminded that they must use their own learning, training and expertise in dealing with their individual patients. This material does not substitute for that duty and is not intended by Siemens Medical Solutions to be used for any purpose in that regard. The treating physician bears the sole responsibility for the diagnosis and treatment of patients, including drugs and doses prescribed in connection with such use. The Operating Instructions must always be strictly followed when operating the MR System. The source for the technical data is the corresponding data sheets.

MR scanning has not been established as safe for imaging fetuses and infants under two years of age. The responsible physician must evaluate the benefit of the MRI examination in comparison to other imaging procedures.

## Clinical Body Imaging

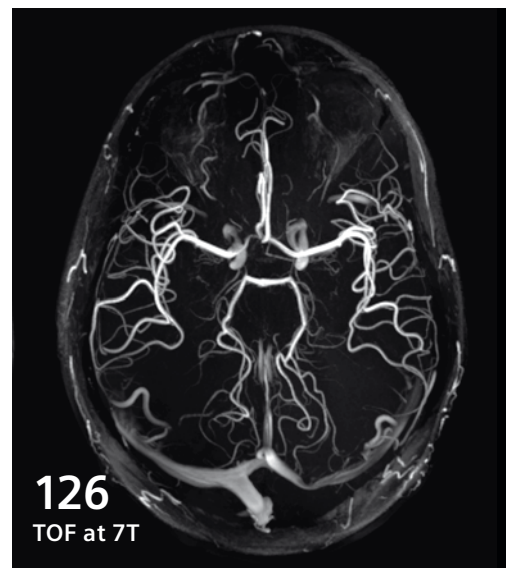
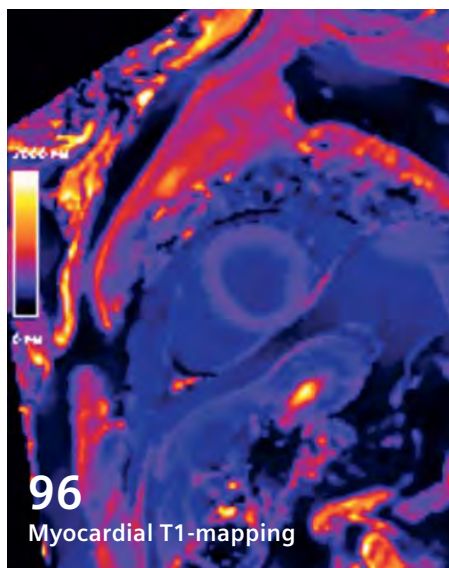
- 6** Clinical Experience with Simultaneous MR-PET Acquisition: Developing Optimal Protocols for Anatomically Focused and Whole-Body Examinations  
*Kathryn Fowler, et al.*
- 13** Case Report: Combining [ $^{18}\text{F}$ ] PET with MR for Detection of Bone Metastases in One Simultaneous Examination  
*Markus Lentschig, Christiane Franzius*

## Clinical Abdominal Imaging

- 20** Magnetic Resonance Elastography: Proven Indications, Challenges and Future Considerations  
*Sudharshan Parthasarathy, et al.*

## How I do it

- 28** Let's Dot it. How to Program a Dot Examination of the Liver  
*Anton S. Quinzen, et al.*



## Clinical Neurology

- 40** Texture Analysis and Classifiers Applied to High-Resolution MRI from Human Surgical Samples in Refractory Mesial Temporal Lobe Epilepsy  
*Maryana de Carvalho Alegro, et al.*
- 44** Towards Understanding the Whiplash Condition at 3 Tesla  
*James M. Elliott, et al.*
- 49** Case Report: Cervical Spine 3D Double Inversion Recovery (DIR) in Demyelination  
*David Shipp*

## How I do it

- 52** Brain Perfusion; How & Why  
*Nader Binesh, et al.*

## Product News

- 62** Imaging at 3 Tesla – luxury item or standard clinical tool? First experiences with MAGNETOM Spectra  
*Axel McKenna-Küttner*
- 74** TimTX TrueShape and syngo ZOOMit Technical and Practical Aspects  
*Mathias Blasche, et al.*

## Clinical Orthopedic Imaging

- 86** Case Report: Distal Medial Collateral Ligament Tear of the Knee  
*Eric K. Fitzcharles, Charles P. Ho*
- 91** Case Report: Posterior Glenoid Labral Tear  
*Eric K. Fitzcharles, Charles P. Ho*

## Clinical Cardiovascular Imaging

- 96** Myocardial T1-Mapping: Techniques and Clinical Applications  
*Juliano Lara Fernandes, et al.*
- 103** High Acceleration Quiescent-Interval Single Shot Magnetic Resonance Angiography at 1.5 and 3T  
*Maria Carr, et al.*

## Clinical Pediatric Imaging

- 108** Pediatric MR Elastography of the Liver  
*Marilyn J. Siegel, et al.*
- 112** MR Biomarkers of Gestational Age in the Human Fetus  
*Judy R. James, et al.*
- 120** 3D Fetal Reconstruction from MR Imaging  
*Heron Werner, et al.*

## Technology

- 126** Cerebral TOF Angiography at 7T: Pushing the Limits to Reap the Benefits of Ultra-High Field Imaging  
*Sebastian Schmitter, et al.*
- 135** Controlled Aliasing in Parallel Imaging Results in Higher Acceleration (CAIPIRINHA)  
*Felix Breuer, et al.*

## How I do it

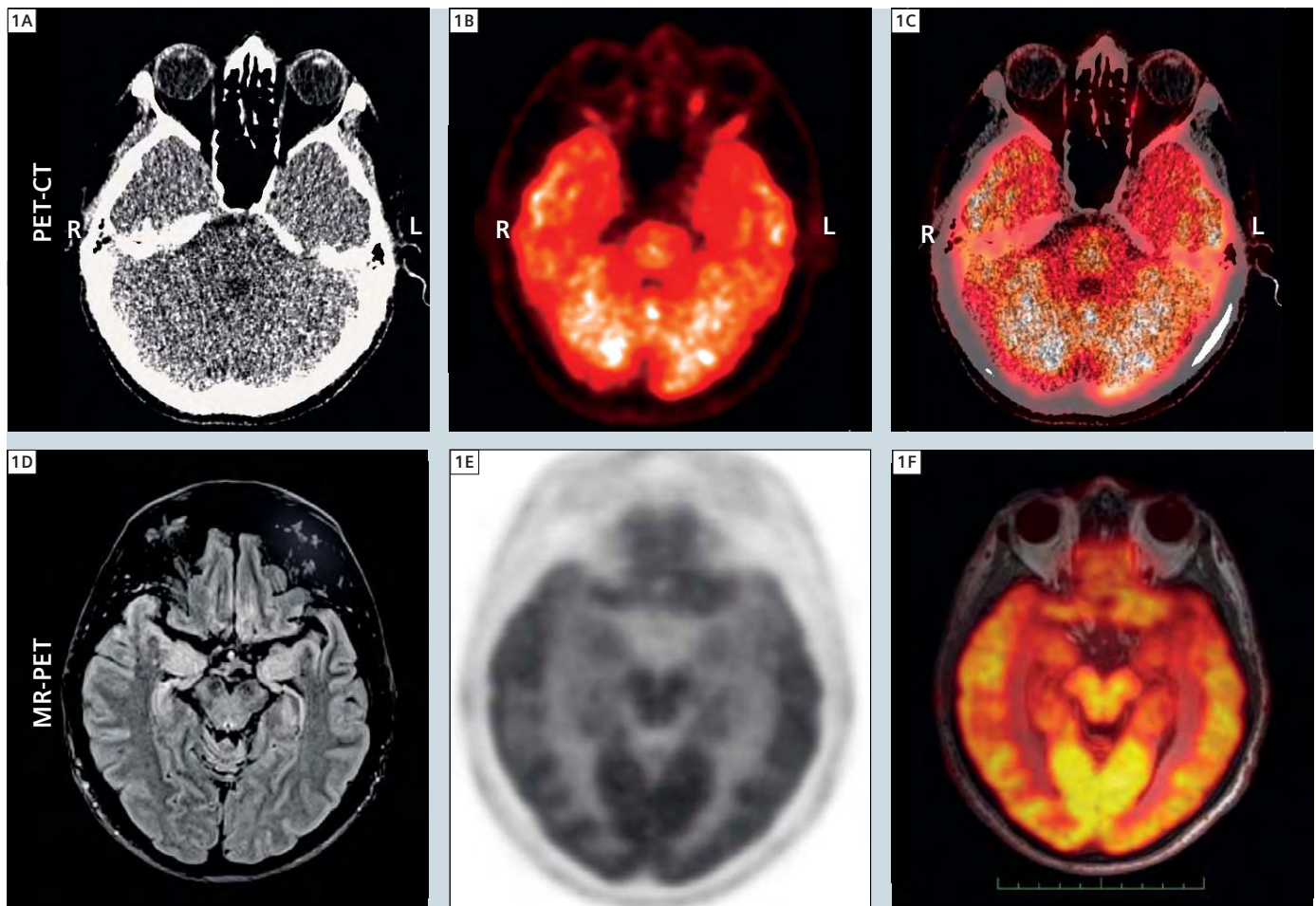
- 144** The Signal-to-Noise Indicator or How to Navigate the 'Bermuda Triangle'  
*Joachim Graessner*

# Clinical Experience with Simultaneous MR-PET Acquisition: Developing Optimal Protocols for Anatomically Focused and Whole-Body Examinations

Kathryn Fowler, M.D.<sup>1</sup>; Farrokh Dehdashti, M.D.<sup>1</sup>; Tammie L.S. Benzinger, M.D., Ph.D.<sup>1</sup>; Michelle Miller-Thomas, M.D.<sup>1</sup>; Jonathan McConathy, M.D., Ph.D.<sup>1</sup>; Matthew Parsons, M.D.<sup>1</sup>; Vilaas Shetty, M.D.<sup>1</sup>; Constantine Raptis, M.D.<sup>1</sup>; Perry Grigsby, M.D.<sup>1</sup>; Pamela K. Woodard, M.D.<sup>1</sup>; Richard Laforest, Ph.D.<sup>1</sup>; Robert J. Gropler, M.D.<sup>1</sup>; Vamsi Narra, M.D.<sup>1</sup>; Barry A. Siegel, M.D.<sup>1</sup>; John Kotyk, Ph.D.<sup>1</sup>; Agus Priatna, Ph.D.<sup>2</sup>; Robert McKinstry, M.D., Ph.D.<sup>1</sup>

<sup>1</sup>Mallinckrodt Institute of Radiology, Washington University School of Medicine, St Louis, MO, USA

<sup>2</sup>R&D Collaborations, Siemens Healthcare, St Louis, MO, USA



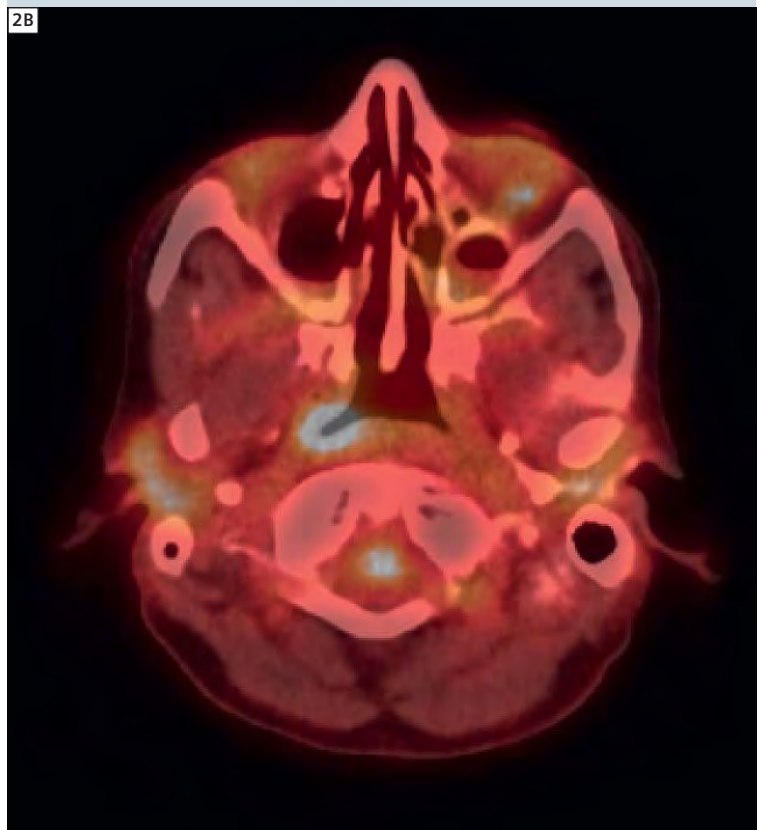
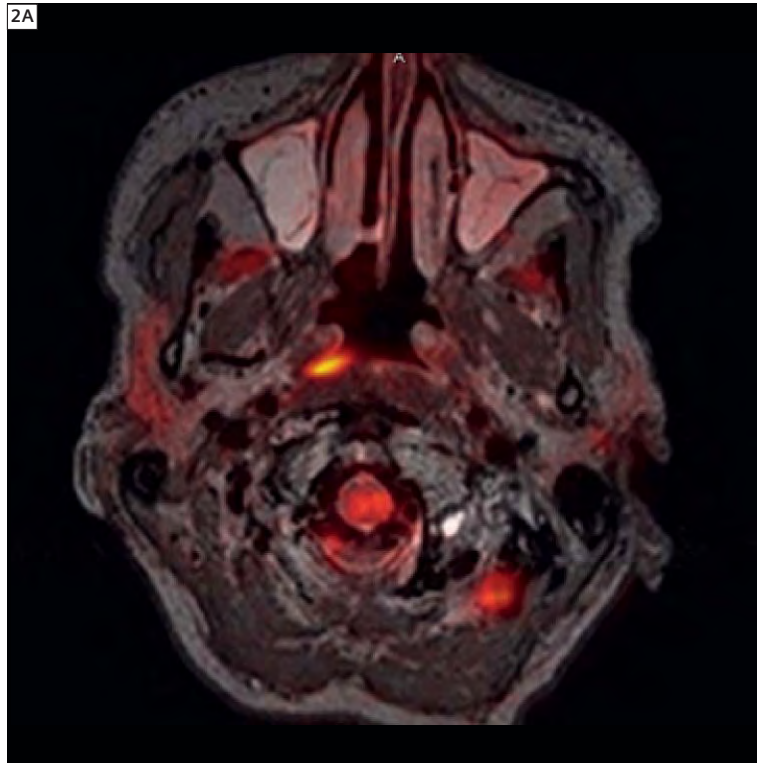
**1** 65-year-old male with a 1-year history of memory loss and episodic acute confusion; brain MRI demonstrated possible bilateral temporal lobe hyper intensity on FLAIR, without associated volume loss. FDG PET recommended for further evaluation. (1A–C) conventional FDG PET/CT shown: (1A) low-dose CT for attenuation correction, (1B) FDG PET, (1C) image fusion; (1D–F) simultaneous MR/PET of the same patient: (1D) FLAIR, (1E) FDG PET data, (1F) overlay of metabolic information.

## Introduction

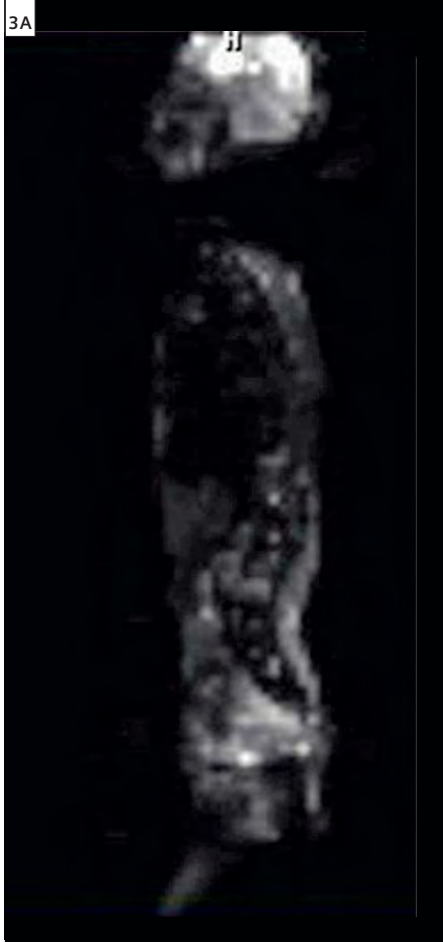
The new Biograph mMR offers simultaneous acquisition of PET and MR imaging data of potential added benefit in oncologic, neurological and other medical imaging [1–3]. The inherent benefit of the simultaneous acquisition is improved registration allowing optimal localization of PET findings to anatomic imaging and shortened overall imaging times through acquisition of PET and MRI in a single session. The purpose of this article is to present initial clinical experience with development of neurological protocols, anatomically focused MR-PET imaging protocols of body organs, including pelvic, thoracic, and liver oncologic imaging, and cardiac imaging experience. Initial experience, validation with PET-CT, challenges, and insights into protocol development are presented through representative examples.

## Methods

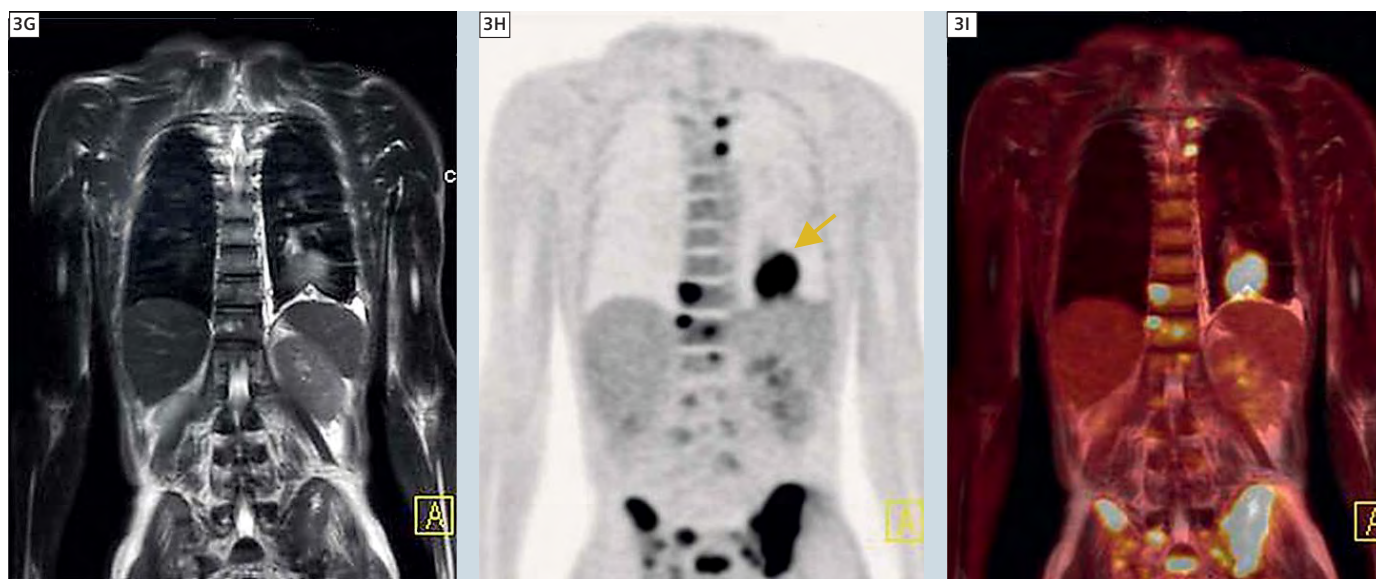
Following IRB approval, patients scheduled for standard of care clinical FDG-PET-CT were recruited and consented for additional MR-PET imaging. The simultaneous MR-PET imaging was acquired on a Biograph mMR system recently installed in the Center for Clinical Imaging Research (CCIR) at Washington University School of Medicine, with total imaging matrix, with attenuation body array and spine matrix coils. By incorporating Avalanche Photodiodes (APDs) into the bore of a 3T magnet, the Biograph mMR system fully integrates the acquisition of state-of-the-art PET and MR images. Attenuation correction imaging was performed utilizing a dual echo VIBE Dixon sequence that separates water and fat with TE1/TE2 1.23 msec / 2.46 msec, TR 3.6 msec, left-right field-of-view (FOV) 500 mm and anterior-posterior FOV 300 mm. The acquisitions were performed in either a single station or a multiple station mode as indicated. Depending on the applications, PET images were simultaneously acquired with the anatomical sequences



**2** Poorly differentiated nasopharyngeal carcinoma with bilateral cervical nodal (and liver) metastases is shown. Simultaneous MR-PET demonstrated excellent MR image quality and excellent localization of FDG uptake. (2A) FDG PET overlaid on T1w (2B) corresponding PET/CT exam.



**3A–F** Patient with metastatic lung cancer; primary tumor is present in the left lower lobe (see arrow in **3H**). Metastatic disease is shown in the mediastinum (lymph nodes), spine, and bony pelvis (osseous metastases). MR images include a STIR acquisition as well as diffusion-weighted imaging. Sagittal reconstructions: (**3A**) DWI, (**3B**) PET, (**3C**) MR/PET fused to DWI; coronal reconstructions: (**3D**) DWI, (**3E**) PET, (**3F**) MR/PET fused to DWI.



**3G-I** (3G) Coronal T2w HASTE for morphology, (3H) corresponding PET MPR, (3I) image overlay of PET and HASTE.

from MR such as HASTE for whole-body acquisition, MPAGE for brain imaging, SPACE or HASTE for pelvic application, or delayed enhancement for cardiac imaging. Additional examinations using high-resolution MR were added for the focused examination such as high resolution T2 TSE, diffusion-weighted imaging or diffusion tensor imaging (DTI) and other sequences depending on the applications.

### Clinical cases

The following are some examples of the clinical cases acquired for anatomically focused and whole-body examinations with the Biograph mMR.

#### Brain imaging

Although fusion of separately acquired brain MR and FDG-PET is readily available with offline software tools, a combined examination can allow for streamlined patient care and potentially improved diagnostic specificity, as illus-

trated by this case. A 65-year-old male with a 1-year history of memory loss and episodic confusion presented for workup at our institution (Fig. 1). A clinical MRI was interpreted as normal; however, there was a question of subtle FLAIR hyperintensity in the mesial temporal lobes. FDG-PET was recommended for further correlation of the MR findings and clinical presentation. The PET acquisition was acquired simultaneously with MRI. Brain MRI shows subtle bilateral mesial temporal lobe hyperintensity on FLAIR. FDG-PET shows mild bilateral mesial temporal lobe hypometabolism. Further clinical workup was then ordered which generated a final diagnosis of limbic encephalitis with voltage-gated potassium channel antibodies (VGKC). In this case, subtle findings on PET and MR performed independently, could be simultaneously reviewed and confirmed with PET/MR, leading to diagnostic confidence and initiation of the correct pathologic workup.

#### Head and neck oncology

Simultaneous head and neck MR-PET performs well compared with PET-CT in our initial experience. In the head and neck, MR-PET combines the metabolic and biochemical information from PET with high spatial resolution, anatomic localization, and soft tissue contrast from MR. The advantages of MR imaging in oral cavity and skull base neoplasms, the superior ability of MR to detect perineural spread of tumor, and improved coregistration of PET imaging with MR imaging during simultaneous acquisition make this a promising new technology for staging and follow-up of select head and neck neoplasms.

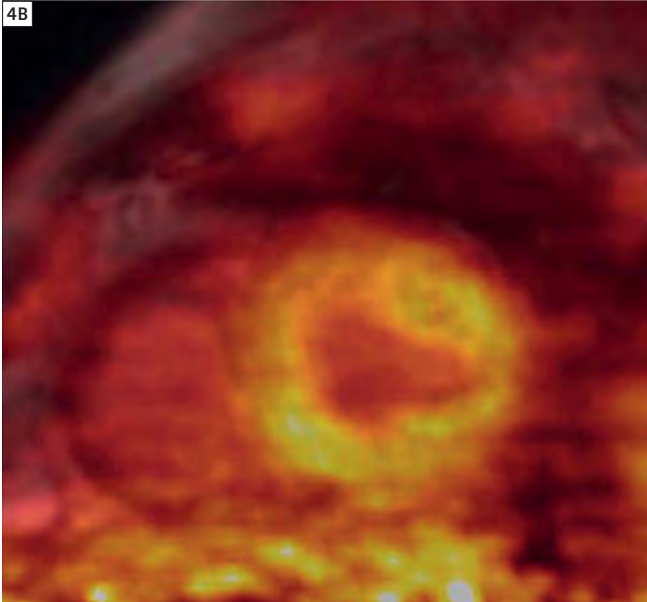
Patient is a 51-year-old woman with poorly differentiated nasopharyngeal carcinoma with bilateral cervical nodal and liver metastases. Simultaneous MR-PET demonstrated excellent MR image quality and excellent localization of FDG uptake. MR provided superior soft tissue resolution in the nasopharynx compared

4A

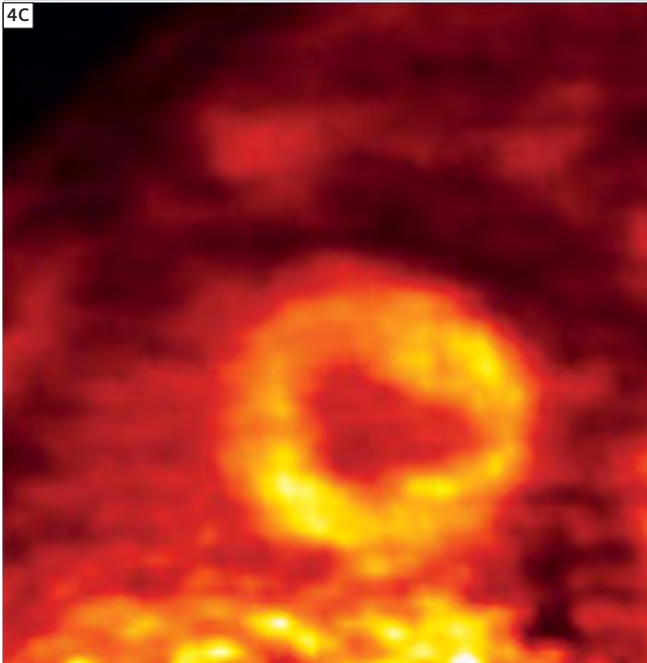


**4A** Simultaneous acquisition of ECG-gated PET and delayed contrast enhanced (DCE) cardiac MR images (simultaneous acquisition of MR 2-point Dixon also acquired for AC). PET data acquired in list mode and binned. DCE MR images acquired in diastole are fused with diastolic PET data to create the center image. Patient has a normal heart. **(4A)** MRI, **(4B)** fused MR/PET, **(4C)** FDG PET.

4B



4C



to PET-CT. Lesion detection based on FDG uptake on the MR-PET was equivalent to PET-CT in this case (Fig. 2).

#### Lung cancer with metastatic disease

While MRI can be used in the assessment of lung cancer, it has typically been reserved for specific cases in which CT and PET-CT, the first-line modalities for the assessment of lung cancer patients, are not able to answer a specific question, such as whether a lesion is invading the chest wall or a vascular structure. One of the key reasons for the secondary role for MRI is the fact that whole-body MR imaging is cumbersome and time consuming, thus preventing assessment of the full extent of disease. MR-PET for lung cancer has the potential to foster the development of new imaging protocols that allow for detailed assessment of the primary tumor while still providing the information regarding more distant metastatic disease. In addition, simultaneously acquired diffusion MR and PET data may prove useful both in the initial evaluation of tumors as well as in follow up after treatment.

Figure 3 shows a 50-year-old man with metastatic lung cancer. Primary lesion is present in the left lower lobe. Metastatic disease is shown in the mediastinal lymph nodes, spine, and bony pelvis. MR images include a HASTE acquisition as well as diffusion-weighted image obtained at a b-value of 600.

#### Cardiac imaging

Cardiac MR-PET imaging has the potential to play a role both in cardiac ischemia and viability assessment. Potential clinical protocols include stable chest pain assessment, playing on the strengths of both modalities, performing MR cine cardiac function assessment,  $^{13}\text{N}$ -ammonia or rubidium-82 PET myocardial perfusion and delayed contrast-enhanced inversion recovery infarct imaging in a single examination. Combined FDG and delayed contrast-enhanced inversion recovery cardiac

imaging may play a role in co-localized, simultaneously acquired functional and anatomic viability assessment that, theoretically, could play a role in imaging-directed ventricular tachycardia radiofrequency ablation or direct biven-tricular pacing in dyssynchrony.

A 68-year-old man injected with FDG for oncologic imaging was recruited immediately after his whole-body PET-CT examination to undergo a cardiac MR-PET imaging for protocol development (Fig. 4). Simultaneous acquisition of ECG-gated PET and delayed contrast-enhanced (DCE) cardiac MR images (simultaneous acquisition of MR 2-point Dixon also acquired for AC) allow for precise fusion of imaging. PET data was acquired in list mode, binned and reconstructed into 3 phases. DCE MR images acquired in diastole are fused with diastolic PET data to create the center image (Fig. 4B). This patient has a normal heart.

#### Cervical and vulvar cancers

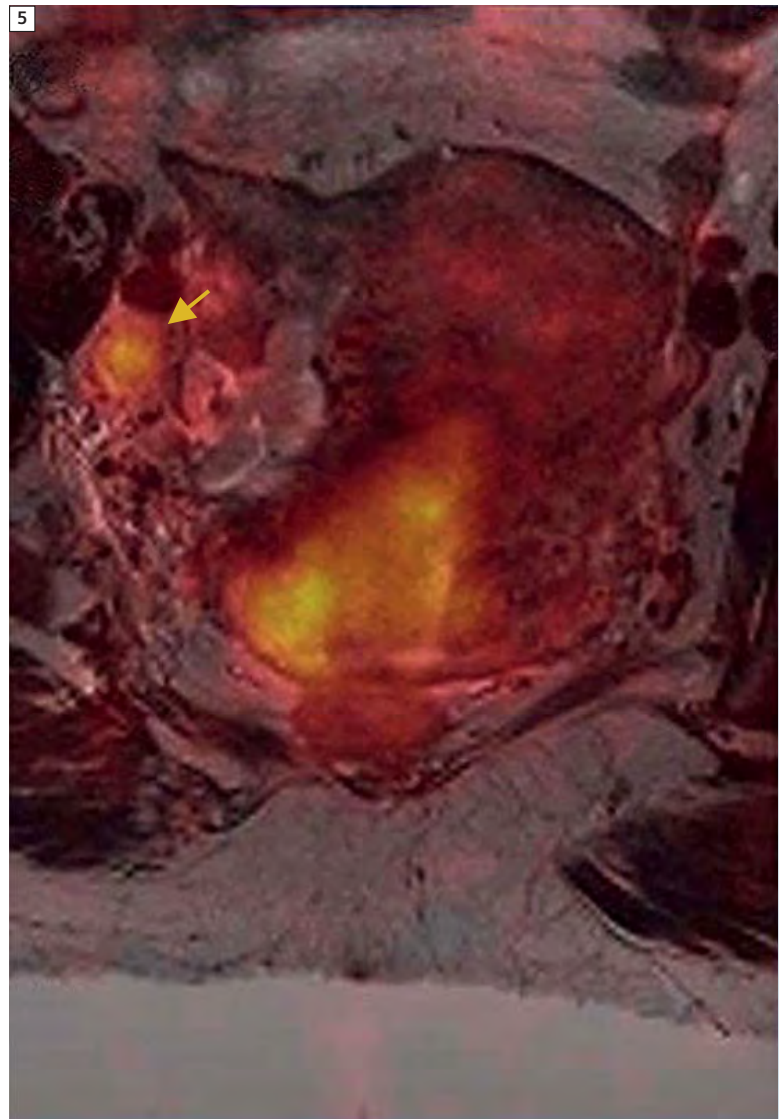
PET-CT and MRI are established modalities in initial staging and monitoring treatment response in patients with cervical cancer and other pelvic malignancies. PET can provide estimated tumor volumes for treatment planning and diagnosis of nodal metastases. High resolution MR imaging of the pelvis can detect parametrial spread of tumor, an essential feature in determining surgical resectability. The combination of metabolic information derived from PET with high resolution MR imaging of the pelvis shows promise in both clinical management and potential research opportunities in correlating functional MRI with tumor metabolism.

Given the complex anatomy of the pelvis, high resolution T2-weighted imaging is best performed utilizing a 3D isotropic dataset, such as SPACE. Isotropic acquisition allows for infinite multiplanar reformations without loss of resolution. Diffusion-weighted imaging, pre- and dynamic post-contrast volumetric

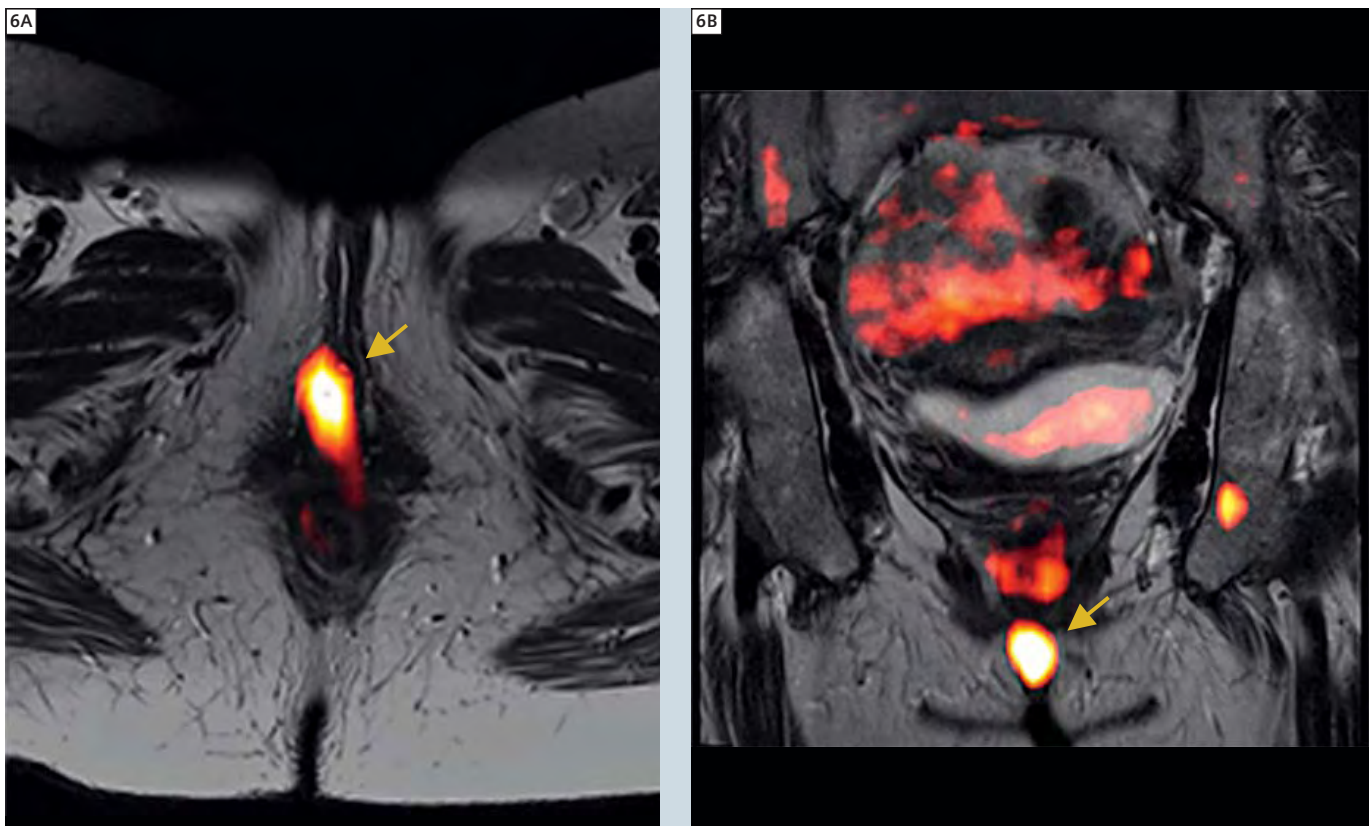
interpolated breath-held examination (VIBE), and inversion recovery T2 fat suppressed images complete a diagnostic MR examination of the pelvis providing additional staging information regarding local invasion, tumor size, and regional metastases. Figure 5 shows a 47-year-old woman with biopsy-proven cervical cancer. Given the large size of the patient's cer-

vical malignancy and presence of metabolically active nodal metastases, the patient subsequently underwent radiation therapy.

Figure 6 is a 31-year-old woman with vulvar carcinoma. A small focus of residual tumor within the pelvis could be missed on MR imaging alone and is in a difficult location with PET alone given the potential for contamination in this



**5** Primary cervical cancer and involved adjacent right external iliac lymph node (arrow); overlay of PET on T2 TSE is shown.



**6** Patient with vulvar cancer; small focus of residual tumor within the pelvis could be missed on MR imaging alone. FDG PET overlay on transversal (**6A**) and coronal (**6B**) T2w TSE is shown.

location from urine activity. The combination of MR-PET; however, nicely demonstrates the metabolically active soft tissue lesion.

## Discussion

MR-PET shows promise as a new oncologic imaging modality with inherent improved soft tissue contrast over CT, lower radiation dose, and potential for better correlation of PET findings to anatomy given the simultaneous acquisition. Several challenges are evident in developing optimal protocols, including optimal MR sequence parameters, motion correction, and validation of semiquantitative analysis using standardized uptake value (SUV) using MR attenuation correction. In some cases, the combination of PET SUV and MR ADC

values may prove more specific in differentiating tumor from surrounding tissue than subjective assessment alone. Potential for benefit from simultaneous MR-PET acquisition also exists in receptor-targeted oncologic imaging, dementia assessment, and cardiac and atherosclerosis imaging.

## Acknowledgement

Jennifer Frye, Glenn Foster, Linda Becker, Deb Hewing, Mike Harrod, Tim Street, Betsy Thomas

## References

- 1 Pichler BJ, Judenhofer MS, Wehrl HF. *Eur Radiol.* 2008; 18:1077-86.
- 2 Antoch G, Bockisch A. *Eur J Nucl Med Mol Imag.* 2009; 36 Suppl 1:S113-20.
- 3 Wehrl HF, Sauter AW et al. *Technol Cancer Res Treat.* 2010;9:5-20.

## Contact

Professor Pamela K. Woodard, M.D.  
Washington University  
Mallinckrodt Institute of Radiology  
510 S. Kingshighway Blvd.  
St. Louis, MO, 63110-1076  
USA  
Phone +1 314-362-7697  
woodardp@mir.wustl.edu

# Case Report: Combining [ $^{18}\text{F}$ ] PET with MR for Detection of Bone Metastases in One Simultaneous Examination

Markus Lentschig, M.D.; Christiane Franzius, M.D.

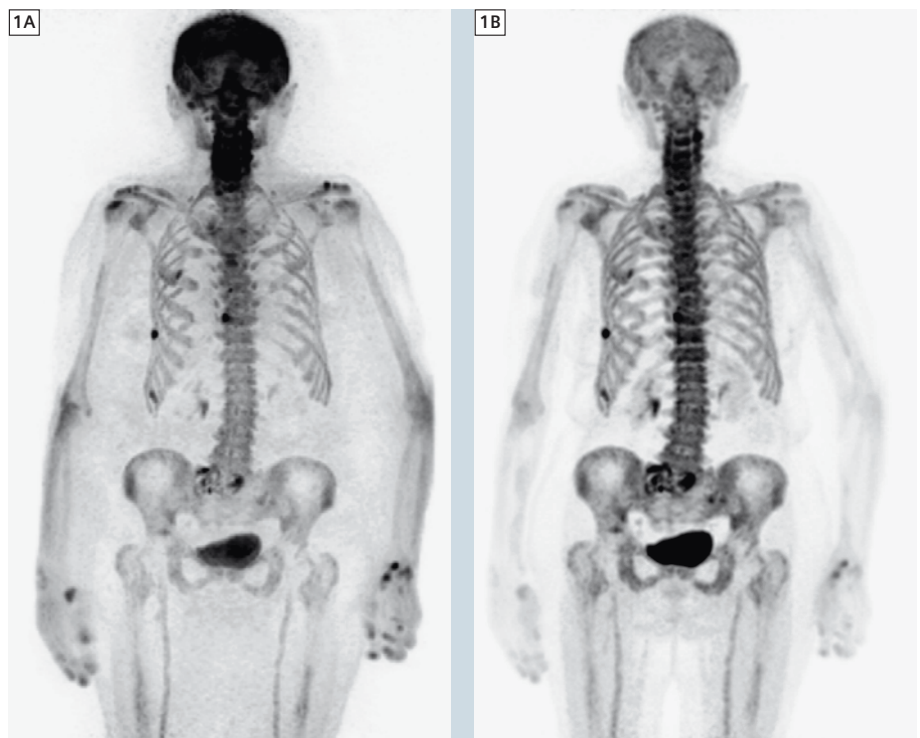
ZEMODI, Zentrum für Moderne Diagnostik, Bremen, Germany

## Background

In nuclear medicine, bone scanning is based on the principle of scintigraphy using bone-seeking radiopharmaceuticals. [ $^{99\text{m}}\text{Tc}$ ] (or [ $^{99}\text{Mo}$ ]) -labelled polyphosphonates are used as tracers for this purpose. They accumulate in sites of increased bone formation; metastases are detected either by increased uptake of the lesion itself (osteoplastic), as reaction of the surrounding healthy bone matrix or as defect (osteolytic). Bone scintigraphy has found its way into several clinical guidelines over the last decades and is a standard procedure in the evaluation of bone metastases. However, degenerative changes of bones are challenging to diagnose accurately especially in elderly patients. The low sensitivity of scintigraphy for (small) osteolytic lesions often requires complementary imaging, either X-ray, computed tomography (CT) or – especially in case of bone tumors and bone marrow involvement – magnetic resonance imaging (MRI). It has to be stated that bone scintigraphy is also associated with poor spatial resolution and as a consequence of the imaging mechanism itself this method has limited diagnostic specificity for lesion characterization and an insufficient sensitivity for bone marrow diseases. Positron emission tomography (PET) using [ $^{18}\text{F}$ ]-fluoride has already demonstrated to be a clinically useful alternative to traditional bone scintigraphy. Interestingly, [ $^{18}\text{F}$ ] was initially replaced by [ $^{99\text{m}}\text{Tc}$ ]-labelled polyphosphonates as osteotropic tracer. But with the development of modern PET/CT technology, the advantages over traditional bone

scintigraphy are eminent; [ $^{18}\text{F}$ ] PET adds diagnostic information mainly by its superior resolution compared to scintigraphy and nowadays PET is routinely acquired as 3D data. In addition, CT used as input for attenuation correction helps to characterize suspicious bone modelling. Also it should be kept in mind that from a patient perspective, [ $^{18}\text{F}$ ] PET/CT is considered to be the more convenient procedure (with special focus on preparation time and scan duration). Independent of its diagnostic advantages, the

importance of [ $^{18}\text{F}$ ] PET has increased recently because of its importance as a substitute for conventional skeletal scintigraphy in a time with limited availability of [ $^{99}\text{Mo}$ ]/[ $^{99\text{m}}\text{Tc}$ ]. To ensure healthcare, [ $^{18}\text{F}$ ] PET has now become part of common outpatient care [1–5]. Within the last decade, MRI has also increasingly challenged the clinical value of bone scintigraphy with superior diagnostic performance. The potential to assess not only changes of the bone but especially of the bone marrow and soft



**1** Maximum intensity projection (MIP) of the [ $^{18}\text{F}$ ] PET data (1A) uncorrected and (1B) after attenuation correction (MR based).

tissue in general at highest sensitivity can add important information and have a clear impact on patient care. This is already proven for dedicated patient cohorts. In combination with the advent of multi-regional MRI and further advances in MR technology, diffusion-weighted imaging (DWI) is used more and more routinely to add functional information to MRI. The images derived from such an exam show PET-like appearance; however, the underlying mechanism is restriction of water motion. How DWI will add further diagnostic accuracy in the detection of bone metastases and especially therapy follow-up is still subject of debate but its potential is more than evident [6–11]. Combining [ $^{18}\text{F}$ ] PET and MRI for evaluation of bone processes is therefore appealing but was only available in a small number of very selected cases up to now. One practical reason is the associated effort for conducting, synchronizing (time and indication wise) and reading two complex exams (this is especially true for MRI, where a standard whole-body scan produces more than 1000 images which have to be read). In addition, fusion techniques, which are often used to assist in this task, are of limited value especially for scans covering a larger volume simply because of different positions of the bones between the two examinations. The limitation of two separate exams can only partially be overcome by positioning aids (with all their associated disadvantages). It can, however, be overcome by using hybrid MR/PET systems (with the advantage to perform only one scan). Much has been written about the need and the technology behind this new hybrid imaging modality (see also the most recent issues of MAGNETOM Flash). It should be pointed out that simultaneous MR and PET imaging also has advantages in clinical routine over a sequential approach – not only from a workflow aspect.

A very obvious aspect is that it clearly improves spatial registration between metabolic and morphological information by reducing the time gap between the acquisition of MR and PET. This is a clear advantage not only in imaging the pelvis, bowel, lung and liver, but also in patients with limited capability for holding still in one position over a longer time period. Also it should be mentioned that there are no limitations in the performance of the individual imaging methods of such a combined simultaneous MR/PET system. Hybrid MR/PET systems rely on segmentation algorithms for providing the input function of the attenuation correction. At this point in time, bone segmentation is available only for dedicated areas like the skull base and not yet integrated in whole-body scanning. Nevertheless, based on existing data and experience, the need for bone segmentation can be negated in a clinical setting especially when a qualitative reading of PET is performed. The need for quantification of PET is unquestioned for follow-up exams and, so far, the introduced error as compared to a standard PET/CT (which has also a certain level of confidence only) seems to be negligible even for longitudinal studies – if performed with an MR/PET system. Nevertheless, the advent of this technology has reminded us that the discussion about the accuracy of PET quantification is of high importance and far from concluded (which is also true for the comparability of results acquired with different PET/CT systems). The diagnostic capabilities of MR and PET alone and in combination are of course dependent on the underlying pathology and the applied MR imaging methods and tracers. [12–15]

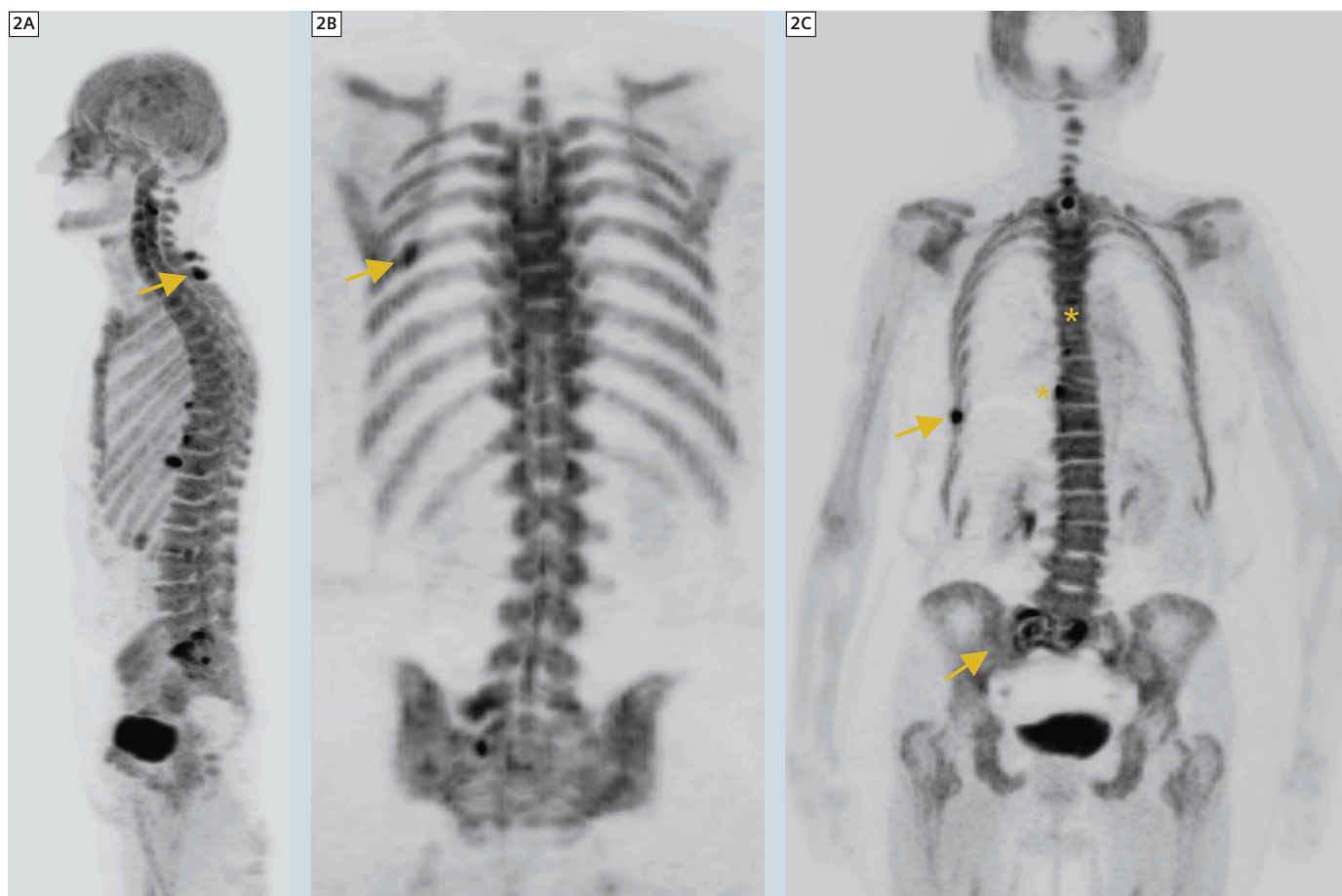
## Case report

### Patient history and sequence details

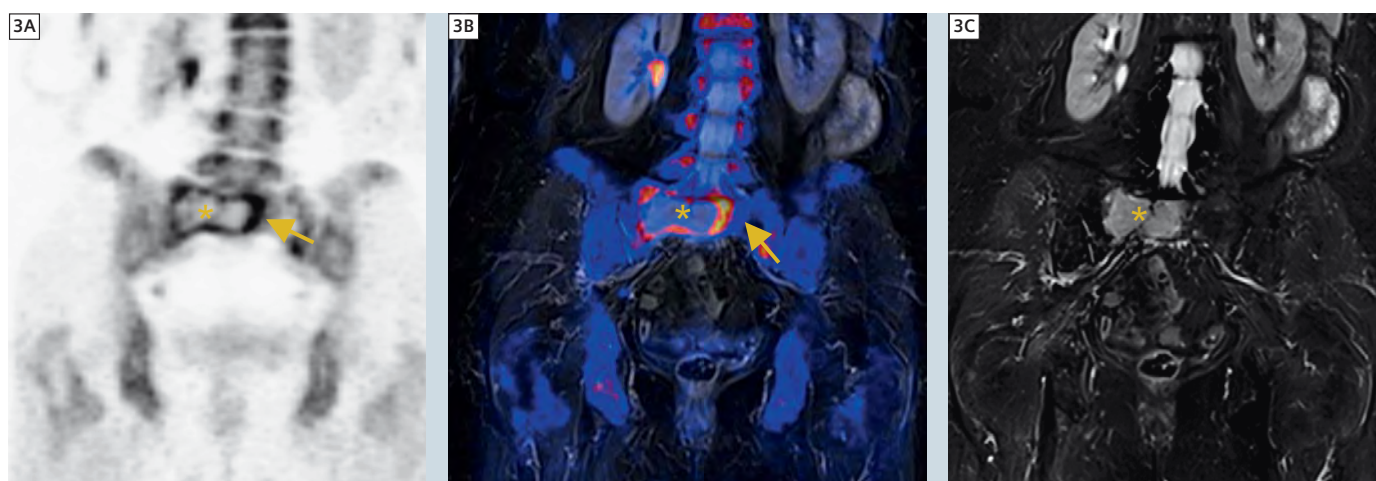
A 91-year-old female with severe sacral pain was referred to our institution for a bone scan with [ $^{18}\text{F}$ ] as substitute to bone scintigraphy. The patient was diagnosed in 1986 with breast cancer and in 2004 a malignoma of the uterus was treated. Application of [ $^{18}\text{F}$ ] was performed according to guidelines. MR/PET was conducted as a multi-step exam covering the whole body. During simultaneous PET acquisition, a coronal T1w TSE (512 matrix, 450 mm FOV, 5 mm SL) and T2w STIR (384 matrix, 450 mm FOV, 5 mm SL) was acquired. In addition, a transversal DWI was measured (b-values 50, 400, 800 s/mm<sup>2</sup>, spectral fat saturation, 192 matrix, 5 mm SL; inline ADC calculation). All images shown were acquired using Biograph mMR (Siemens Healthcare, Erlangen, Germany) and a combination of the head/neck, spine and body coils.

### Imaging findings

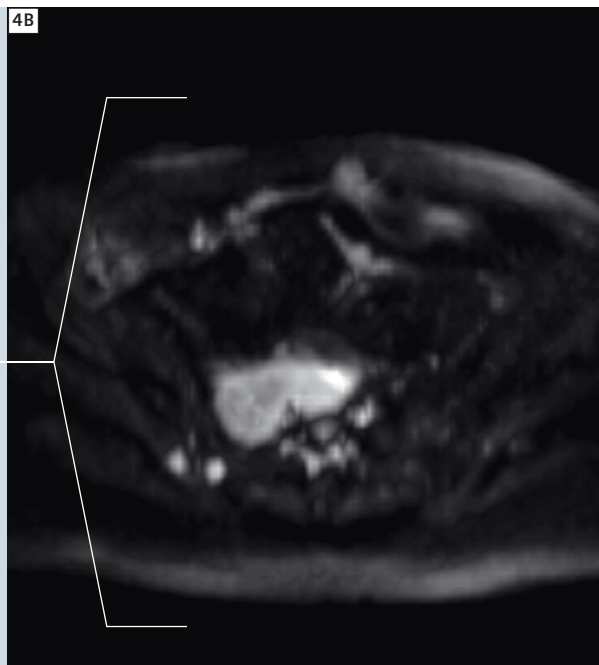
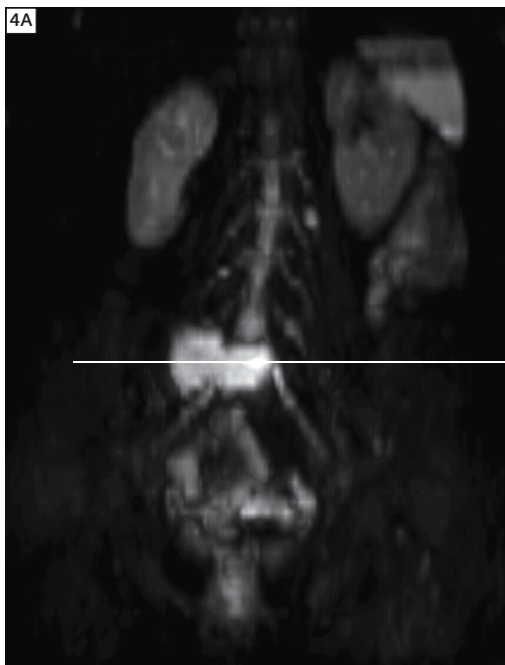
A large osteolytic lesion is shown within the sacral bone (massa lateralis). A clear mismatch between lesion size and corresponding bone formation is obvious. In addition, tumor-suspicious bone formation with corresponding lytic aspect in MRI is demonstrated for the 10<sup>th</sup> and 7<sup>th</sup> right rib. Based on DWI, these lesions are characterized by high signal on the original b-value images and restriction of water diffusion. In addition, multiple degenerative bone formations without corresponding oedema in MRI are visualized: spondylosis of the thoracic spine and coxarthrosis of the right hip are the most obvious ones. Focal uptake is also seen in the dorsal process of the 6<sup>th</sup> and 7<sup>th</sup> cervical vertebra. Based on T2w STIR images at least for the bone formation of the 7<sup>th</sup> vertebra a corresponding hyperintense lesion with space occupying aspects at least on the coronal original orientation can be shown. Often reactive oedema can be seen also in degenerative findings, however, based on the space occupying appearance further manifestation of the bone metastases



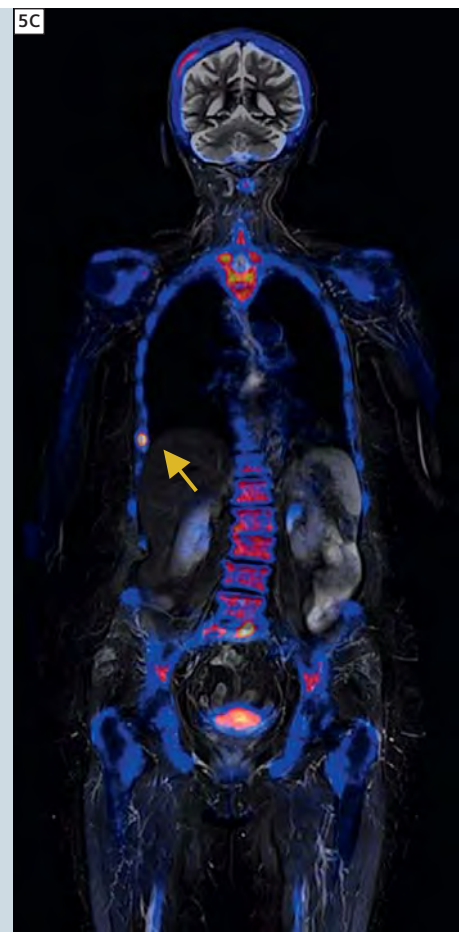
**2** Sagittal MIP (2A), coronal (2B), thick-slice MIP (2C) showing pathologic bone formation within the os sacrum and the 10<sup>th</sup> and 7<sup>th</sup> right rib as well as the 7<sup>th</sup>/6<sup>th</sup> cervical vertebra (dorsal processus) (arrows). In addition, multiple degenerative bone formation can be seen (e.g. spondylosis of the thoracic spine; asterisk).



**3** Clear mismatch between bone formation (arrows) and true extend of the metastasis (asterisk) in the massa lateralis of the os sacrum is shown. Coronal multiplanar reconstruction (MPR) of the [<sup>18</sup>F] PET (3A), overlay of metabolic information on MRI (3B), corresponding coronal T1w TIRM (3C).



**4** Thick-slice MPR based on the  $b = 800 \text{ s/mm}^2$  DWI images. By suppression of the background the tumor tissue is well delineated. ADC mapping (not shown) did proof restriction of water diffusion. Coronal (4A) and transversal (4B) reformation.



must be concluded. No evidence for further metastases within the long bones of the upper and lower (not shown) extremities, no fractures or soft tissue involvement, no spinal cord compression. The used protocol was mainly focused on the skeletal system, however, further tumor manifestations outside the bone (including lymph nodes) can be ruled out with sufficient diagnostic accuracy.

### Diagnosis

Multifocal metastatic disease of the skeletal system has to be concluded. Based on imaging findings and patient history, a late metastatic manifestation of the mamma carcinoma seems to be the most plausible explanation. With increased

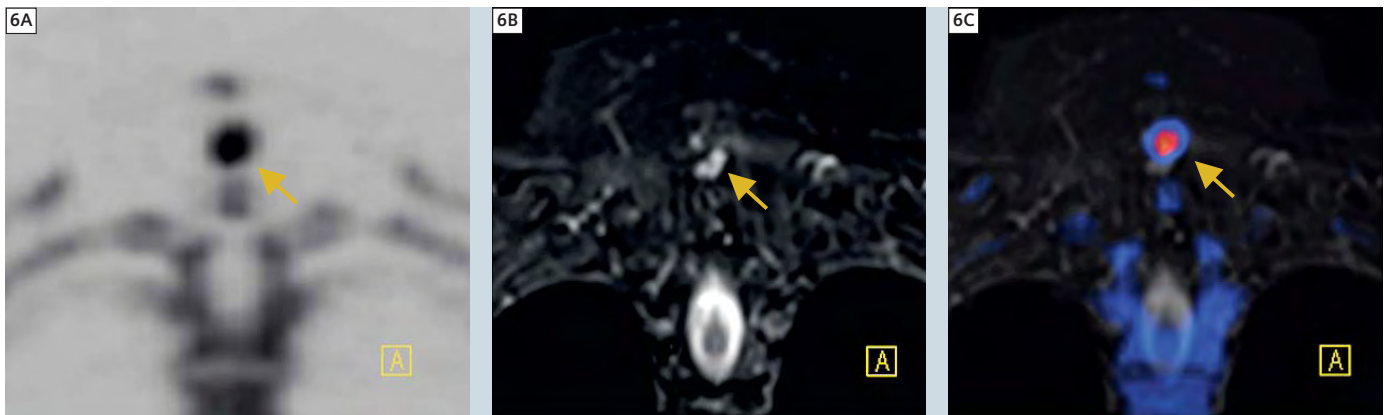
numbers of successful treatment of the primary tumor and also in concordance with latest epidemiological data, tumor recurrence of mamma carcinoma after the 5-years follow-up interval has to be taken into account. However, a third tumor manifestation cannot be ruled out based only on imaging findings and missing presence of a potential primary tumor. Therefore the final conclusion of this exam has to be bone metastases of a cancer of unknown primary (CUP). Because of clinical presentation (severe pain), a therapy relevance is obvious but further diagnosis and therapy will be to be discussed in detail and based on a very individual decision as a consequence of the patients age and general condition.

### Conclusion

Combining [ $^{18}\text{F}$ ] PET and MRI in one simultaneous exam is appropriate when it comes to providing best patient care. Based on the knowledge with PET and MRI alone, it is more than justified in our opinion to state that this imaging method can be applied to a large cohort of patients. While the presented case may be a not so common clinical scenario for the future application of MR/PET, it clearly demonstrates the potential of this method as the most accurate method for evaluation of osseous and bone marrow processes. Especially in cases with suspicion of bone marrow involvement and for younger patients, simultaneous MR/PET will play an important role in the future. How far



**5** Excellent spatial registration between MRI and PET data is shown exemplary with the small osteolytic metastasis of the right lateral thoracic wall (10<sup>th</sup> rib). Coronal MPR of [ $^{18}\text{F}$ ] PET (5A), corresponding T2w TIMR (5B), overlay of PET data on T2w TIRM (5C), corresponding T1w TSE without (5D) and with (5E) overlay of PET information.



**6** The pathologic bone formation of the 6<sup>th</sup> and especially 7<sup>th</sup> (coronal MPR of the PET is shown in (6A)) dorsal processus of the cervical vertebra has also to be rated as potentially metastastic. A space occupying lesion with similar imaging features as shown for the other metastases can be demonstrated on the coronal T2w TIRM MRI (6B); the overlay of the PET data (6C) shows a slight spatial mismatch of the two imaging modalities as a consequence of the different imaging mechanisms of [<sup>18</sup>F] PET (bone formation metabolism) and MRI (soft tissue characteristics).

this method will be added to, or will even replace, conventional imaging will of course be also a question of upcoming therapy options and tracers e.g. for evaluation of hormone receptor status. But certainly the presented combination of [<sup>18</sup>F] PET and MRI is already a further step towards a more accurate and patient-specific diagnoses and therapy selection – and all within one exam.

#### References

- 1 Cook GJ. PET and PET/CT imaging of skeletal metastases. *Cancer Imaging*. 2010 Jul 19;10:1-8.
- 2 Hellwig D, Krause BJ, Schirrmeister H, Freesmeyer M. [Bone scanning with sodium <sup>18</sup>F-fluoride PET and PET/CT. German guideline Version 1.0.]. *Nuklearmedizin*. 2010;49(5):195-201. Epub 2010 Sep 13.
- 3 Hahn S, Heusner T, Kümmel S, Köninger A, Nagarajah J, Müller S, Boy C, Forsting M, Bockisch A, Antoch G, Stahl A. Comparison of FDG-PET/CT and bone scintigraphy for detection of bone metastases in breast cancer. *Acta Radiol*. 2011 Nov 1;52(9):1009-14. Epub 2011 Oct 3.
- 4 Withofs N, Graye B, Tancredi T, Rorive A, Mella C, Giacomelli F, Mievie F, Aerts J, Waltregny D, Jerusalem G, Hustinx R. <sup>18</sup>F-fluoride PET/CT for assessing bone involvement in prostate and breast cancers. *Nucl Med Commun*. 2011 Mar;32(3):168-76.
- 5 Yen RF, Chen CY, Cheng MF, Wu YW, Shiau YC, Wu K, Hong RL, Yu CJ, Wang KL, Yang RS. The diagnostic and prognostic effectiveness of F-18 sodium fluoride PET-CT in detecting bone metastases for hepatocellular carcinoma patients. *Nucl Med Commun*. 2010 Jul;31(7):637-45.
- 6 Pfannenbergs C, Aschoff P, Schanz S, Eschmann SM, Plathow C, Eigentler TK, Garbe C, Brechtel K, Vonthein R, Bares R, Claussen CD, Schlemmer HP. Prospective comparison of <sup>18</sup>F-fluorodeoxyglucose positron emission tomography/computed tomography and whole-body magnetic resonance imaging in staging of advanced malignant melanoma. *Eur J Cancer*. 2007 Feb;43(3):557-64. Epub 2007 Jan 16.
- 7 Müller-Horvat C, Radny P, Eigentler TK, Schäfer J, Pfannenbergs C, Horger M, Khorchidi S, Nägele T, Garbe C, Claussen CD, Schlemmer HP. Prospective comparison of the impact on treatment decisions of whole-body magnetic resonance imaging and computed tomography in patients with metastatic malignant melanoma. *Eur J Cancer*. 2006 Feb;42(3):342-50. Epub 2005 Dec 20.
- 8 Schmidt GP, Reiser MF, Baur-Melnyk A. Whole-body MRI for the staging and follow-up of patients with metastasis. *Eur J Radiol*. 2009 Jun;70(3):393-400. Epub 2009 May 19. Review.
- 9 Ketelsen D, Röthke M, Aschoff P, Merseburger AS, Lichy MP, Reimold M, Claussen CD, Schlemmer HP. [Detection of bone metastasis of prostate cancer – comparison of whole-body MRI and bone scintigraphy]. *Rofo*. 2008 Aug;180(8):746-52. Epub 2008 May 29. German.
- 10 Wu LM, Gu HY, Zheng J, Xu X, Lin LH, Deng X, Zhang W, Xu JR. Diagnostic value of whole-body magnetic resonance imaging for bone metastases: a systematic review and meta-analysis. *J Magn Reson Imaging*. 2011 Jul;34(1):128-35. doi: 10.1002/jmri.22608. Epub 2011 May 25.
- 11 Padhani AR, Koh DM, Collins DJ. Whole-body diffusion-weighted MR imaging in cancer: current status and research directions. *Radiology*. 2011 Dec;261(3):700-18. Review.
- 12 Schlemmer HP, Pichler BJ, Krieg R, Heiss WD. An integrated MR/PET system: prospective applications. *Abdom Imaging*. 2009 Nov;34(6):668-74.
- 13 Schwenzer NF, Schmidt H, Claussen CD. Whole-body MR/PET: applications in abdominal imaging. *Abdom Imaging*. 2012 Feb;37(1):20-8.
- 14 Delso G, Martinez-Möller A, Bundschuh RA, Ladebeck R, Candius Y, Faul D, Ziegler SI. Evaluation of the attenuation properties of MR equipment for its use in a whole-body PET/MR scanner. *Phys Med Biol*. 2010 Aug 7;55(15):4361-74. Epub 2010 Jul 20.
- 15 Delso G, Fürst S, Jakoby B, Ladebeck R, Ganter C, Nekolla SG, Schwaiger M, Ziegler SI. Performance measurements of the Siemens mMR integrated whole-body PET/MR scanner. *J Nucl Med*. 2011 Dec;52(12):1914-22. Epub 2011 Nov 11.

#### Contact

Markus G. Lentschig, M.D.  
ZEMODI  
Zentrum für Moderne Diagnostik  
Schwachhauser Heerstr. 63a  
28211 Bremen  
Germany  
Phone +49 421 69641-600  
Fax +49 421 69641-649  
www.zemodi.de

# What's your favorite Dot Feature?

Dot (Day optimizing throughput) is the most comprehensive MRI workflow solution, and it helps take the complexity out of MRI. Dot has now established itself in the field and our customers have told us what they like best about Dot:



“Within our environment, we just could not provide a cardiac MRI service without the Cardiac Dot Engine.”

**Dr. Russell Bull, MRCP, FRCR**  
Consultant Radiologist  
*Royal Bournemouth Hospital, Bournemouth, UK*



“The Dot Decisions functionality in Abdomen Dot has enabled us to schematize and simplify these protocols. With Dot, we can now ensure our examinations are far more reproducible and of excellent quality.”

**Arnaud Lambert**  
Technologist  
*Imagerie Médicale Saint Marie, Osny, France*



“Cardiac Dot (Engine) allows us to obtain automatic positioning of the main slices necessary to evaluate cardiac function with a high degree of reproducibility.”

**Professor Philippe Cluzel, MD, PhD**  
*Service de Radiologie Polyvalente Diagnostique et Interventionnelle Hôpital Pitié-Salpêtrière, Paris, France*



“AutoAlign is helpful especially for colleagues who rarely perform knee examinations because the slices are positioned automatically, which saves a lot of time. Furthermore, our knee examinations have become reproducible.”

**Linda Willeke**  
Technologist  
*St. Franziskus Hospital, Münster, Germany*

Experience a Dot workflow yourself and hear from more customers at

**[www.siemens.com/Dot](http://www.siemens.com/Dot)**

Dot is now available for 3T MAGNETOM Skyra and MAGNETOM Verio and for 1.5T MAGNETOM Aera and MAGNETOM Avanto.

Visit our site  
optimized for  
tablets and  
smartphones



# Magnetic Resonance Elastography: Proven Indications, Challenges and Future Considerations

Sudharshan Parthasarathy, MS<sup>1</sup>; Bradley D. Bolster, Jr, Ph.D.<sup>2</sup>; Frank H. Miller, M.D.<sup>3</sup>

<sup>1</sup>Chicago Medical School, Rosalind Franklin University of Medicine, North Chicago, IL, USA

<sup>2</sup>Siemens Healthcare, Rochester, MN, USA

<sup>3</sup>Northwestern Memorial Hospital, Northwestern University Feinberg School of Medicine, Department of Radiology, Chicago, IL, USA

## Introduction

Magnetic Resonance Elastography (MRE)\* is a rapidly developing, non-invasive, accurate and reproducible imaging technique to assess the mechanical properties of tissue, which are dramatically affected by pathological disease processes such as inflammation, cancer and fibrosis. Physicians have long relied on the 'palpation' of tissue as a qualitative diagnostic tool in the detection of these pathologies, but this technique is limited

to only superficial organs and pathologies and lacks objectivity [1]. Developed by Dr. Richard Ehman and colleagues at Mayo Clinic, MRE serves as a technique to quantitatively evaluate the propagation of mechanical shear waves through tissue. Using a modified phase-contrast magnetic resonance imaging (MRI) technique that generates spatial maps and measurements of shear wave displacement patterns called elastograms, MRE can be implemented onto a conventional MRI system with a few hardware and software modifications [2]. While the technique has been reported in a variety of organs including brain [3–7], breast [8–12], blood vessels, heart [13–15], lung [16–20], pancreas and kidneys [21, 22], MRE is developing as a safe, reliable and non-invasive alternative to liver biopsy in the detection and staging of chronic liver fibrosis [2, 23–26]. To date, MRE has also been compared to other non-invasive imaging techniques including ultrasound-based transient elastography (TE) [27], diffusion-weighted imaging (DWI) [24] and conventional MR imaging markers [28]. It may be used to monitor treatment response or disease progression. Moreover, MRE has also been investigated in helping to identify individuals with steatohepatitis in patients with non-alcoholic fatty liver [29], characterize hepatic tumors [30], assess fibrosis in pediatric populations [31] and liver transplant patients with recurrent



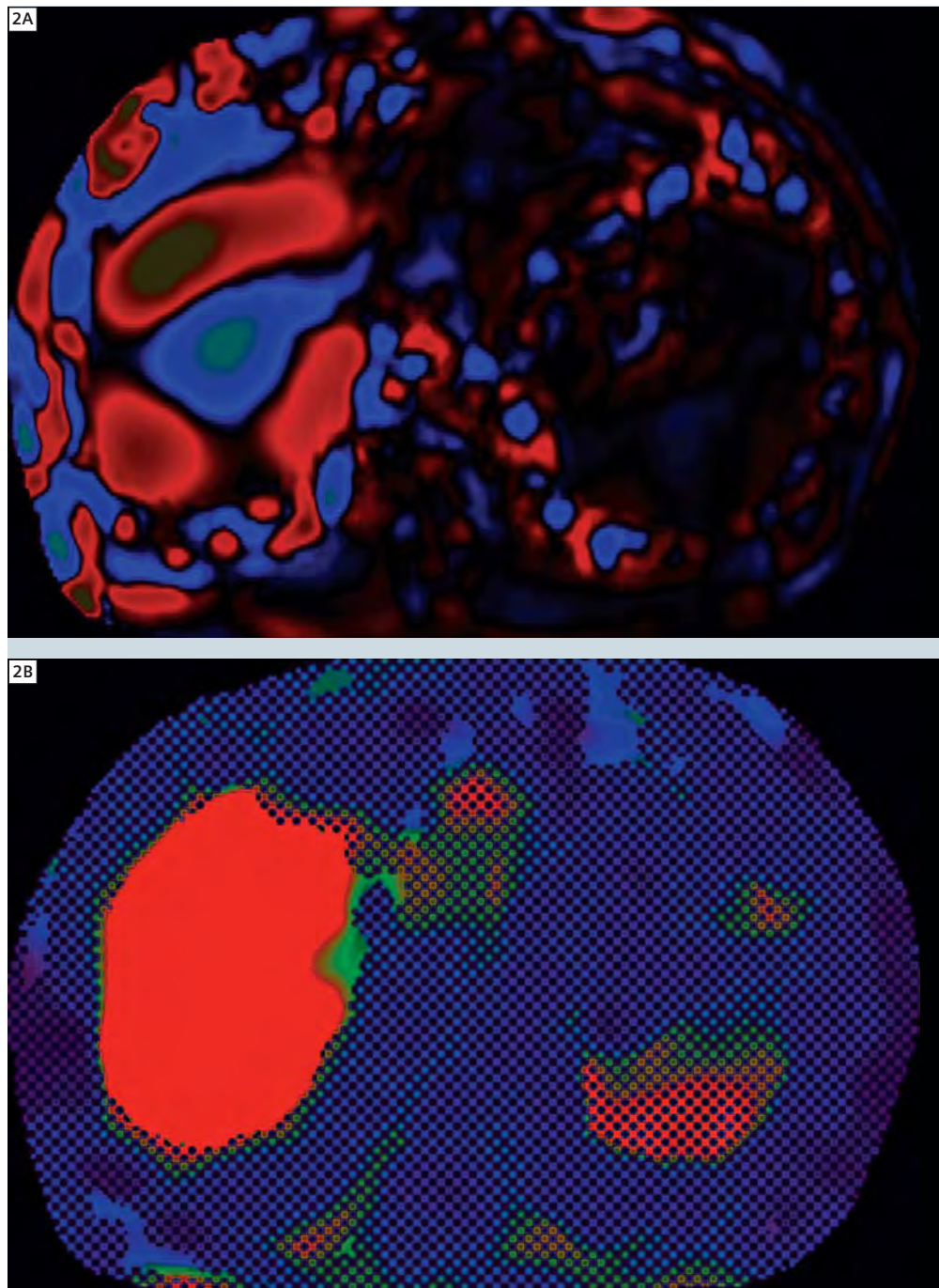
**1** Photograph of an acoustical active and passive driver system for MRE with connecting tubing. The active driver is shielded from the imaging magnet and delivers vibrational energy to the passive driver at 60 Hz through the connecting tube. The passive driver is placed across the right anterior chest wall to deliver vibrations transcostally into the liver.

\*This technology is not currently available with Siemens scanners in the US.

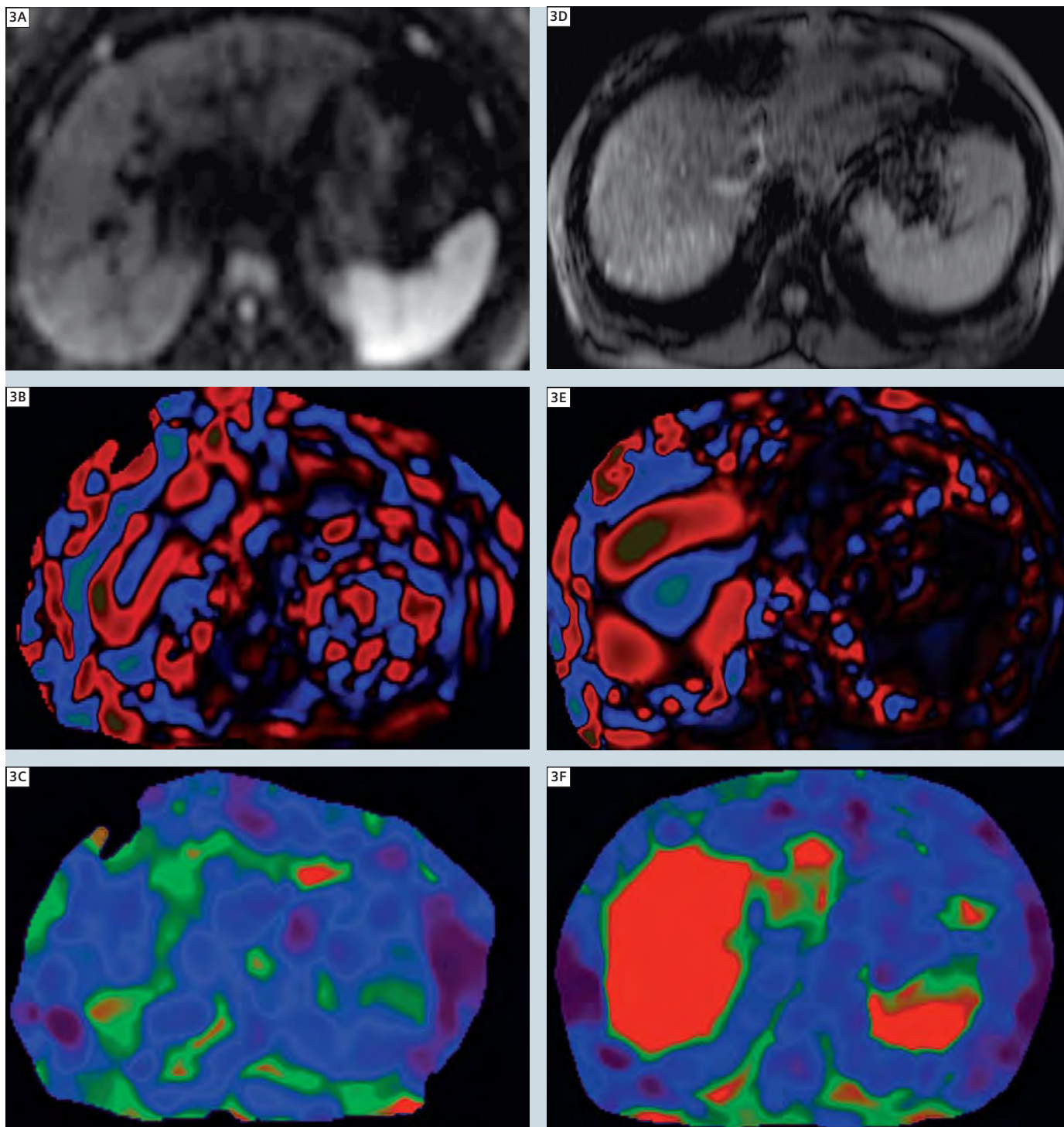
hepatitis C [32] and serve as a guide for MR-guided biopsies [33]. The following provides a summary of some of the proven indications, challenges and future considerations for MRE as an evolving imaging technique.

### MRE protocol in our institution

MRE is well tolerated by patients, it is non-invasive and does not require contrast material. To perform hepatic MRE, mechanical waves are generated in the liver with a special MRI-compatible driver system (Resoundant Inc, Rochester, MN, USA). The system consists of an active driver, located outside the magnet room, which generates continuous low frequency vibrations. These vibrations are transmitted via a flexible tube to a drum-like passive driver (19 cm diameter, 1.5 cm thick flat and disc shaped), which is placed directly against the anterior right chest wall over the liver and held in place by an abdominal binder (Fig. 1). The propagating shear waves are imaged with a modified phase difference gradient-echo sequence which incorporates first moment nulled cyclic motion encoding gradients sensitive to through-plane motion. The Resoundant system is synchronized to these gradients via a trigger provided by the imager. The trigger time is stepped to provide a sample of the propagating wave field at four different phase offsets. The parameters of the MRE sequence are as follows: repetition time (TR) / echo time (TE), 50/22.9 msec; flip angle 25°; bandwidth 260 Hz/pixel; acquisition matrix 256 x 64; section thickness 5 mm; field-of-view (FOV) 390 x 390 mm<sup>2</sup>. The scanning time of each trans-axial slice is 21 seconds with breath-hold. Four trans-axial slices at different anatomic levels are acquired. The resulting phase images depicting the waves in the liver for each slice are automatically processed using an inversion algorithm to generate quantitative images depicting the stiffness of the liver (elastograms) [23, 34–36].



**2** (2A) Wave image shows the propagation of the shear waves through the hepatic parenchyma. (2B) Color-coded elastogram shows markedly elevated stiffness values with a mean 15 kPa consistent from severe fibrosis.



**3** Example anatomic images, wave images and shear stiffness maps (elastograms) in a normal patient with elevated liver enzymes (3A–C) and biopsy-proven stage 4 fibrosis (F4) (3D–F). Shear stiffness was measured to be 2.1 kPa in the normal patient and 14 kPa in the patient with F4 fibrosis.

## MR Elastography analysis

To analyze the MRE results, regions of interest (ROI) are placed on the MR elastograms. When placing an ROI, care is taken to avoid bile ducts and large vessels within the liver, motion artifacts, the region immediately below the driver, and the left lobe of liver (which is prone to artifacts due to transmitted cardiac motion). For the measurement of shear stiffness using MRE, the ROIs are first visually transposed onto the wave images to ensure that they were placed in regions with adequate wave quality. A region is determined to have adequate wave quality if the propagating waves had both good amplitude and the presence of a clear dominant propagation direction. Subsequently, the ROI locations are visually transposed onto the quantitative elastogram image and mean stiffness values (in kilopascals, kPa) are calculated (Figs. 2A, B).

### MRE in the detection and staging of liver fibrosis

Liver biopsy is currently the gold standard for detecting fibrosis and cirrhosis. As an invasive procedure, it has an increased risk for potential complications such as procedural pain, bleeding, pneumothorax, biliary tree puncture and death (approximately 1 in 10,000–12,000) [37]. From a clinical perspective, one of the greatest limitations with biopsy is a significant sampling error of up to 14.5% and 25% when determining presence or absence of cirrhosis [38]. Based on recent studies, MRE is receiving attention as a non-invasive alternative. Thus far, MRE has shown that it can be an accurate method for both the detection (Figs. 3A–F) and staging (Figs. 4A–D) of hepatic fibrosis [2, 23–26]. Receiver operating characteristic (ROC)

analysis by Yin et al. comparing 50 patients with biopsy-proven liver disease and 35 healthy controls showed 98% sensitivity and 99% specificity for the detection of liver fibrosis with a shear stiffness cutoff value of 2.93 kPa [26]. ROC analysis also showed that MRE was able to discriminate between patients that had moderate to severe fibrosis (F2–F4) and those that had mild fibrosis based on the METAVIR histopathological staging system (F0–F1) [26]. The ability to distinguish moderate to severe fibrosis from mild fibrosis is clinically significant, as treatment is advised for a score of F2 or greater by the American Association for the study of liver diseases [39]. More recent studies by Wang et al. [24], Rustogi et al. [28], Kim et al. [40] and Huwart et al. [25] have demonstrated comparable sensitivity and specificity ranges (Table 1).

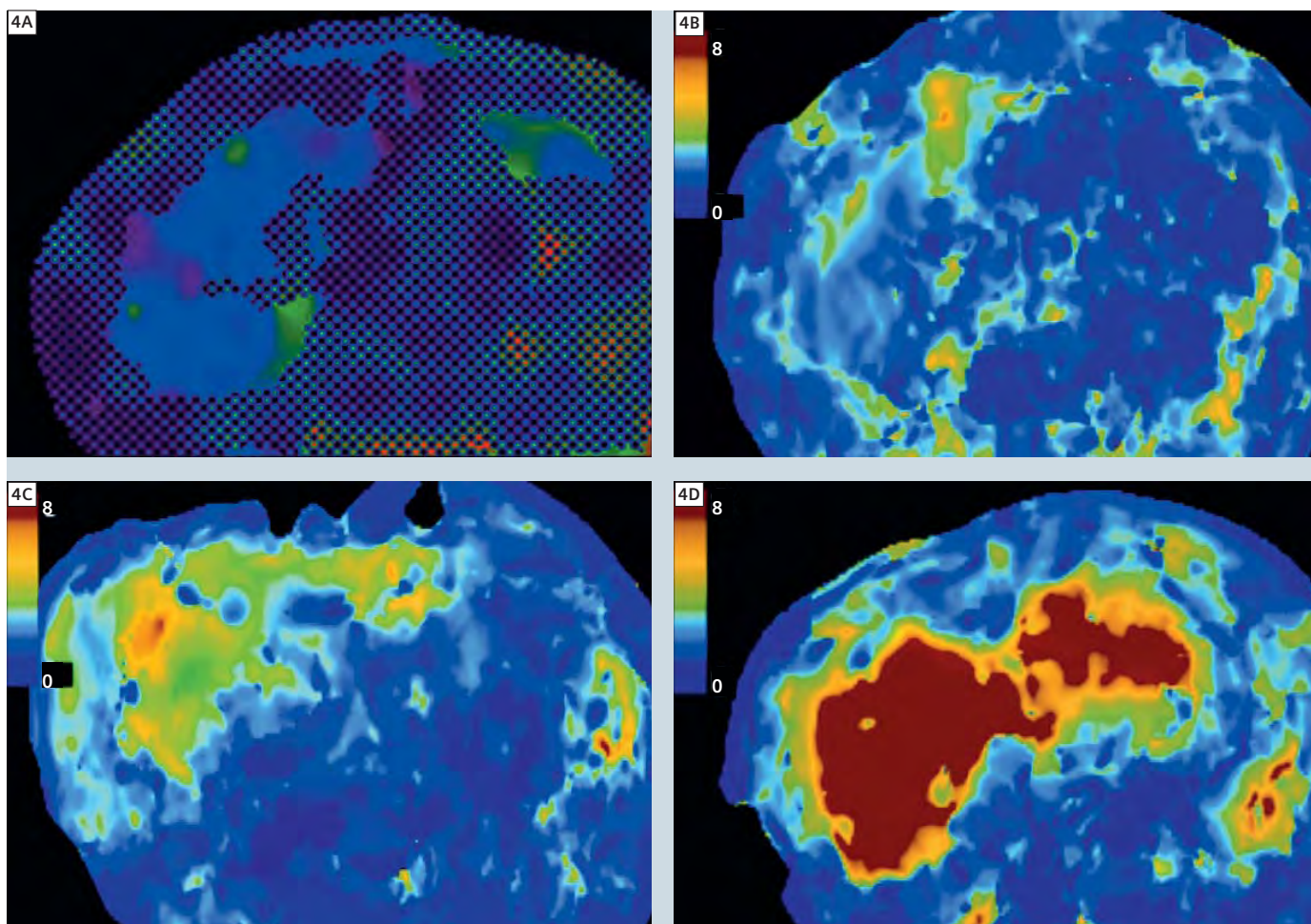
### MRE versus other non-invasive assessments of liver fibrosis

Studies have also begun to compare MRE to other non-invasive techniques in the detection and staging of liver fibrosis. One study of 141 patients with chronic liver disease comparing MRE and ultrasound transient elastography (TE) showed that MRE had a higher technical success rate (94%) than TE (84%) [25]. In addition, areas under the curve (AUC) in ROC analysis for MRE were significantly larger than those of TE, aspartate aminotransferase to platelets ratio index (APRI), and the combination of TE and APRI [25]. Significantly, MRE measurements did not seem to be influenced by the presence of obesity or ascites, which cause TE to fail, or steatohepatitis [41]. Furthermore, MRE evaluates a global view of the liver, whereas TE looks at only a 1 cm x 4 cm area over the right liver edge. While TE has also demonstrated excellent sensitivity and specificity for the detection of fibrosis compared to biopsy, it has reduced values of 70%

and 80%, respectively, compared to MRE (86% and 85% respectively) [26] in the detection of intermediate stages of fibrosis (F2–F4) [42].

More recently, the diagnostic performance of MRE was compared to diffusion-weighted imaging (DWI). ROC analysis showed that MRE had greater accuracy in assessing the severity of fibrosis compared with DWI using histopathology as a reference standard. In a group of 76 patients [32], MRE had greater predictive ability in distinguishing the stages of liver fibrosis than DWI [24]. Specifically, MRE showed greater capability than DWI in discriminating stages F2 or greater, F3 or greater and F4 as shown as significant differences in AUC analysis. While stiffness values on MRE increased in relation to increasing severity of fibrosis, no consistent relationship between apparent diffusion coefficient (ADC) values and stage of fibrosis was shown.

Another recent study has compared the diagnostic accuracy of MRE and conventional anatomic MR imaging features in the diagnosis of severe hepatic fibrosis and cirrhosis [28]. Three readers independently assessed 72 patients with liver biopsy for conventional imaging features such as caudate to right lobe ratios and expanded gallbladder fossa sign compared with shear stiffness values from MR elastograms. Sensitivity, specificity and diagnostic accuracy was calculated and intra-class correlation coefficient was used to assess inter-reader reproducibility. MRE proved to be a more accurate and reproducible technique compared to conventional imaging features with a higher intra-class correlation coefficient and better diagnostic accuracy.



**4** Liver stiffness values (kPa) represented through elastograms increased in parallel with the degree of fibrosis (stages F0-F4). **(4A)** Shear stiffness was measured to be 2.1 kPa in normal liver tissue, **(4B)** 2.9 kPa in fibrosis stage F1, **(4C)** 4.1 kPa in fibrosis stage F2, and **(4D)** 10.5 kPa in fibrosis stage F4.

### MRE for the early detection of non-alcoholic steatohepatitis (NASH)

Associated with obesity and type 2 diabetes mellitus, non-alcoholic fatty liver disease (NAFLD) is a clinical condition now estimated to affect 1 in 3 adults in the US [43]. Up to 25% of NAFLD patients develop non-alcoholic steatohepatitis (NASH), which can progress to cirrhosis in susceptible individuals [44]. Since a diagnosis of NASH currently requires an invasive liver biopsy to help detect and stage liver cell injury, MRE has been investigated as an alternative

technique that could help in early detection. Using a rat model of fatty liver disease, Salameh et al. showed that MRE could help to discriminate the presence of steatohepatitis from simple steatosis before the onset of fibrosis [45]. This led to a retrospective study of 58 NAFLD patients to investigate the variation of liver stiffness in patients ranging from simple steatosis to NASH. MRE was able to show that NAFLD patients with NASH but no fibrosis had higher hepatic stiffness measurements than patients with simple steatosis [29] (Fig. 4).

### MRE in the characterization of liver tumors

While it is well known that cirrhosis is the strongest predisposing factor for the development of hepatocellular carcinoma (HCC), the detection of small tumors presents the greatest challenge to imaging in HCC [46]. The application of MRE to HCC may be a promising tool in the characterization of hepatic tumors. A preliminary investigation has shown that malignant liver tumors have a significantly greater mean shear stiffness than benign liver tumors as well as normal liver tissue parenchyma by estab-

**Table 1: Selected diagnostic ranges of MRE-assessed hepatic fibrosis in patients with chronic liver disease from various studies.**

Reference	N	Cutoff	Sensitivity	Specificity	Liver Stiffness, kPa
Yin et al.	85	F0-1:F2-4	86	85	4.9
		F0-2:F3-4	78	96	6.7
Huwart et al.	88	F0-1:F2-4	98	100	2.5
		F0-2:F3-4	95	100	3.1
Huwart et al.	133	F0-1:F2-4	100	91	2.5
		F0-2:F3-4	91	97	3.1
Kim et al.	55	F0-1:F2-4	89	87	3.1
Wang et al.	76	F0-1:F2-4	91	97	5.4
		F0-2:F3-F4	92	95	5.9

lishing a cutoff value of 5 kPa [30]. Since the technique can be readily combined as a complement to conventional MRI of the abdomen, it shows potential in further characterization and early detection of liver tumors [47]. A potential limitation may be in the cirrhotic liver where the background liver may be as stiff as the HCC but further investigation will be required.

### MRE in the assessment of fibrosis in liver transplant recipients

MRE has also been compared to various biomarkers to assess efficacy in the staging of fibrosis in liver transplant recipients with recurrent hepatitis C (HCV) with HCC [32]. While limited by graft complications, MRE and serum panels like FIBROSpectII have high sensitivity in detecting fibrosis from recurrent HCV, but are limited by poor specificity and positive predictive value (PPV). MRE could avert the need for liver biopsy, as values below the MRE and FIBROSpectII cutoffs strongly suggested the absence of fibrosis in transplant recipients with recurrent HCV.

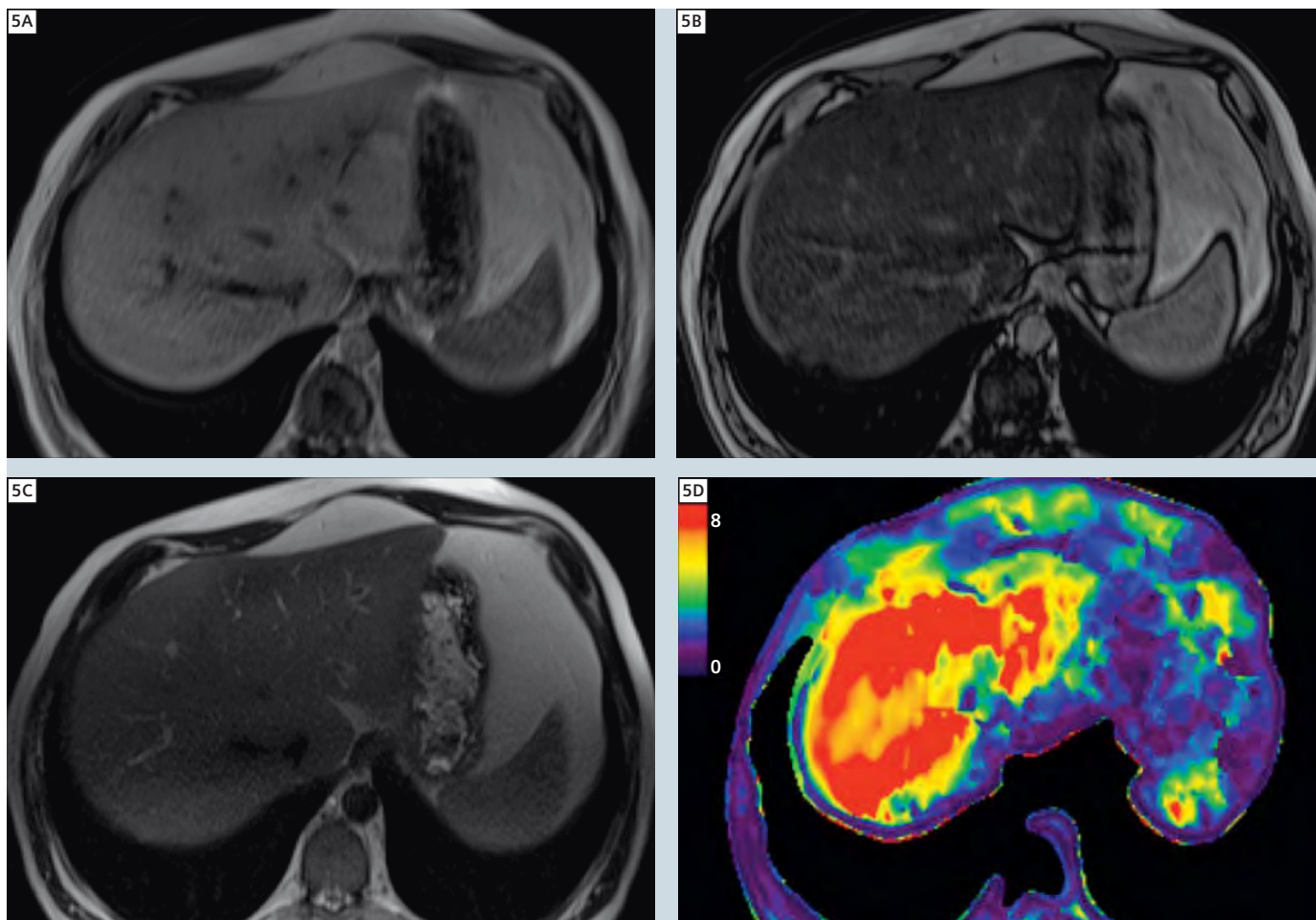
### Challenges / difficulties with MRE

Future challenges and difficulties with MRE lie mainly in further technical development. The widespread use of MRE relies on the same technology and infrastructure as conventional MR imaging, and so claustrophobic or very obese patients and those with contraindications to MRI will be excluded from investigation due to an inability to enter the scanner. Other challenges include technical failure in patients with hemochromatosis and iron overload conditions because of signal-to-noise limitations [25]. Falsely elevated shear stiffness values have been reported in regions just below the passive driver used to generate shear waves. Liver stiffness can be increased without the presence of fibrosis in pathological processes such as inflammation, hepatic congestion, and vascular abnormalities [24, 28]. Since MRE is a relatively new technique, improved driver technologies [48] and refined imaging sequences [49] are currently under development to produce more accurate shear stiffness values and improve signal-to-noise ratios. Moreover, in its bid to replace liver biopsy as a non-invasive technique in

the staging of detection of liver fibrosis, MRE must be evaluated for cost-effectiveness versus other non-invasive techniques. While researchers have proposed diagnostic algorithms to help define how to stage fibrosis incorporating these techniques, these algorithms are yet to be externally validated in independent populations.

### Conclusions and future outlook

MRE has received considerable interest as a quantitative technique to assess the same information evaluated pathology by the more qualitative clinical tool of palpation. As a non-invasive, accurate and reproducible technique, it is receiving consideration as a viable alternative to liver biopsy for the diagnosis and staging of hepatic fibrosis. Since many applications of MRE are currently under investigation in the liver, heart, brain and kidney, it is likely that MRE will continue to elucidate invaluable information about tissue structure and function. As the field continues to evolve rapidly, this information should help to guide clinicians and researchers improve clinical outcomes and management.



**5** (5A) In-phase (top left) and (5B) out-phase (top right) images show significant SI decrease, suggesting a diagnosis of non-alcoholic steatohepatitis (NASH). (5C) Liver cirrhosis cannot be identified based on routine T2-weighted image (bottom left). (5D) MRE elastogram (bottom right) shows shear stiffness of 7.51 kPa, suggesting fibrosis stage F4.

## Acknowledgement

The authors thank Bradley Bolster, Saurabh Shah, and Sven Zuehlsdorff of Siemens Healthcare and Dr. Richard Ehman of Mayo Clinic for their development of the MR technology used in this study and for the support of our program and reviewing this article. We would also like to acknowledge the hard work of Charles Fasanati RT and Judy Wood RT for the program's success.

## References

- Mariappan YK, Glaser KJ, Ehman RL. Magnetic resonance elastography: a review. *Clin Anat*. 2010;23(5):497-511.
- Yin M, Chen J, Glaser KJ, Talwalkar JA, Ehman RL. Abdominal magnetic resonance elastography. *Topics in magnetic resonance imaging : TMRI*. 2009;20(2):79-87.
- Kruse SA, Rose GH, Glaser KJ, et al. Magnetic resonance elastography of the brain. *NeuroImage*. 2008;39(1):231-7.
- Green MA, Bilston LE, Sinkus R. In vivo brain viscoelastic properties measured by magnetic resonance elastography. *NMR in biomedicine*. 2008;21(7):755-64.
- Sack I, Beierbach B, Hamhaber U, Klatt D, Braun J. Non-invasive measurement of brain viscoelasticity using magnetic resonance elastography. *NMR in biomedicine*. 2008;21(3):265-71.
- Streitberger KJ, Wiener E, Hoffmann J, et al. In vivo viscoelastic properties of the brain in normal pressure hydrocephalus. *NMR in biomedicine*. 2010.
- Streitberger KJ, Sack I, Krefting D, et al. Brain viscoelasticity alteration in chronic-progressive multiple sclerosis. *PloS one*. 2012;7(1):e29888.
- McKnight AL, Kugel JL, Rossman PJ, Manduca A, Hartmann LC, Ehman RL. MR elastography of breast cancer: preliminary results. *AJR American journal of roentgenology*. 2002;178(6):1411-7.
- Van Houten EE, Doyley MM, Kennedy FE, Weaver JB, Paulsen KD. Initial in vivo experience with steady-state subzone-based MR elastography of the human breast. *JMRI*. 2003;17(1):72-85.
- Sinkus R, Siegmann K, Xydeas T, Tanter M, Claussen C, Fink M. MR elastography of breast lesions: understanding the solid/liquid duality

- can improve the specificity of contrast-enhanced MR mammography. *Magnetic resonance in medicine*. 2007;58(6):1135-44.
- 11 Doyley MM, Perreard I, Patterson AJ, Weaver JB, Paulsen KM. The performance of steady-state harmonic magnetic resonance elastography when applied to viscoelastic materials. *Medical physics*. 2010;37(8):3970-9.
  - 12 Plewes DB, Bishop J, Samani A, Sciarretta J. Visualization and quantification of breast cancer biomechanical properties with magnetic resonance elastography. *Physics in medicine and biology*. 2000;45(6):1591-610.
  - 13 Kolipaka A, McGee KP, Manduca A, Anavekar N, Ehman RL, Araoz PA. In vivo assessment of MR elastography-derived effective end-diastolic myocardial stiffness under different loading conditions. *JMRI*. 2011;33(5):1224-8.
  - 14 Elgeti T, Laule M, Kaufels N, et al. Cardiac MR elastography: comparison with left ventricular pressure measurement. *Journal of cardiovascular magnetic resonance : official journal of the Society for Cardiovascular Magnetic Resonance*. 2009;11:44.
  - 15 Sack I, Rump J, Elgeti T, Samani A, Braun J. MR elastography of the human heart: noninvasive assessment of myocardial elasticity changes by shear wave amplitude variations. *Magnetic resonance in medicine*. 2009;61(3):668-77.
  - 16 Mariappan YK, Kolipaka A, Manduca A, et al. Magnetic resonance elastography of the lung parenchyma in an in situ porcine model with a noninvasive mechanical driver: correlation of shear stiffness with trans-respiratory system pressures. *Magnetic resonance in medicine*. 2012;67(1):210-7.
  - 17 Mariappan YK, Glaser KJ, Hubmayr RD, Manduca A, Ehman RL, McGee KP. MR elastography of human lung parenchyma: technical development, theoretical modeling and in vivo validation. *JMRI*. 2011;33(6):1351-61.
  - 18 McGee KP, Hubmayr RD, Levin D, Ehman RL. Feasibility of quantifying the mechanical properties of lung parenchyma in a small-animal model using (1)H magnetic resonance elastography (MRE). *JMRI*. 2009;29(4):838-45.
  - 19 McGee KP, Hubmayr RD, Ehman RL. MR elastography of the lung with hyperpolarized <sup>3</sup>He. *Magnetic resonance in medicine*. 2008;59(1):14-8.
  - 20 Goss BC, McGee KP, Ehman EC, Manduca A, Ehman RL. Magnetic resonance elastography of the lung: technical feasibility. *Magnetic resonance in medicine*. 2006;56(5):1060-6.
  - 21 Warner L, Yin M, Glaser KJ, et al. Noninvasive In vivo assessment of renal tissue elasticity during graded renal ischemia using MR elastography. *Investigative radiology*. 2011;46(8):509-14.
  - 22 Shah NS, Kruse SA, Lager DJ, et al. Evaluation of renal parenchymal disease in a rat model with magnetic resonance elastography. *Magnetic resonance in medicine*. 2004;52(1):56-64.
  - 23 Rouviere O, Yin M, Dresner MA, et al. MR elastography of the liver: preliminary results. *Radiology*. 2006;240(2):440-8.
  - 24 Wang Y, Ganger DR, Levitsky J, et al. Assessment of chronic hepatitis and fibrosis: comparison of MR elastography and diffusion-weighted imaging. *AJR American journal of roentgenology*. 2011;196(3):553-61.
  - 25 Huwart L, Sempoux C, Vicaux E, et al. Magnetic resonance elastography for the noninvasive staging of liver fibrosis. *Gastroenterology*. 2008;135(1):32-40.
  - 26 Yin M, Talwalkar JA, Glaser KJ, et al. Assessment of hepatic fibrosis with magnetic resonance elastography. *Clinical gastroenterology and hepatology : the official clinical practice journal of the American Gastroenterological Association*. 2007;5(10):1207-13 e2.
  - 27 Huwart L, van Beers BE. MR elastography. *Gastroenterologie clinique et biologique*. 2008;32(6 Suppl 1):68-72.
  - 28 Rustogi R, Horowitz J, Harmath C, et al. Accuracy of MR elastography and anatomic MR imaging features in the diagnosis of severe hepatic fibrosis and cirrhosis. *JMRI*. 2012.
  - 29 Chen J, Talwalkar JA, Yin M, Glaser KJ, Sanderson SO, Ehman RL. Early detection of nonalcoholic steatohepatitis in patients with nonalcoholic fatty liver disease by using MR elastography. *Radiology*. 2011;259(3):749-56.
  - 30 Venkatesh SK, Yin M, Glockner JF, et al. MR elastography of liver tumors: preliminary results. *AJR American journal of roentgenology*. 2008;190(6):1534-40.
  - 31 Binkovitz LA, El-Youssef M, Glaser KJ, Yin M, Binkovitz AK, Ehman RL. Pediatric MR elastography of hepatic fibrosis: principles, technique and early clinical experience. *Pediatric radiology*. 2011.
  - 32 Lee VS, Miller FH, Omary RA, et al. Magnetic resonance elastography and biomarkers to assess fibrosis from recurrent hepatitis C in liver transplant recipients. *Transplantation*. 2011;92(5):581-6.
  - 33 Perumpail R, Jin N, Wang Y, et al. Real-time MR-guided Biopsies to Target Focal Hepatic Fibrosis Detected with Magnetic Resonance Elastography. *International Society for Magnetic Resonance in Medicine*; 2010.
  - 34 Manduca A, Oliphant TE, Dresner MA, et al. Magnetic resonance elastography: non-invasive mapping of tissue elasticity. *Medical image analysis*. 2001;5(4):237-54.
  - 35 Muthupillai R, Lomas DJ, Rossman PJ, Greenleaf JF, Manduca A, Ehman RL. Magnetic resonance elastography by direct visualization of propagating acoustic strain waves. *Science*. 1995;269(5232):1854-7.
  - 36 Taouli B, Ehman RL, Reeder SB. Advanced MRI methods for assessment of chronic liver disease. *AJR American journal of roentgenology*. 2009;193(1):14-27.
  - 37 Carey E, Carey WD. Noninvasive tests for liver disease, fibrosis, and cirrhosis: Is liver biopsy obsolete? *Cleveland Clinic journal of medicine*. 2010;77(8):519-27.
  - 38 Regev A, Berho M, Jeffers LJ, et al. Sampling error and intraobserver variation in liver biopsy in patients with chronic HCV infection. *The American journal of gastroenterology*. 2002;97(10):2614-8.
  - 39 Strader DB, Wright T, Thomas DL, Seeff LB. Diagnosis, management, and treatment of hepatitis C. *Hepatology*. 2004;39(4):1147-71.
  - 40 Kim BH, Lee JM, Lee YJ, et al. MR elastography for noninvasive assessment of hepatic fibrosis: experience from a tertiary center in Asia. *JMRI*. 2011;34(5):1110-6.
  - 41 Talwalkar JA. Elastography for detecting hepatic fibrosis: options and considerations. *Gastroenterology*. 2008;135(1):299-302.
  - 42 Talwalkar JA, Kurtz DM, Schoenleber SJ, West CP, Montori VM. Ultrasound-based transient elastography for the detection of hepatic fibrosis: systematic review and meta-analysis. *Clinical gastroenterology and hepatology*. 2007;5(10):1214-20.
  - 43 Browning JD, Szczepaniak LS, Dobbins R, et al. Prevalence of hepatic steatosis in an urban population in the United States: impact of ethnicity. *Hepatology*. 2004;40(6):1387-95.
  - 44 Fassio E, Alvarez E, Dominguez N, Landeira G, Longo C. Natural history of nonalcoholic steatohepatitis: a longitudinal study of repeat liver biopsies. *Hepatology*. 2004;40(4):820-6.
  - 45 Salameh N, Larrat B, Abarca-Quinones J, et al. Early detection of steatohepatitis in fatty rat liver by using MR elastography. *Radiology*. 2009;253(1):90-7.
  - 46 Willatt JM, Hussain HK, Adusumilli S, Marrero JA. MR Imaging of hepatocellular carcinoma in the cirrhotic liver: challenges and controversies. *Radiology*. 2008;247(2):311-30.
  - 47 Lee JM, Choi BI. Hepatocellular nodules in liver cirrhosis: MR evaluation. *Abdominal imaging*. 2011;36(3):282-9.
  - 48 Mariappan YK, Rossman PJ, Glaser KJ, Manduca A, Ehman RL. Magnetic resonance elastography with a phased-array acoustic driver system. *Magnetic resonance in medicine*. 2009;61(3):678-85.
  - 49 Faria SC, Ganesan K, Mwangi I, et al. MR imaging of liver fibrosis: current state of the art. *Radiographics*. 2009;29(6):1615-35.

#### Contact

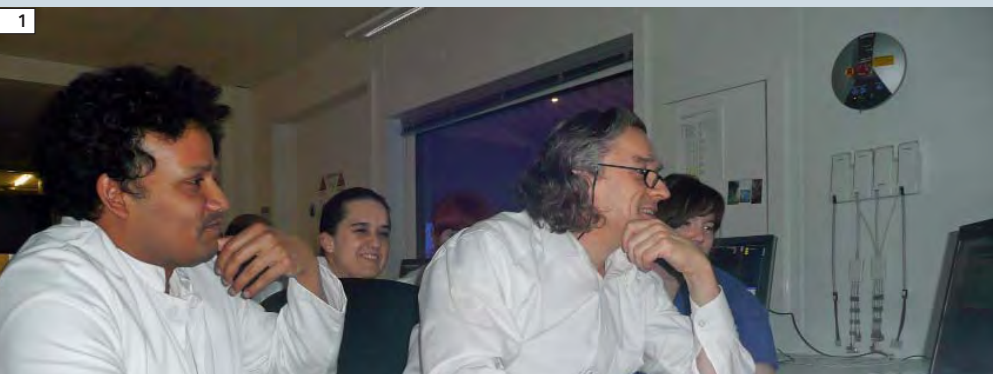
Frank H. Miller, M.D.  
 Professor of Radiology  
 Chief, Body Imaging Section  
 Medical Director MR Imaging  
 Department of Radiology  
 Northwestern University  
 Feinberg School of Medicine  
 676 N. St. Clair, Suite 800  
 Chicago, Illinois 60611  
 USA  
 Phone: +001 312-695-3775  
 Fax: +001 312-695-5645  
 fmiller@northwestern.edu

# Let's Dot it. How to Program a Dot Examination of the Liver

Anton S. Quinsten, RT<sup>1</sup>; Samantha Horry, RT<sup>1</sup>; Justine Molinnus, RT<sup>1</sup>; Simone Lohbeck, RT<sup>1</sup>; Dipl. Ing. Karl-Heinz Trümmeler<sup>2</sup>

<sup>1</sup>Institute for Diagnostic and Interventional Radiology and Neuroradiology, University Hospital Essen, Germany

<sup>2</sup>Siemens AG, Aachen, Germany



**1** First Dot training.

## Introduction

The Institute for Diagnostic and Interventional Radiology and Neuroradiology headed by Univ. Prof. Dr. med. M. Forsting at the University Hospital Essen is one of the largest radiology departments in Germany. We work with six MR systems in our institute. These include a 1.5T MAGNETOM Avanto, two 1.5T MAGNETOM Aera systems, one 3T MAGNETOM Skyra, one Biograph mMR and one 7 Tesla system\*, all from Siemens. Our department was one of the first clinical users of Dot<sup>§</sup> (day optimizing throughput) engines worldwide. After we had applied our basic knowledge in clinical operation, advanced training in Dot was held at our institute by Dipl. Ing. Karl-Heinz Trümmeler (an MRI application specialist from Siemens Healthcare). We enjoyed familiarizing ourselves with this software so much that, at the end, we even held a little competition to see who can

program best with Dot. If you take a close look at Dot you'll notice that this software is easy to program and will simplify your working life extremely. The following article should give you a better idea of how Dot works and encourage you to create your own examination programs tailored to your wishes.

## A brief insight into Dot

Using Dot, it is possible to optimize examination workflows and shorten examination times, e.g. through automated procedures. An automatic adaptation to the patient and his or her possibilities occurs. The system e.g. adapts the Dot protocol in the area of abdominal measurements to the patient's breath-holding capability while maintaining constant image quality. Furthermore, the field-of-view (FOV), number of slices and slice thickness also are

adapted automatically, thus reducing the acquisition time and increasing the efficiency of the examination. With Dot, the user is guided through the examination and made aware of important decision points. Even inexperienced Radiographers are thus able to perform more complex examinations without assistance.

Dot navigates the user through various examinations step-by-step while displaying helpful and practical hints and sample images during each sequence. Sequences can easily be added or removed via integrated decision points at the push of a button. Dot can easily be adapted to our standards with respect to examination routines, exposures and protocols.

Following registration, the patient data and positioning information appear in the Dot display on the scanner and are used to accelerate patient positioning and preparation, since the most important points are already visible on the scanner display in the examination room.

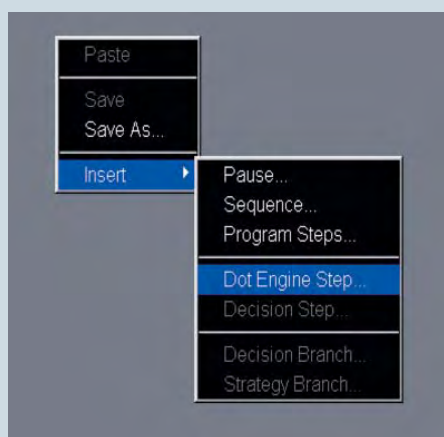
Dot ensures optimal timing between breathing and scanning via automatic breath-hold commands. The auto bolus detection ensures that the exposure will be taken at the correct point-of-time during contrast medium examinations. A new Dot engine can be created with an amazingly small number of mouse clicks. Dot constitutes a basic framework of strategies, patient context decisions and clinically decision points. In the following, we will explain some of the most important points that are inte-

\*This product is still under development and not yet commercially available. Its future availability cannot be ensured.

<sup>§</sup> Dot is now available for 3T MAGNETOM Skyra and MAGNETOM Verio and for 1.5T MAGNETOM Aera and MAGNETOM Avanto.

grated in a Dot engine.

**Dot engine step:** Each Dot engine begins with the Dot engine step. This specifies the kind of Dot involved and contains the exam-related configurations depending on the patient view. Additional functions open along with the different patient views, depending on the body region involved. There is a special patient view for each type of examination. These include Neuro, Onco (Abdomen), Cardio and Angio. During this first step, the entire framework is filled with strategies, patient context decisions and clinical decision

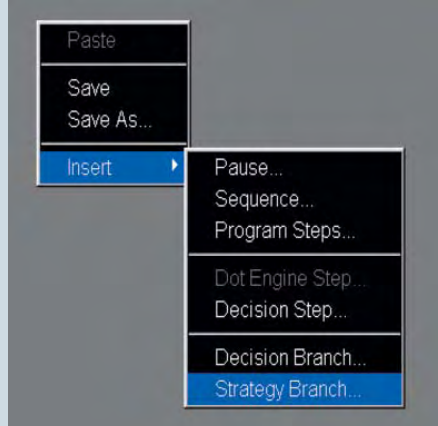


points.

**Strategy:** The strategies employed include the varying tactics required for different patients due to wide variations among the patient population, and may sometimes result in different sequences. This enables us to store the right sequences for each patient under a single Dot engine. Thus for example, a standard protocol can be saved for normal patients and a protocol with correspondingly faster sequences can be stored for restless patients and started during the examination. The user can coordinate the strategies to suit his or her own needs.

**Strategy branch:** The strategies previously defined when creating the Dot engine step are listed here. The appropriate strategy is selected while registering the patient and the corresponding sequences then open automatically. The

sequences that are suitable for the strategy are already selected and saved while creating the Dot engine.

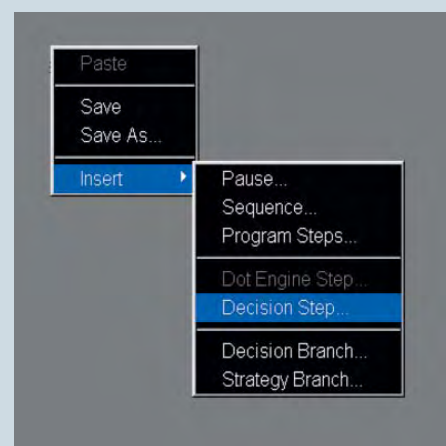


**Patient context decision:** Patient context decisions involve decisions that already have been made at the beginning of an examination. Like the desired strategy, they also can be selected after registering the patient and changed again during the course of the examination. The patient context decision is integrated in the examination in the form of a decision branch that enables branching of the protocol in two opposite directions. The user can decide for or against a specific patient context decision, e.g. contrast medium. All subsequently desired procedures then open linked to this patient context decision. In contrast to the decision step, a patient context decision is already made in the patient view at the beginning of the examination and does not require any decisions during the further course of the examination.

**Clinical decision point:** Decisions related to the clinic are initially made during the course of the examination and, as their name implies, are dependent on the patient's clinic. Sequences that are additionally required for clinical reasons are integrated in the examination procedure in the form of a decision step. The sequences desired can be added to the standard examination while it is in progress by selecting a previously defined decision step. The sequences that are run during the corresponding decision are stored in the deci-

sion branch.

**Decision step:** A decision that remains to be made can be selected during the course of the examination. This automatically creates a decision branch under which the corresponding sequence can be found. The sequences are saved in advance here, too, so that they will become available immediately following a corresponding decision. A decision step is required during a Dot engine run only in cases concerning a clinical decision that is initially made



while the examination is in progress.

**Decision branch:** This involves branching of the examination procedure due to a patient context decision or a clinical decision. The user can decide in favor of or against a procedure. Once a decision has been made, the corresponding protocols saved there are made available.



## Automatic procedures / additional functions

**Auto position:** All Dot engines offer the possibility of automatically moving the patient into the isocenter of the respective examination region without previous centering and positioning the patient in the isocenter.

**AutoAlign:** This function is available only for head, knee and spine examinations and performs automatic positioning of the examination area based on previously set reference points.

**AutoFOV:** The field-of-view (FOV) is automatically adapted to the structure under examination. The system always selects the FOV with a tolerance range that is slightly larger than necessary to make allowances for patient-related changes, e.g. varying breath-hold phases.

**AutoCoilSelect:** During examinations, the coils located in the examination area are selected automatically so that the user does not have to select them manually for each sequence. This ensures that the measuring field always remains fully illuminated.

**AutoBolus detection:** Auto bolus detection promotes optimal timing during dynamic contrast medium examinations. The position where the signal intensity is to be measured in the vessel is determined via a region-of-interest (ROI). The

sequence then starts automatically as soon as the previously selected reference value has been reached. Therefore, false starts seldom occur, which is why examinations in which the exposure is to be taken during a specific blood circulation phase (e.g. the aortic arterial phase) often show a better contrast.

**AutoVoice commands:** The automatic breath-hold commands improve the timing between contrast medium enrichment, the breath-hold command and the scan. A large number of languages can be programmed to simplify examinations without having to rely on an interpreter. In combination with AutoBolus detection, the length of the automatic breath-hold command also must be accounted for in the contrast medium timing.

### Different patient views:

Only the Neuro patient view is available in the standard package. The patient views specify which additional functions can be accessed during the examination. It is thus for example possible to automate the dynamic 3D VIBE measurements in the liver study and add AutoBolus detection with the help of the Dot add-in ABLE.

- ABLE (abdomen breath-hold liver examination) = Abdomen with contrast medium dynamics, automatic breath-hold commands, automatic start of sequences after contrast medium detection. Delay times can be inserted variably.
- Angio bolus timing = for angiographies with breath-hold command; graphic regions, veins, arteries, automatic arterial time calculation (delay).

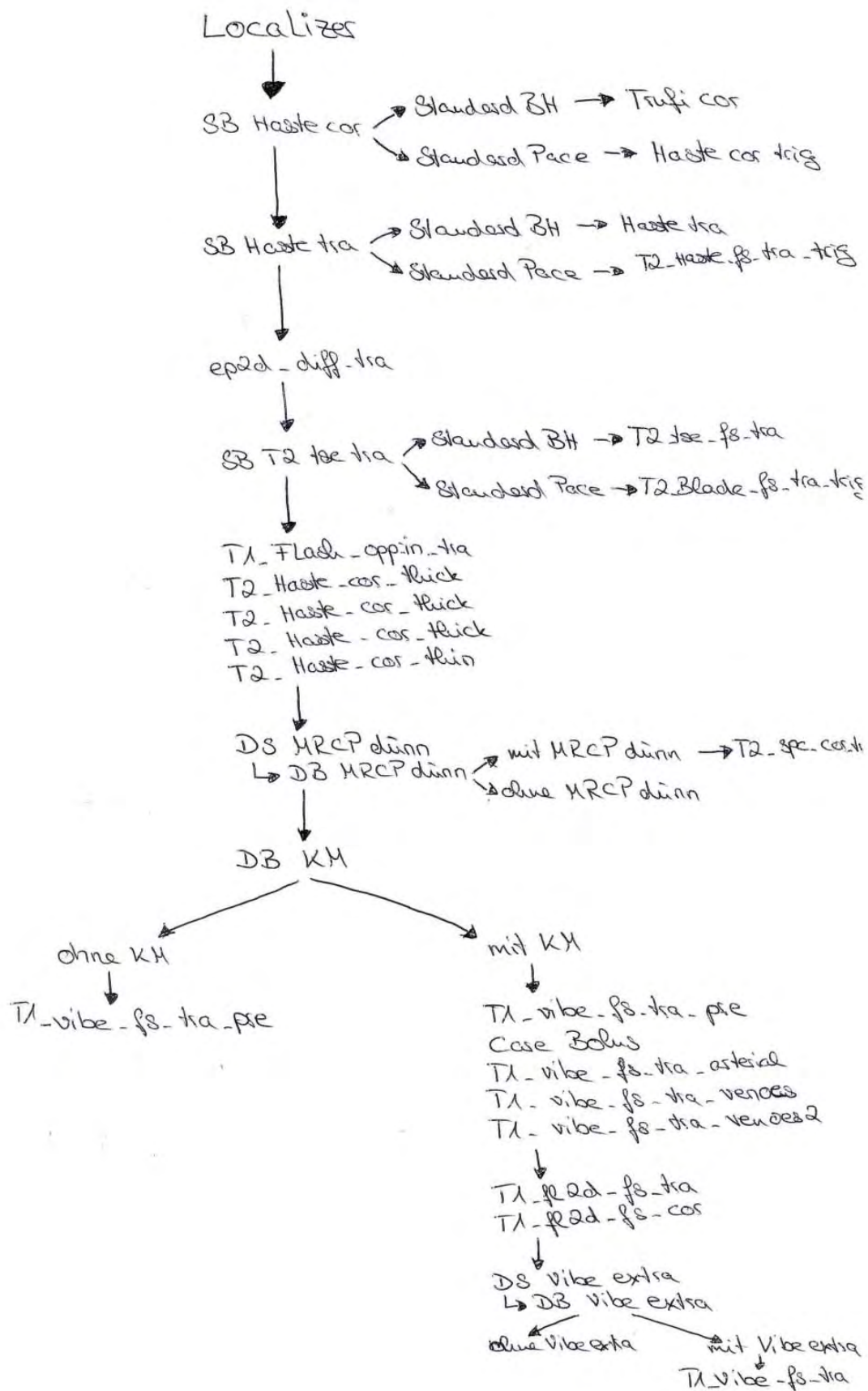
- AutoAlign scout = Automatic tilting according to specific reference points.
- Generic views = Guidance images and scope of parameters.
- MPR planning = Planning of multiplanar reconstruction (MPR), can be used only once per Dot engine.
- MPR assignment = Executes the plan, automatic reconstruction.
- Cardiac basic
- Cardiac marker lock = Sets axial points when planning the heart axes.
- Cardiac SAX planning = For planning short axes.
- BOLD = Blood Oxygenation Level Dependent imaging for functional measurement.

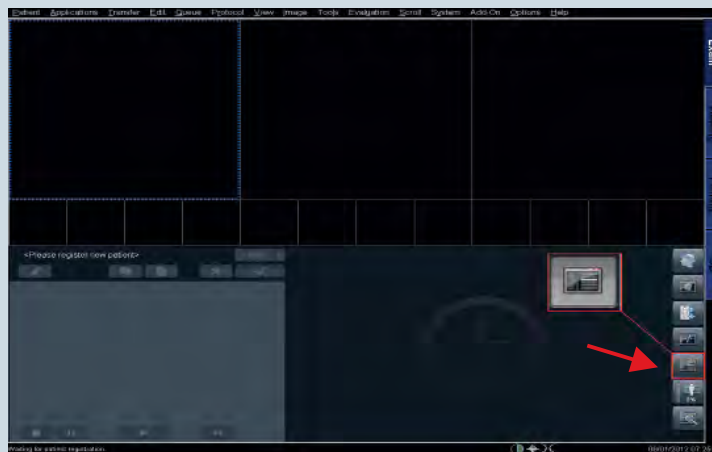
## Example of application

Now we will show you how to create a Dot engine based on the example of a liver study.

It is advisable to make a sketch of the desired protocol before you start creating the Dot engine.

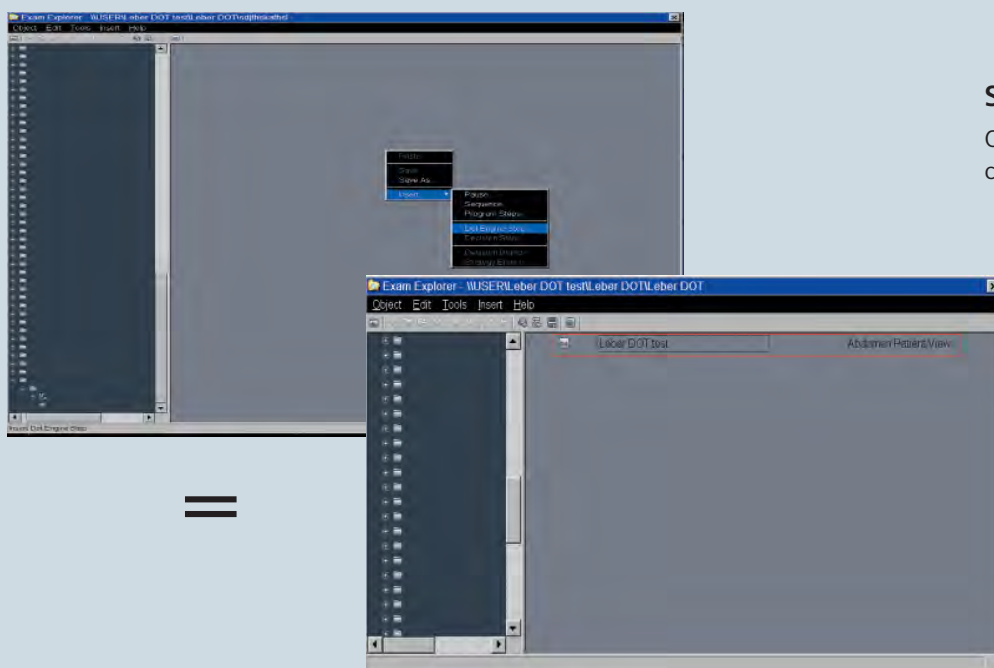
## Leber Untersuchung





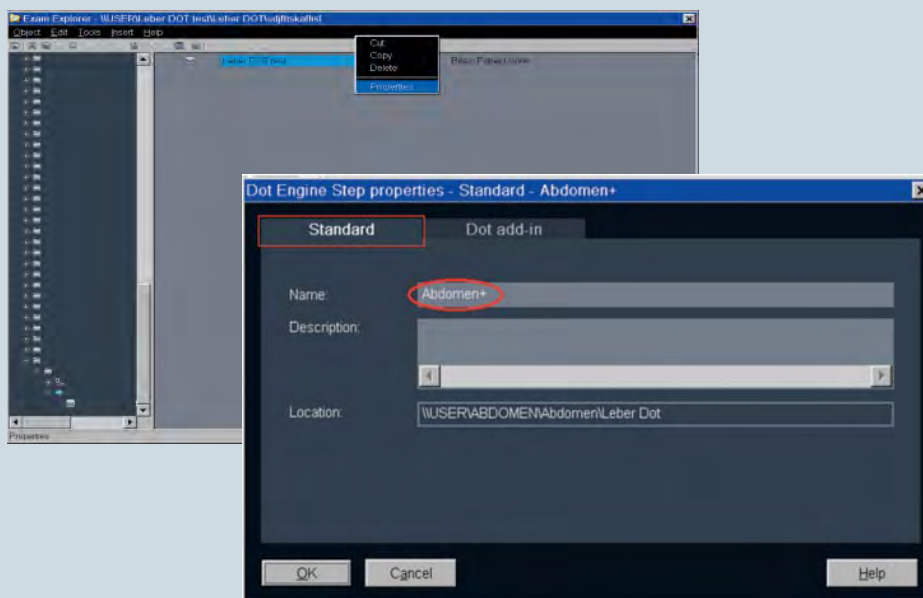
Then the Dot engine is created as shown in this example based on a liver study.

Open the user tree.



### Step 1:

Open the subfolder and create a Dot engine.

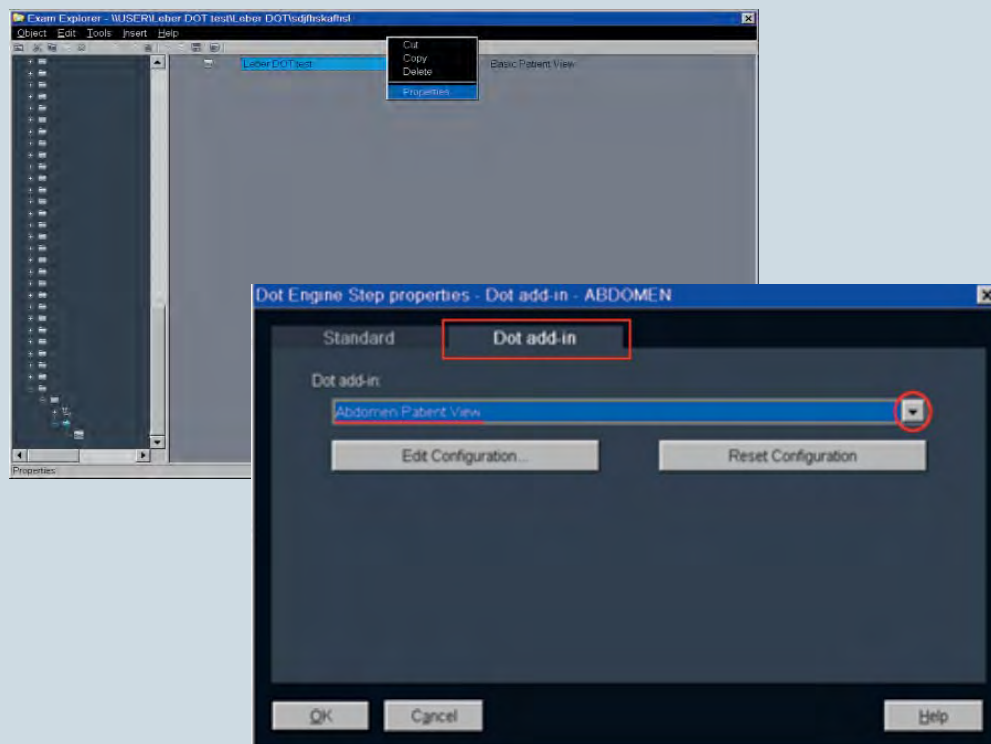


### Step 2:

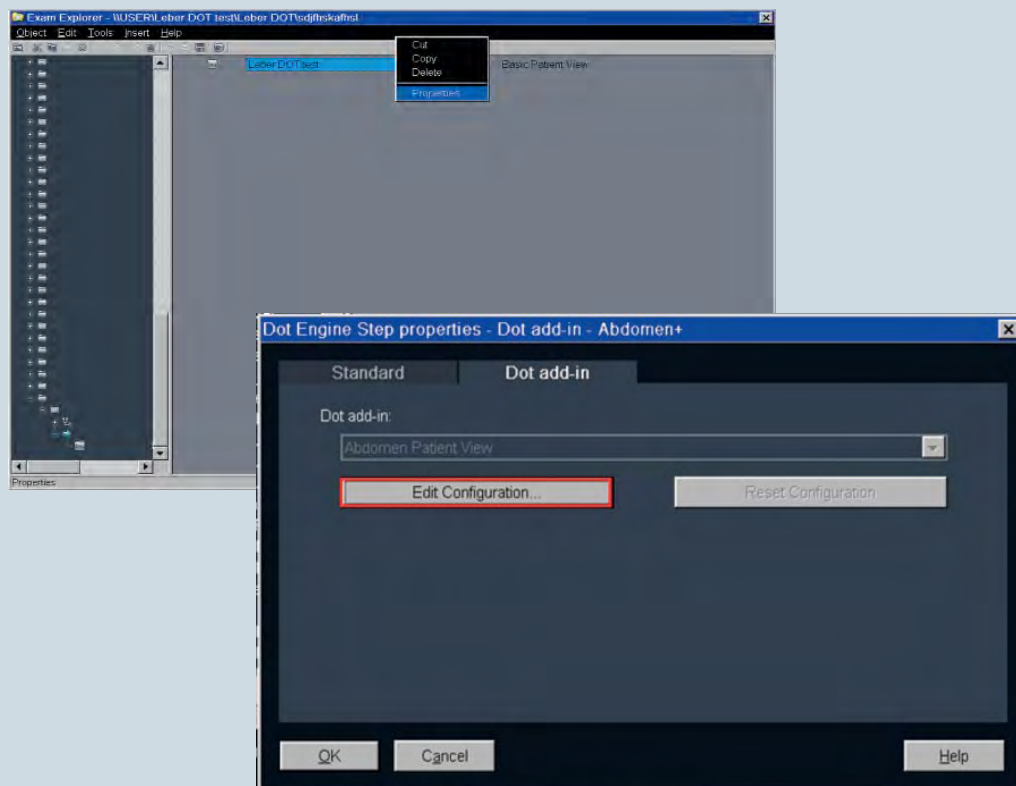
E.g. right-click the Dot engine and select "Properties" or double-click, open and name it.

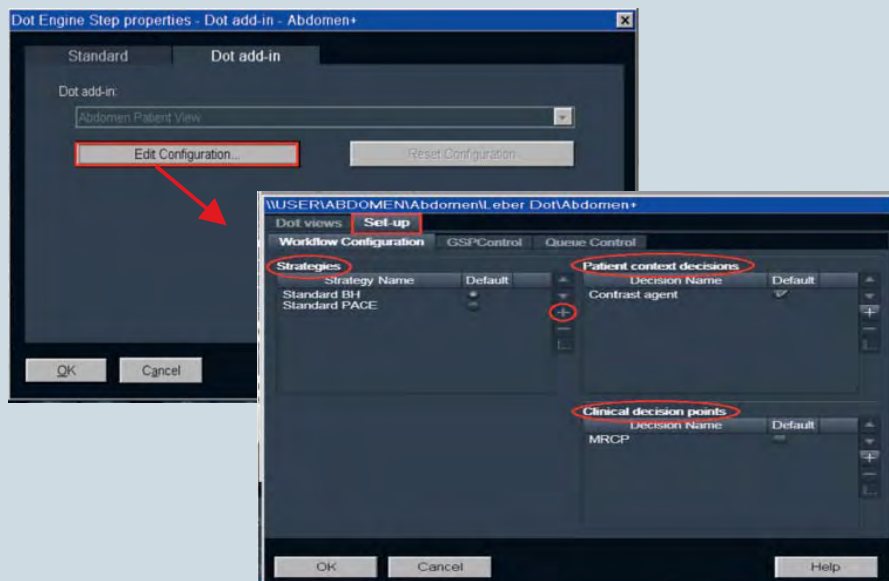
**Step 3:**

Select the patient view suitable for the examination via Dot add-in.

**Step 4:**

Select "Edit Configuration" to configure the Dot engine.

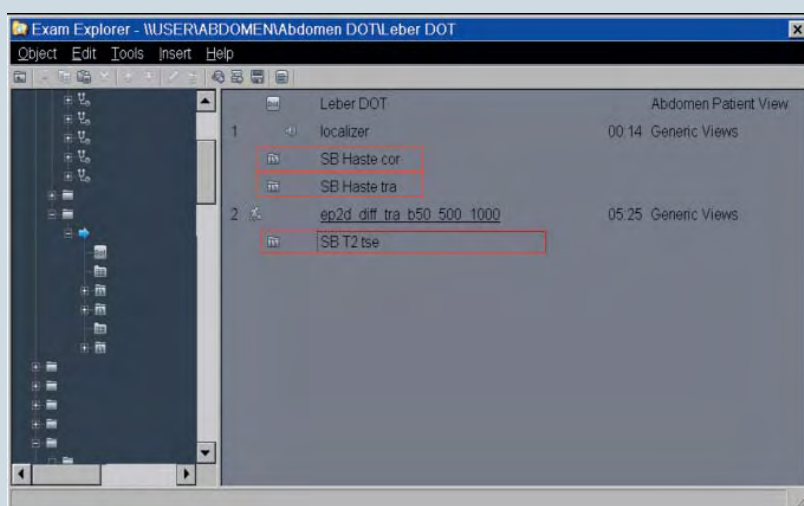




### Step 5:

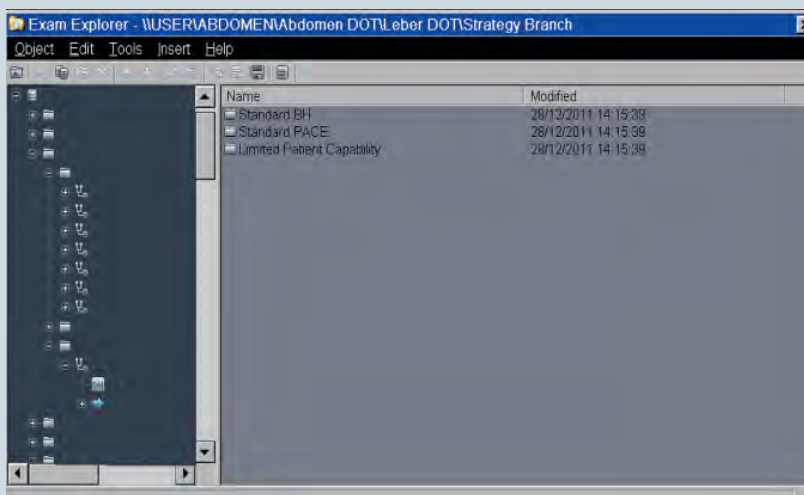
Define the strategies (strategy branch), patient context decisions (decision branch) and clinical decision point (decision step) for the examination by adding them.

**Hint:** The number of strategies can no longer be changed once the protocol has been put into operation. In order to keep this option open, you might want to insert a placeholder under "Strategies" at the beginning.



### Step 6:

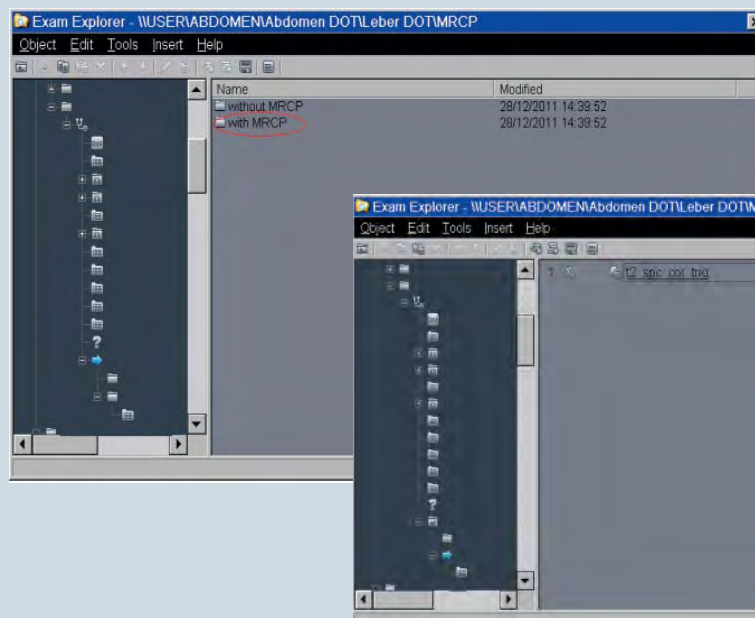
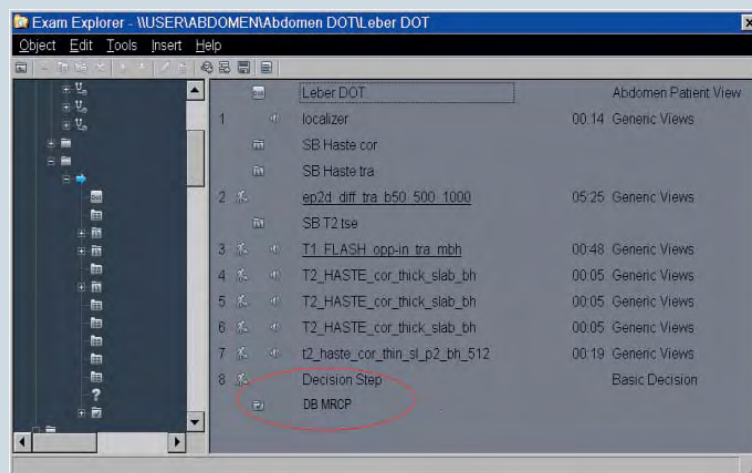
A strategy branch can then be integrated whenever varying sequences are to be used for different strategies. If the sequences are the same for all strategies, they can be inserted directly without generating a branch.



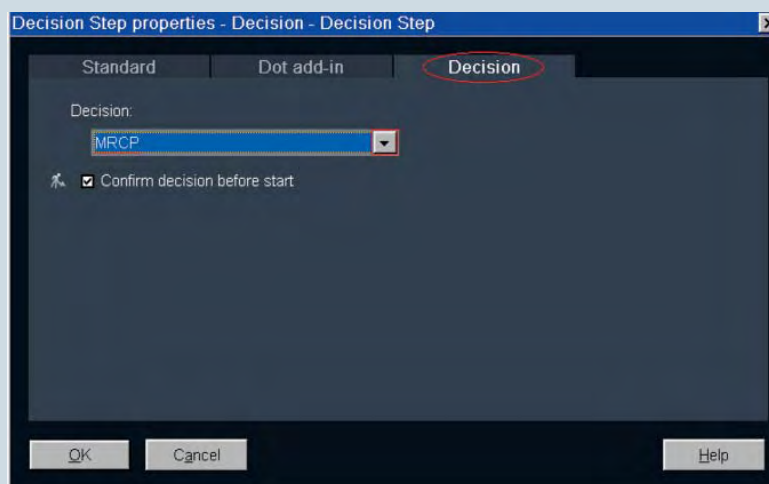
Finally, the correct sequences are saved under the individual strategies.

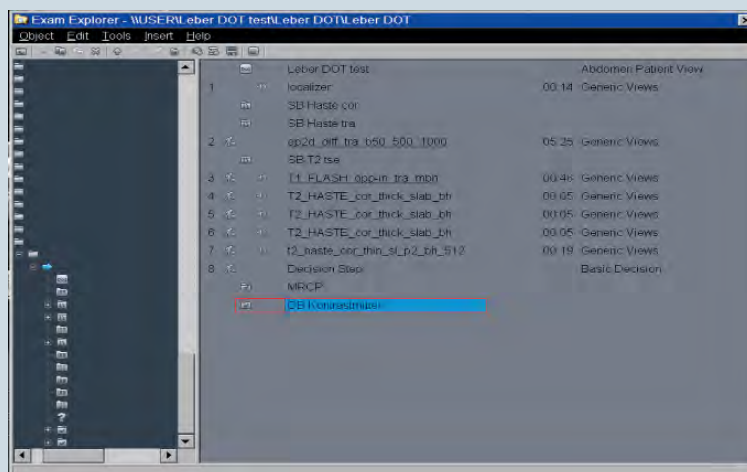
**Step 7:**

Insert a decision step to enable a decision for a thin MR colangiopankreatography (MRCP) during the course of the examination. The decision step always includes the Dot “basic decision” add-in.



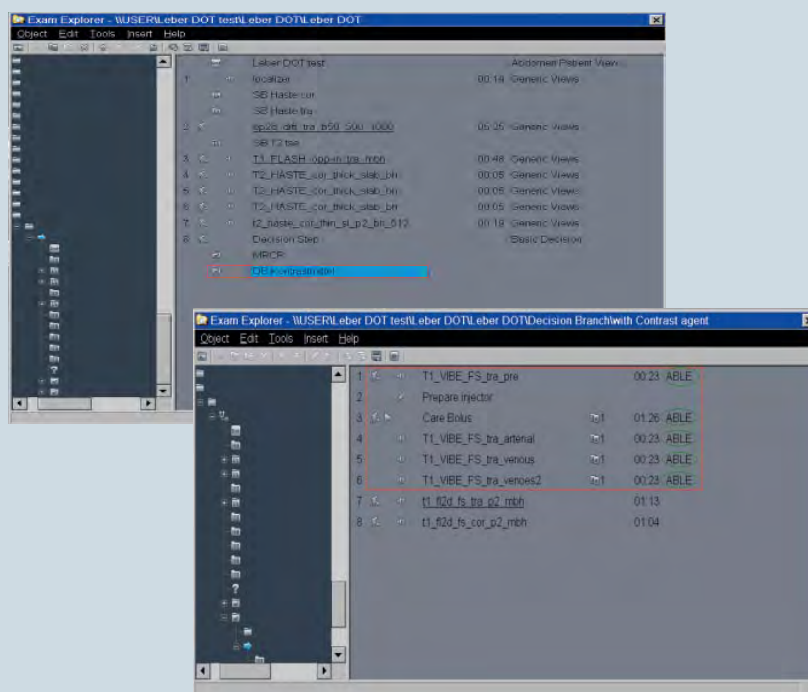
A decision step automatically generates a decision branch. However, a clinical decision point, in this case MRCP, always must be selected under “Decision” for this purpose. The clinical decision point must however already be defined in the patient view.



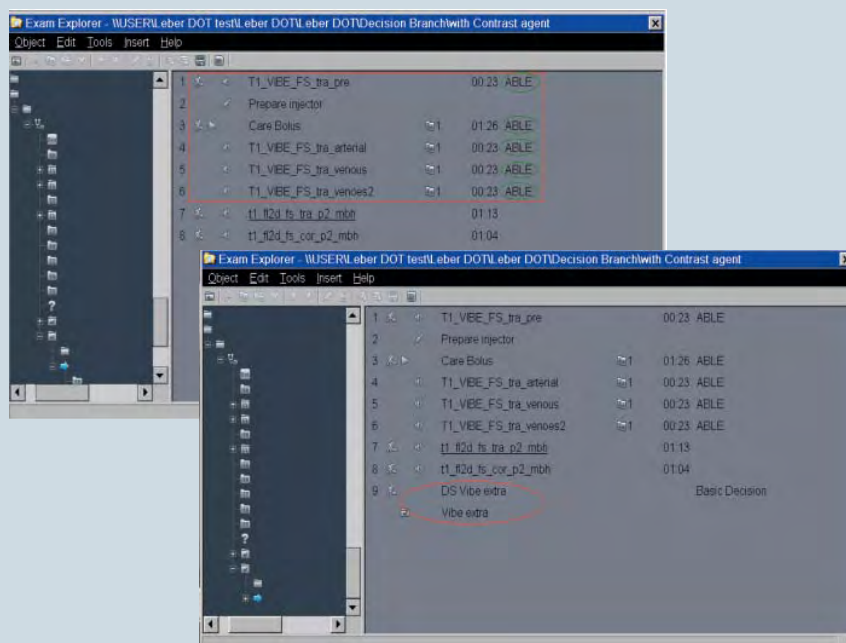


### Step 8:

Insert a decision branch for contrast medium administration and save the VIBE protocols for the dynamic contrast medium examination there.



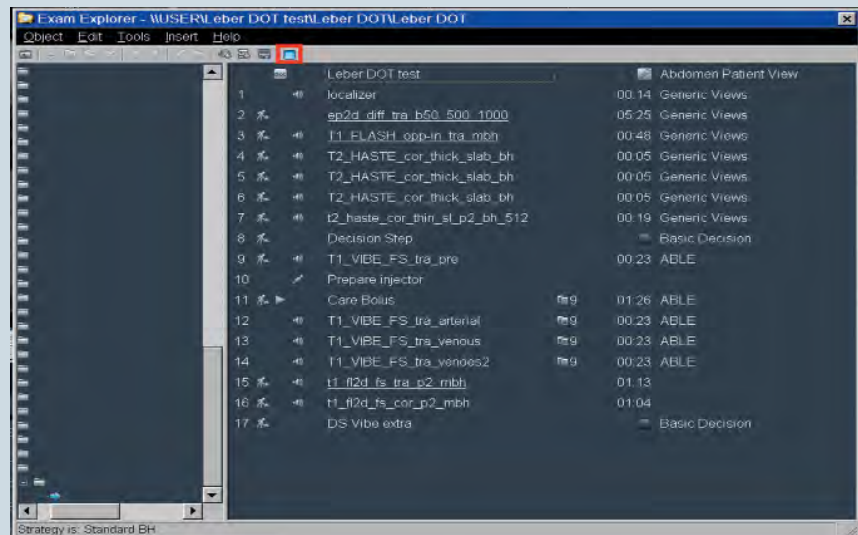
The VIBE is assigned the Dot add-in ABLE. The VIBE always contains 4 measurements (vibe native, vibe arterial, venous and equilibrium). Additional VIBEs cannot be integrated in ABLE.



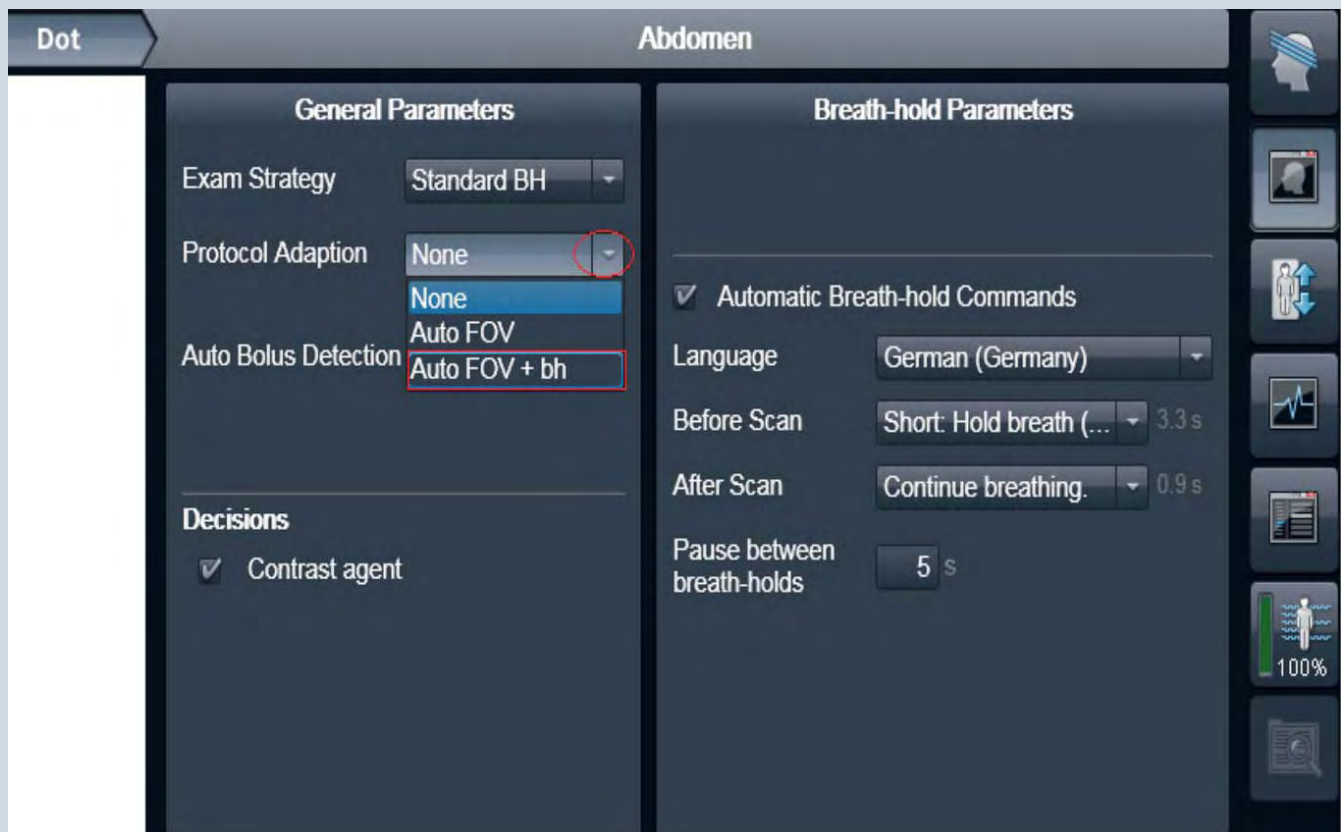
It is, however, possible to equip additional VIBEs with a generic view add-in and attach them to the examination.

**Step 9:**

Fill the basic framework with sequences. Measurements which are the same for all strategies and are not subject to any further decisions can be inserted under the Dot engine without a strategy branch.

**Special features of the liver Dot engine****Automatic adaptation**


The automatic adaptation can be switched off completely or, as an alternative, either the AutoFOV or the breath-hold command can be used separately. This setting also can be changed during the course of the examination.

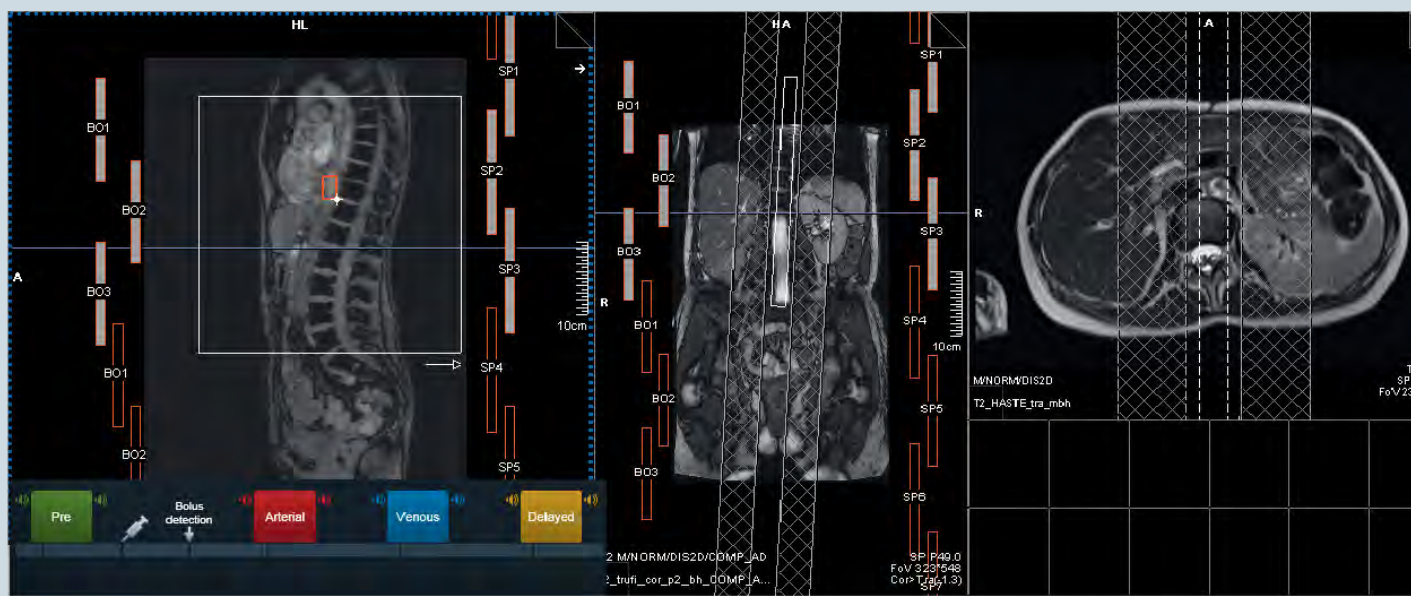


### Guidance

Position the slice and the ROI for Care Bolus:

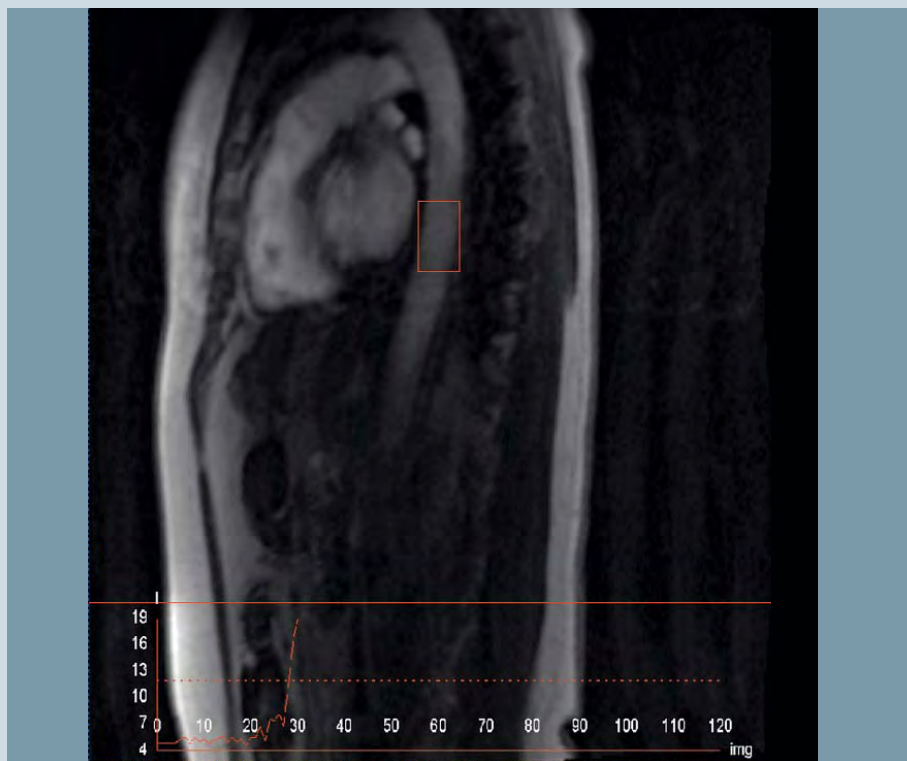
1. Select the sagittal slice with the best vessel visualization.
2. Position the ROI in the sagittal slice with a left mouse click (if **Auto Bolus Detection** is on).
3. Adjust slice position for Care Bolus.
4. Start Care Bolus and then start the contrast agent injection.





### Automatic execution of contrast-medium-supported sequences

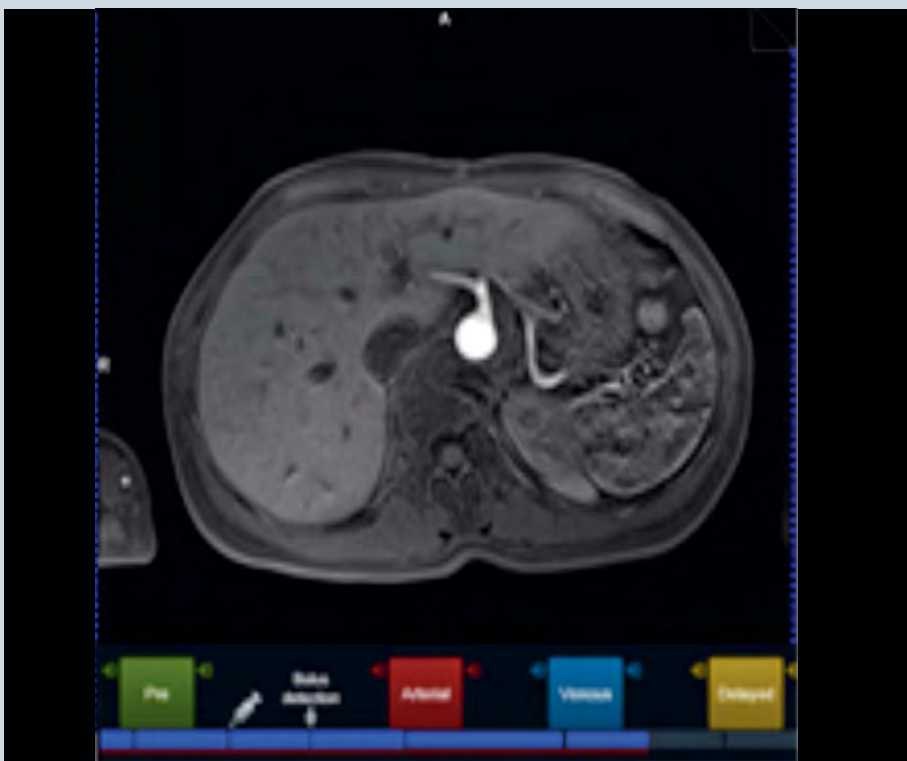
The guidance images specify optimal positioning of the ROI. Thus oriented, the ROI on the sagittal image is placed in the ascending aorta.



Once the VIBE has been started, the examination is then executed fully automatically. The enhancement curve displays the increase of the contrast medium and can be used to check that the arterial VIBE starts in time. The rest of the examination is performed automatically and can be followed on the graphic display.

## Conclusion

In conclusion it can be said that, from the perspective of the technologists, Dot simplifies examination workflows considerably. And it's even more important to know that you can use Dot to make your work a lot easier. We hope that this introduction marked a first step towards familiarizing you with the Dot application. We hope you will have lots of fun creating your own Dot programs tailored to your own individual standards.



## Contact

Anton S. Quinsten  
Institute for Diagnostic and  
Interventional Radiology and  
Neuroradiology  
University Hospital Essen  
Hufelandstraße 55  
45122 Essen  
Germany  
Phone: +49 (0)201/723-84506  
anton.quinsten@uk-essen.de

# Texture Analysis and Classifiers Applied to High-Resolution MRI from Human Surgical Samples in Refractory Mesial Temporal Lobe Epilepsy

Maryana de Carvalho Alegro<sup>1,2</sup>; Silvia Yumi Bando<sup>3</sup>; Alexandre Valotta Silva<sup>1,4</sup>; Bruno Cunha Medeiros<sup>1</sup>; Felipe Brunetto Tancredi<sup>1</sup>; Roseli de Deus Lopes<sup>2</sup>; Carlos Alberto Moreira-Filho<sup>3</sup>; Edson Amaro Jr.<sup>1,5</sup>

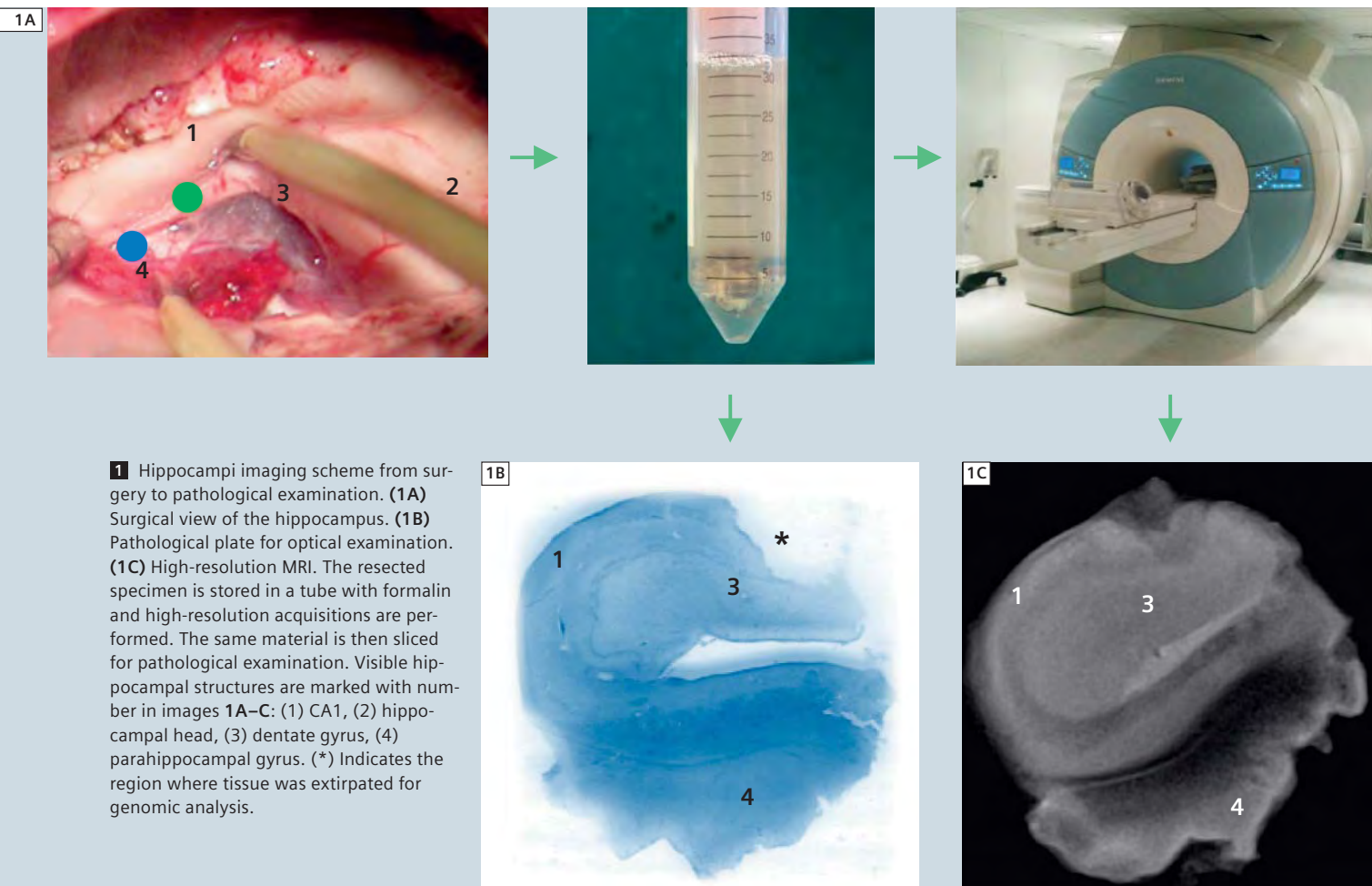
<sup>1</sup>Brain Institute, IIEP Albert Einstein, São Paulo, Brazil

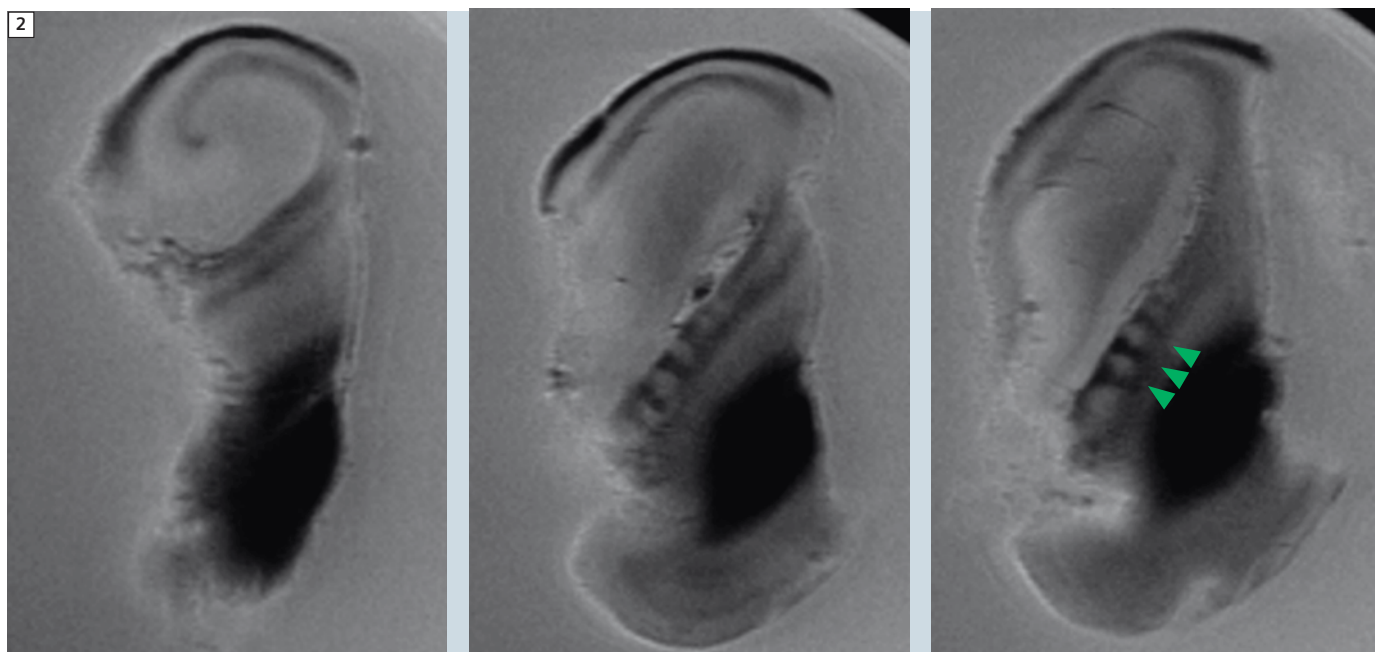
<sup>2</sup>Integrated Systems Laboratory, Escola Politécnica da Universidade de São Paulo, Brazil

<sup>3</sup>Department of Pediatrics; Faculdade de Medicina da Universidade de São Paulo (FMUSP), Brazil

<sup>4</sup>Department of Biosciences, Universidade Federal de São Paulo, Campus Baixada Santista, Brazil

<sup>5</sup>Department of Radiology and Oncology, FMUSP, São Paulo, Brazil





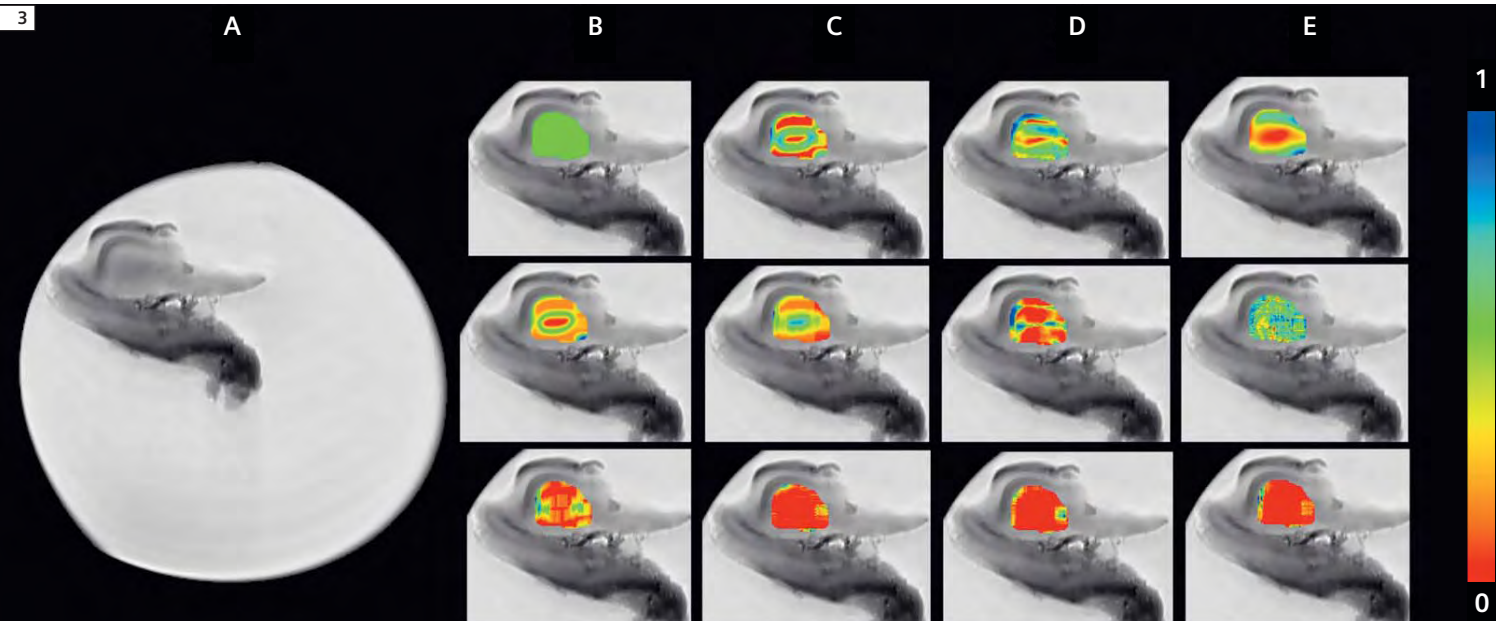
**2** Three examples of high-resolution MRI of ex-vivo hippocampi. Attained resolution allows the visualization of nervous fiber bundles crossing between different hippocampus regions (green arrowheads).

## Introduction

There has been a significant increase in the number of papers using image processing techniques to improve our understanding of MR images. One family of image analysis methods is based on the relationship of a given voxel signal and the signal of its neighbors: texture analysis. Texture of an image can be characterized as the spatial distribution and spatial dependency between the pixel values of an image. Texture analysis provides a set of computational techniques that aim to mathematically characterize these distributions and dependencies. Texture features are basically numeric parameters, which are calculated by the analysis algorithms and can be fed into investigation tools, such as statistical and classification systems. They are roughly separated into four groups: statistical, structural, model-based and transform-based (see Ref. 1 for an in-depth overview of texture analysis). Texture features do not usually carry a direct 'meaning' about the physical properties of the imaged tissue, although there are some exceptions, such as the fractal dimension [2] that approximately

correlates with the 'roughness' of the image. A texture parameter alone is only a number and may be considered useless by a human observer. But sometimes it can be a powerful tool for revealing subtle changes between image samples. In fact, texture features were shown to be able to detect small signal changes in MR images, which are not detectable by human vision [3]. Although texture analysis has a long history in the medical image-processing field [4–6], there are only a few studies using MR datasets, and even fewer including patients with epilepsy, a condition characterized by high incidence in global population, varying from 1 to 3%. The most common form of human epilepsy is mesial temporal lobe epilepsy (MTLE), which affects primarily the amygdala and hippocampus, brain areas that are involved in learning and memory processes. MTLE onset is frequently associated with long febrile seizures in the early years of childhood, although some patients develop it later in life [7, 8]. The MR findings include hippocampal sclerosis: the 'shrinkage' of hippocampal formations, mainly caused

by neuronal death, and associated with occurrence of disabling seizures. Some patients with MTLE may not respond to conventional non-surgical therapy, a condition known as refractory MTLE. Such patients usually undergo detailed evaluation in order to prepare for surgical extraction of the epileptogenic hippocampus. Pathological examination of resected sclerotic hippocampi reveals typical histological features in some hippocampal areas, such as gliosis and neuronal cell loss [9, 10]. Genomic analysis of the ex-vivo hippocampi samples also reveals changes in the expression of several genes, which leads to inflammatory processes [11, 12] that could also be detected immunostaining histological samples. Our group conducted comparative genomic analysis of MTLE patients with (FS) or without (NFS) febrile seizure history, which showed the correlation between hippocampal gene signature and initial precipitating injury in MTLE [13]. Ultimately, these differences could be represented in the parameters obtained by texture analysis, but not necessarily providing any hints on how the proposed



**3** High-resolution MRI and some of the used texture features: a pre-processed high-resolution MRI slice can be seen in column a. Column b displays the hand drawn dentate gyrus mask in green (top), co-occurrence correlation (middle) and co-occurrence contrast (bottom). Column c displays the co-occurrence entropy (top), run-length SRE (middle) and 1<sup>st</sup> level Daubechies 4 wavelet horizontal orientation (bottom). Column d displays the fractal dimension (top), 1<sup>st</sup> order Markov random field (middle) and 1<sup>st</sup> level Coiflet 3 wavelet – diagonal orientation (bottom). Column e displays the Gabor filter (top), 5<sup>th</sup> order Markov random field (middle) and 2<sup>nd</sup> level Symlet 2 wavelet – vertical orientation. All texture features values were rescaled to the [0,1] interval.

disease mechanisms could be distinguished by texture features. On the other hand, the magnitude of the representation is large enough to induce MR signal disturbances, although too subtle to be detected by visual inspection. Both genomic and histological techniques are widely applied in the MTLE studies, but have the drawback of being destructive procedures, preventing the samples from being used in subsequent investigations. It is yet undetermined if advanced MR acquisition and image analysis could help to better characterize each individual case.

Our goal here is to explore the application of MRI imaging for conducting ‘tissue-level’ studies of the sclerotic hippocampal structure. For this paper, we acquired high-resolution images of the resected specimens with a customized MRI protocol in a clinical MR system (Siemens 3T MAGNETOM Trio, a Tim system). Texture features were the main source of information for analysis, due to their aforementioned ability for detecting subtle differences in MRI images. All high-resolution images were

processed in a pipeline setup to facilitate routine analysis of the surgical samples. Our first experiment was to try to discriminate between patients with febrile (FS) and non-febrile (NFS) initial precipitating injury. This differentiation by imaging is challenging since these conditions have similar clinical courses and imaging features are non specific using classical radiological assessment. In fact, such a challenge is attainable by texture analysis techniques, since only subtle morphological alterations are expected [13].

### Experimental details and results

This study is part of the CInAPCe-FAPESP program, a multicenter project targeted to study epilepsy via neuroimaging ([www.cinapce.org.br](http://www.cinapce.org.br)) performed at four main research centers equipped with 3T MR systems. Here we report findings from twelve patients with refractory MTLE who underwent surgical resection of the sclerotic hippocampus. Four patients had a clear episode of febrile seizure during childhood (2 males) and eight (5 males) had no records related to

specific precipitating injury reported after careful history assessment. All surgical specimens were freshly removed, fixed in formalin solution and stored in Falcon plastic tubes.

Acquisitions were performed in a 3T MAGNETOM Trio, a Tim system (60 cm bore, 40 mT/m, 230 mT/m/s) using a surface loop coil (7 cm diameter). The Falcon tube was firmly held in the center of the coil with the aid of anti-vibration pads to avoid motion artifacts. High-resolution images were acquired using a Turbo Spin Echo (TSE) protocol, with TR 3700 ms, TE 76 ms, fat sat by IR, TF 7, FA 180°, BW 40 Hz/px, FOV 43 mm (70% AP phase oversampling), a 512 x 464 matrix, slice thickness of 1.6 mm and 32 NEX. Attained in-plane resolution was 80  $\mu$ m x 80  $\mu$ m and CNR (gray/white matter) 15. Figures 1 and 2 illustrate the acquisition process and hippocampus high-resolution images, respectively. Image analysis was performed in a three-stage pipeline: preprocessing, feature extraction and analysis (see Ref. 14 for an in-depth methods description). We designed this pipeline so that future

investigations could be done using a standardized process. The preprocessing stage includes noise filtering, background segmentation and intensity normalization and is designed to reduce MRI artifact effects, such as noise and intensity non-standardization. In the feature extraction stage texture features are calculated from the MR images. We adopted different texture features, which are computed using a texture extraction library implemented using Matlab (MathWorks, USA). This stage is computationally demanding, including the determination of statistical, transform and model-based features, resulting in a total of 158 features. Features are calculated for each pixel with the aid of a spatial sliding window. Masks were manually drawn by a neuropathologist on top of every considered MRI slice and used to guide the texture calculation process (Fig. 3). We chose the dentate gyrus (DG) area for analysis since it is one of the most affected structures in MTLE patients. In the last (analysis) stage of the pipeline we used classification methods (Support Vector Machine – SVM, LIBSVM SVM – details in Ref. 14) to discriminate pixels belonging to either FS or NFS classes. Features are selected based on the information gain coefficient (IG), prior to classification. Only features with the highest IG are considered. We have trained/tested our SVM classifier using a leave-one-out scheme (for each iteration one subject is left out of the training phase, and SVM is performed with the remaining data). A permutation test was performed in order to validate the classification results. In the permutation test, class values are randomly permuted and reassigned to each subject; the leave-one-out routine is then performed again. This process is repeated 70 times and every time the classification accuracy reaches values equal or higher to those obtained by the original cross-validation, a counter is increased. The p-value is calculated by dividing the counter number by the number of permutations. Using this approach it was possible to correctly classify 76% of the

test instances (p-value < 0.001).

## Conclusions and future directions

The proposed pipeline proved to be adequate for accurate pixel classification of high-resolution ex vivo images obtained in a clinical MR system. We were able to show a significant correlation between MRI texture parameters and clinical characteristics of a group of MTLE patients. So far, and to our knowledge, it has not yet been shown that such high performance can be achieved by routine radiological reading. In fact, there is no single description of radiological signs pointing to either FS nor NFS etiology. Our findings indicate the existence of distinct characteristics between cases with (FS) and without (NFS) antecedent febrile seizure history. This is in line with a recent epidemiological study showing that MTLE cases with febrile IPI constitute, due to their clinical features, a unique phenotype, distinct from the non-febrile cases [15]. We are now investigating whether the same texture analysis and SVM approach holds the same performance when analysing data from pre-surgical MRI images.

## Acknowledgements

This work was supported by FAPESP grant no. 2005/56.446-0 to CAM-F. MCA is a research fellow from FAPESP (grant no. 2010/00180-0) and Federico Foundation. We would like to thank Dr. Bruno Medeiros and Dr. João R. Sato for their insightful help in various phases of this project.

### Contact

Edson Amaro Jr, M.D., Ph.D.  
Brain Institute  
IIEP Albert Einstein  
Av Albert Einstein 627/701  
05652-900, São Paulo, SP  
Brazil  
Phone: +55-11-2151-3727  
Cell phone: +55-11-8122-7201  
Fax: +55-11-2151-0273  
edson.amaro@gmail.com

### References

- Petrou M, Sevilla PG. Image Processing: Dealing With Texture. Wiley; 2006.
- Pentland AL. Fractal-based description of natural scenes. *IEEE Transactions on Pattern Analysis and Machine Intelligence* 1984; 6:661–674.
- Zhang J, Ma J, Er MH. Tumor segmentation from magnetic resonance imaging by learning via one-class support vector machine. *International Workshop on Advanced Image Technology* 2004.
- Zhang Y, Zhu H, Mitchell JR, Costello F, Metz LM. T2 MRI texture analysis is a sensitive measure of tissue injury and recovery resulting from acute inflammatory lesions in multiple sclerosis. *NeuroImage* 2009; 47:107–111.
- Bernasconi A, Bernasconi N, Caramanos Z, Reutens DC, Andermann F, Dubeau F, Tampieri D, Pike BG, Arnold DL. T2 relaxometry can lateralize mesial temporal lobe epilepsy in patients with normal MRI. *NeuroImage* 2000; 12:739–746.
- Oliveira MS, Balthazar MLF, D'Abreu A, Yasuda CL, Damasceno BP, Cendes F, Castellano G. MR Imaging Texture Analysis of the Corpus Callosum and Thalamus in Amnesic Mild Cognitive Impairment and Mild Alzheimer Disease. *American Journal of Neuroradiology* 2011; 32:60–66.
- Engel J. Mesial Temporal lobe epilepsy: what have we learned? *The Neuroscientist* 2001; 7:340–352.
- Cendes F. Febrile seizures and mesial temporal sclerosis. *Current Opinion in Neurology* 2004; 17:161–164.
- Hattiangady B, Rao MS, Shetty AK. Chronic temporal lobe epilepsy is associated with severely declined dentate neurogenesis in the adult hippocampus. *Neurobiol Dis* 2004; 17: 473–90.
- Bae EK, MD, Jung KH, Chu K, Lee ST, Kim JH, Park KI, Kim M, Chung CK, Lee SK, Roh JK. Neuropathologic and clinical features of human medial temporal lobe epilepsy. *J Clin Neurol* 2010; 6:73–80.
- Majores M, Schoch S, Lie A, Becker AJ. Molecular neuropathology of temporal lobe epilepsy: complementary approaches in animal models and human disease tissue. *Epilepsia* 2007; 48 (Suppl 2):4–12.
- Nakayama J. Progress in searching for the febrile seizure susceptibility genes. *Brain Dev* 2009; 31:359–365.
- Bando SY, Alegro MC, Amaro-Jr E, Silva AV, Castro LHM, Wen HT, Lima LA, Brentani H, Moreira-Filho CA. Hippocampal CA3 transcriptome signature correlates with initial precipitating injury in refractory mesial temporal lobe epilepsy. *PLoS One* 2011; 6(10):e26268.
- Alegro MC, Silva AV, Bando SY, Lopes RD, Castro LHM, Tsu WH, Moreira-Filho CA, Amaro-Jr E. Texture Analysis of High Resolution MRI Allows Discrimination between Febrile and Afebrile Initial Precipitating Injury in Mesial Temporal Sclerosis. *EPub Magnetic Resonance in Medicine* 2012.
- Heuser K, Cvancarova M, Gjerstad L, Taubøll E. Is Temporal Lobe Epilepsy with childhood febrile seizures a distinctive entity? A comparative study. *Seizure* 2011; 20:163–166.

# Towards Understanding the Whiplash Condition at 3 Tesla

Elliott JM, PT, Ph.D.<sup>1,2</sup>; McMahon K, Ph.D.<sup>3</sup>; Cowin G Ph.D.<sup>3</sup>; Parrish TB, Ph.D.<sup>4</sup>

<sup>1</sup>Department of Physical Therapy and Human Movement Sciences, Feinberg School of Medicine, Chicago, IL, USA

<sup>2</sup>School of Health and Rehabilitation Sciences, Division of Physiotherapy, Centre for Clinical Research Excellence in Spinal Pain, Injury and Health. The University of Queensland, Brisbane, Australia

<sup>3</sup>Centre for Advanced Imaging, The University of Queensland, Brisbane, Australia

<sup>4</sup>Department of Biomedical Engineering and Radiology, Feinberg School of Medicine, Chicago, IL, USA

The accurate and consistent radiological observation of head and neck soft-tissue damage in patients with whiplash injuries has been largely inconsistent and highly variable [6, 33, 34, 39, 40, 44]. As a result there exists the proposition that tissue damage does not, or cannot occur, as a result of a low-speed motor vehicle collision [9]. Engineering applications [26–28, 37, 38, 49] and controlled animal studies [48, 51–53] have informed us of what can happen to a number of vulnerable tissues in the cervical region following whiplash, including the facet capsule, dorsal root ganglion and nerve roots [36, 46, 48, 51–53]. At the forefront of clinical enquiry however, is how to best determine what has happened to these tissues in patients with whiplash injury. Due to the persistent nature of symptoms in some sub-

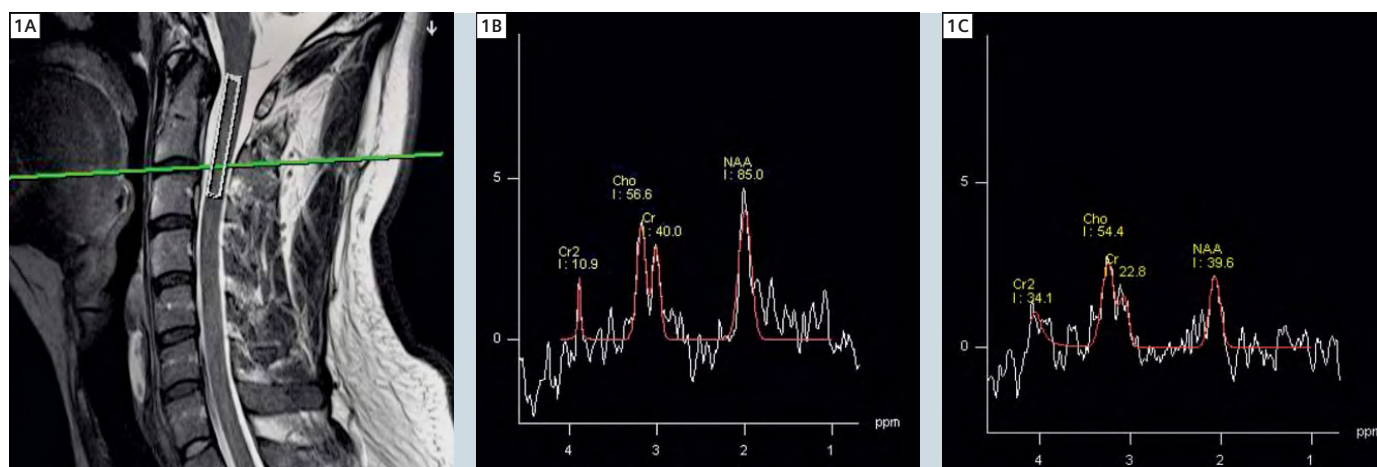
jects with whiplash injury, it is clinically important that objective and quantifiable measures to characterize the whiplash condition be made available. This is especially important for the exploration and development of more informed treatment strategies aimed at retarding if not preventing the expression of persistent pain for some patients.

For many of the laboratory-created lesions shown to occur in animal and bioengineering models, there are currently very few, if any, clinical means for their diagnosis available to practicing clinicians. Plain films lack sensitivity for ruling out bony lesions and the images lack the detail to quantify strained facet joint capsules and/or tears in discs.

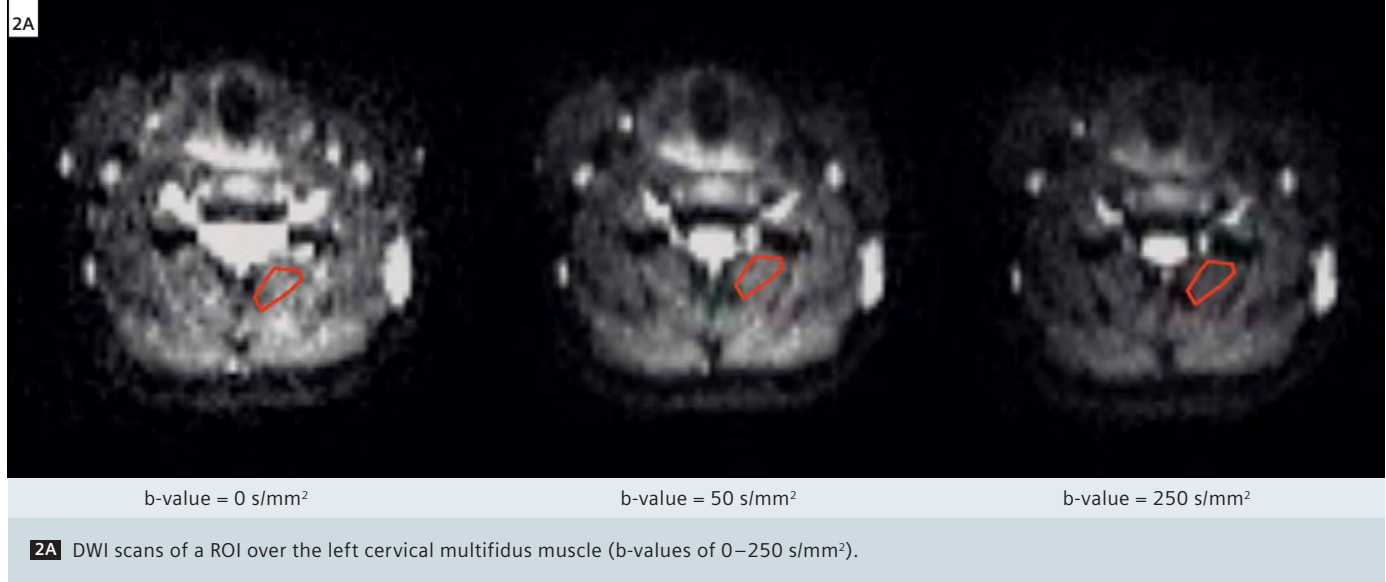
Computed tomography (CT) can identify some cervical spine fractures but rigorous longitudinal studies have not been under-

taken to determine fracture prevalence in this population. More importantly, CT is unable to assess soft tissue damage in the cervical spine and surrounding muscles.

Conventional magnetic resonance imaging (MRI) has largely failed to consistently reveal soft-tissue damage in patients with whiplash, but this may relate to the use of generic clinical protocols (typically 1.5T and lower) and limitations in the resolution. The advent of higher-field systems (3T and greater) has provided a foundation for measuring physiologic processes that could be associated with tissue damage. Preliminary MRI evidence identifying the unique expression of neck muscle degeneration (fatty infiltrates) at 4-weeks post injury in those who transit from acute to chronic pain suggests that this may be so [12]. Muscle changes



**1** (1A) Localization of SVS for the cervical cord at the C2/3 segmental level with (1B) corresponding metabolic peaks for NAA, Cr, and Cho in healthy control and (1C) subject with chronic whiplash (adapted from Elliott et al., *Spinal Cord* [16]).



did not occur in patients with lower levels of initial pain or in patients with chronic non-traumatic neck pain [13] suggesting traumatic factors play a role in altering the make-up of the neck muscles.

We have developed a comprehensive advanced MR imaging protocol that assesses the cervical spine at the metabolic, microscopic and macroscopic level. Furthermore, by applying this protocol, in tandem with clinical signs and symptoms, over several weeks, it may be possible to classify which patients are at risk for transiting to a persistent pain state. This non-invasive methodology to quantify several physiologic processes may afford clinicians the ability to triage their patients with confidence. Furthermore, it may be possible to determine if a person has suffered a traumatic event,

which may be contributing to their pain and disability.

### MR Spectroscopy – metabolite scale

Alterations in MR visible metabolites, such as Lactate (Lac), N-Acetylaspartate (NAA), Creatine (Cr) and Choline (Cho) have been demonstrated in neurological disorders [5, 31] traumatic brain injury [7], and cervical myelopathy [24] and may have predictive capacity [7]. Our previous work has reported the presence of altered cord biochemistry in a small sample of patients with chronic whiplash related pain and disability [16]. However, this study did not resolve the temporal development of these changes or if they are unique to those with poor functional recovery. Such work is well underway.

The current protocol uses a single voxel spectroscopic (SVS) technique to investigate the spinal cord at the C2-C3 level. Using a high resolution T2 TSE sagittal scan along with the axial and coronal localizer scans, a long rectangular voxel (5 mm x 7 mm x 40 mm) is placed in the middle of the cord (Fig. 1). The parameters are listed in Table 1. The acquisition is not cardiac triggered but this is possible to reduce movement artifacts induced by CSF flow. We currently are using a long TE (135 ms) SVS PRESS acquisition to reduce the contamination of short T2 metabolite species as well as have lactate out of phase with the nearby lipid signal. This acquisition is 5:28 minutes after the voxel has been shimmed properly. We are using the

ADVANCED shim\* WIP that provides a robust and rapid shim map. The typical shim result is a FWHM of ~15 Hz at 3T, which translates into a metabolite line width of 6 Hz. The optimized shim is achieved by manually setting the shim volume to be slightly larger (5 mm in each direction) than the actual acquisition voxel. Following this acquisition, a quick (8 average) acquisition is obtained without water suppression to use as a standard over time, which is helpful with repeated measures. These 30-second spectra assess the total amount of water present and can be used for control over placement of the voxel over time and calculate actual concentration of metabolites.

\*Work in progress. This information about this product is preliminary. The product is under development and not commercially available in the U.S., and its future availability cannot be ensured.

### Diffusion-weighted imaging of muscle – microscopic scale

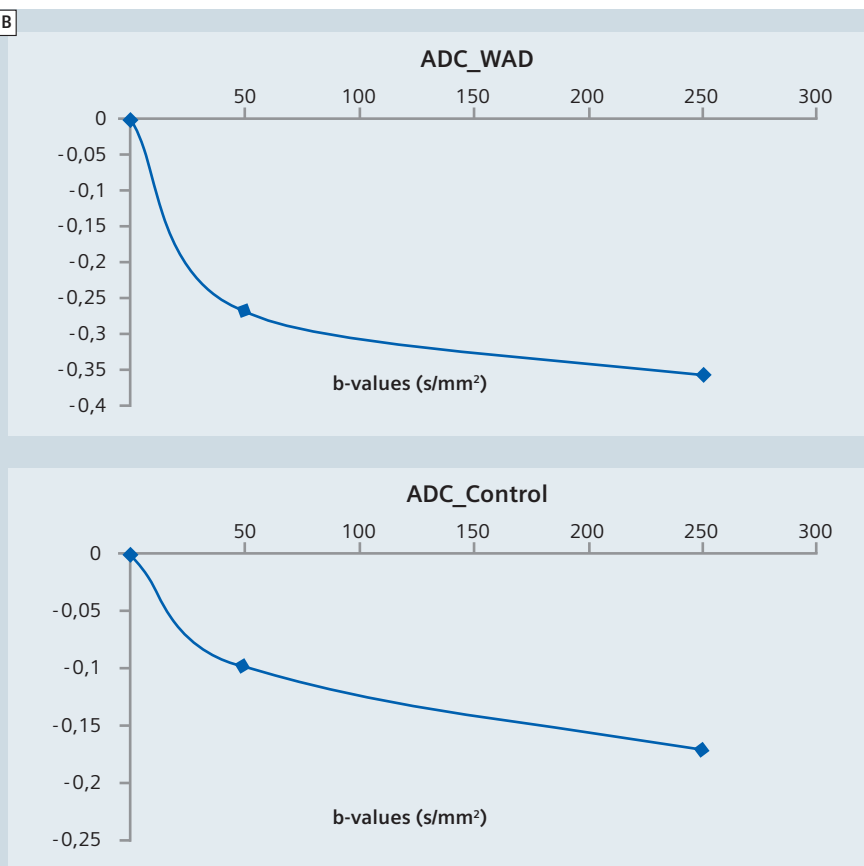
Diffusion-weighted imaging (DWI) of the muscle system has the potential advantage over conventional sequences to help uncover the early physiological mechanisms underlying the manifestation of intra- or inter-muscular fatty infiltrates. Diffusion properties of water have been quantified with DWI in many different organ systems (e.g. brain and spinal cord, kidneys, heart, lumbar intervertebral disc and the prostate) [1, 2, 29, 22, 25, 30, 35, 43, 17, 18, 47, 3, 4, 50]. Normal water diffusion is affected by the presence and orientation of physical tissue barriers (e.g. cell membranes,

**Table 1: SVS\_SE Sequence**

TR 2000 ms
TE 135 ms
160 averages with HEP
coil elements neck 1,2
coil elements spine 1

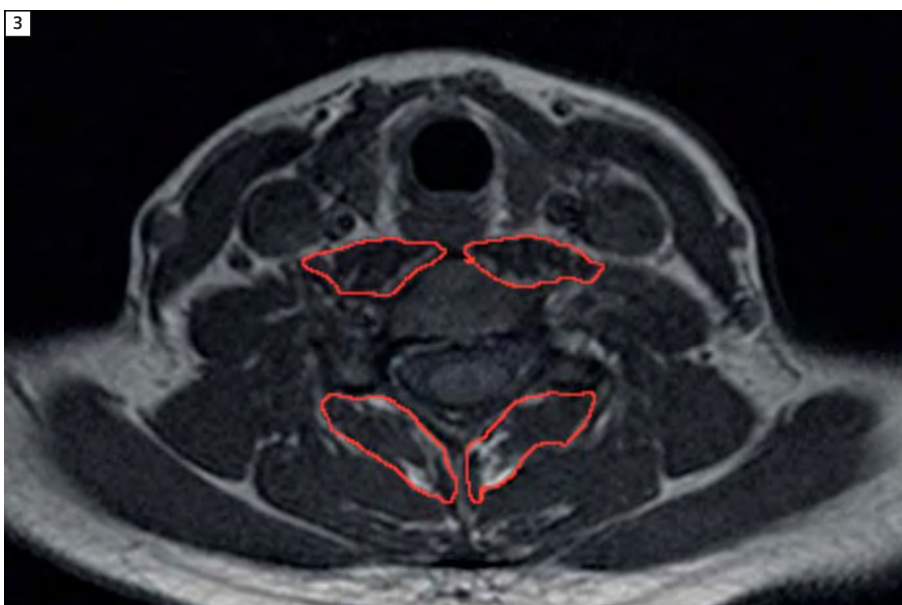
**Table 1:** Parameters for the SVS\_SE Sequence.

2B



**2B** ADC maps (at 1.5T) for the left cervical multifidus muscle in patients with chronic whiplash associated disorders (WAD) and healthy controls [16].

3



**3** T1-weighted axial MR image at the C6 vertebral level demonstrating outlined ROIs for the right and left longus colli and the right and left posterior cervical multifidus. Increased signal, indicative of fatty infiltration, is noted in both sets of muscles in a subject with chronic whiplash associated disorders.

proteins, myelin sheaths and/or lipids) [45]. The measure quantifies the microscopic movements of water diffusion via the mean apparent diffusion coefficient (ADC) [20, 45, 39]. Passive enlargement of the muscle cell following tissue damage may be associated with an increase in ADC [23]. We have shown altered ADC maps for the cervical multifidus in a small sample of subjects with chronic whiplash when compared to healthy controls [16], suggesting a passive enlargement of the muscle cell (e.g. atrophy) (Figs. 2A, B). However, the temporal development of such changes and whether they are unique to those at risk for chronicity is unknown at this stage. Such evidence could provide for a sensitive indicator of early tissue injury at a stage when muscle degeneration remains potentially salvageable [23, 32]. Thus, the potential diagnostic and prognostic value of in-vivo DWI sequences for quantifying the temporal degeneration of muscle tissue, at a cellular level, in whiplash is clear.

#### Diffusion-weighted imaging parameters:

The DWI scan uses a spin-echo, echo-planar acquisition with an in-plane resolution of 1.6 mm, a thickness of 5 mm, TR 4000 ms and TE 65 ms to reduce artifacts. The acquisition is taken in the axial plane using an inversion pulse to reduce the signal from fat with a TI of 160 ms. The diffusion scan is the simple 3-scan trace acquisition but the number of diffusion-weightings is increased to 5. The b-values used at 3T are 0, 50, 100, 200, and 300 s/mm². This is quite different from brain DWI where a typical b-value is 1000 s/mm². Due to signal-to-noise constraints and distortions of the signal, the b-values are small. From all of the b-value data, trace and ADC images are generated for each of the 14 slices in 7:08 minutes.

#### Fat/water imaging – macroscopic scale

The demonstration of neck muscle fatty infiltrates on T1-weighted imaging in chronic whiplash (Fig. 3) [11, 14, 15] is interesting as such findings were not

featured in those with chronic non-traumatic neck pain [13] and their expression (between 4 weeks and 3 months post-injury event) on standard T1-weighted images appears unique to only those who transit [12]. It is postulated that these muscle changes represent one neuro-physiologic basis for the transition to chronic pain in this population. While the mechanisms underlying their temporal development and contribution towards the transition remain unclear, it is possible that newer MRI techniques (MRS and DWI) could help quantify earlier physiologic changes at the spinal cord and muscle cell that may precede observable muscle changes on T1-weighted sequences. An earlier detection of such mechanisms could prove crucial for identifying the early presence of select biochemical changes in spinal cord metabolism with the attendant later changes in muscle physiology and the development of chronic pain and disability.

#### Fat/water separation

Several approaches are possible to measure the water and fat composition of a voxel. These include a dual acquisition method, where one image is fat suppressed [19] (water image) and a standard image is collected (fat and water image). The difficulty of this type of acquisition is that it relies on the uniform frequency difference between water and fat across the whole volume of excitation, which is often difficult to obtain especially at high magnetic fields. A fat suppressed acquisition using a short-tau inversion recovery (STIR) sequence is possible, but the T1 of fat has to be assumed, which may vary depending on the subject or the evolution of the infiltration of the muscle [8]. An alternative is the Dixon method [10], where one collects data at an echo time when water and fat are in-phase and at an echo time when water and fat are out of phase. The data can be combined in such a way that they generate a fat and water image. This method works well when there are no field inhomogeneities, which is often not the case. Current methods collect multiple echo time data to improve the estimation of the fat and water images.

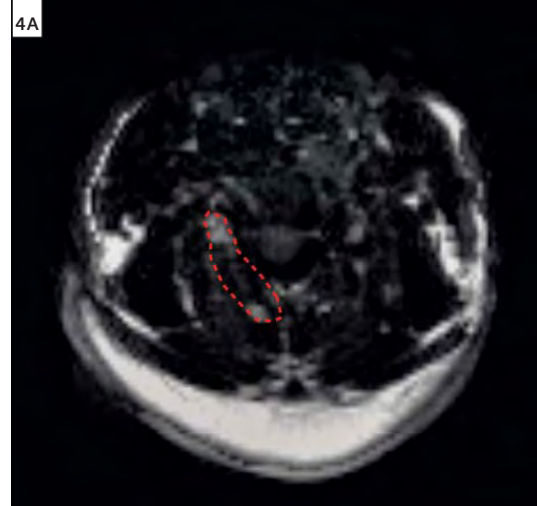
This method has been applied successfully in the liver and musculoskeletal application using an iterative least squares solution called IDEAL [41, 42]. The method we have used in the study of whiplash subjects collects 8 different echo times sufficiently spaced on the unit circle to provide adequate phase information for the variable projection (VARPRO) algorithm\*, generating a globally optimal solution for the water/fat decomposition [21].

Saurabh Shah implemented the VARPRO algorithm and acquisition sequence in the Cardiovascular R&D team located at Northwestern University, Chicago, IL, USA. Currently this feature is a WIP at syngo MR B17 software (Fig. 4A, B). A three-dimension 230 mm field-of-view (FOV) axial gradient echo acquisition was used to collect the data required for the VARPRO algorithm. The sequence parameters are TR 23.81 ms, 8 echo times with a spacing of 1.78 ms starting at 1.36 ms. A single slab is placed over the cervical spine with 36 partitions and a partition thickness of 3 mm and slab oversampling of 22% to prevent aliasing in the 3D direction. The in-plane resolution is 1.4 mm using a rectangular FOV of 75% resulting in an acquisition time of 2:06 minutes.

\*Work in progress. This information about this product is preliminary. The product is under development and not commercially available in the U.S., and its future availability cannot be ensured.

#### Conclusions

The observed alterations in spinal cord biochemistry, muscle water diffusion, and fatty infiltration in chronic whiplash [16] provides preliminary evidence for the early detection and classification of the patient with a whiplash injury. Current studies indicate that the physiologic measures assessed with the multi-dimensional imaging protocol outlined above show promise for detecting which patients may be at risk for transitioning from acute to persistent pain following a low-velocity traumatic event involving the head and neck.



**4** ROIs in (4A) fat (VARPRO\* based) and (4B) water for the right cervical multifidus muscle. The ROIs are automatically copied to the same location for both images and relative differences (signal loss) between the fat and water images can be calculated.

#### References

- 1 Bassar PJ, Mattiello J, LeBihan D. MR diffusion tensor spectroscopy and imaging. *Biophys J* 1994;66:259-67.
- 2 Bassar PJ, Pierpaoli C. Microstructural and physiological features of tissues elucidated by quantitative-diffusion-tensor MRI. *J Magn Reson B* 1996; 111:209-19.
- 3 Beattie P. Diffusion-Weighted Magnetic Resonance Imaging of the Musculoskeletal System: An Emerging Technology with Potential to Impact Clinical Decision Making. *J Orthop Sports Phys Ther* 2011.
- 4 Beattie PF, Arnot CF, Donley JW, et al. The immediate reduction in low back pain intensity following lumbar joint mobilization and prone press-ups is associated with increased diffusion of water in the L5-S1 intervertebral disc. *JOSPT* 2010;40:256-64.
- 5 Blamire AM, Cader S, Lee M, et al. Axonal damage in the spinal cord of multiple sclerosis patients detected by magnetic resonance spectroscopy. *Magnetic Resonance in Medicine* 2007;58:880-5.
- 6 Borchgrevink G, Smevik O, Haave I, et al. MRI of cerebrum and cervical columna within two days after whiplash neck sprain injury. *Injury* 1997; 28:331-5.

- 7 Brenner T, Freier MC, Holshouser BA, et al. Predicting neuropsychologic outcome after traumatic brain injury in children. *Pediatr Neurol* 2003; 28:104-14.
- 8 Bydder GM, Steiner RE, LH. B. MR imaging of the liver using short T1 inversion recovery. *J Comput Assist Tomogr* 1985;9(6):1084-90.
- 9 Curatolo M, Bogduk N, Ivancic PC, et al. The Role of Tissue Damage in Whiplash Associated Disorders: Discussion Paper 1. *Spine* 2011; 36(25 Suppl): S309-15.
- 10 Dixon W. Simple proton spectroscopic imaging. *Radiology*. 1984;153:189-94.
- 11 Elliott JM, Jull G, Noteboom JT, et al. Fatty infiltration in the cervical extensor muscles in persistent whiplash-associated disorders: a magnetic resonance imaging analysis. *Spine (Phila Pa 1976)* 2006;31:E847-55.
- 12 Elliott JM, Pedler A, Kenardy J, et al. The temporal development of Fatty infiltrates in the neck muscles following whiplash injury: an association with pain and posttraumatic stress. *PLoS One* 2011; 6:e21194.
- 13 Elliott JM, Sterling M, Noteboom JT, et al. Fatty infiltrate in the cervical extensor muscles is not a feature of chronic, insidious-onset neck pain. *Clin Radiol* 2008;63:681-7.
- 14 Elliott JM, Sterling M, Noteboom JT, et al. The clinical presentation of chronic whiplash and the relationship to findings of MRI fatty infiltrates in the cervical extensor musculature: a preliminary investigation. *Eur Spine J* 2009;18:1371-8.
- 15 Elliott JM, O'Leary S, Sterling M, et al. Magnetic resonance imaging findings of fatty infiltrate in the cervical flexors in chronic whiplash. *Spine (Phila Pa 1976)* 2010;35:948-54.
- 16 Elliott JM, Pedler AR, Cowin G, et al. Spinal cord metabolism and muscle water diffusion in whiplash. *Spinal Cord* 2011; PMID: 21383759.
- 17 Frindel C, Robini M, Croisille P, et al. Comparison of regularization methods for human cardiac diffusion tensor MRI. *Med Image Anal* 2009;13:405-18.
- 18 Frindel C, Robini M, Rapacchi S, et al. Towards in vivo diffusion tensor MRI on human heart using edge-preserving regularization. *Conf Proc IEEE Eng Med Biol Soc* 2007;2007:6008-11.
- 19 Haase A, Frahm J, Hänicke W, et al. 1H NMR chemical shift selective (CHESS) imaging. *Phys Med Biol* 1985;30.
- 20 Hagmann P, Jonasson L, Maeder P, et al. Understanding diffusion MR imaging techniques: from scalar diffusion-weighted imaging to diffusion tensor imaging and beyond. *Radiographics* 2006;26 Suppl 1:S205-23.
- 21 Hernando D, Kellman P, Haldar JP, et al. Estimation of water/fat images, B0 field map and T2\* map using VARPRO. In *Proceedings of the 16th Annual Meeting of ISMRM, Toronto, Canada*. 2008:1517.
- 22 Hoischen A, Landwehr C, Kabisch S, et al. Array-CGH in unclear syndromic nephropathies identifies a microdeletion in Xq22.3-q23. *Pediatr Nephrol* 2009;24:1673-81.
- 23 Holl N, Echaniz-Laguna A, Bierry G, et al. Diffusion-weighted MRI of denervated muscle: a clinical and experimental study. *Skeletal Radiol* 2008;37:1111-7.
- 24 Holly LT, Freitas B, McArthur DL, et al. Proton magnetic resonance spectroscopy to evaluate spinal cord axonal injury in cervical spondylotic myelopathy. *J Neurosurg Spine* 2009;10:194-200.
- 25 Hsieh TJ, Chang JM, Chuang HY, et al. End-stage renal disease: in vivo diffusion-tensor imaging of silent white matter damage. *Radiology* 2009; 252:518-25.
- 26 Ito S, PM, Ivancic PC, Pearson AM. Spinal canal narrowing during simulated whiplash. *Spine* 2004;29:1330-9.
- 27 Ivancic PC, Sha D, Lawrence BD, et al. Effect of Active Head Restraint on Residual Neck Instability due to Rear Impact. *Spine* 2010;35:2071-78.
- 28 Ivancic PC, Pearson AM, Panjabi MM, et al. Injury of the anterior longitudinal ligament during whiplash simulation. *Eur Spine J* 2004;13:61-8.
- 29 Jones DK, Simmons A, Williams SC, et al. Non-invasive assessment of axonal fiber connectivity in the human brain via diffusion tensor MRI. *Magn Reson Med* 1999;42:37-41.
- 30 Kataoka M, Kido A, Yamamoto A, et al. Diffusion tensor imaging of kidneys with respiratory triggering: optimization of parameters to demonstrate anisotropic structures on fraction anisotropy maps. *J Magn Reson Imaging* 2009;29:736-44.
- 31 Kendi AT, Tan FU, Kendi M, et al. MR spectroscopy of cervical spinal cord in patients with multiple sclerosis. *Neuroradiology* 2004;46:764-9.
- 32 Lindenberg R, Renga V, Zhu LL, et al. Structural integrity of corticospinal motor fibers predicts motor impairment in chronic stroke. *Neurology*; 74:280-7.
- 33 Myran R, Kvistad KA, Nygaard OP, et al. Magnetic resonance imaging assessment of the alar ligaments in whiplash injuries: a case-control study. *Spine* 2008;33:2012-6.
- 34 Myran R, Zwart JA, Kvistad KA, et al. Clinical characteristics, pain and disability in relation to alar ligament MRI findings. *Spine (Phila Pa 1976)* 2011.
- 35 Notohamiprodjo M, Glaser C, Herrmann KA, et al. Diffusion tensor imaging of the kidney with parallel imaging: initial clinical experience. *Invest Radiol* 2008;43:677-85.
- 36 Ortengren T, Hansson HA, Lovsund P, et al. Membrane leakage in spinal ganglion nerve cells induced by experimental whiplash extension motion: a study in pigs. *J Neurotrauma* 1996;13:171-80.
- 37 Panjabi MM, Ito S, Pearson AM, et al. Injury mechanisms of the cervical intervertebral disc during simulated whiplash. *Spine* 2004;29:1217-25.
- 38 Panjabi MM, Maak TG, Ivancic PC, et al. Dynamic intervertebral foramen narrowing during simulated rear impact. *Spine* 2006;31:E128-34.
- 39 Pettersson K, Hildingsson C, Toolanen G, et al. Disc Pathology after whiplash injury: a prospective magnetic resonance imaging and clinical investigation. *Spine* 1997;22:283-8.
- 40 Pettersson K, Hildingsson C, Toolanen G, Fagerlund M, Bjornebrink J. MRI and neurology in acute whiplash trauma. No correlation in prospective examination of 39 cases. *Acta Orthopaed Scand* 1994;65:525-8.
- 41 Reeder SB, Pineda AR, Wen Z, et al. Iterative decomposition of water and fat with echo asymmetry and least-squares estimation (IDEAL): Application with fast spin-echo imaging. *Magn Reson Med* 2005;54:636-44.
- 42 Reeder SB, Wen Z, Yu H, et al. Multicoil Dixon chemical species separation with an iterative least squares estimation method. *Magn Reson Med* 2004 2004;51:35-45.
- 43 Ries M, Jones RA, Basseau F, et al. Diffusion tensor MRI of the human kidney. *J Magn Reson Imaging* 2001;14:42-9.
- 44 Ronnen HR, de Korte PJ, Brink PR, et al. Acute whiplash injury: is there a role for MR imaging? – a prospective study of 100 patients. *Radiology* 1996;Oct;201:93-6.
- 45 Sehy JV, Ackerman JJH, Neill JJ. Evidence that both fast and slow ADC components arise from intracellular space. *Magn Res Med* 2002;48:765-70.
- 46 Siegmund GP, Winkelstein BA, Ivancic PC, et al. The anatomy and biomechanics of acute and chronic whiplash injury. *Traffic Inj Prev* 2009; 10:101-12.
- 47 Sosnovik DE, Wang R, Dai G, et al. Diffusion MR tractography of the heart. *J Cardiovasc Magn Reson* 2009;11:47.
- 48 Svensson MY, Aldman B, Bostrom O, et al. [Nerve cell damages in whiplash injuries. Animal experimental studies]. *Orthopade* 1998;27:820-6.
- 49 Tominaga Y, Maak TG, Ivancic PC, et al. Head-turned rear impact causing dynamic cervical intervertebral foramen narrowing: implications for ganglion and nerve root injury. *J Neurosurg Spine* 2006;4:380-7.
- 50 Virta A, Barnett A, Pierpaoli C. Visualizing and characterizing white matter fiber structure and architecture in the human pyramidal tract using diffusion tensor MRI *Magn Reson Imaging* 1999;17:1121-33.
- 51 Winkelstein BA, McLendon RE, Barbir A, et al. An anatomical investigation of the human cervical facet capsule, quantifying muscle insertion area. *J Anat* 2001 Apr;198:455-61.
- 52 Winkelstein BA, NR, Richardson WJ, et al. The cervical facet capsule and its role in whiplash injury: a biomechanical investigation. *Spine* 2000 May 15;25:1238-46.
- 53 Winkelstein BA, Rutkowski MD, Sweitzer SM, et al. Nerve injury proximal or distal to the DRG induces similar spinal glial activation and selective cytokine expression but differential behavioral responses to pharmacologic treatment. *J Comp Neurol* 2001; 439:127-39.

#### Contact

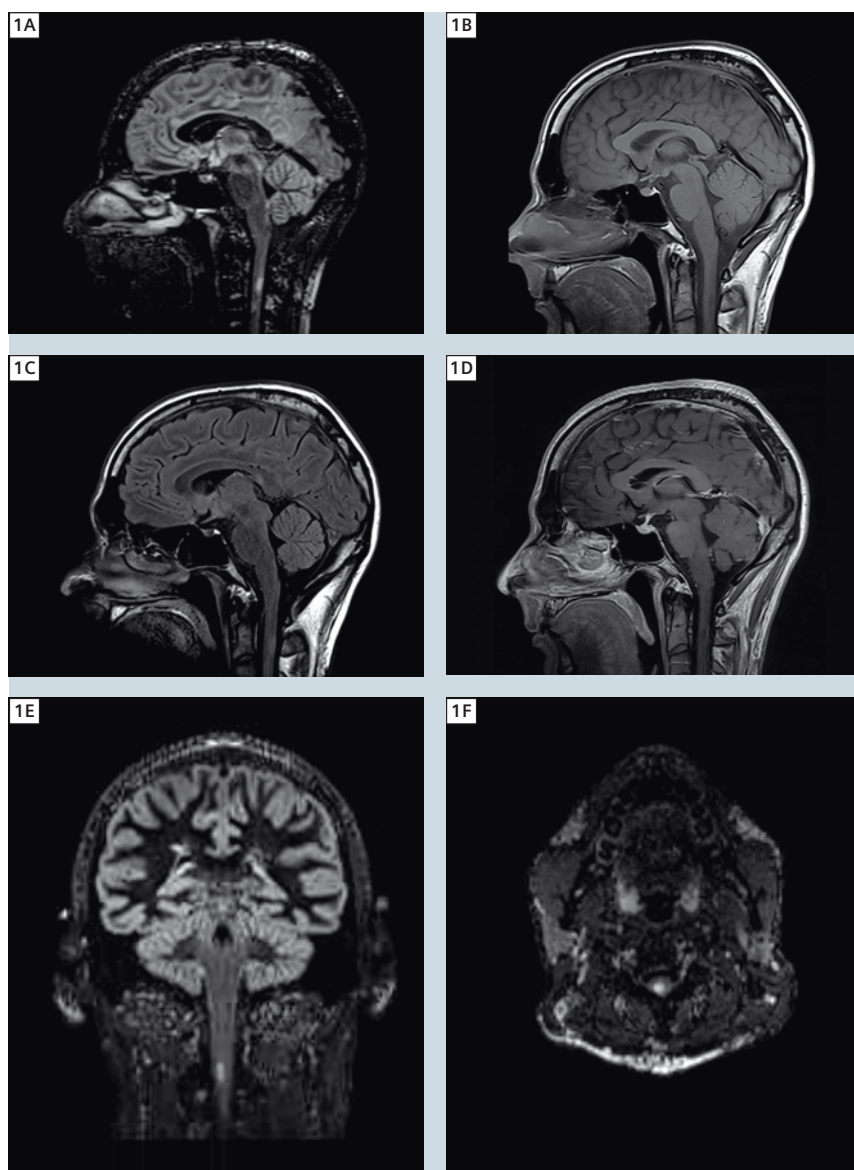
James M. Elliott PT, Ph.D.  
Department of Physical Therapy  
and Human Movement Sciences  
Feinberg School of Medicine  
Northwestern University  
645 N. Michigan Ave  
Suite 1100  
Chicago, IL, 60611  
USA  
j-elliott@northwestern.edu

# Case Report:

## Cervical Spine 3D Double Inversion Recovery (DIR) in Demyelination

David Shipp

Monash Medical Centre, Clayton, Australia



**1** SPACE DIR (1A) and corresponding sagittal T1w image (1B), FLAIR (1C), post contrast T1w image (1D), coronal (1E) and transversal MPR of the SPACE DIR (1F).

### Introduction

The Double Inversion Recovery (DIR) sequence\* is beginning to be widely accepted in brain MRI examinations to display multiple sclerosis (MS) plaques [1]. DIR employs two inversion times (TI); in our case the 3T MAGNETOM Verio works in progress (WIP) sequence uses one fixed TI of 450 ms, and an adjustable TI of 3000 ms, resulting in suppression of the signal from white matter and cerebrospinal fluid (CSF) leading to increased conspicuity for white matter lesions. Thus far the sequence has been essentially confined to use in the brain. We recently investigated extending the technique into the cervical spine.

### Patient history

#### Case 1

A 32-year-old male referred with possible MS underwent DIR of the brain which included the upper cervical cord within the field-of-view. An upper cervical cord lesion is well appreciated (Fig. 1).

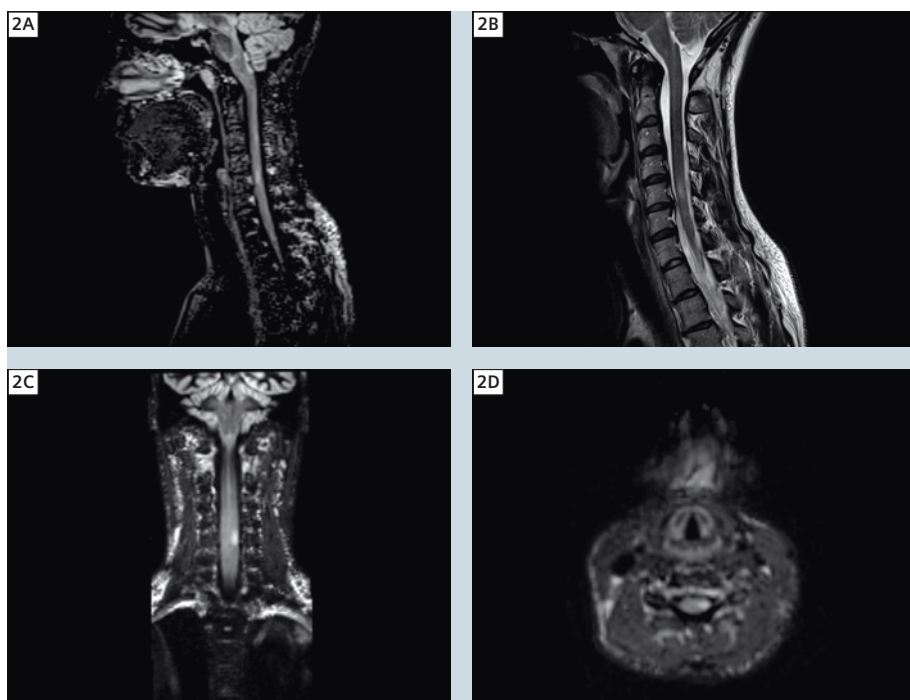
#### Case 2

A 37-year-old female for an annual review post immune therapy for optic neuritis and MS. Dedicated cervical spine DIR was performed (Fig. 2).

### Sequence details

Images obtained utilizing a Siemens 3T MAGNETOM Verio with the Head and

\*WIP – Works in progress. This information about this product is preliminary. The product is under development and not commercially available in the U.S., and its future availability cannot be ensured.



**2** SPACE DIR (2A) and corresponding T2w image (2B) in sagittal orientation. Coronal (2C) and transversal (2D) MPR of the SPACE DIR.

Neck Matrix coil combination. Sequence parameters for 3D sagittal DIR: TR 7500 ms, TE 325 ms, 1.5 mm isotropic voxel size, TI of 3000 ms, iPAT factor 2, 100 % slice oversampling (to reduce the likelihood of aliasing involving the shoulders), scan time 7 min 39 sec. Axial and coronal multiplanar reconstructions (MPR) post processing.

## Imaging findings

### Case 1

The 3D sagittal DIR demonstrates a lesion at the level of C2 consistent with a demyelination plaque (Fig. 1A). Comparing the lesion's appearance on the other sagittal sequences performed; T1 (Fig. 1B), T2 FLAIR (Fig. 1C) and T1 SPACE post-contrast (Fig. 1D) the lesion is most conspicuous on the sagittal DIR. The DIR MPRs further increase diagnostic confidence (Fig. 1E coronal 2 mm MPR, Fig. 1F axial 2 mm MPR).

### Case 2

3D sagittal DIR demonstrates a lesion at the level of C5 on the left (Fig. 2A); a

new lesion from previous MR exams. Comparison between the sagittal T2 (Fig. 2B) and the 3D sagittal DIR demonstrates relative increased conspicuity on the DIR sequence. MPRs were again employed (Figs. 2C, D coronal and axial).

## Discussion

Where the clinical query is MS and in the monitoring of established MS cases the sagittal 3D DIR WIP sequence has proven helpful. Based on these experiences we are sure that the sequence will find its way into clinical routine for brain MR exams.

Early promising results in the cervical cord have been seen whether this has been when combined with brain visualization (e.g. case 1) or with dedicated cervical cord imaging (e.g. case 2). Demyelination plaques may be challenging to visualize on T2-weighted imaging alone as the lesions are often adjacent to CSF. The DIR sequence results in high lesion to background signal in the cord, CSF suppression and the ability to review

multiple planes resulting in apparent more confident lesion detection in this case series warranting further evaluation. We are now progressing to a formal pilot evaluation in a larger case series.

## Reference

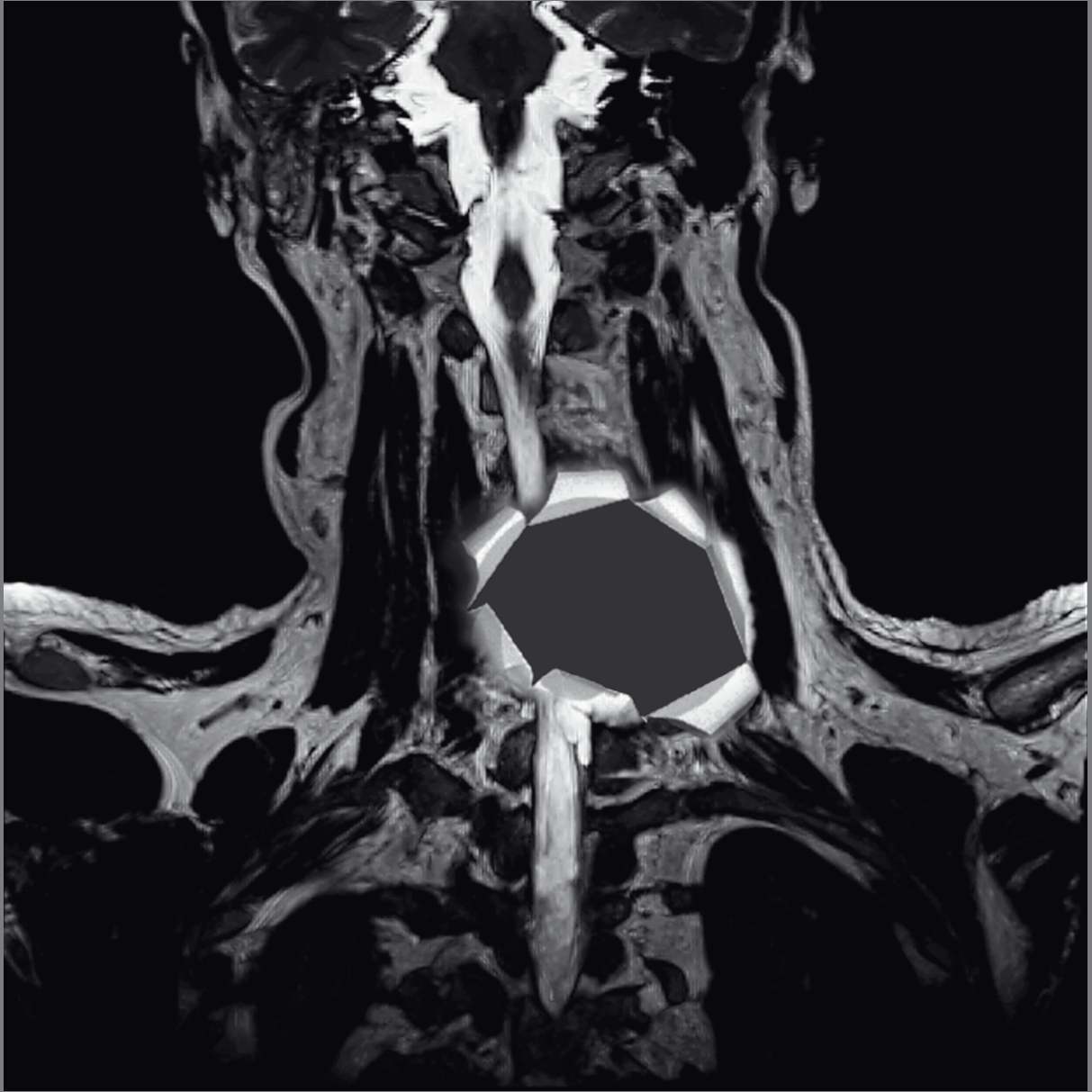
- 1 J.J.G. Geurts et al., Consensus recommendations for MS cortical lesion scoring using double inversion recovery MRI. *Neurology* 76, February 2011.

## Contact

David Shipp  
MRI Supervisor  
Monash Medical Centre  
Clayton  
Australia  
Phone: +61 9594 2014  
Fax: +61 9594 6009  
David.Shipp@southernhealth.org.au

\*WIP – Works in progress. This information about this product is preliminary. The product is under development and not commercially available in the U.S., and its future availability cannot be ensured.

# Missing information?



To make sure you have all the information you need, register for our free monthly newsletter on clinical MRI information. Check out case reports from MAGNETOM users around the world and stay up-to-date with Siemens software applications.

Register at  
[www.siemens.com/magnetom-world](http://www.siemens.com/magnetom-world)  
Go to  
**Publications > Subscriptions**

# Brain Perfusion; How & Why

Nader Binesh, Ph.D.<sup>1</sup>; Marcel M. Maya, M.D.<sup>1</sup>; Helmuth Schultze-Haakh, Ph.D.<sup>2</sup>; Franklin G. Moser, M.D.<sup>1</sup>

<sup>1</sup>Department of Imaging, Cedars Sinai Medical Center, Los Angeles, CA, USA

<sup>2</sup>Siemens Medical Solutions, Cypress, CA, USA

## Introduction

Cerebral perfusion is defined as the steady-state delivery of nutrients and oxygen via blood to brain tissue parenchyma per unit volume and is typically measured in milliliters per 100 g of

tissue per minute. In perfusion MR imaging, however, the term 'perfusion' comprises several tissue hemodynamic parameters (cerebral blood volume – CBV, cerebral blood flow – CBF, and

mean transit time - MTT) that can be derived from the acquired data. In the evaluation of intracranial mass lesions, however, CBV appears to be the most useful parameter.



1 Slice positioning for the perfusion series (copied to the position of DarkFluid T2).

Perfusion MR imaging methods take advantage of signal changes that accompany the passage of tracer (most commonly gadolinium based MR contrast agents) through the cerebrovascular system. Perfusion imaging can be performed with techniques based on dynamic susceptibility contrast (DSC) or based on vascular permeability. DSC imaging allows approximately 10 MR sections every second and is ideal for rapid dynamic imaging. As the gadolinium contrast enters the circulation, it induces susceptibility changes by way of its paramagnetic properties; this in turn results in shorter T2\* values and significant signal loss. Curves showing intensity changes based on the concentration of gadolinium over time can be generated. The concentration of gadolinium is a direct representation of the capillary density. From this, the relative cerebral blood volume (rCBV) can be determined, which corresponds to the volume of blood within brain tissue. rCBV mirrors the neovascularization associated with tumor angiogenesis; in adults with glial tumors, angiogenesis is highly correlated to tumor grade, and the rCBV of most high-grade glial tumors is greater than that of low grade tumors. Perfusion MR imaging is increasingly being used as a diagnostic and research tool that provides maps of the regional variations in cerebral microvasculature of normal and diseased brains. With relatively short imaging and data processing times and the use of a standard dose of contrast agent, perfusion MR imaging is a promising tool that can easily be incorporated as part of the routine clinical evaluation of intracranial mass lesions. Although still investigational, MR imaging CBV measurements can be used as an adjunct to conventional imaging to help assess the degree of neovascularization in brain tumors, evaluate tumor grading and malignancy, identify tumor-mimicking lesions (such as radiation necrosis, cerebral abscess, and tumefactive demyelinating lesion (TDL)) by demonstrating their lack of angiogenesis, and assess the status of viable tissue surrounding an acute infarct. It must be emphasized, however, that perfusion MR imaging is a relatively new and prom-

ising imaging tool rather than a standard proven technique for tumor grading and staging. In the future, perfusion MR imaging may become useful in the monitoring of treatment, and its results may also potentially serve as an arbiter when determining the efficacy of novel therapeutic agents, especially antiangiogenic therapy.

The DSC-MRI measurements can help investigate hemodynamic abnormalities associated with inflammation, lesion reactivity and vascular compromises. Even a non-enhancing lesion may show high perfusion which suggests inflammatory reactivity that cannot be seen on conventional MRI.

Although brain perfusion has been around for while [2] and its uses and advantages known for more than a decade [2–4], it is not yet widely performed. This could be due to the following reasons:

1. The interpretation/quantification is not well established (or accepted) among radiologists.
2. The post-processing of the images is not yet automated and still needs someone with expertise to perform all or part of the post-processing.
3. The technologists and radiologists assume that it is hard to integrate into the usual protocol.

Brain perfusion can easily be integrated into any brain imaging routine with contrast. Instead of hand injection the contrast bolus should be delivered by a power injector. However, it is at the discretion of the physician to apply contrast media if need be. The perfusion does not add any extra risk to a normal brain MRI examination, as in all these cases the patient would have been given a contrast agent anyway. The perfusion data is acquired during the injection without increasing the amount of Gadolinium contrast. The addition of the perfusion adds about 2 minutes to the examination time. Easy post-processing may add informative maps aiding the radiologists in their diagnoses of various brain lesions.

We have worked on brain perfusion in our clinical setting for the past three

years and have scanned, post-processed and dictated more than 1000 cases. Here we would like to present our method of scanning and post-processing with a few clinical examples to highlight the importance of perfusion in the diagnosis of the lesion in question.

## Methodology

### Scanning

All the brain perfusion studies have been acquired on Siemens MRI scanners and have been post-processed on a Siemens Multi-Modality Work Place (MMWP), with Siemens perfusion evaluation software. The scanners used were:

MAGNETOM Symphony with Quantum gradients (software version *syngo* MR A25 and *syngo* MR A30), MAGNETOM Symphony a Tim System (*syngo* MR B15 and *syngo* MR B17), MAGNETOM Sonata (*syngo* MR A25), MAGNETOM Avanto (*syngo* MR B15 and *syngo* MR B17), all 1.5T and the 3T MAGNETOM Verio (*syngo* MR B15 and *syngo* MR B17).

The perfusion was done as part of the routine (with contrast) brain examination for patients who were scheduled for surgery or at the request of a radiologist. Our routine brain exam consists of sagittal T1 (TSE), axial T2 (TSE), axial FLAIR (TSE), axial EPI diffusion and post-contrast axial MPAGE T1. The perfusion series uses the sequence *ep2d\_perf* that can be found in the Siemens protocol tree under head-Advance-Diffusion & Perfusion. We modified the Siemens standard protocol slightly to suite the rest of our protocols to match primarily the slice thickness, slice gap and field-of-view (FOV).

The following are the steps to perform a brain perfusion study on a Siemens MR scanner:

- Make sure the patient has a good intra-venous line (IV) with a needle gauge of 18 or 20. Use the antecubital veins and avoid more peripheral placement of the needle.
- Hook the patient's IV to an injector and set the injection rate to 4 ml per second. A normal contrast dose of 0.1 mM/kg should be used.

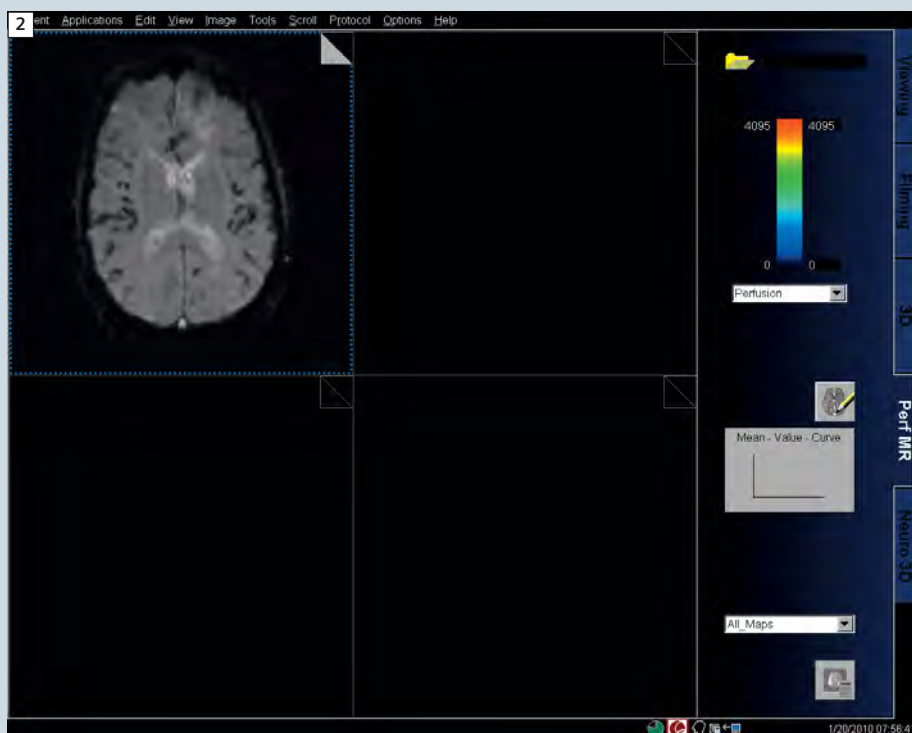
- Make sure the IV is good and shows no resistance to flow.
- Start the routine exam, and insert the perfusion procedure just before the post-contrast T1.
- The perfusion imaging slices should have the same **positioning, thickness and gap** as the axial FLAIR or T2 sequences to facilitate a direct comparison of the perfusion results with other pre- and post-contrast images (Fig. 1).
- Make sure that both the lesion and cortical white matter are covered.
- The phase encoding direction needs to be anterior-posterior (A/P) to reduce susceptibility artifacts.

After the pre-contrast portion of the brain exam is done, be ready with the injection: start the scan and inject the contrast at the 8<sup>th</sup> measurement. The scan has 50 time points (measurements) of ~2 s each resulting in total time just below 2 min.

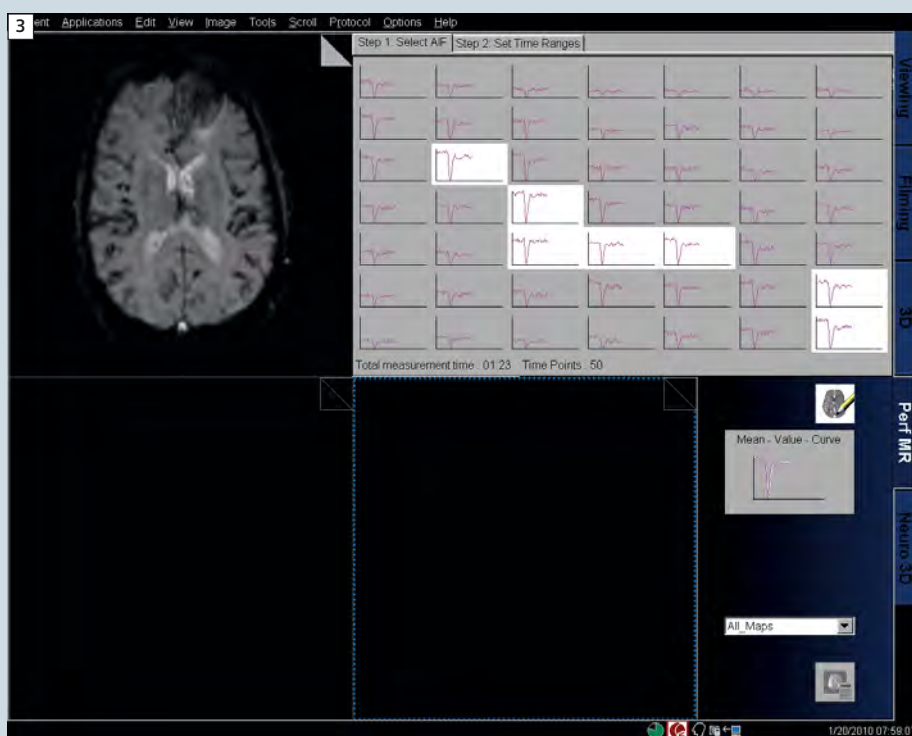
Send the main series to the workstation where you want to do the post-processing of the images.

### Post-Processing

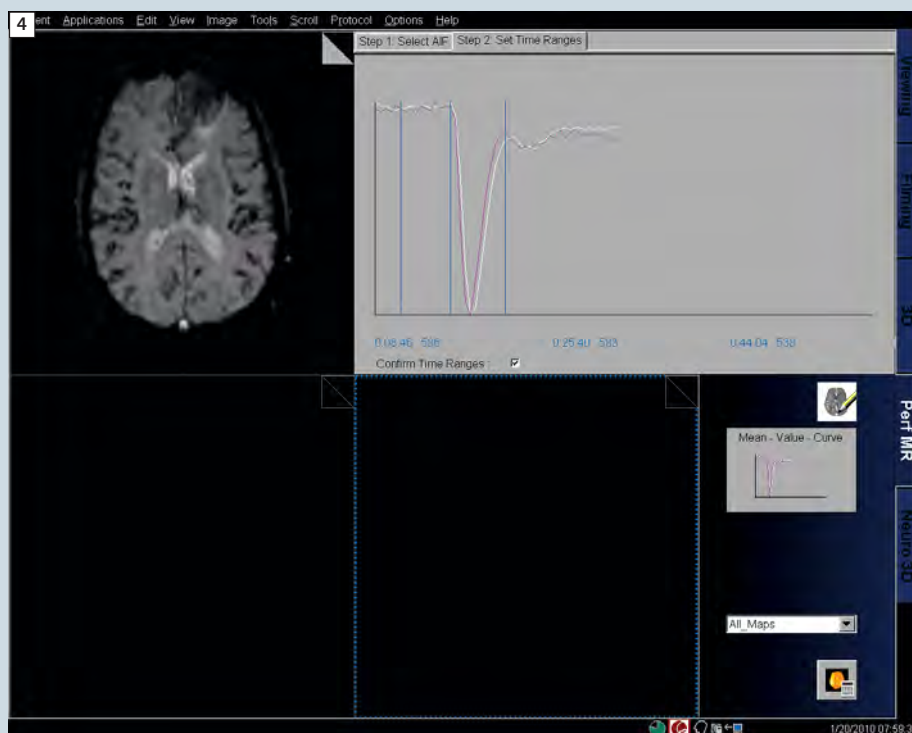
- On the Siemens workstation (MMWP or Leonardo), open the perfusion application (Application-Perfusion).
- Open the Patient Browser and load the main perfusion series into the Perfusion Page (Fig. 2).
- Click on the images and page through to get to the slice where you can see the area of interest (tumors etc.).
- Identify an artery on the same slice.
- Click on the small AIF icon:
  - A square appears on the image.
  - Place the square on the artery (Fig. 3).
- On the right side of the screen (Fig. 3), select AIF, by choosing the best time graphs, the ones with significant signal drop (highlighted squares). Do so for 4 or more time-points, hold the Contr.-key while clicking with the left mouse-button.




**2** Opening page of the perfusion application. The perfusion series has been dropped and can be seen in the first quadrant (top left).

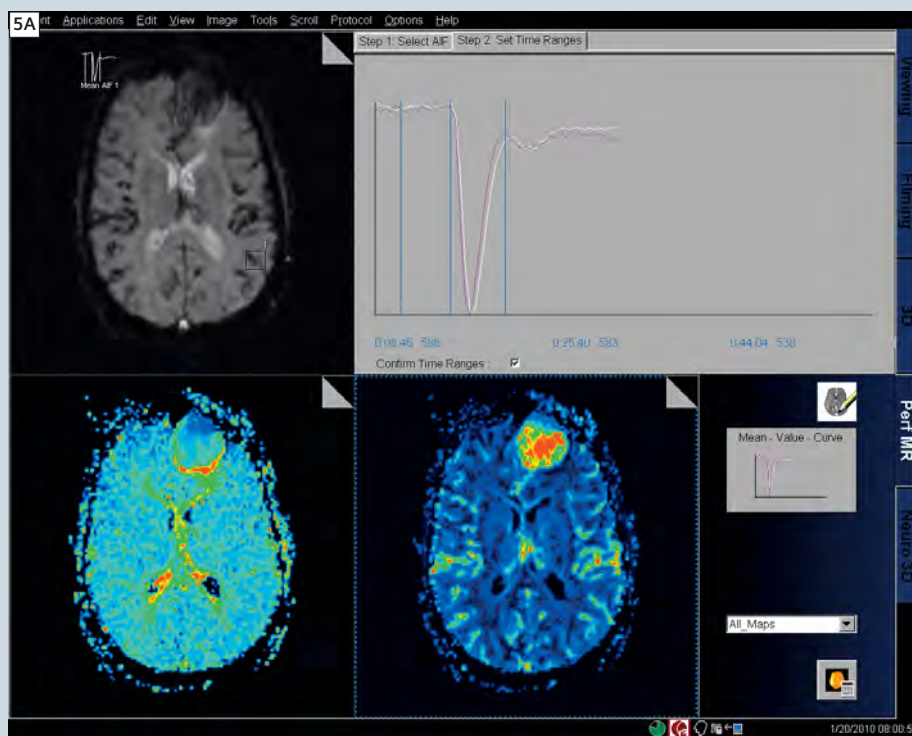


**3** The arterial input function (AIF) square is shown on a slice of the perfusion image data, with the resulting 9x9 pixels time points on the right side. The highlighted region-of-interest (ROI) is used to calculate the AIF from.



**4** The resulted AIF, with the three time points properly shown. The first one is at the baseline, second at the start of the drop and the third at the end of the drop (peak of recovery).

- When done, click on the second tab: Step 2: Set Time Ranges (Fig. 4). Move the three time-lines, so that the first one is at the start of the baseline, the second one at the beginning of the drop (Gad entry) and the third one at the peak of the recovery, as shown in Figure 4. Then click the check box 'Confirm Time Ranges'.
- Make sure the selector at the lower-right side of screen is on 'All Maps'.
- Click on the color calculator/brain icon  at the bottom-right corner of the screen. If the icon is dimmed (grayed out) the time selection has not been done yet. The calculation takes about 20–30 seconds.



**5A** Figure shows the perfusion screen, after the calculation is done. (5A) The rCBF is displayed in the fourth quadrant (lower right) and the TTP is displayed in 3<sup>rd</sup> quadrant (lower left).

Once the calculation is done, the rCBV (relative cerebral blood volume) and rCBF (relative cerebral blood flow) color images are displayed in the 4<sup>th</sup> quadrant, of the screen, as shown in figure 5 (A and B). Toggle between series using the '4' and '5' keys on the numerical key pad (on right of keyboard). The third quadrant shows the MTT (mean transit time) and TTP (time-to-peak) maps. We don't bother with these.

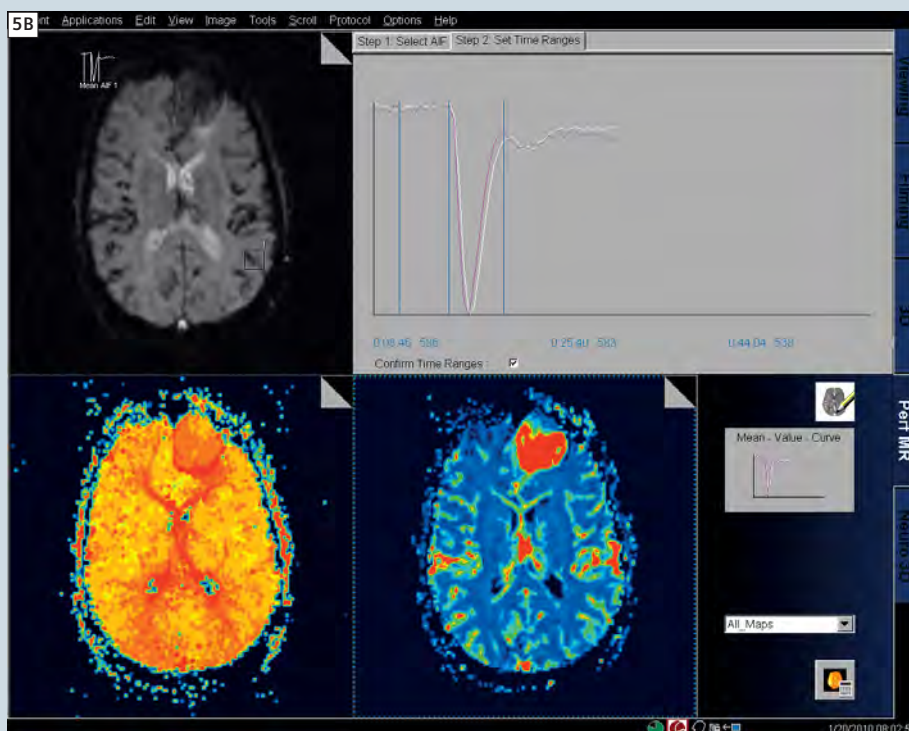
- In the 4<sup>th</sup> quadrant, i.e. the bottom right segment, select series (right mouse button), adjust the windowing (center mouse button) and save as new series (from the top menu, File-Save As... (e.g. call them **CBV\_color** or **CBF\_color** depending on which one was selected).

These are just the color maps but the pixel values are arbitrary.

## Normalization of pixel values

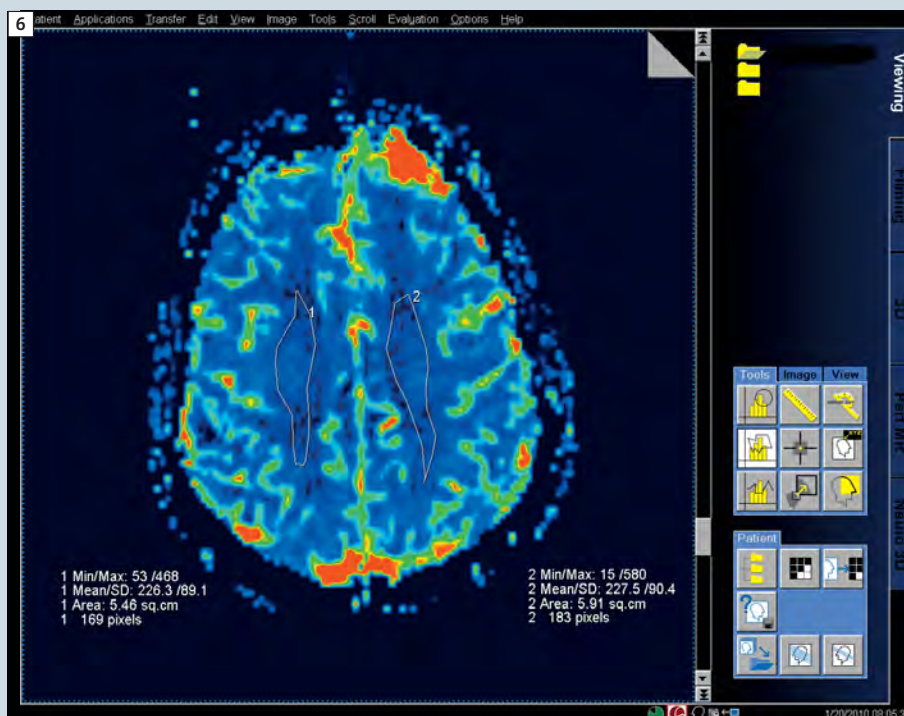
To normalize the values:

- Go to the Viewing card (right side tabs) and open the series 'CBV\_color'.
- Scroll to the top of the brain where you can see the cortical white matter without any distortions.

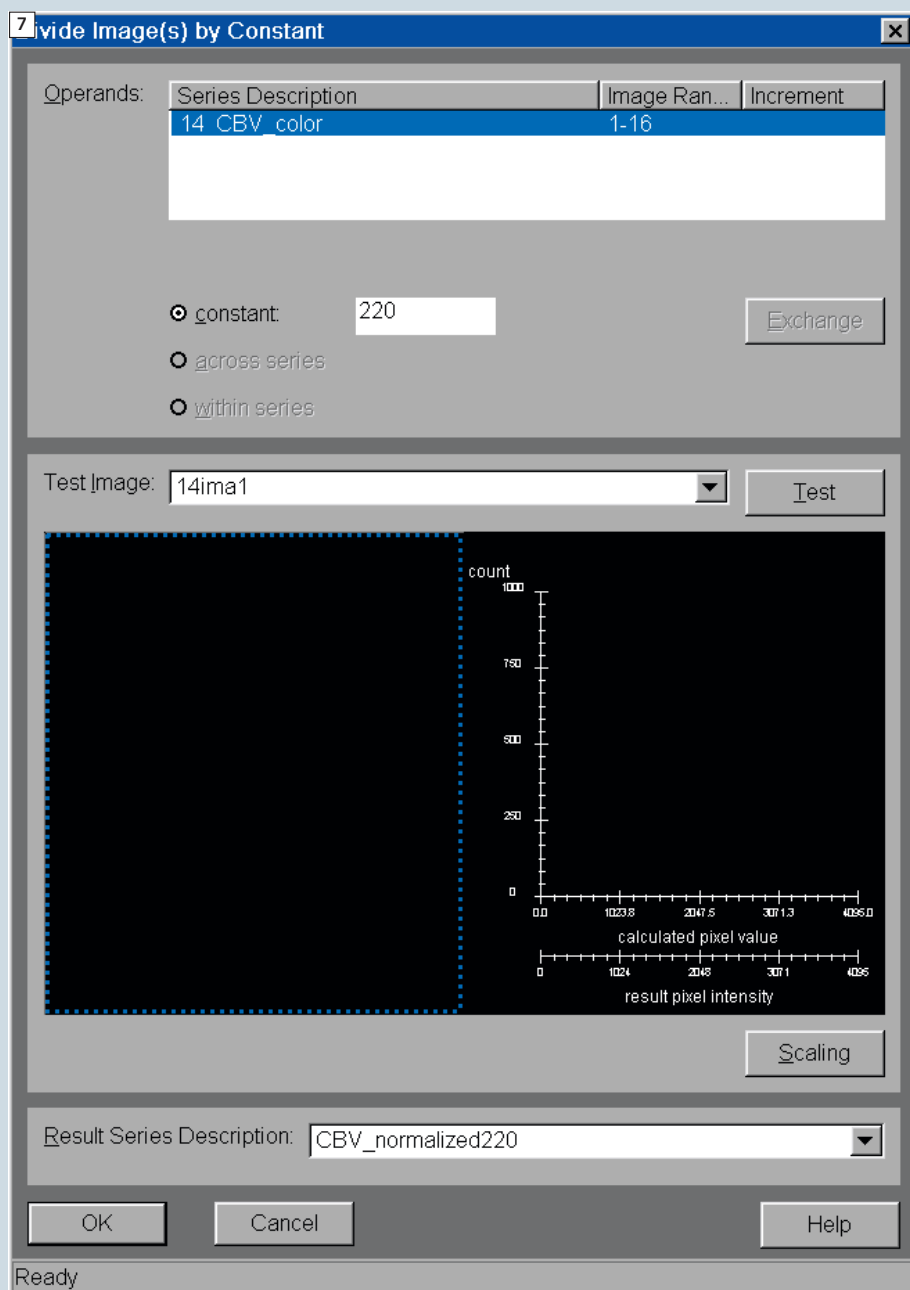


**5B** The rCBV is displayed in the fourth quadrant (lower right) and the MTT is displayed in 3<sup>rd</sup> quadrant (lower left).

- Using the free hand drawing (right side panel), draw an enclosure (Fig. 6), which only contains healthy white matter, one on each side, if possible, and on two slices, if possible.
- Read the mean signal values and calculate their average (avg) mean value (adding all the values and divide by the number of samples used).
- Select the whole series (right mouse button). From the top menu choose 'Evaluation- Dynamic Analysis – Divide...'.



**6** Typical region selection for the cortical white matter tissue, to find the average healthy white matter intensity.



- In the new window (Fig. 7) enter the mean value (avg from above) as the constant and rename the final series to **CBV\_normalized\_avg** under 'Result Series Description'. Press ok.
- Open the browser and select the 'CBV\_color' series.
- From the Application tab, choose: MR – DICOM – Save as RGB. This creates a series automatically named 'CBV\_color\_RGB', adding '\_RGB' to the original series name. This makes the CBV\_color series RGB-color coded so that it can be seen in color on PACS workstations.
- Do the same for 'CBF\_color'.

**7** The dialog box which opens for dividing the whole rCBV by a number (average Cortical WM).

## Discussion

Following the above procedure we have done many brain perfusion studies and have used them to grade tumors. The idea of having the color maps and the normalized version is that the normalized version appears only in gray scale on PACS stations, but its pixel intensities

have CBV values normalized to white matter. By simultaneously displaying and correlating the color CBV images with the normalized ones, the radiologist is able to see the tissues color coded and can read the corresponding perfusion values with respect to healthy white

matter (normalized value). In the literature describing a few studies with an aggressive tumor the perfusion ratio (with respect to white matter) was above 2.5 [5]. By using this method a radiologist can evaluate and grade a tumor more quantitatively.

## Case reports

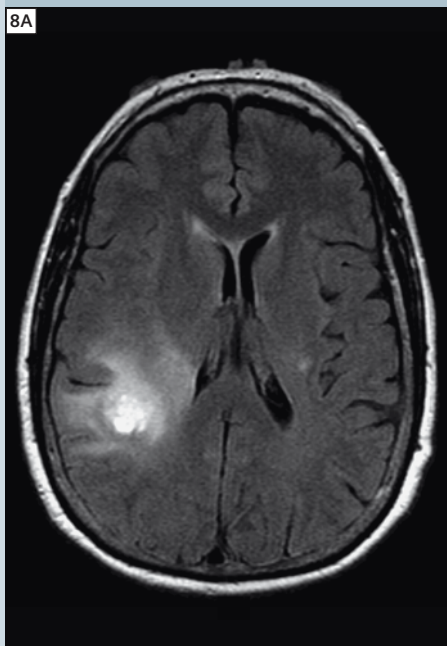
To illustrate the usefulness of perfusion imaging in clinical practice, here are four clinical examples from our practice:

### Case 1

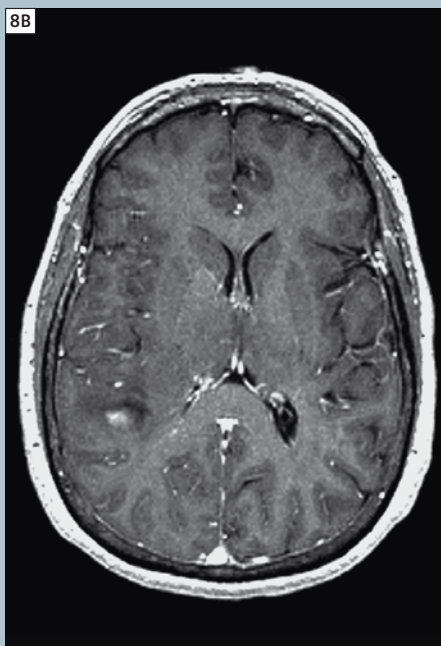
A 64-year-old female with a history of brain tumor received radiation and chemotherapy treatment a few months prior to our examination. The initial MRI showed abnormal signal on FLAIR (IR T2), but the T1w post-contrast

showed no enhancement. This pointed to a low grade tumor. A follow-up MRI with perfusion was performed, which again showed abnormal hyperintensity on FLAIR (Fig. 8A) and no gadolinium enhancement (Fig. 8B), but the perfu-

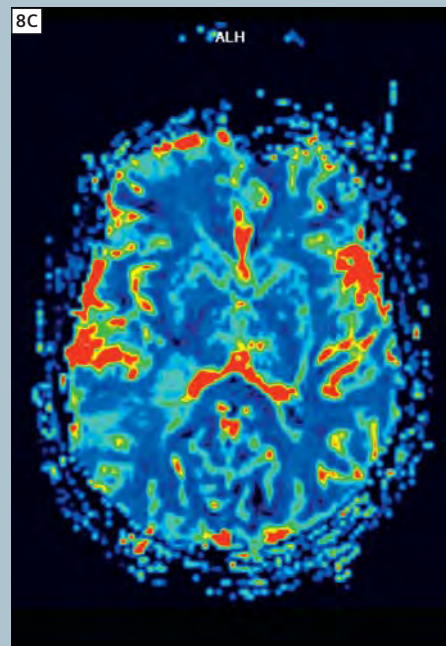
sion images (rCBV) (Fig. 8C) showed highly perfused tissues pointing to a high grade neoplasm, which was subsequently resected. Histology confirmed high grade astrocytoma.



**8A** Axial FLAIR



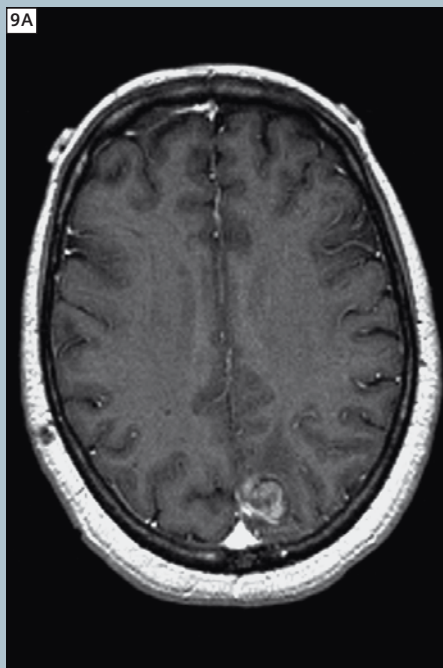
**8B** Axial post T1



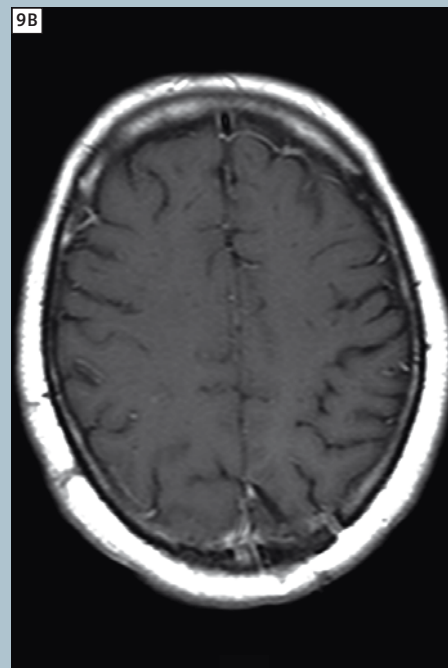
**8C** Perfusion map CBV

## Case 2

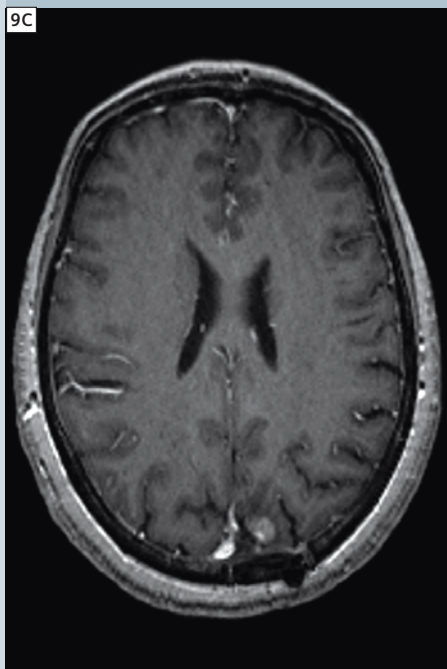
A 60-year-old female with history of metastatic lung cancer, presented with metastatic nodule in the left occipital lobe. She underwent craniotomy followed by postoperative radiotherapy to the surgical bed. The one year follow-up brain MRI showed minimal enhancement on post-contrast MRI. The two year follow-up showed a nodular mass, which further grew on short term follow-up. The diagnosis could be either new tumor growth or radiation necrosis. The low signal of rCBV in her perfusion examination pointed toward radiation necrosis rather than tumor re-growth. The enhancing part was subsequently excised and pathology confirmed radiation necrosis.



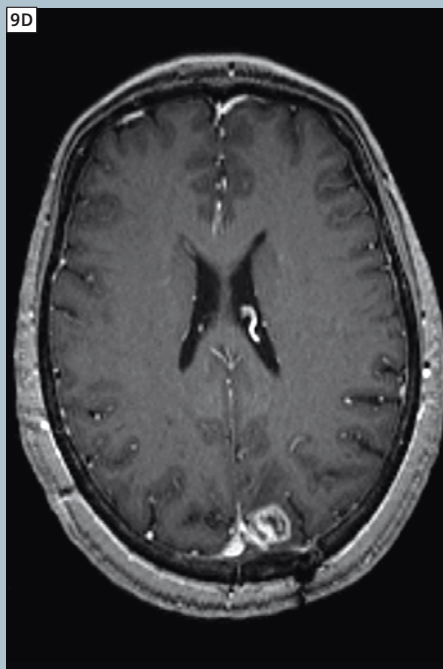
**9A** Axial post T1 (pre-surgical)



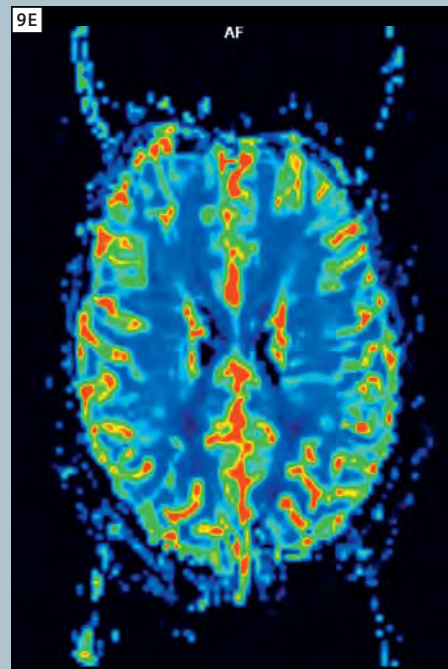
**9B** Axial post T1 (one year post surgery)



**9C** Axial post T1 (two years post surgery)



**9D** Axial post T1  
(2 years and 2 months post surgery)



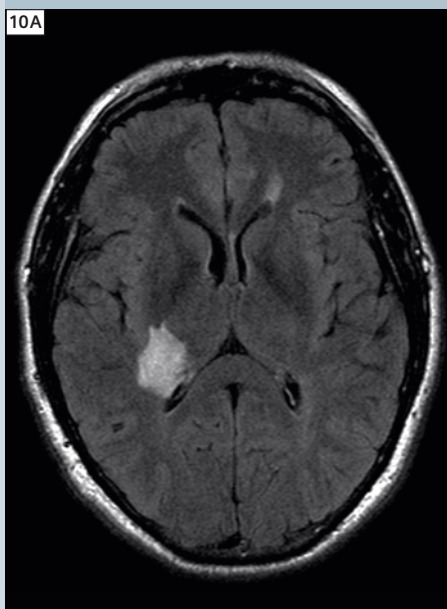
**9E** Axial perfusion map CBV  
(2 years and 2 months post surgery)

### Case 3

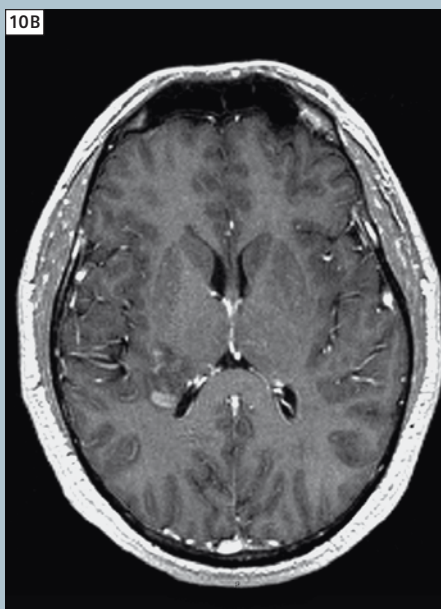
The routine MRI of a 48-year-old right-handed man showed a lesion at the right thalamus suspected of low grade glioma. Subsequent imaging showed a lesion involving the right posterolateral thalamus posterior to the periven-

tricular white matter, which had features suggestive of tumoractive multiple sclerosis (MS), but the possibility of primary brain neoplasm could not be excluded, especially as the MR spectroscopy (MRS) showed elevated

choline signal. The perfusion protocol was performed and both the rCBV and rCBF showed low values (close to those of normal white matter). That pointed to MS with a low possibility of an additional primary brain neoplasm.



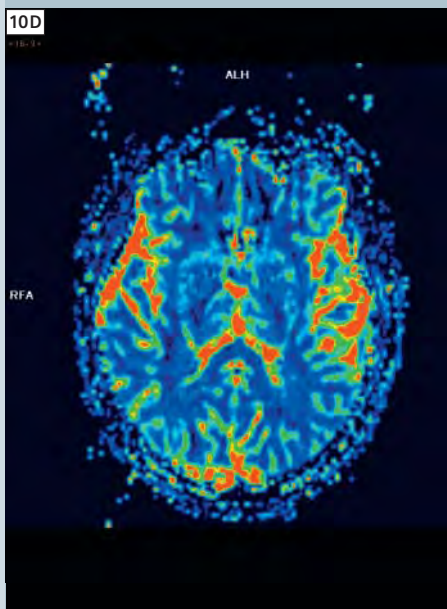
**10A** Axial FLAIR



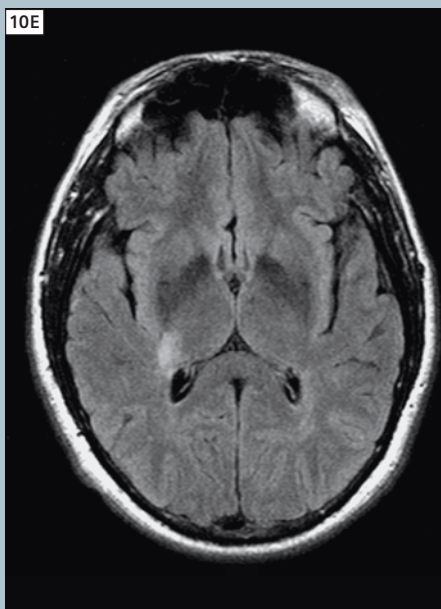
**10B** Axial post T1



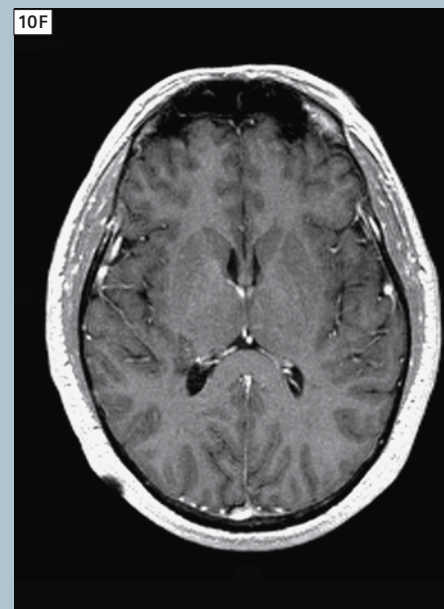
**10C** Single Voxel Spectroscopy



**10D** Axial perfusion map CBV



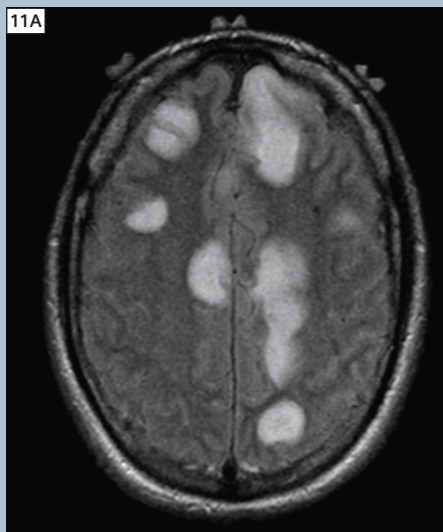
**10E** Follow-up axial FLAIR



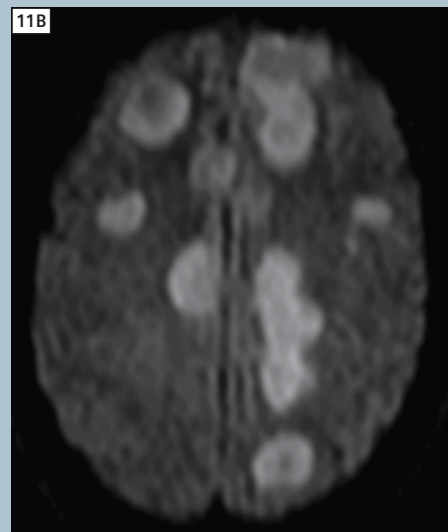
**10F** Follow-up axial post T1

## Case 4

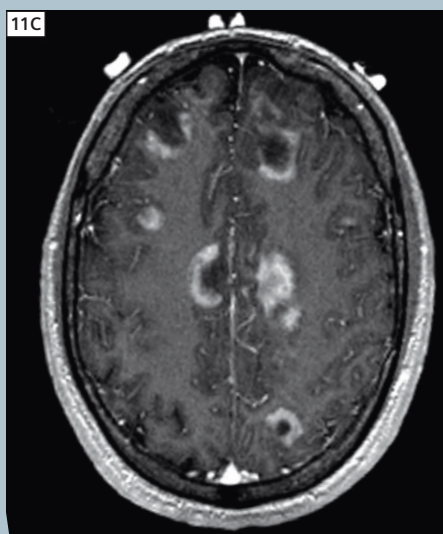
A 31-year-old HIV-positive male with history of head trauma, and drug abuse, was admitted to emergency with chief complaint of right side weakness and confusion. The initial CT exam of the brain indicated findings consistent with multiple, predominantly cortically based infarcts in the bilateral frontal and temporal lobes. No hemorrhage was seen. The following MRI showed multiple areas of abnormal T2 signal. The diffusion images showed T2 shine through effect. There was no significant mass effect from these lesions. The findings were suggestive of a diagnosis of acute disseminating encephalomyelitis or tumefactive MS. No sign of hemorrhage was observed. On the CBV images obtained from perfusion, the abnormal areas appeared dark, indicating low perfusion. In view of the immunosuppressed condition of the patient, craniotomy and biopsy was performed to exclude opportunistic infections and neoplasms. Surgical pathology confirmed the diagnosis of acute disseminating encephalomyelitis. Follow-up MRI demonstrated slight regression of the lesions.



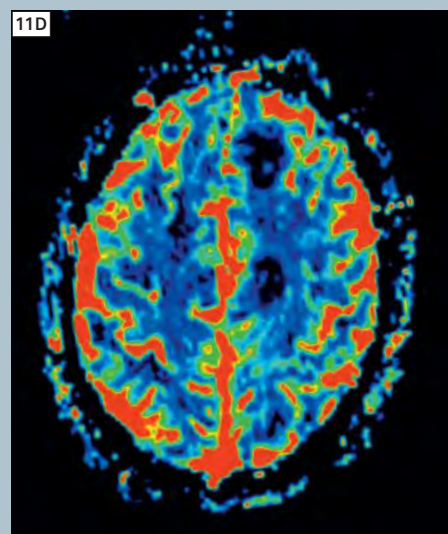
**11A** Axial FLAIR



**11B** Axial diffusion-weighted imaging (b=1000)



**11C** Axial post T1



**11D** Perfusion map CBV

## References

- 1 L. Ostergaard. "Principles of Cerebral Perfusion Imaging by Bolus Tracking" J Mag Reson Imaging 22 (2005) 710.
- 2 C.L. Partain. "Brain Perfusion Imaging Using Magnetic Resonance". Editorial J Mag Reson Imaging, 22 (2005) 691.
- 3 Soonmee Cha. "Perfusion MR Imaging of Brain Tumors" Top Magn Reson Imaging 15 (2004) 279.
- 4 Rosen BR, et al. "Susceptibility contrast imaging of cerebral blood volume: Human experience" Magn Reson Med 22 (1991) 293.
- 5 E.A.Knopp et al. Glial Neoplasms: "Dynamic Contrast-enhanced T2\*-weighted MR Imaging" Radiology 211 (1999) 791.
- 6 Cha S, Pierce S, Knopp EA, et al. Dynamic contrast-enhanced T2\*-weighted MR imaging of tumefactive demyelinating lesions. AJNR Am J Neuroradiol 2001; 22:1109 –1116.

## Contact

Nader Binesh, Ph.D.  
 Director of Clinical and Interventional  
 Neuroradiology  
 Department of Imaging  
 Cedars-Sinai Medical Center  
 8700 Beverly Boulevard  
 Los Angeles, California 90048  
 USA  
 Phone: +1 310 423 3705  
 bineshn@cshs.org

# Imaging at 3 Tesla – luxury item or standard clinical tool? First experiences with MAGNETOM Spectra

Axel McKenna-Küttner

*Radiology and Nuclear Medicine, Sportklinik Bad Nauheim, Germany*



**1** The Radiology Practice is located in the 'Sportpark' next to stables and open fields, creating a vacation-like feel to a high tech radiology facility, thereby making the patient feel relaxed and at ease.

## Introduction

### Background information on our department

The 'Gemeinschaftspraxis Radiologie und Nuklearmedizin' was founded by Dr. A. Halbsguth and B. Lochner in Frankfurt almost 30 years ago and has grown continuously since then, now serving 10 facilities in the greater Rhein-Main-Taunus area. Started as a classical outpatient practice, it acquired the first MRI scanner in Frankfurt in 1984. The group's 20 staff and partner radiologists today perform around 150,000 exams annually. The opening of the latest facility in

Bad Nauheim in January 2011 reflects a decades-long collaboration with the Sportklinik Bad Nauheim, a renowned medical center for orthopedic and trauma surgery, as well as cardiology and rehabilitation under its founder Dr. Johannes Peil. It creates a strong demand for MR imaging, since sports injuries are a major focus of its work. The Sportklinik attracts world-class athletes of many different disciplines, including Michael Schumacher and Timo Boll. Over the years, imaging was performed in Frankfurt, just 30 km away. However, with traffic situation worsen-

ing and the imaging demand ever increasing the decision was taken to move to Bad Nauheim (Fig. 1).

### Where do we stand and what do we need?

The new practice next to Sportklinik was opened with the 1.5T MAGNETOM Area in January 2011. It immediately became fully booked and the need for increased capacity was apparent within weeks. The decision to go for a second magnet was made by the never ending influx of patients.

### Pros and cons of investing in 3T

When deciding on the new magnet, a 3T system was not a first line priority. Of course 3T MR imaging is offered in many radiological services and proved its advantages, however there are some drawbacks associated with it. The higher magnetic field strength changes a number of physical effects as compared to 1.5T systems and, over the years, ultra-high field magnetic resonance tomography (3 Tesla) proved to be especially advantageous for examinations in the area of neuro-radiology or orthopedics. While the signal-to-noise ratio (SNR) increases with a higher magnetic field resulting in better image quality many other physical property are changed, such as the resonance frequency or the T1 and T2\* relaxation times. Similarly, the dielectric resonance frequencies are changed and this may have a negative effect on image quality if not used properly. Another factor was the considerably higher cost of both

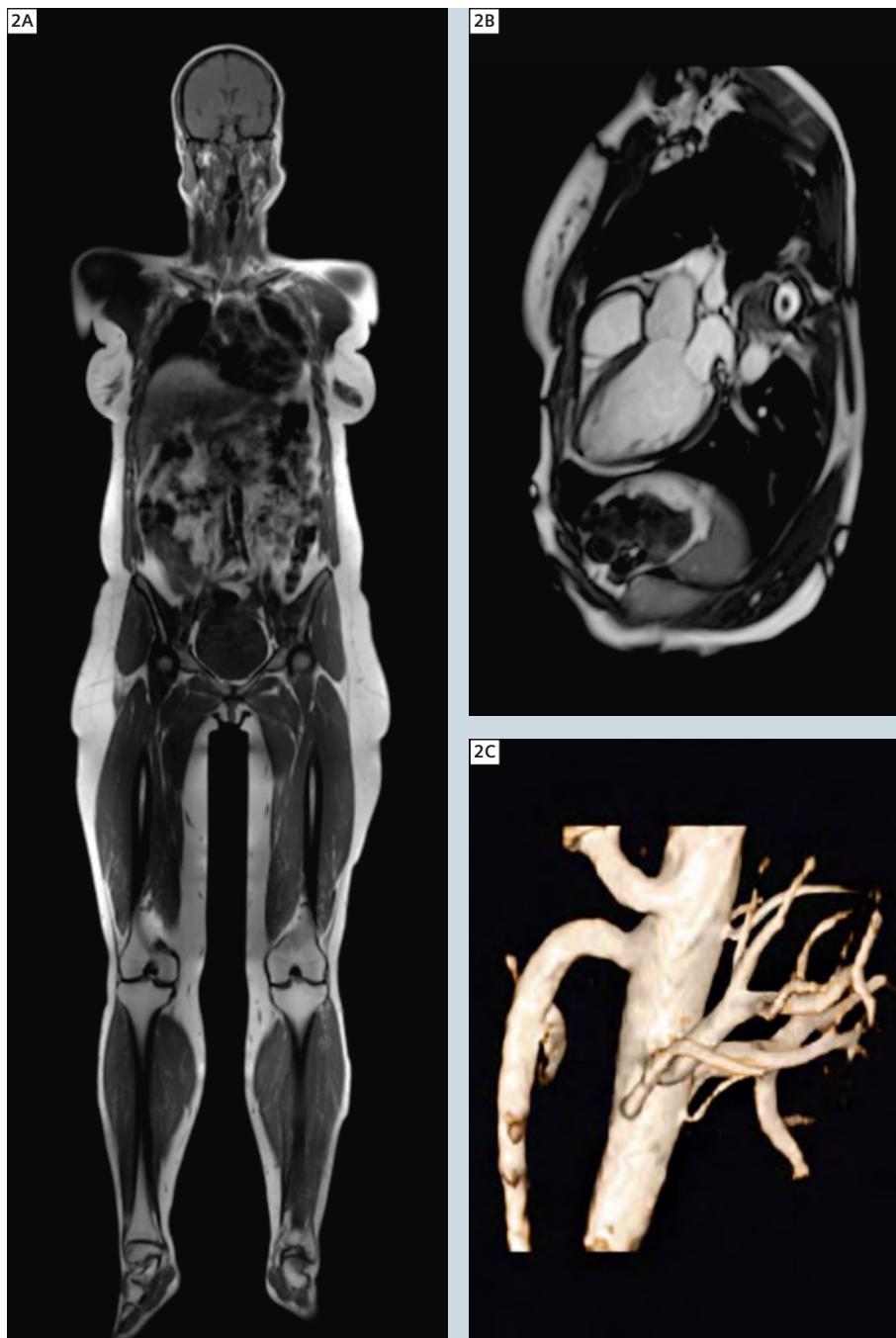
procuring and operating the system due to its higher energy and cooling requirements and higher servicing costs. We concluded that a 3T magnet could be a valuable addition for our patients if the problems described could be overcome.

Cost was a significant issue since the reimbursement for medical imaging has declined steadily over the past years. With an average of 60 € per patient reimbursed for an MRI examination with statutory health care in Germany, the investment in a 3T system seemed impossible.

### Installation of the MAGNETOM Spectra

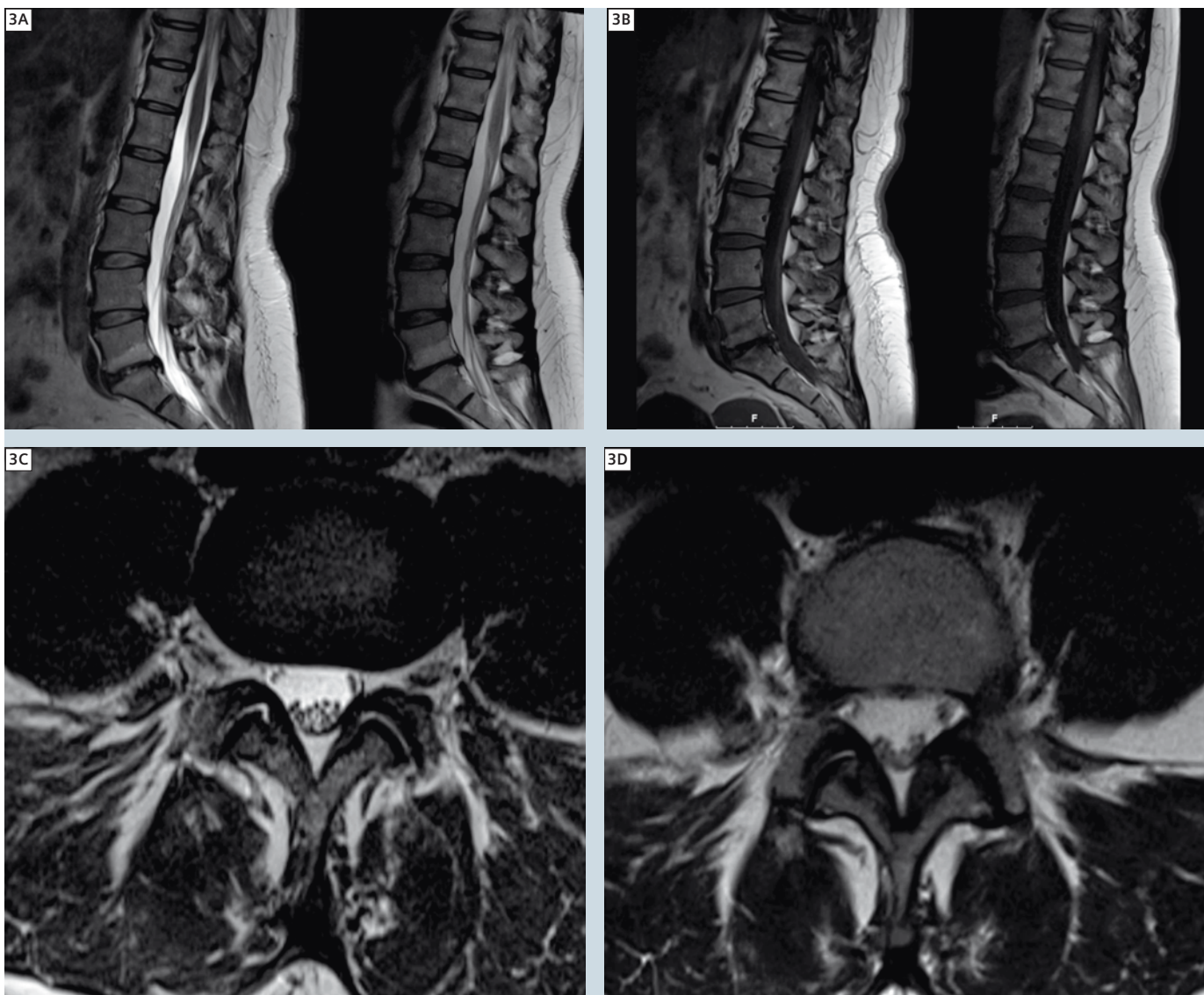
In June 2011, only 5 months after the opening of the facility in Bad Nauheim, the team around the managing partner Dr. Thomas Maier was asked by Siemens Healthcare whether it would like to become the first customer for the new 3T MAGNETOM Spectra\*. The offer almost seemed too good to be true: not only did the technical advantages of the system seem ideal for our patient base, but the cost structure was such that an investment in a 3T MRI system could be feasible (Fig. 2). Soon it became clear that given our organizational structure we could also conduct the required studies for clinical approval (CE labeling) for the system.

After preparing the existing RF-room ("3T fits in the footprint of 1.5T"), the system was delivered in the second half of November 2011 and ready on December 6<sup>th</sup>. The installation time took only a few days and went without a hitch. This was especially surprising since it was the first prototype to be installed worldwide. The easy-to-use and cross-scanner available user platform *syngo*, together with a very welcome multifaceted sequence spectrum with its software preinstalled by Siemens allowed direct system implementation without large changes to the



**2** Throughout the history of medical technology, our maxim has been further, better, higher and – unfortunately – more expensive. Due to cost, many technological developments do not reach the public, especially in the realm of statutory health care. The new MAGNETOM Spectra manages to break that law by delivering high class 3T imaging quality at an affordable price.

\*This product is still under development and not yet commercially available. Its future availability cannot be ensured.



**3** This lumbar spine comparative exam demonstrates how a high-quality 3T exam delivers a better image quality that does not necessarily translate into better patient care. The gain in image quality makes no difference to clinical decision making. (3C–D) shows that the gain in SNR can be used, however, to speed up exam time and thus make medical imaging more economical.

measurement sequences into a clinical (testing) setting. The measurements corresponded in principle to the known sequences of our 1.5T MAGNETOM Aera. In parallel to the diagnostics, only the protocols needed to be fine-tuned in the coming weeks and months according to the special requirements of our institute.

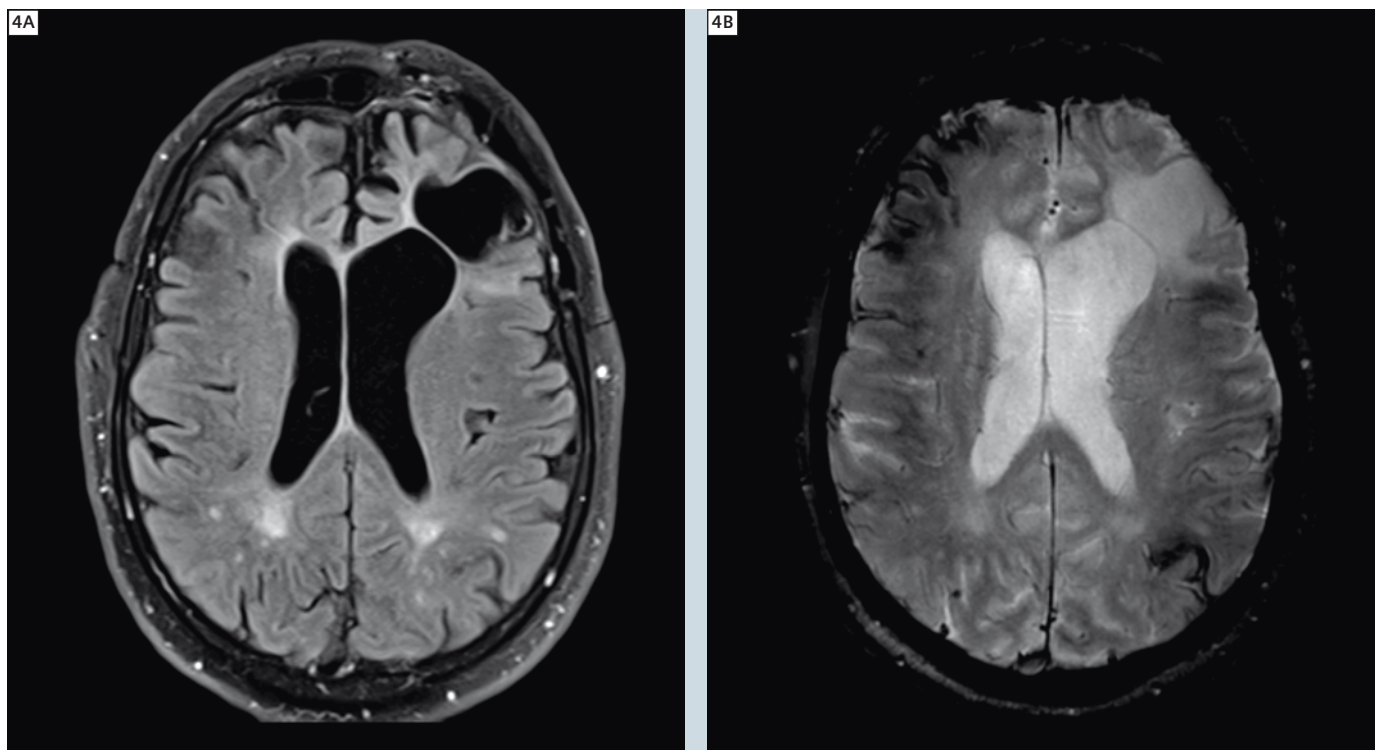
### Technical advantages of 3T MAGNETOM Spectra

MAGNETOM Spectra is a magnet with zero helium boil-off, which reduces the

life-cycle costs. Given the ever increasing helium shortage of the past years and thus the rising price, this is almost a *conditio sine qua non*.

The magnetic field strength of twice that of 1.5T systems increases the signal, essentially doubling the SNR. However, the higher magnetic field strength changes the relaxation times and makes for stronger susceptibility effects so that, depending on their influence, the real signal gain does not correspond to 100% for all measurements. The increase in

SNR can be used to shorten the acquisition time as compared to 1.5T with the same spatial resolution or vice versa, to increase spatial resolution at the same acquisition time, that is, to improve the quality of the examination, for example, through improved detail display, higher resolution, thinner slices, or a higher matrix. During routine examinations we usually use both effects, i.e. sequence protocols with higher resolution and tolerable acquisition times when highest image quality is needed. Another strat-



**4** This shows the superior image quality in this dark fluid inversion recovery sequence. The liquORIZED zone of the left frontal lobe after a serious road traffic accident is extremely clear. In the hemosusceptibility sequence the residual ferritin deposits are well assessed.

egy is to reduce the acquisition time when imaging speed is required and highest resolution is not a focus of the exam, resulting in higher diagnostic safety, higher patient comfort, and consequently higher system acceptance in combination with acceptable costs under the given conditions of statutory healthcare (Fig. 3).

The optimally linked magnet design, the RF pulses, the gradients and the examination sequences resulted in the application of 3T technology and thus MAGNETOM Spectra in clinical routine diagnostics where it is readily tolerated by patients. SAR warnings did not appear at all in our examinations. Another considerable advantage in routine examination is the Tim 4G (Total imaging matrix) technology which we already use on our other 1.5T systems. The multi-coil concept and parallel imaging in combination with technical improvements, such as 'scan@center', 'AutoCoilSelect', 'Inline composing' or even 'syngo Tim CT', provide for consid-

erably easier examination planning with almost no changes in patient positioning and coils. In addition, any combination of multi-station exam up to whole-body examination is possible. Furthermore, the workflow was largely improved by facilitating planning of larger examination volumes or so-called multi-station examinations in different table positions as well as by providing easy to operate 'Set-and-Go' protocols.

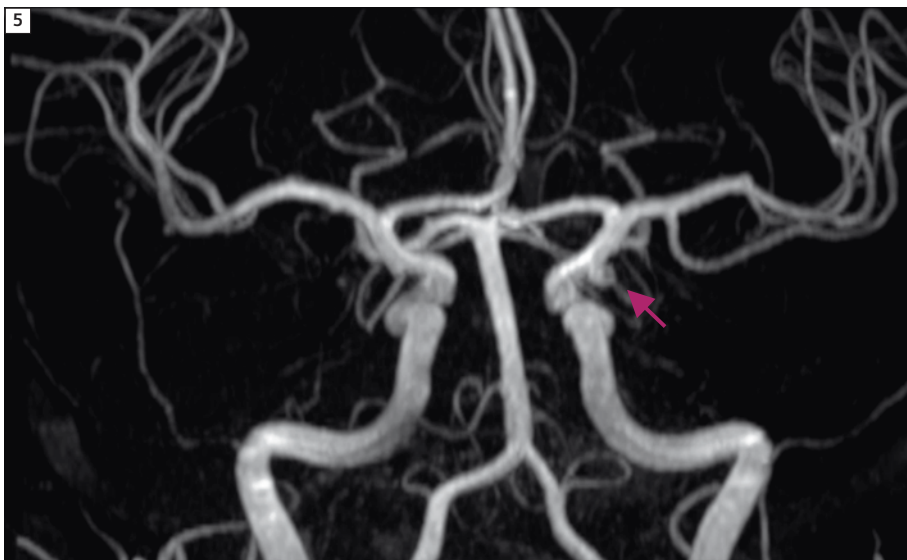
#### **Tim and syngo workflow**

Technologists performing examinations at the MAGNETOM Spectra find the workflow largely simplified and improved. Tim technology allows easy planning, especially for whole-body examinations, angiography or examinations of the entire spine. For these multi-station examinations, the localizers of the different stations are already combined via Inline composing. This means that the technologists can use the composed localizers and plan as well as perform the remaining course of the exami-

nation, making patient repositioning or coil changes unnecessary. To ensure the best possible magnetic field homogeneity, the existing 'scan@center' technology guarantees that the measurement volume to be examined is always positioned in the magnet's isocenter. At the same time, the necessary coils are detected and selected with 'AutoCoilSelect' which avoids any kind of error. To make things even better, the new dedicated hand coil can be even used out of isocenter, making uncomfortable patient positioning unnecessary. The workflow is further improved by the ease of use of the "Set-and-Go" protocols, also leading to shorter examination times.

#### **The Dot engine concept**

Our practice employs over 60 radiographers and technicians to work in various facilities in rotation. While this concept assures that every radiographer sees all various different examination techniques and stays on top, this concept may be challenging when introducing



**5** One of the biggest advantages of 3T in clinical routine is the time-of-flight angiography since no contrast medium is needed and even the smallest aneurysms can be detected with ease using either MIP imaging or a conventional 2D imaging plane.

new scanners, especially when 3T imaging was not part of the daily routine. This is where the Dot concept assures a constant high quality. In this examination strategy the workflow is preset and the radiographers only have to tell the system which examination is required, e.g. left knee. The software then automatically performs all necessary tasks on its own. Even the localizers and the scan range are automatically detected. All scanning sequences are pre-programmed, so that not even the examination sequence for each individual exam has to be selected. Also no adaptation to a chosen sequence is necessary. This means that radiographers with little or almost no MRI experience can perform exams of high quality standard without mistakes.

## Neuro imaging

All neuro applications used with 1.5T systems can be implemented using the 3T MAGNETOM Spectra leading to significant quality improvements because the improved SNR which can be usefully applied in a variety of ways (Fig. 4). The extension of the longitudinal relaxation rate of static tissue as compared to blood is advantageous for MR angiog-

raphy at 3T. Due to saturation effects, greater suppression of the static tissue is obtained, thus Time-of-flight (TOF) angiographies can be performed with much higher resolutions, using the same or reduced examination times. As a result, intracranial arteries can be evaluated far into the periphery. A dramatic effect can be seen in the detection or exclusion of small intracranial aneurysms. The detailed image quality allows for 3D interpretation of images. Sometimes small aberrant vessels suggest the presence of a possible aneurysm which can be better visualized at 3T than at 1.5T. For patients this is of utmost clinical importance since a suspected aneurysm in an MRI exam has to be excluded via conventional intracerebral angiography, an exam that carries a non-negligible procedural risk (Figs. 5, 6).

Furthermore, the *syngo* SWI sequences (susceptibility-weighted imaging) implemented with, e.g., blood diagnostics are more sensitive with MAGNETOM Spectra than with 1.5T systems due to higher susceptibility sensitivities that help detect the smallest blood deposits or calcifications.

The quality of the *syngo* SPACE sequence was also greatly improved for our profile

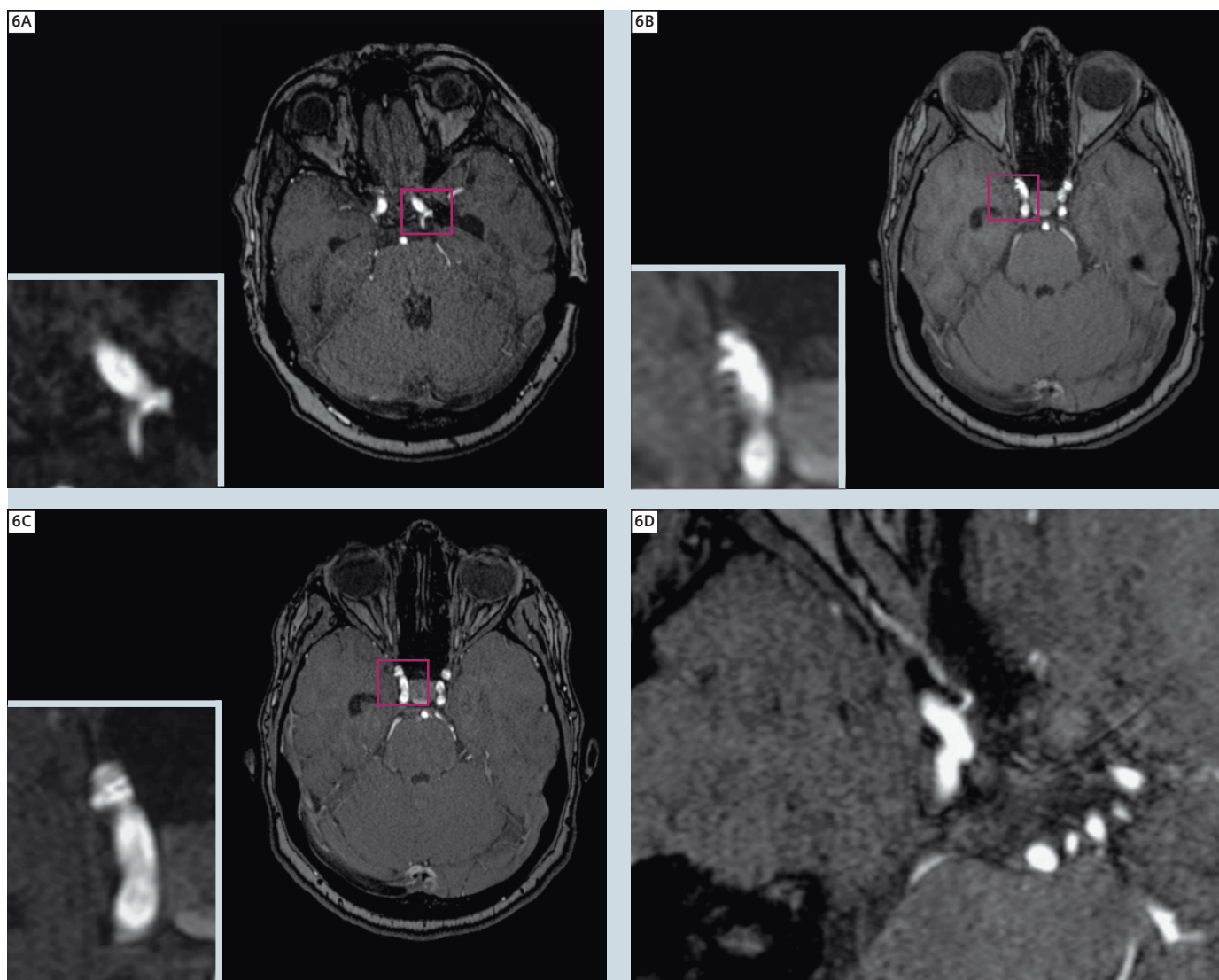
by using 3T technology in clinically feasible examination times. Examinations with isotropic voxels, even in the sub-millimeter range, are possible, resulting in largely improved reconstructions in all planes. This facilitates a more rapid and more confident assessment of small intracerebral lesions such as MS plaques. While for the primary diagnosis the presence of the typical lesions is enough to establish the differential diagnosis of a possible neurodegenerative disorder, the follow-up is often a chore. All lesions have to be compared to the previous exam, so that the application of 3D sequences helps to assure that all the lesions are compared to the corresponding ones in the previous exam.

Tim Planning Suite allows, for example, the examination of the entire spine in a simple workflow. The individually acquired images in the different stages are automatically combined via Inline composing.

Another advantage of the higher spectral resolution of 3T imaging vs. 1.5T imaging is the application of sequences such as the Dixon fat saturation technique. Not only is the Dixon sequence less susceptible for artifacts when compared to STIR or TIRM sequences, but it also allows for reduced examination times. In spine imaging usually a T2 and T1-weighted sequence in sagittal orientation is used as base sequence. To rule out fresh fractures, spondylodiscites or activated osteochondrosis, an additional inversion recovery such as STIR or TIRM is used to visualize bone edema. Due to imaging properties of the Dixon sequence a single acquisition allows the read out of a fat image and a water image. These images correspond very well to a conventional STIR sequence (water image) as well as to the T1 sequence (fat image), thus a single acquisition sequence can replace two individual imaging sequences and thus save time (Fig. 7).

## Orthopedic imaging

Compared to examinations with systems of lower field strengths, the improved quality of examinations with a 3T system is undisputed. In contrast to 1.5T sys-



**6** Figures **6A** and **6B** display a suspected aneurysm at 1.5T. Figures **6C** and **6D** show the same patient at 3T. One can clearly see that the suspected aneurysm is an aberrant vessel, giving the impression of a pseudo aneurysm. The 3D double oblique angulated MPR image (**6D**) displays the vessel nicely.

tems, spatial resolution can be increased at comparable examination times, allowing for examinations with unseen resolution at 1.5T whereas images with an examination quality comparable to a 1.5T system are generated at considerably shorter acquisition times. A routine knee examination can be performed in 8 minutes. We usually combine the increase in resolution and the time savings according to the purpose of the examination or the patient. Special coils, such as the 18-channel knee coil (Fig. 8) or the 16-channel hand/wrist coil (Fig. 9) enable the use of parallel imaging with

higher PAT factors. Again, these result in shorter measurement times and higher resolution (Fig. 10).

In the Bad Nauheim facility high-quality orthopedic imaging is of particularly vital importance since about 60% are MSK exams.

The advantage of high-quality cartilage imaging is evident. Many of our patients suffer from sports-induced injuries and require surgical treatment and follow-up exams. The exquisite detail of cartilage injury allows for dedicated treatment decisions that simply cannot be achieved using 1.5T imaging.

Also the use of the dedicated whole-hand/wrist coil allows for unprecedented image quality. The new coil allows for a comfortable hand positioning next to the body, making the 'superman' position in isocenter unnecessary. Motion artifacts related to an uncomfortable position during a lengthy exam are readily less frequent.



**7** Using the 3T advantage to better differentiate between the spectral resonance frequencies of fat and water, the Dixon sequence not only delivers superior image quality (left images 3T, right images same patient at 1.5T), but also help to save acquisition time. While at 1.5T both a T1-weighted and a STIR sequence were necessary, at 3T a single Dixon T2-weighted sequence is sufficient to produce a dual read out of the fat image and the water image and to obtain the same medical information.

## Cardiac imaging

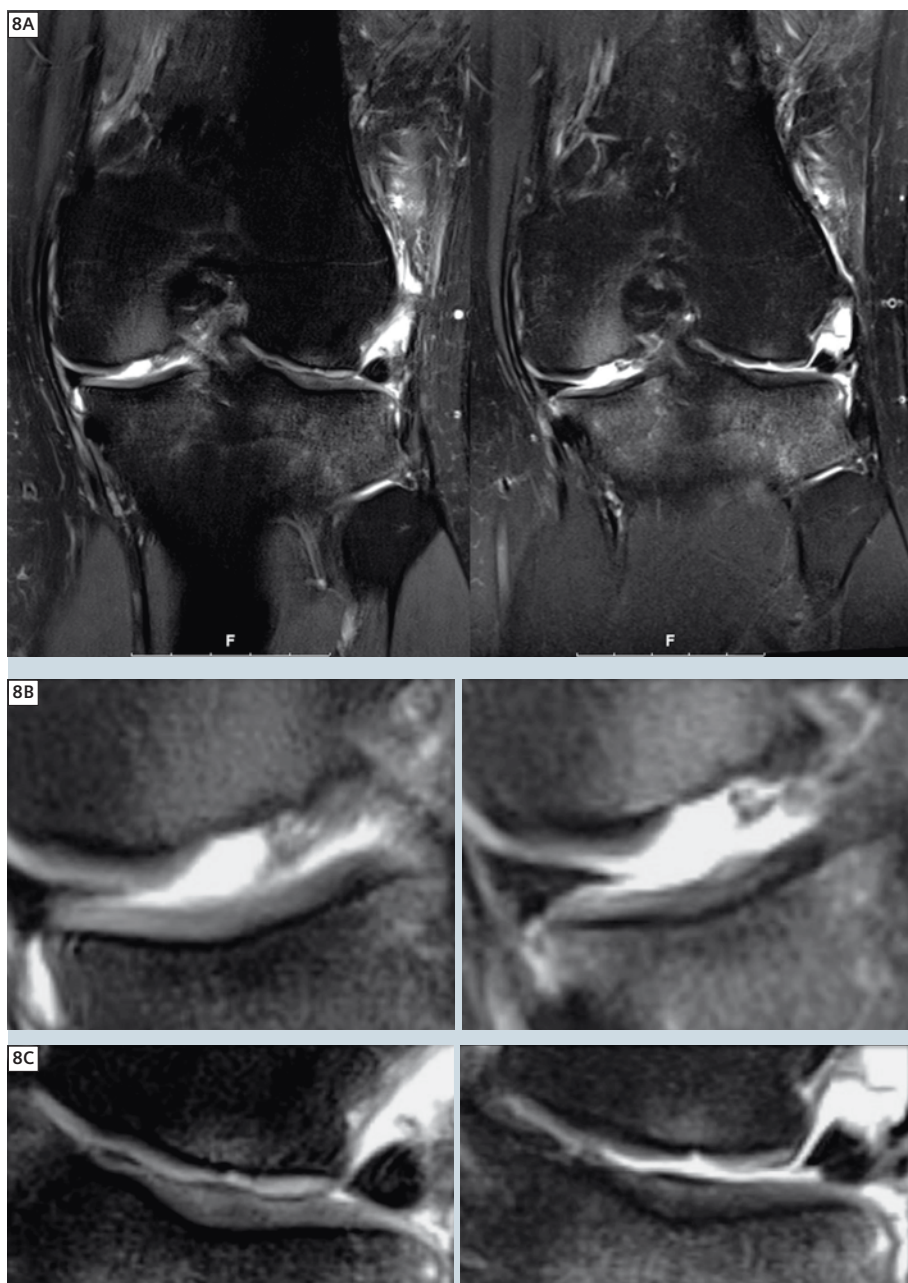
In the last decade MR imaging of the heart has been introduced to clinical routine. However, the widespread use of this formidable examination technique outside dedicated cardiac centers was hampered by the inadequate reimbursement of the statutory health system as well as the fact that only highly-trained and skilled technologists were able to perform a cardiac exam with sufficient image quality. In our institution there are only 5 technologists out of 60 that are experienced enough to carry out an exam without the radiologist's constant presence. While a general examination strategy can be preset, finding the correct standard cardiac angulations such as the short axis or the 2, 3, and 4-chamber view can be challenging for non-experts. Also due to physical conditions, the sequences have to be in part adjusted to avoid 3T-specific artifacts. These include susceptibility effects that increase at 3T, or off-resonance artifacts that reduce image quality as low-signal bands or ghosting artifacts. For frequency adjustments, an additional 'frequency scout' has to be measured to determine the frequency where banding artifacts are not present. In the subsequent function measurement, the frequency determined is changed automatically, reducing the artifacts. The cardiac Dot engine is able to fully automatically find all cardiac axes and carry out the exam with minimal user interaction including the suppression of 3T specific artifacts. A complete cardiac study including late enhancement is now possible under 30 minutes even for a non-experienced technologist. Another advantage is the integrated, fully automated Inline left ventricular function assessment. In the past, the dataset had to be transferred to specific post processing consoles and semi-automatically evaluated by either a technologist or a radiologist. Although this process took only 10 or 15 minutes per case, this was too long considering that a new patient is usually scheduled every 20–30 minutes. With the new Dot engine the evaluation of the left ventric-

ular function occurs instantaneously at the end of the data acquisition without any user interaction at all on the image acquisition console and is automatically transferred to the PACS, so that image reading can be done like any other exam. The Dot engine allows for the first time cardiac examination with reliable image quality under the condition of statutory healthcare in a general outpatient practice (Fig. 11).

## Abdominal imaging

Whilst there is no dispute that 3T imaging delivers superior image quality in MSK and neuro imaging the advantages of abdominal imaging are less apparent. As in cardio-vascular diagnostics, abdominal imaging is negatively affected by the physiological respiratory motion and pulsation artifacts of abdominal vessels. Added to these are motion artifacts caused by gut mobility and increased susceptibility effects resulting from air in intestinal loops. To date, implementation of 3T systems for routine abdominal imaging has been limited due to B<sub>1</sub> inhomogeneities caused by dielectric effects. Additionally, the specific absorption rate (SAR) limits were reached early on, especially in the first days of 3T imaging – often examinations had to be performed by increasing slice thickness or reducing the number of slices, thus losing spatial resolution. These limited the implementation of routine diagnostics. MAGNETOM Spectra has a 60 cm bore and concern was raised whether patients with normal western European body habitus or overweight patients could be examined. We were also unclear at this time-point whether a 'budget' magnet would deliver all physical properties needed to acquire high quality exams.

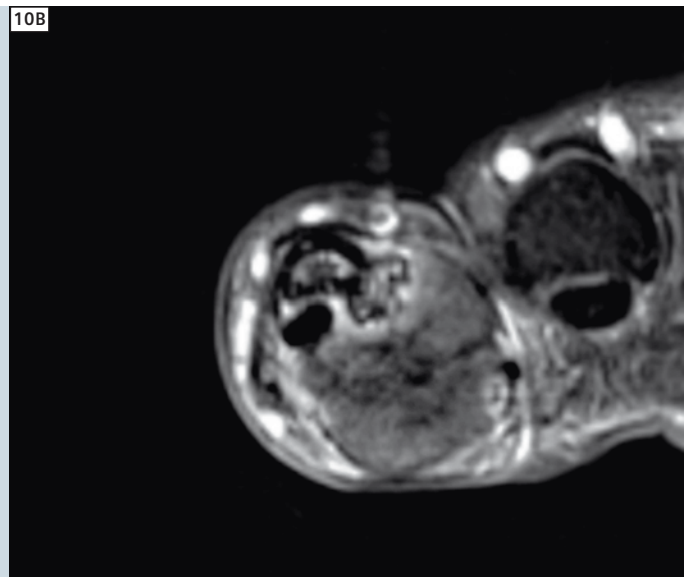
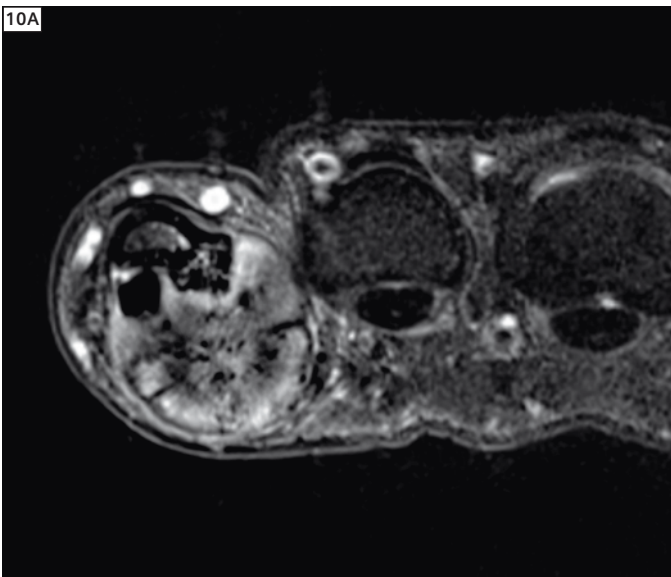
Exceeding our expectations, the optimally linked magnet design, the RF pulses, the gradients, and the examination sequences resulted in more than acceptable image quality. Even at the off-center regions of the magnetic field, a fully diagnostic image quality even in heavier patients could be acquired. Fat-suppressed sequences often stricken by



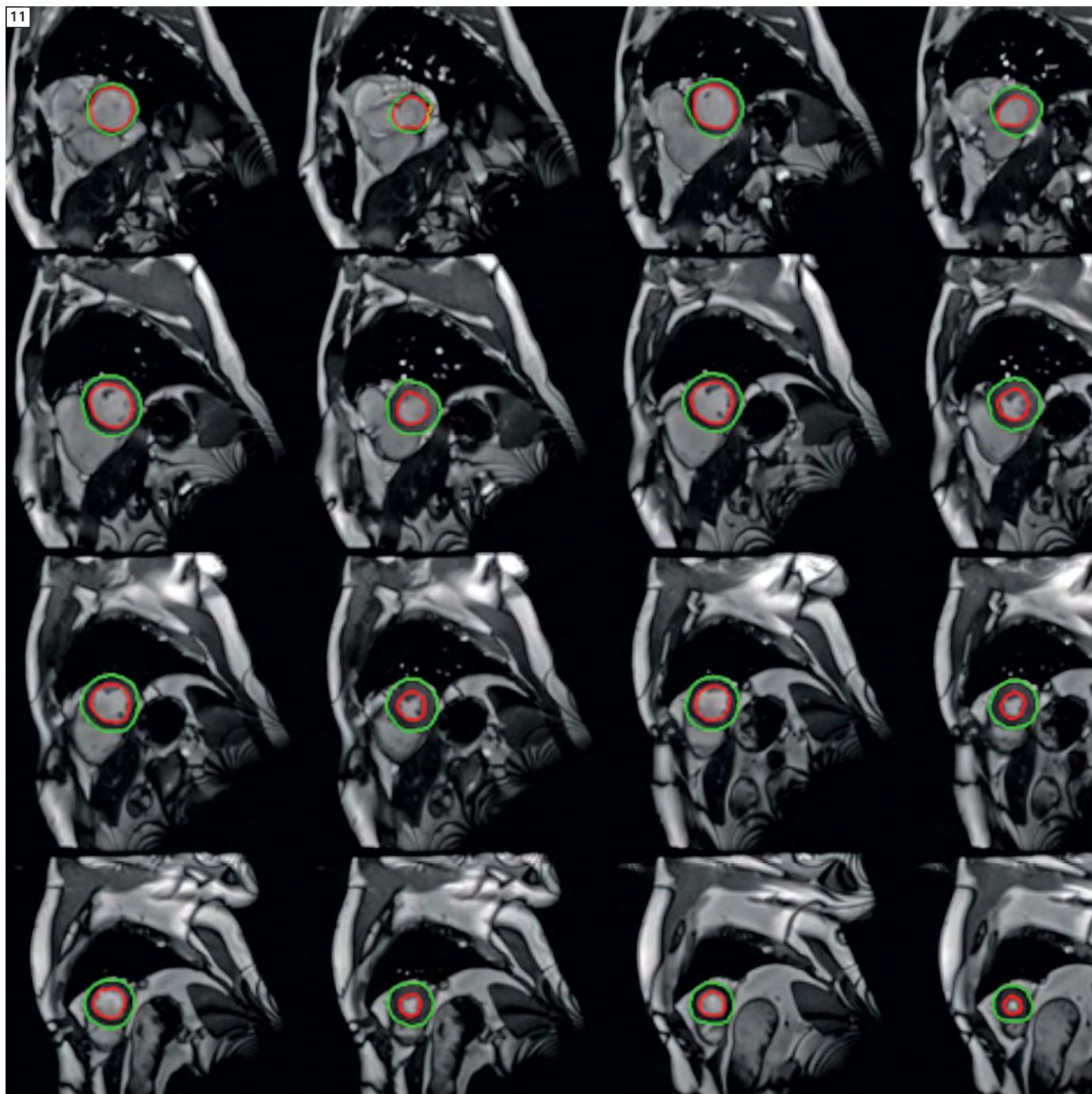
**8** Advantages of cartilage knee imaging at 3T: 3T imaging (left side) compared to 1.5T imaging (right side). While the 4<sup>th</sup> grade cartilage injury of the medial condyle is apparent in both sequences, the cartilage damage of the lateral condyle is much more subtle. 3T images the damage much more realistically and enables a better assessment. The PD fat sat sequence at 1.5T exaggerates the damage and indicates a 4<sup>th</sup> grade damage, while in reality there is only a 3<sup>rd</sup> grade injury.



**9** The new 16-channel whole-hand coil delivers extraordinary image quality that clearly surpasses that of 1.5T.



**10** The SNR gain is dramatically seen in small volume imaging such as finger imaging. The comparative study of this cartilaginous exostosis demonstrates the higher detail resolution and the superior diagnostic information.



**11** Cardiac imaging: One of the most impressive features of the MAGNETOM Spectra Cardiac Dot engine is the fully automated user-independent Inline left ventricular analysis. The software instantaneously delivers all functional parameters without a single mouse click directly after the last acquisition of the cine sequences. This technology enables a complete functional assessment of the heart with all qualitative and quantitative parameters within a timescale of just 14 minutes!

artifacts resulting from field inhomogeneity were of full diagnostic image quality. Small structures, vital for a full assessment of the abdomen such as the pancreatic duct, could be visualized with

such detail that even smaller side ducts were assessable. Of all body regions the abdomen was certainly the one where our initial expectations based on the known challenges were exceeded by far.

In our experience 3T abdominal imaging is absolutely possible in a clinical routine workflow with the implemented technologies in the MAGNETOM Spectra (Fig. 12).



MAGNETOM Spectra (left) is the newest addition to the Siemens 3T imaging portfolio. The system is the key to a new level of usability and diagnostic confidence. And it provides access to a new realm of opportunities - regarding patient care and business.

The ACUSON S1000 ultrasound system is a new member of the ACUSON S Family of premium solutions. This entry-level system encompasses state-of-the-art ultrasound technology, stellar imaging performance, and versatile applications at an exceptional cost of ownership.

## Accessible Innovations

Across the globe, economic pressure on healthcare systems and its providers is eminent. Industrialized countries are challenged with an aging population and growing demand for healthcare services. Emerging markets and their growing healthcare systems are increasingly in demand of access to premium patient care and imaging capabilities. As a result, reimbursement policies across the globe are being adapted towards increasing accountability for quality and cost across the entire care continuum. Providers must demonstrate lower hospital re-admissions, high-quality outcomes, and low operational costs to stay competitive. With *Accessible Innovations* Siemens offers sensible solutions to meet these demands in the field of medical imaging.

Emerging countries are dedicated to building accessible healthcare systems that ensure high quality patient care. At the same time, developed countries are driving towards making healthcare more efficient, more applicable and more personalized for all parties involved. All across the globe, the amount of people in need for health services is rising and the financial range has limits.

It is no surprise that Total Cost of Ownership (TCO) is an important factor influencing the international

healthcare environment. Determining the economic value of an investment is important for all healthcare providers – regardless of their circumstances. Assessing total cost of acquisition, operating costs and investment protection highly contributes to profitability over time. Profitability may by no means be confused with our responsibility to provide high level imaging standards that benefit the patient in the end. Within this context and to serve common goals among the global healthcare landscape, Siemens is introducing a new range of imaging systems. With *Accessible Innovations* we are equally improving the availability, quality and efficiency

of healthcare by combining state-of-the-art diagnostic capabilities with a highly sensible TCO argumentation for our customers. Quantifying the financial impact of deploying a healthcare product over its lifecycle goes hand in hand with making healthcare more accessible for more people all over the world. SOMATOM Perspective, ACUSON S1000 and MAGNETOM Spectra are the first products that prove we are taking our responsibility seriously – the responsibility to innovate and invest in cost-efficient, premium imaging standards.

[www.siemens.com/the-key-to-3T](http://www.siemens.com/the-key-to-3T)  
[www.siemens.com/somatom-perspective](http://www.siemens.com/somatom-perspective)  
[www.siemens.com/S1000](http://www.siemens.com/S1000)



SOMATOM Perspective is the first high-end CT scanner to facilitate CT business without compromising clinical results. The business class scanner can help manage financial performance while focusing on patient needs and easing your daily routine.



**12** Although 3T is not considered to be the best imaging modality for the abdomen, MAGNETOM Spectra delivers undisputable image quality. The example here is of a patient with multiple enlarged side ducts of the pancreas, a typical condition of suspected IPMN. The cross-sectional image using a fat saturation technique proves that larger patients can also be imaged and that the MAGNETOM Spectra magnet delivers a very homogenous  $B_0$  and  $B_1$  field for uncompromised abdominal image quality.

## Summary

After only a short experience with the 3T MAGNETOM Spectra, we can already recommend the system for routine performance for all organs. This especially applies to the user interface and system operation which is largely the same as that for 1.5 Tesla systems and indeed considerably easier when using Dot engines. The sequence spectrum already included in the delivered software allows MAGNETOM Spectra to be immediately put into clinical operation. The benefit of the higher signal-to-noise ratio available by doubling the field strength also allows for a considerably improved image quality even when comparing it to high-end 1.5 T systems. This applies in particular to neurological examinations as well as joint diagnostics. The higher signal can be used to increase spatial resolution or to accelerate the examination as such (a combination of both under ideal circumstances).

In conclusion, MAGNETOM Spectra is an MR system that has the potential of a workhorse in the private radiology practice especially under the harsh economic conditions of statutory healthcare. As a result, 3T technology is no longer reserved just for scientific or university based centers. For us the upcoming challenge will be to explain to patients and referring physicians why not every medical question needs to be answered by a 3T MRI.

### Contact

Axel McKenna-Küttner, M.D.  
Gemeinschaftspraxis Radiologie  
und Nuklearmedizin  
In der Aue 30-32  
61231 Bad Nauheim  
Germany  
Phone: +49 (0) 60 32-14 54  
Fax: +49 (0) 60 32-92 73 78  
kuettner@radiologen-frankfurt.de

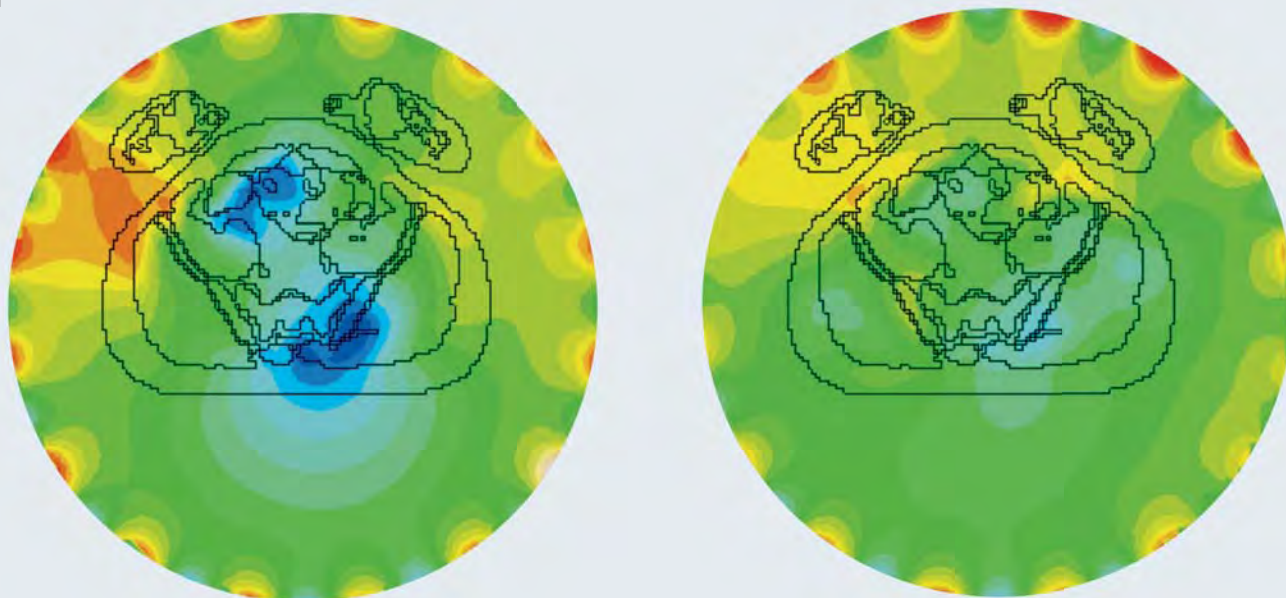
# TimTX TrueShape and syngo ZOOMit Technical and Practical Aspects

Mathias Blasche, MSc<sup>1</sup>; Philipp Riffel, M.D.<sup>2</sup>; Matthias Lichy, M.D.<sup>1</sup>

<sup>1</sup>Siemens AG, Healthcare Sector, Erlangen, Germany

<sup>2</sup>Institute of Clinical Radiology and Nuclear Medicine, University Medical Center Mannheim, University of Heidelberg, Germany

1



**1** B<sub>1</sub> homogeneity with circular polarization (left) and with TimTX TrueForm (right) for a typical anatomical region (pelvis) where B<sub>1</sub> inhomogeneity can occur at 3T. Note the blue-colored areas with the conventional CP excitation. The dielectric shading effects are practically eliminated on the right side, while the example shown on the left would have been of non-diagnostic quality at least for these specific anatomical regions because of potential contrast variations.

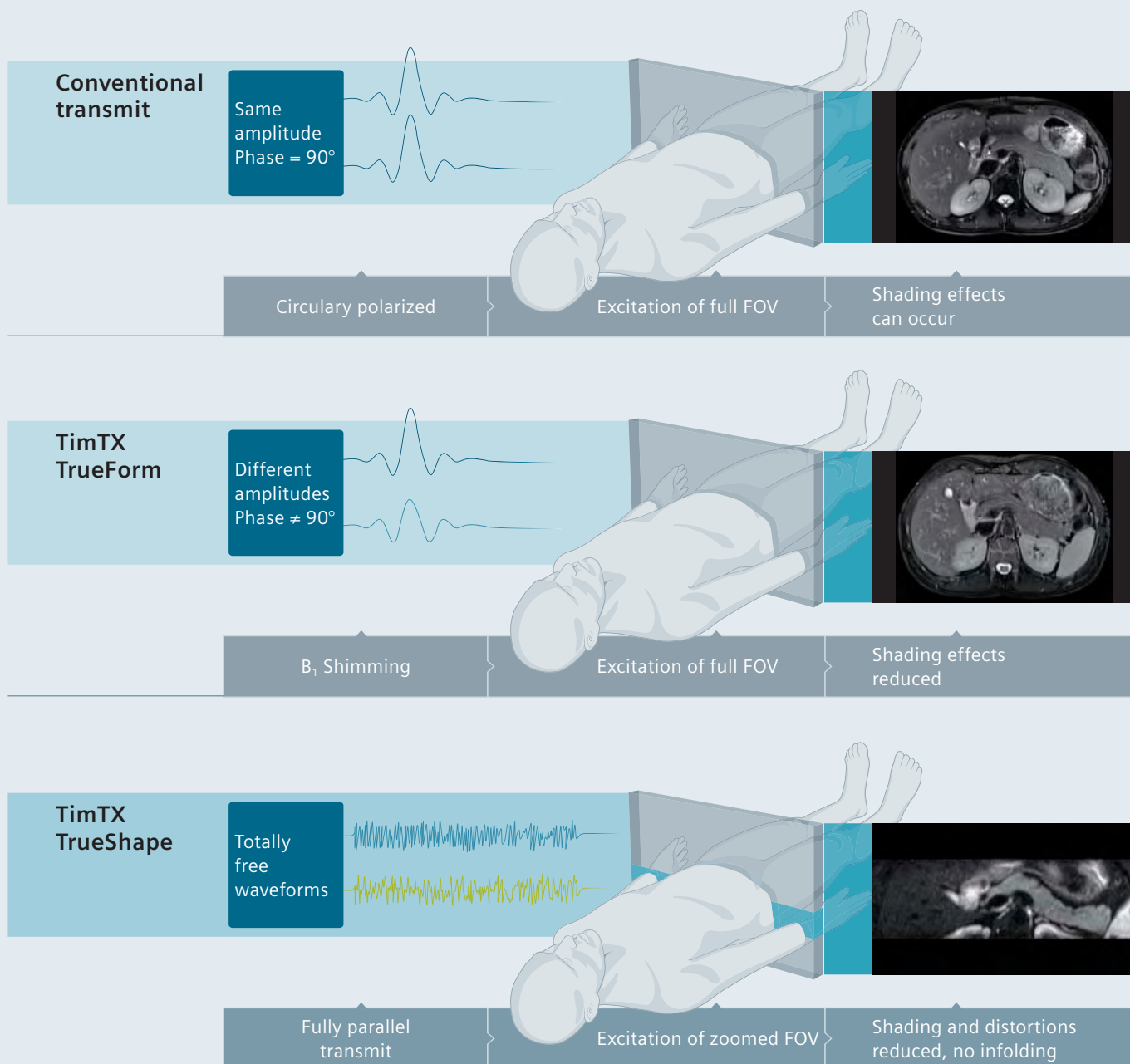
At the RSNA 2011, Siemens was the first to introduce sequence techniques for clinical MR systems that take full advantage of parallel transmission: zooming without aliasing. This application, called *syngo ZOOMit\**, is enabled by the technology platform TimTX TrueShape. TimTX TrueShape is the first platform in the MR industry to make full use of the dynamic capabilities of a transmit array system. And *syngo ZOOMit* is the first fully dynamic application based on TimTX TrueShape.

The purpose of this article is to provide some background information about the new dynamic parallel transmission techniques (pTX), compare them to the existing static B<sub>1</sub> shimming, and point out potential applications based on dynamic pTX.

## Background – from parallel receive to parallel transmit

The implementation of multi-channel radio frequency (RF) receive systems and receive array coils in the early 1990s

marked a revolution in MR imaging. This technology offered the very attractive combination of high signal-to-noise ratio (SNR) from small coil elements with the large coverage of large coils. Starting with 2 and 4 RF channels in the 90s, systems with up to 8 RF channels were available around the year 2000. Multi-channel RF received a further boost with the advent of parallel acquisition techniques (PAT) at this time. A variety of parallel acquisition techniques were developed, such as SMASH [1], SENSE [2],



**2 (Top)** Conventional transmit (circular polarization) with severe shading effect due to  $B_1$  inhomogeneities; **(Middle)**  $B_1$  Shimming with TimTX TrueForm (different amplitude/phase settings on the two channels of the RF body coil), eliminating the  $B_1$  shading and resulting in homogeneous image contrast; **(Bottom)** Fully dynamic pTX with TimTX TrueShape (arbitrary waveforms of the two RF channels as well as the gradients), resulting in a zoomed image with higher image quality and shorter scan time.

\*This product is still under development and not yet commercially available. Its future availability cannot be ensured.

and GRAPPA [3]. PAT on the receive side offers shorter scan times, higher temporal and/or spatial resolution as well as reduced blurring and distortion artifacts in single-shot imaging. PAT is an integral part of many exams today. Applications like contrast-enhanced 3D liver dynamics, MR angiography or diffusion-weighted imaging (DWI), to name just a few, would not be possible in a clinical setting without PAT. In addition, with the availability of flexible scalable coil technology, PAT can be applied in any body region, ranging from a dedicated brain scan to a whole-body examination.

Tim (Total imaging matrix) was the first RF system that was specifically designed for maximizing the benefits from PAT. Introduced in 2003, the MAGNETOM Avanto, the first MR system which enabled high-quality whole-body scanning in a clinical setting, offered up to 32 RF channels. Today, up to 128 RF channels are available as a product.

In parallel to the development of these new receive technologies (multi-channel coils, Tim, PAT), further efforts were undertaken over the last decade to increase the field strength beyond 1.5 Tesla, in order to gain even higher SNR – which could be invested in, for example, higher spatial resolution or even faster imaging with PAT. But 3 Tesla field strength, besides the obvious advantage of higher SNR, also showed the disadvantage of a lower  $B_1$  homogeneity in some body regions. This is where the so-called  $B_1$  shimming, based on multi-channel transmit technology, came in, as a remedy to  $B_1$  inhomogeneities.

### From circular polarization to $B_1$ shimming

Ideally, circular polarization is the best way to perform conventional slice-selective imaging. The benefit of circular polarization (CP) over linear polarization (LP) manifests itself in a more homoge-

neous  $B_1$  distribution over the object, a lower specific absorption rate (SAR), and higher SNR in the receive path. Technically, the circular polarization is achieved by feeding two ports of the transmit coil with identical amplitudes and a phase shift of 90 degrees (Fig. 2, top).

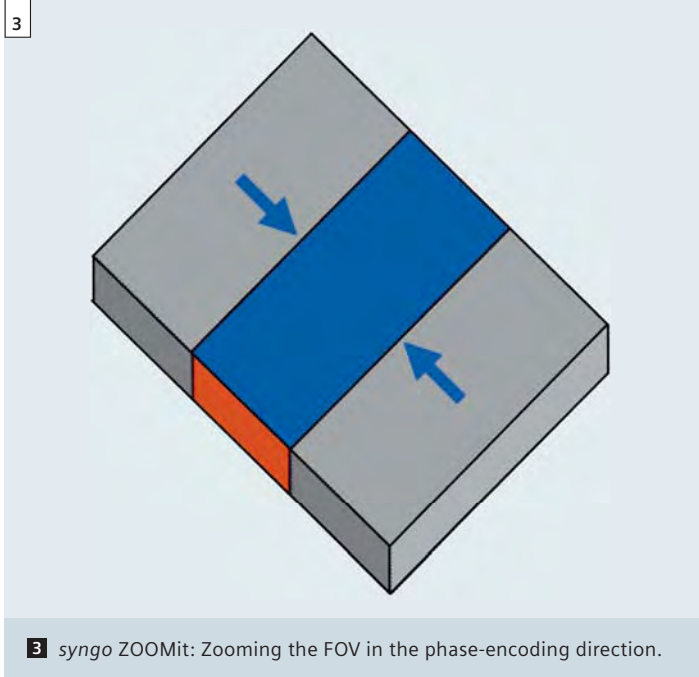
It turns out that at high field strengths, such as 3T, the 'ideal' circular polarization is not necessarily the optimum anymore. The reason is that at such high frequencies, the wavelength of the MR signal approaches the dimensions of the object. At 3T, the wavelength is approximately 26 cm. It is therefore smaller than, for example, the dimensions of the abdomen. This can result in interferences of the  $B_1$  field and signal shading. The critical point here is that not only the signal intensity is altered (which can be corrected for with post-processing), but, most critically, also the contrast behavior can be altered.

A remedy to this RF shading effect is  $B_1$  Shimming. The two ports of the transmit coil are fed with different amplitudes and a phase shift  $\neq 90$  degrees (see Fig. 2, middle). With a 2-channel transmit system, this results in an 'elliptical' excitation. This can potentially, including the interaction with tissue characteristics, result in a more homogeneous  $B_1$  distribution than the conventional circular polarization (Fig. 1). At 3T, mainly abdominal and pelvic imaging is critical, the head is still smaller than the MR wave-

length. At ultra-high field strength such as 7T,  $B_1$  shading is also very severe in the head region as a consequence of even shorter wavelengths.

From a clinical perspective, dielectric shading can negate the advantage of a 3T system and there was intense debate in the first years of 3T MRI as to whether such a scanner would ever be fully operational as a clinical whole-body system. If a robust and homogeneous image quality could not be assured in the abdomen, what would be the clinical use of such a scanner? A solution was therefore urgently needed to take advantage of the higher field strength, without negating the MR scanner's daily clinical usability. In the first days, clinicians tried to manipulate the  $B_1$  distribution by applying heavy dielectric cushions on the patients – with limited success and practicability. So,  $B_1$  shimming became a key to the further success of 3T MRI.

In 2007, Siemens pioneered  $B_1$  shimming with the **TimTX TrueForm** technology (TrueForm RF design). This technology was first implemented in the MAGNETOM Verio, which also happened to be the first open-bore system available at 3 Tesla (Tim coil technology had already been introduced at this time point also for 3T). TimTX TrueForm offers 2-channel transmit array functionality for  $B_1$



**3** syngo ZOOMit: Zooming the FOV in the phase-encoding direction.

shimming. It works with anatomy-specific settings, optimized for improved  $B_1$  homogeneity [4]. This approach has the advantage that no time is required, for example, for patient-specific  $B_1$  mapping and adjustments (which can easily require 1 minute for each body region to be examined). And, more importantly, the workflow of an MRI exam compared to a 1.5T scanner is completely unchanged. Routine one-station exams (also with small table movements due to automatic table positioning to isocenter), multi-region exams, breath-hold versus gated sequences, especially TimCT (scanning during continuous table move) – all this is not affected. TimTX TrueForm is virtually invisible for the user – apart from the improvement in image quality.

As important as  $B_1$  Shimming is at 3T and above – this type of  $B_1$  Shimming is still a conventional approach with ‘static’ excitation pulses, i.e. the combination of a sinc ( $\sin(x)/x$ ) RF pulse with a static slice-select gradient to excite a slice, which works irrespective of how one determines the required settings (anatomy-specific or based on previous  $B_1$  mapping). In fact, it is ‘only’ a repair mechanism to counteract the effects of the shorter wavelength at high field and to compensate for effects introduced by the human body itself.

But it was soon realized that parallel transmission technology (pTX) can offer a much greater potential than only  $B_1$  shimming. Dynamic pTX can be used to enable new applications.

### **Beyond simple $B_1$ shimming: dynamic parallel transmission with TimTX TrueShape**

TimTX TrueShape is a new transmit platform introduced for the MAGNETOM Skyra. It features a new RF body coil and two independent transmitters that are fully integrated into the Tim 4G DirectRF

architecture, i.e. both transmitters are situated in the TX-Box at the magnet side, directly adjacent to the receivers. While it is also possible to perform patient-specific  $B_1$  Shimming for dedicated examinations, extensive testing has shown that the anatomy-specific  $B_1$  Shimming (already introduced in 2007) shows comparable results to patient-specific  $B_1$  shimming for clinical applications. The potential of this technology platform lies elsewhere – in enabling entirely new applications.

With TimTX TrueShape equipment, ‘fully dynamic’ parallel transmission is made available for a clinical whole-body system. It enables the fully flexible and independent switching of arbitrary RF waveforms on the two RF channels, simultaneously with arbitrary gradient shapes on 1, 2 or all 3 gradient channels (Fig. 2, bottom). By this means, it is possible to excite arbitrarily shaped volumes (instead of a ‘simple slice’), or, more generally, to spatially control the magnitude as well as the phase of the excitation. The first clinical application to take advantage of this technology is ‘zoomed’ imaging.

### **syngo ZOOMit: The ‘Optical Zoom’ in MR imaging**

It is a well-known phenomenon in MR imaging that if the field-of-view (FOV) is smaller than the object, aliasing (fold-over artifacts) will occur. This is not an issue in the readout direction, since it can be overcome by frequency oversampling ‘for free’, i.e. without an increase in scan time, nor a penalty in SNR. But oversampling in the phase-encoding direction comes at a cost: more phase-encoding steps directly result in longer scan times, longer echo trains, etc. These disadvantages make the use of phase oversampling unfavorable in many cases. And if phase oversampling is not possible at all (e.g. because of too long scan times or echo trains), the only way to zoom into an image is a simple magnification – the analogy to a **digital zoom** of a camera that does not really

### **syngo ZOOMit offers distinct advantages:**

#### **Higher image quality:**

##### ■ **Less distortion and blurring artifacts**

For the zoomed FOV, the same spatial resolution can be achieved with shorter echo trains. This is a similar effect as (and can additionally be combined with) the echo train shortening with iPAT (then called ZOOPPA). It is especially valid for zoomed echo-planar-imaging (EPI; used for DWI and functional MRI), or similar for single shot TSE (HASTE).

##### ■ **Less motion and flow artifacts**

Regions outside the FOV (with organs that may be moving, or vessel pulsation) are not excited, do not contribute to the MR signal, and hence reduce artifacts.

##### ■ **Increased spatial resolution in region of interest**

Only the reduced FOV (zoomed) needs to be encoded.

#### **Higher speed:**

##### ■ **Faster scan times**

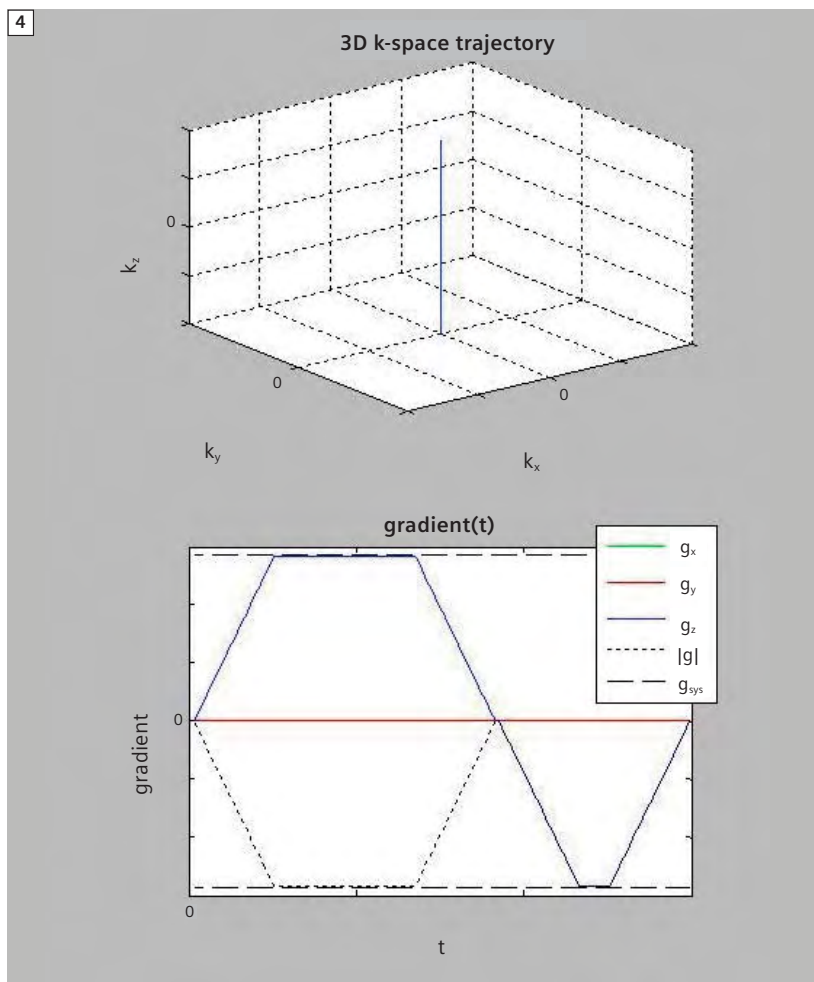
For the zoomed FOV, the same spatial resolution can be achieved with fewer phase-encoding lines. This is a similar effect as (and can be combined with) the scan time reduction with iPAT. It is especially valid for zoomed 3D TSE (syngo SPACE).

increase spatial resolution. For many imaging techniques, e.g. DWI or 3D data sets, one would therefore like to simply 'zoom' into the object in the phase-encoding direction (the one that is critical). It can be seen as the MR analogy to the **optical zoom** of a camera. A smaller quadratic FOV or only a reduced FOV in phase-encoding direction ('stripe') is excited (Fig. 3). Consequently, there will be no signal from the non-excited regions and only the small stripe needs to be encoded. The encoding time can be decreased while maintaining spatial resolution, or the spatial resolution can be increased - or a combination thereof.

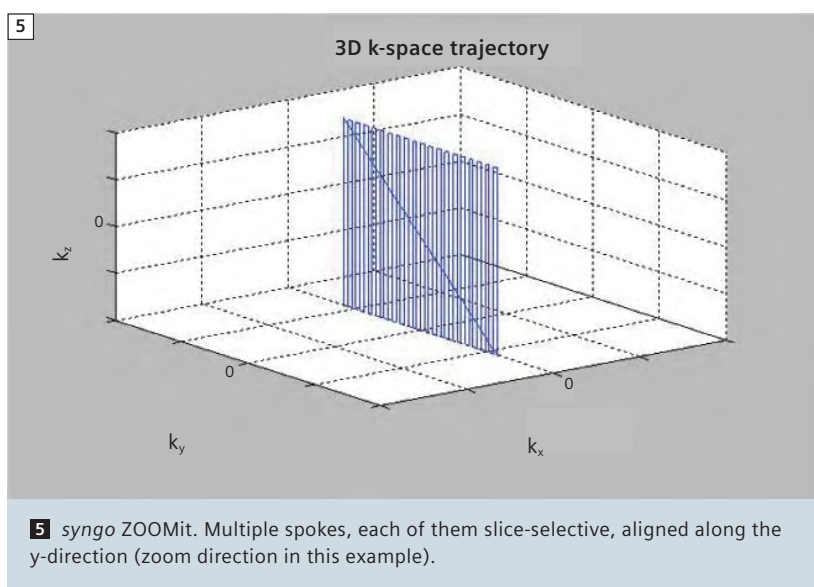
### The Details: How does *syngo* ZOOMit work?

In conventional imaging, a slice is excited by playing out a sinc ( $\sin(x)/x$ )-shaped RF pulse in the presence of a static gradient plateau. The reason for the sinc shape of the RF pulse is the fact that the Fourier transform of a sinc is a rectangle. By this means we achieve a rectangular slice profile of a defined slice thickness. For further explanation it is useful to introduce the concept of the '**excitation k-space**' [5]. Analogous to the receive k-space, 'movement' on a k-space trajectory is done with the gradients - the gradient amplitude defines the 'speed' in k-space, while the gradient slew rate defines the 'acceleration' in k-space. In a similar way as the signal is read out in receive k-space on the trajectory defined by the gradients (with multiple RF receive channels), the RF pulse is modulated during the trajectory (possibly with multiple TX channels).

For a conventional slice excitation (in z-direction), we first 'move' to +z with the z-gradient (Fig. 4, bottom left). During the plateau of the z-gradient (Fig. 4, bottom right) which 'moves' us from +z to -z, we play out the RF pulse - which consequently looks like one 'spoke' in excitation k-space, positioned at  $x = y = 0$  (since no x- or y-gradient was used), ranging from +z to -z (due to the z-gradient plateau). This RF pulse is amplitude-modu-



4 Conventional slice selection: One spoke, at  $x = y = 0$ , ranging from +z to -z. The RF is played out during the plateau of the z-gradient (left part of the graph).



5 *syngo* ZOOMit. Multiple spokes, each of them slice-selective, aligned along the y-direction (zoom direction in this example).

lated with a sinc function. The result of this excitation is a slice with defined thickness in z-direction and 'infinite' extension in x and y.

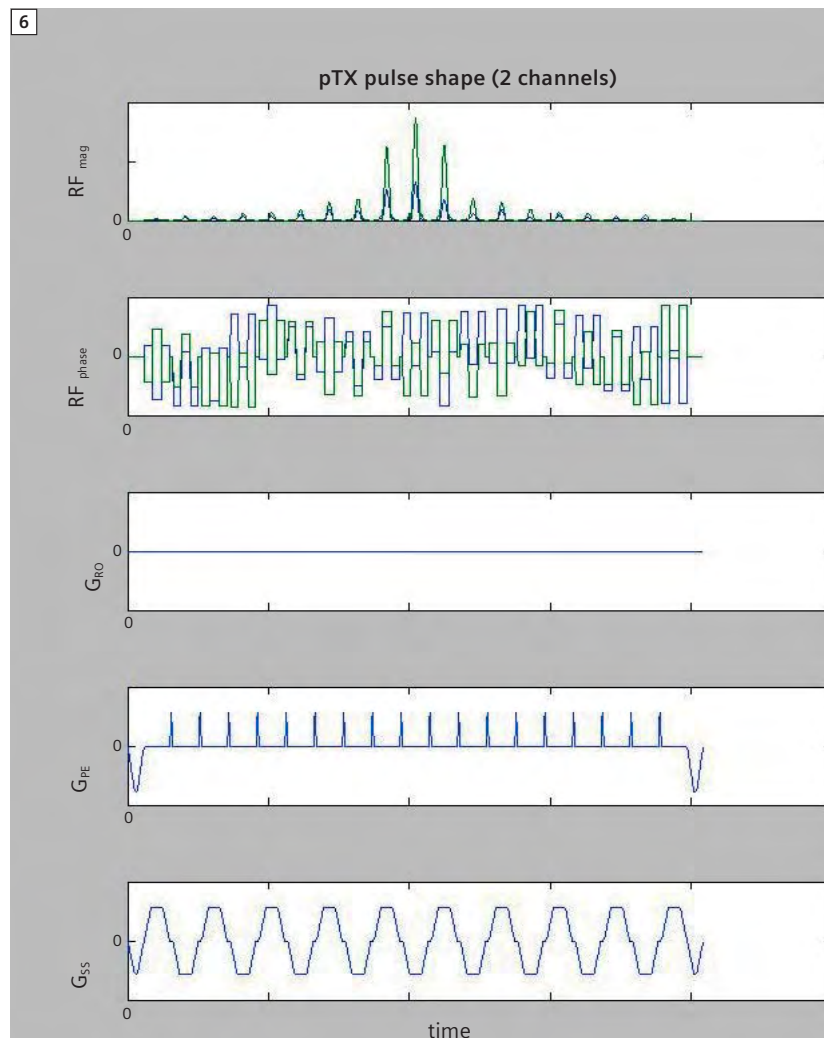
In order to 'zoom', i.e. to reduce the extension of the slice in one direction in-plane, we need to implement an encoding in, for example, y-direction. This combination is achieved by using multiple slice-selective spokes (each of them similar to conventional slice selection). The different spokes are aligned along y-direction (the 'zoom direction') at  $x = 0$  (x being the readout direction that is not affected). The spokes are modulated in amplitude and phase in a way that a FOV selection in y is realized. The trajectory in excitation k-space is similar to an EPI readout in receive k-space. In the analogy, the RX readout gradient pulses correspond to the TX slice-select gradients, the RX phase-encode blips correspond to the TX 'zooming' blips along y-direction, while the RX echoes correspond to the TX sinc pulses.

Figure 5 shows the 'EPI trajectory' of *syngo* ZOOMit in the excitation k-space. For the complete transmission diagram (RF and gradients, including additional pTX mechanisms), see Figure 6.

### The benefits of Tim 4G for dynamic pTX

The accurate excitation of arbitrarily shaped objects places high demands on the system hardware. It is imperative that the gradients have highest fidelity for an exact definition of the excitation k-space trajectory.

Tim 4G's **DirectRF** offers full 'digital in / digital out' of the transmitter and the receiver. Both the TX-Box and the receivers are situated directly at the magnet, as close as possible to the RF body coil and the local RX coils, but far enough from the bore in order to reduce any risk of RF interferences and to minimize the bulk and weight of the coils on the patient. A major benefit of the integration of the TX-Box and receivers are the short cables with defined cable lengths. This makes the whole architecture installation-inde-



**6** Typical sequence diagram of *syngo* ZOOMit. Excitation RF pulses with free modulation of amplitudes and phases on 2 TX channels, simultaneous use of two gradient channels.

pendent (everything can be pre-tuned in the factory) and reduces potential phase shifts between the signals of the different components that might be the consequence of varying siting conditions with potentially different cable lengths. The **Real-time Feedback Loop** for the RF data and the **Real-time Data Transfer** between the components offers several advantages, e.g. high stability of the  $B_1$  field and very tight control between transmitter, receiver and the RF body coil. The architecture guarantees highest

accuracy, synchronicity, stability and signal purity in the complete chain.

### Software and sequences for dynamic pTX

TimTX TrueShape incorporates new software, setting the stage for fully dynamic pTX. This includes the user interface (e.g. for graphic positioning of the zoomed FOV), new sequence parameters, and the underlying architecture and algorithms for the inline waveform calculations as well as SAR monitoring.

*syngo* ZOOMit is the first product application, but the TimTX TrueShape architecture is prepared for extended pTX applications in the future like variable pTX acceleration with 8+ channels or arbitrarily shaped excitation. It is also open for researchers who want to develop their own applications. Pulse sequences allowing for zooming are (currently) derived from the EPI and the SPACE sequences. The option is completed by optimized protocols for body, cardiac, neuro and MSK imaging.

### Potential advantages of dynamic pTX for zoomed imaging

While zoomed imaging can in principle also be performed with conventional scanners [6, 7], the following unique 'treasures' can utilize the benefits of dynamic parallel transmission for *syngo* ZOOMit:

#### Focused B<sub>1</sub> Shimming

With the current product implementa-

tions in the market, a global B<sub>1</sub> Shimming of the whole imaging volume is performed.

*syngo* ZOOMit offers a local B<sub>1</sub> Shimming, focused on the zoomed FOV. 'Concentrating' the B<sub>1</sub> shim optimization on a small volume increases the accuracy of the local shim and increases B<sub>1</sub> homogeneity.

#### B<sub>1</sub> mitigation

In conventional imaging, the flip angle is proportional to the B<sub>1</sub> field. With B<sub>1</sub> Shimming, a higher B<sub>1</sub> homogeneity and, consequently, higher flip angle homogeneity can be achieved.

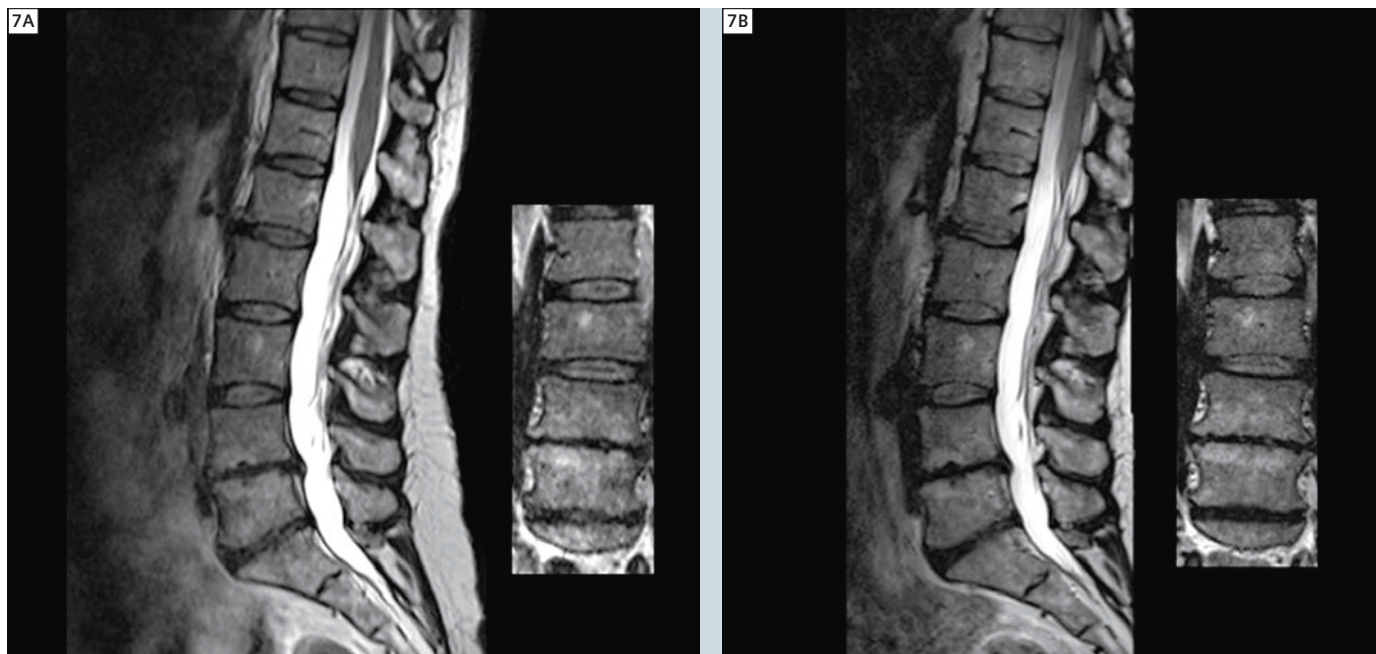
However, even after ('static') B<sub>1</sub> Shimming, B<sub>1</sub> homogeneity might not be perfect. B<sub>1</sub> mitigation is a 'dynamic' application to improve flip angle homogeneity beyond what can be achieved with B<sub>1</sub> Shimming alone. This is achieved with sophisticated excitation pulses, typically multiple excitation 'spokes' in the excitation k-space [8, 9].

Since *syngo* ZOOMit incorporates multiple spokes (Fig. 5). These spokes can be modified to achieve – simultaneously to the zooming – a B<sub>1</sub> Mitigation in the zoom direction (in addition to focused B<sub>1</sub> Shimming), for higher flip angle homogeneity.

#### B<sub>0</sub> compensation

The main magnetic field B<sub>0</sub> has imperfections/inhomogeneities. Furthermore, local magnetic field inhomogeneities are induced by the patient (susceptibility effects). B<sub>0</sub> homogeneity can be improved with conventional (high-order) B<sub>0</sub> Shimming.

B<sub>0</sub> compensation with dynamic pTX pulses is an additional means to compensate for remnant B<sub>0</sub> inhomogeneities relevant for the RF excitation. With sophisticated excitation pulses, the phase of the spins can locally be altered to counteract and compensate the phase shift due to B<sub>0</sub> inhomogeneities [9]. This will improve the accuracy of the zoomed FOV



**7** Comparison of a conventional SPACE acquisition (**7A**) (sagittal orientation and coronal MPR shown) with a zoomed SPACE (**7B**) in the same volunteer at same resolution. By simply zooming the FOV, a reduction of scan time of one third was achieved.

(exact shape, profile steepness) and can potentially also improve fat suppression.

#### Transmit SENSE (TX-SENSE)

In general, the more advanced the excitation is, the more time it can take for the excitation pulse. A zoomed image (restriction in 2 dimensions, y, z) is more 'complex' than the excitation of a slice (restriction in only 1 dimension, z).

Transmit SENSE, possible with multi-channel TX systems, is a remedy against too-long excitation pulses. The duration of the excitation pulse can be shortened and thus also concurrent  $B_0$  effects (that scale with the pulse duration).

There is some similarity between Transmit SENSE and parallel imaging on the receive side. While the latter results in fewer phase-encoding steps for the same spatial resolution and, consequently, shorter scan times, Transmit SENSE results in a reduction of the length of the excitation pulse to achieve the same 'excitation quality', e.g. the

steepness of the excitation profile.

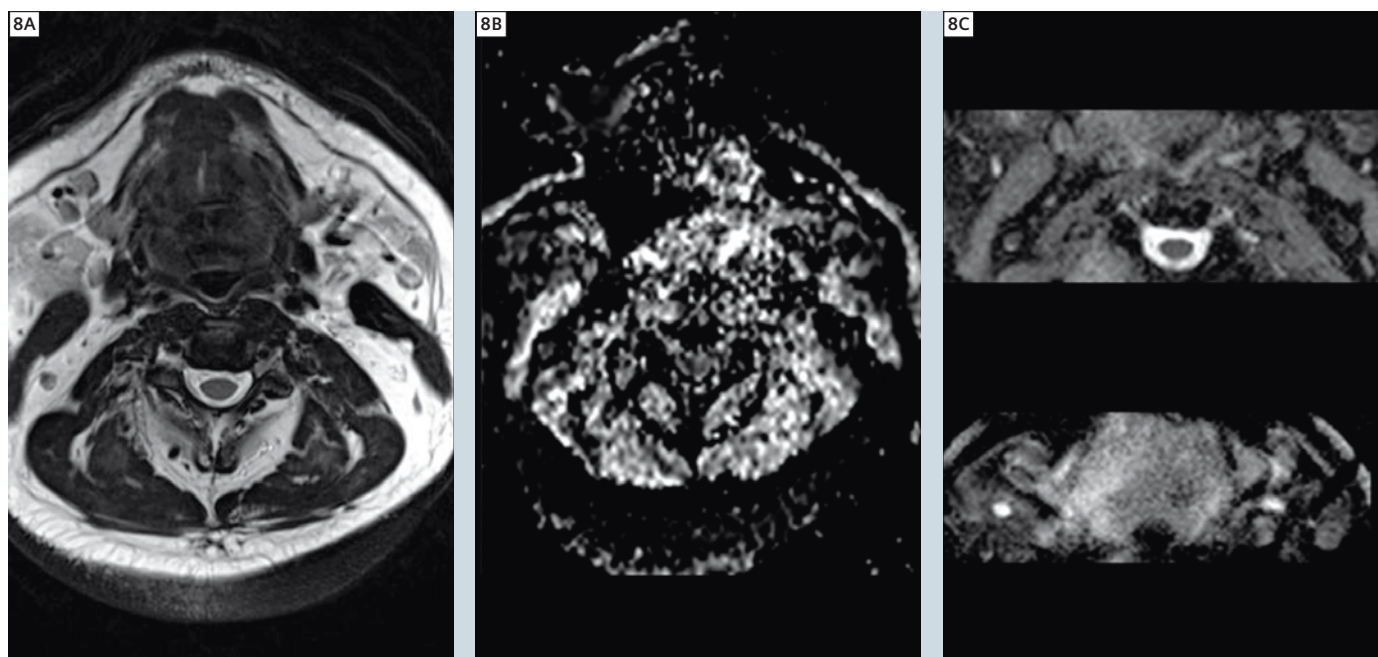
Figure 6 shows the complete transmit diagram for *syngo* ZOOMit, incorporating all the 'treasures' mentioned above: RF amplitude of 2 TX channels (row 1), RF phase of 2 TX channels (row 2), read-out gradient (row 3, not active during excitation), phase-encoding gradient with blips in the zoom direction (row 4), slice-select gradient (row 5). Each short RF pulse is a slice-selective sinc pulse. The envelope of all these pulses define the zoomed FOV. The envelope of the RF amplitude (row 1) would again look similar to a 'long sinc', but is modified by the effects of the said 'treasures'.

#### First results with *syngo* ZOOMit

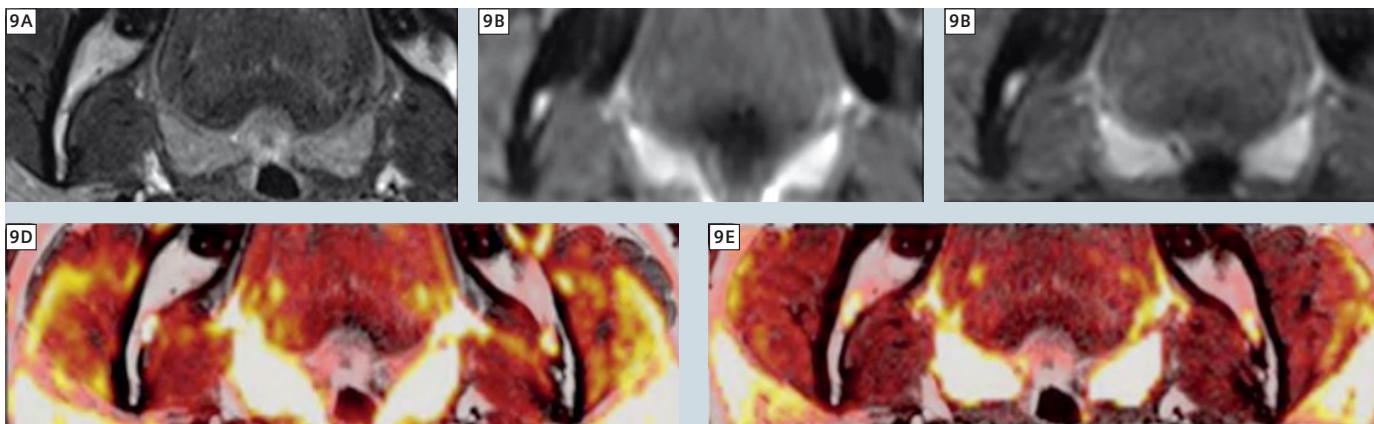
At this time-point, two sequence techniques are available for *syngo* ZOOMit – EPI based imaging for DWI and fMRI, together with SPACE as a 3D TSE imaging technique.

■ In clinical routine, the main challenge of 3D imaging is acquisition time because of the large volume which has to be scanned to avoid aliasing. Figure 7 shows a simple comparison between a conventional and a zoomed SPACE scan. In this example the scan time was reduced by 33% from approx. 6 to 4 mins – maintaining the same excellent image quality.

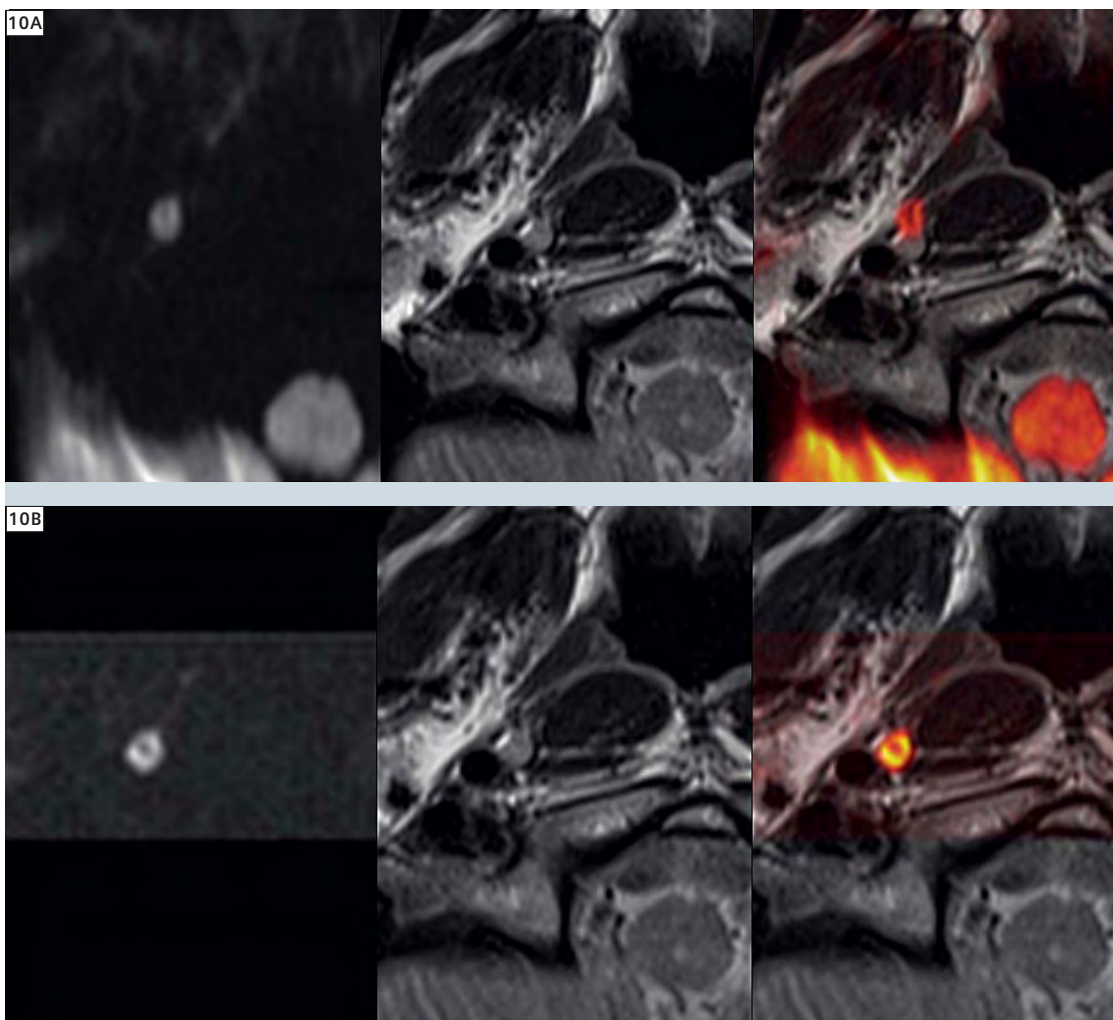
■ Quality of DWI is especially crucial when this technique is used for the detection of potentially smallest changes, (e.g. tumor staging in the oral cavity), in areas with high differences of susceptibility, (e.g. the spine or abdomen – bowel, pancreas, stomach), or when quantification of diffusion restriction is required. Figure 8 demonstrates the development of DWI during the past years in one of the most challenging areas – the oral cavity and neck.



**8** DWI has seen tremendous evolution during the past years. To visualize this and the potential of zoomed DWI, an ADC map acquired with a standard DWI sequence and conventional parameters, as still often used in clinical routine, is compared with the corresponding ADC maps acquired with *syngo* ZOOMit DWI in the same volunteer. In addition to reduced distortion, the zoomed DWI is characterized by a higher SNR and spatial resolution as a consequence of the TE shortening enabled by parallel transmission. **(8A)** Morphology (T2w TSE) **(8B)** ADC map without optimization **(8C)** ADC maps derived from a zoomed DWI exam with parallel transmission.



**9** Even compared to optimized conventional DWI protocols, zoomed imaging can be used to improve SNR and geometrical accuracy as shown in this example of the tongue base. **(9A)** T2w TSE, **(9B)** original b-value image derived from an optimized (magnified image; fusion with morphology shown in **(9D)**) **(9C)** same volunteer and comparable sequence parameters (TE, b-value) examined with zoomed DWI (fusion shown in **(9E)**).



**10** High-resolution DWI of a small lymph node in the same volunteer ( $1.0 \times 1.0 \text{ mm}^2$  in-plane resolution) **Upper row:** conventional DWI, **lower row:** zoomed DWI. Note the precise match between original b-value image (left) and anatomy (middle, right fusion) for the zoomed exam.

Conventional DWI has seen a lot of improvements and the latest developments include read-out segmented EPI (*syngo* RESOLVE). But also by comparing optimized protocols, further improvements can be achieved with zoomed imaging. Figures 9–11 show some further potential advantages.

### Future developments

Zoomed imaging offers a high potential to significantly increase image quality and decrease scan times, as shown in the examples above. However, dynamic parallel transmission (TimTX TrueShape) offers a wide field of additional potential applications. Some examples:

- Creation of curved saturation pulses (e.g. along the spine) for optimal suppression of motion and flow artifacts. Such a saturation pulse would be achieved with a 2D spiral excitation.
- 3D-selective excitation, for example a cuboid or a sphere or even the exact shape of the object. This might be

interesting for e.g. 3D CSI of the prostate.

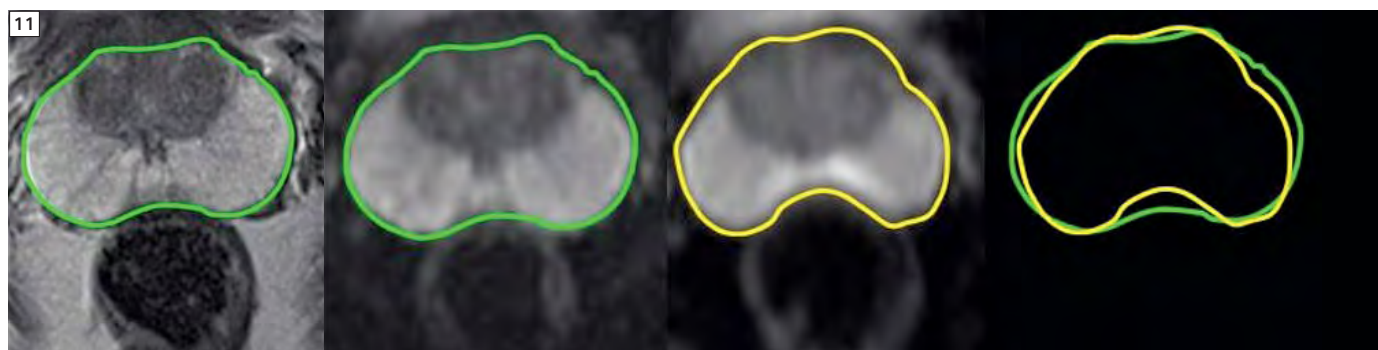
Figure 7 shows what a 3D-selective excitation with a 3D spiral looks like in excitation k-space. This does not bear much resemblance anymore to the conventional slice excitation from Figure 4.

- Vessel-selective excitation, e.g. for ASL (selective Arterial Spin Labeling).

Besides new applications, also going to a higher number of transmit channels is an interesting option, with the potential to go to higher TX-SENSE factors and shorter excitation pulses. This might be useful for multi-channel B<sub>1</sub> Shimming and B<sub>1</sub> Mitigation, especially at ultra-high field strength. Multiple channels would also facilitate the excitation of complex multi-dimensional excitation shapes. The 1980s were the decade of the magnets, the 1990s saw a vast increase of gradient performance. While the 2000s can be seen as the decade of RF receive technology with multi-channel array coils and Parallel Imaging, the 2010s might well become the decade of RF transmit. TimTX TrueShape sets the stage for a new act in MRI.

### Acknowledgements

A heartfelt thank you to Dr. Dieter Ritter for preparing the figures and to Dr. Hans-Peter Fautz, Matthias Gebhardt, Dr. Stephan Kannengiesser, Jürgen Nistler, Dr. Josef Pfeuffer, Dr. Thorsten Speckner, and many others, too numerous to mention, for in-depth discussions on the exciting topic of pTX.



**11** Distortion-free imaging with *syngo* ZOOMit of the prostate. Anatomy and high-resolution DWI show an excellent match of the outlined prostate. In contrast, conventional DWI shows distortion especially in the area of the peripheral gland – the main area for prostate cancer.

#### References

- 1 Sodickson DK, Manning WJ. Simultaneous acquisition of spatial harmonics: fast imaging with radiofrequency coil arrays. *Magn Reson Med* 1997; 38:591–603.
- 2 Pruessmann KP, Weiger M, Scheidegger MB, Boesiger P. SENSE: sensitivity encoding for fast MRI. *Magn Reson Med* 1999;42:952–962.
- 3 Griswold MA, Jakob PM, Heidemann RM, et al. Generalized autocalibrating partially parallel acquisitions (GRAPPA). *Magn Reson Med* 2002;47: 1202–1210.
- 4 J. Nistler, D. Diehl, W. Renz, and L. Eberler: Homogeneity Improvement Using A 2 Port Birdcage Coil. *Proc. Intl. Soc. Mag. Reson. Med.* 15 (2007), 1063.
- 5 Pauly, J., D. Nishimura, and A. Macovski, A k-space analysis of small-tip angle excitation. *J Magn Reson*, 1989. 81: p. 43-56.
- 6 Susanne Rieseberg, Jens Frahm, and Jürgen Finsterbusch: Two-Dimensional Spatially-Selective RF Excitation Pulses in Echo-Planar Imaging. *Magnetic Resonance in Medicine* 47:1186–1193 (2002).
- 7 Emine Ulku Saritas, Charles H. Cunningham, Jin Hyung Lee, Eric T. Han, and Dwight G. Nishimura: DWI of the Spinal Cord with Reduced FOV Single-Shot EPI. *Magnetic Resonance in Medicine* 60:468–473 (2008).
- 8 Lawrence L. Wald, Elfar Adalsteinsson: Parallel Transmit Technology for High Field MRI, *MAGNETOM Flash magazine*, issue 1/2009.
- 9 Rainer Schneider, Dieter Ritter, Jens Hauelsen, and Josef Pfeuffer Evaluation of 2DRF echo planar pulse designs for parallel transmission. Presented at the ISMRM 2012.

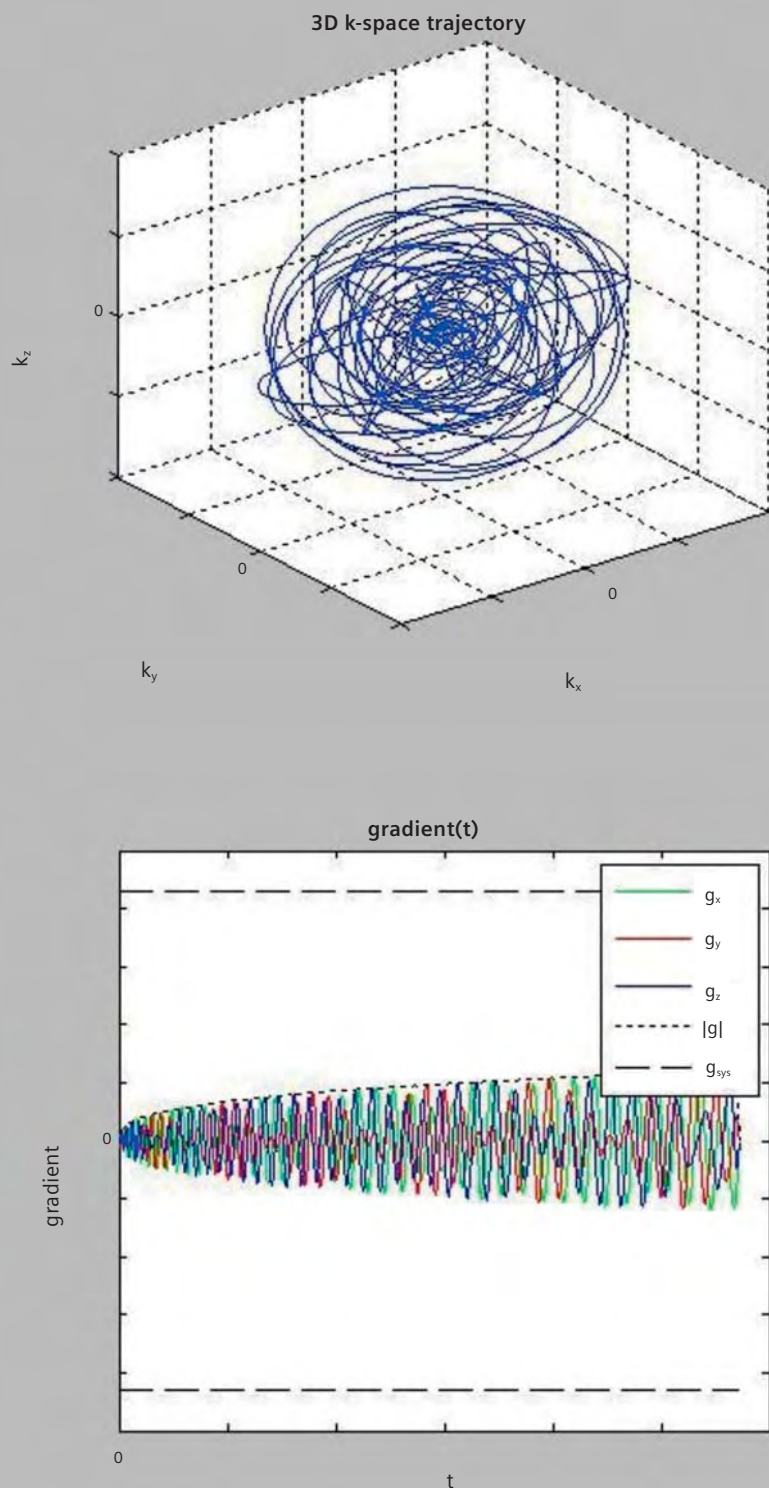
#### Contact

Matthias Blasche  
Siemens AG  
H IM MR MK CPR  
Postbox 32 60  
91050 Erlangen  
Germany  
mathias.blasche@siemens.com

#### Disclaimer:

TimTX TrueShape (with syngo ZOOMit) is Works in Progress. The information about this product is preliminary. The product is under development and is not commercially available in the U.S., and its future availability cannot be ensured.

12

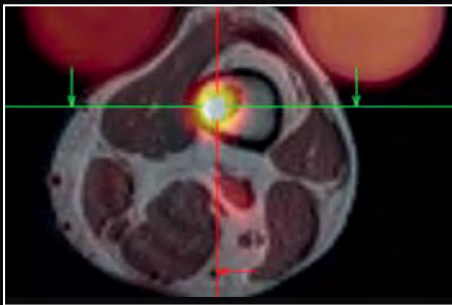
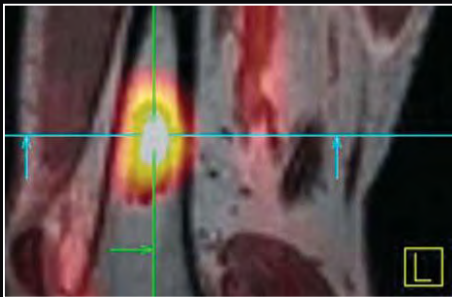


**12** Example of a sequence diagram for 3D-selective excitation with a 3-dimensional spiral with simultaneous use of 2 TX channels and all 3 gradient channels.

# Heidelberg Summer School

## Musculoskeletal Cross Sectional Imaging 2012

**August 24<sup>th</sup> – 25<sup>th</sup>, 2012**  
**Heidelberg, Germany**



### Programme

(all lectures are in English)

**Block 1: Bone and soft-tissue tumors**

**Block 2: Spine**

**Block 3: Sports imaging**

**Block 4: Whole-body MRI**

**Block 5: Upper extremity**

**Block 6: Lower extremity**

**Block 7: New (functional) methods of MRI**

Course director:

Marc-André Weber, MD, MSc

### CME Accreditation

The symposium will be accredited by the "Landesärztekammer Baden-Württemberg" with CME credits (category A). Also, the symposium is accredited for 1 category 3 credit point for the ESSR diploma by the European Society of Musculoskeletal Radiology.

### Registration and further information

Mrs. Marianne Krebs, Secretary of the Section Musculoskeletal Radiology

Marianne.Krebs@med.uni-heidelberg.de



# Case Report: Distal Medial Collateral Ligament Tear of the Knee

Eric K. Fitzcharles, M.D.; Charles P. Ho, Ph.D., M.D.

Steadman Philippon Research Institute Vail, CO, USA



**1** Coronal fat suppressed proton density-weighted image (19/36) showing diffuse soft tissue edema and fluid about the medial knee. There is partial tearing and stripping of the proximal MCL attachment (curved arrow). There is undulating, stretched ligament contour (arrow head). Retracted distal ligament fibers (medium arrow) are superior and superficial to the intact pes anserinus tendon (long arrow).

## History of present illness

New patient evaluation for right knee pain. Patient is a professional ski patrol-ler. He was out skiing for fun, landed and felt a pop in his knee. He was able to ski down to the base area, but felt like his knee was unstable and he was unable to continue to ski. He had knee pain and feelings of instability since then. He has not been able to return to his athletics. He states that his pain at rest is a 1/10 and at its worse, it is 4/10. It is improving and occasional. He also experiences giving away and popping in his knee. He has never had a knee injury before. He has tried bracing, ice and decreased activity to treat it. No history of knee surgery.

## Musculoskeletal examination

The patient is tender to palpation over the right knee medial collateral liga-ment. Otherwise, he is nontender to pal-pation throughout his bilateral knees. His range of motion today is -5 to 135 on the right, and -5 to 150 on the left. He is stable to Lachman, anterior and posterior drawer, and varus stress. He opens significantly to valgus stress on the right knee, but not on the left knee. He has normal patellar motion and glide. He has no crepitus. His light touch is intact in all dermatomes distally. His motor strength is 4+/5 on the right and 5/5 on the left in all myotomes. X-rays show that he has no bony abnor-malities, but he does have opening to valgus stress on the right knee.

**Table 1: MRI technique.**

Weighting and planes	Field-of-view	TR	TE	Sequence	Slice thickness	Gap	Matrix size
T2-weighted axial	115	5320	100	Turbo Spin Echo	3.2 mm	0.3 mm	512 x 512
Proton Density-weighted axial fat suppressed	150	1200	45	Turbo Spin Echo fat suppressed	2 mm	0.0 mm	256 x 256
Proton Density-weighted sagittal	140	2570	41	Turbo Spin Echo	2 mm	0.0 mm	256 x 256
Proton Density-weighted sagittal fat suppressed	150	1200	45	Turbo Spin Echo fat suppressed	2 mm	0.0 mm	256 x 256
Proton Density-weighted coronal	120	2770	31	Turbo Spin Echo	3 mm	0.3 mm	640 x 640
Proton Density-weighted coronal fat suppressed	160	6040	41	Turbo Spin Echo fat suppressed	2 mm	0.3 mm	512 x 512

### Clinical assessment

High-grade Medial Collateral Ligament (MCL) disruption.

MRI (Table 1, Figs. 1– 4): High-grade complete tear and stripping and retraction of the distal medial collateral ligament from its tibial insertion site, with possibly a few residual continuous but

elongated and stretched fibers, which may be from interstitial tearing. The majority of ligament fibers appear retracted to a level 4.5 cm below the joint line, proximal to pes anserinus and superficial to the distal pes tendons. There also appears to be partial tear involving the proximal medial collateral

ligament, with adjacent edema and evidence of stretching. Osteochondral impaction fracture injury of the posterolateral femoral condyle with mild cortical flattening and underlying osseous edema, as well as some overlying chondral thinning. Small joint effusion is noted.

## Discussion

### Anatomy

There are three tissue layers in the medial knee [1]. The superficial crural and sartorial fascia form the outer layer. The superficial and deep medial collateral ligament forms the middle and deep layers [1]. The superficial MCL proximal attachment site is the posterior aspect of medial femoral condyle, proximal and posterior to the medial epicondyle. There are two distal attachments:

1. The anterior arm of the semimembranosus tendon.

2. A broad insertion just anterior to the posteromedial crest of the tibia.

The broad tibial insertion of the superficial medial collateral ligament is located deep and posterior to the pes tendons [2]. The superficial ligament can also be divided into anterior and posterior portions. Anterior fibers tighten with knee flexion. Posterior fibers form the posterior oblique ligament (POL). The POL extends distally from adductor tubercle with three arms [3]:

1. Tibial arm to the posterior tibia.

2. Capsular arm blends into the capsule and the proximal oblique popliteal ligament.

3. Inferior arm to the semimembranosus tendon sheath, and inserts just distal to the semimembranosus.

The superficial layer of the MCL provides restraint to valgus stress at knee, providing from > 60–70% of restraining force depending on knee flexion angle. At 25° of flexion, the MCL provides 78% of the support to valgus stress. At 5° of flexion, it contributes 57% of the support against valgus stress [1]. The semimembranosus, pes anserinus, and quadriceps tendons also provide medial stability [3]. The deep MCL is divided into meniscofemoral and meniscotibial ligaments. It inserts directly onto the edge of tibial plateau and medial meniscus. Unlike the superficial MCL, it does not provide significant resistance to valgus force [1].

### Clinical history and examination findings

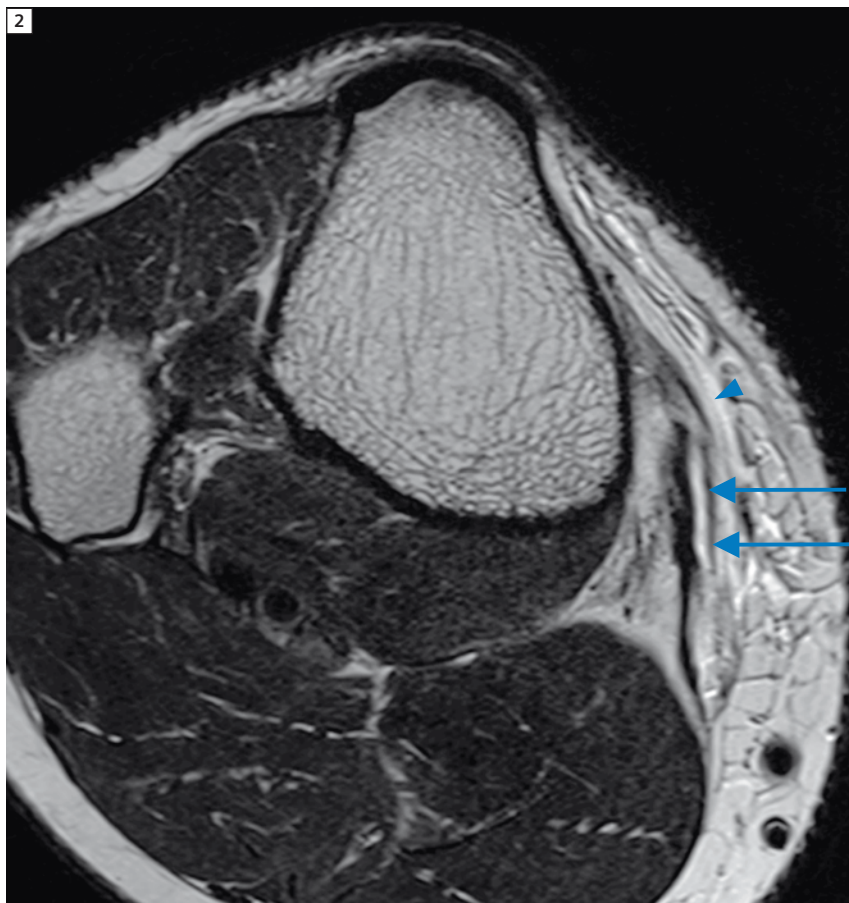
The overall cause of MCL injury is valgus stress across the knee joint. There are several mechanisms of injury. The most common is a direct blow to the lateral side of the knee while the foot is planted on the ground and the knee is partially flexed, exemplified by the common football 'clipping' injury. MCL injury may also occur without ground contact, by a forced external rotation of the tibia, as is often seen in skiers. A valgus force to the knee with the foot in unloaded external rotation may also act as a mechanism.

MCL sprains can and often do occur along with other injuries, such as Anterior Cruciate Ligament (ACL) / Posterior Cruciate Ligament (PCL) tears and meniscal injuries.

Exam findings may be subtle, even with complete MCL rupture. Comparison to the opposite knee is essential. It is very important to assess for valgus laxity, with or without an endpoint, and to determine the point of maximal tenderness.

In mild flexion, such as 30 degrees, valgus stress testing is specific for just the MCL [1]. In extension, the examiner is testing the posterior portion of the MCL, the posterior oblique ligament, the ACL, medial portion of posterior capsule, and possibly also the PCL.

If the ligament is torn from medial epicondyle, it may avulse or elevate a small bony fragment, causing focal tenderness to palpation. This is the classic Pellegrini-Stieda phenomenon, showing calcification or a bone fragment at origin of MCL on X-ray.



**2** Axial T2-weighted image (27/40) showing retracted distal MCL fibers (arrow head) superficial to the intact pes tendons including most anterior, the sartorius tendon (long arrows).

If there is a mid-MCL tear, the overlying tendons may also be torn. There can be a palpable defect with focal tenderness at the level of the medial joint line. With a distal tibial tear, tenderness may be felt 6–8 cm down medial tibial shaft, along length of the ligament insertion. A 'Stener-like' injury (see below) should be suspected in the presence of remarkable, abnormally tender swelling and ecchymosis over the medial joint line and proximal tibia [4]. Valgus laxity testing is not necessarily conclusive. Associated knee injuries, most commonly ACL and meniscal tears, will obviously exhibit additional exam findings.

### MRI

The vertical and posterior oblique components of the MCL are depicted consistently on coronal MRI sequences. The

MCL appears as a thin, taut, well-defined, low signal linear structure running from the medial femoral epicondyle to the medial tibial metaphysis [5]. The MCL runs parallel and adjacent to the medial femoral epicondyle and medial tibial metaphysis. The grading system for MCL and other ligament tears [5] is:

Grade I: Sprain

Grade II: Partial tear

Grade III: Complete tear

Calcification in and near the proximal MCL can be seen radiographically in the setting of chronic MCL tear, or acute avulsion fracture.

Acute MCL tear appearance depends on severity. Grade I sprains of the MCL are the most frequent ligamentous injury of the knee [4]. Sprains exhibit an intact

ligament of normal thickness, surrounded to a variable degree by soft tissue edema.

Grade II tears show thickening and/or partial disruption of MCL fibers, with surrounding soft tissue edema and possibly hemorrhage. There are residual intact ligament fibers visible.

Grade III MCL tears show complete disruption of the ligament with corresponding surrounding hemorrhage and edema. There may be avulsion of either attachment site, and there is often an undulating, stretched appearance to the ligament. Proximal tears are more common than distal tears. If there is complete ACL tear, complete disruption of the MCL is more likely.

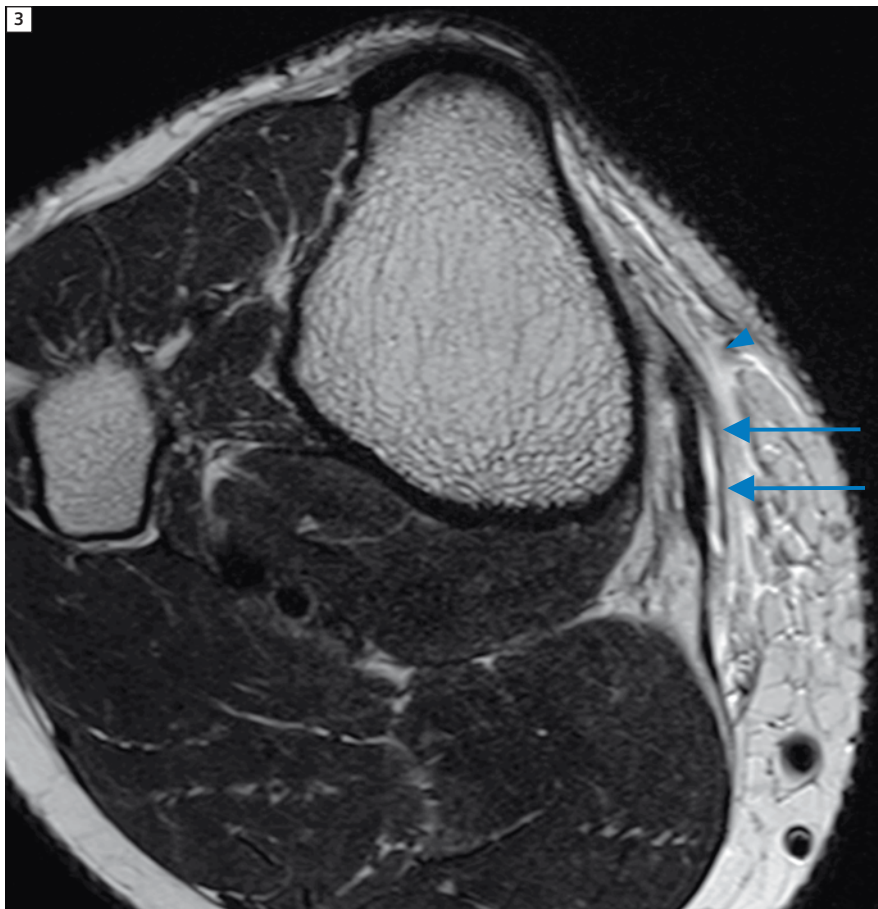
A chronic MCL tear is seen as an ill-defined, thickened ligament with low T1 and T2 signal. The MCL can partially ossify in a chronic setting, and normal bone marrow signal may be seen proximally.

### 'Stener-like' MCL tear

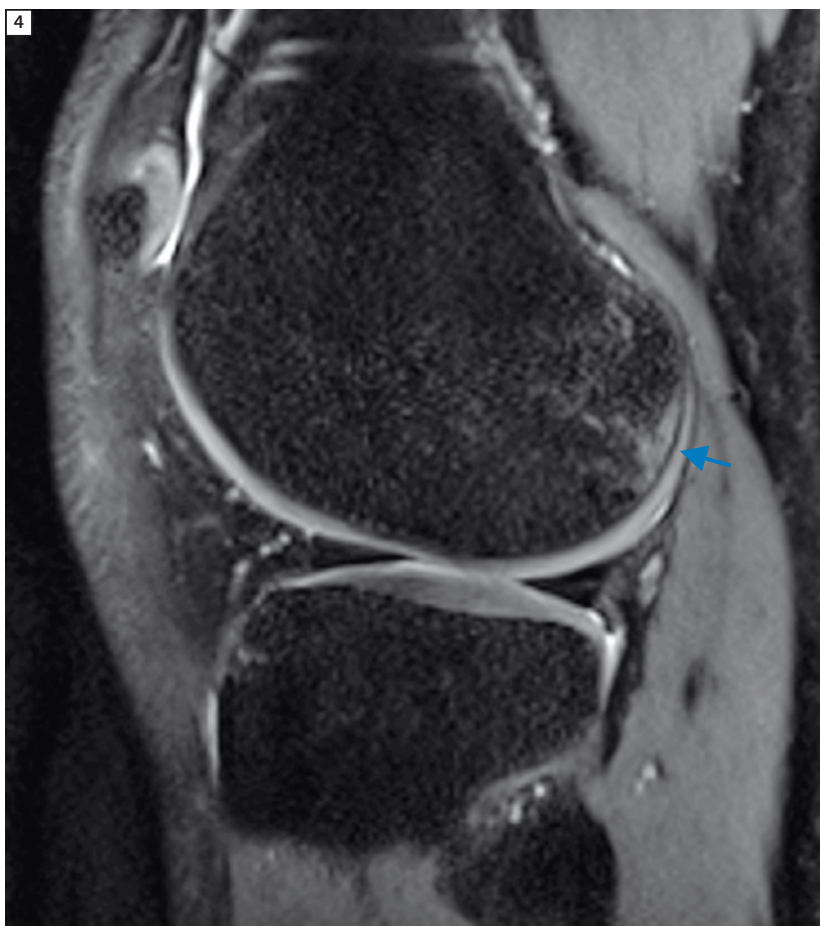
In the thumb, disruption of the distal insertion site of the ulnar collateral ligament of the first metacarpophalangeal (MCP) joint and displacement over the adductor aponeurosis were described by Stener [6] in 1962. A similar 'Stener-like' tear of the MCL is uncommon, but warrants special consideration due to its unique features and treatment [4]. Valgus laxity testing is not always conclusive, but MRI will show MCL fibers retracted from their normal position deep to the pes tendons [2]. Similar to a Stener lesion of the thumb, if these stripped or torn MCL fibers are displaced superficial to the pes tendons, direct healing is not possible, resulting in persistent valgus laxity and instability. Surgical repair should be considered in these cases.

### Bone contusions

With a classic clip injury, bone marrow edema is most prominent in the lateral femoral condyle, due to the direct blow. There is often a second smaller area of edema in the medial femoral condyle or medial tibial plateau, from avulsive MCL stress [7].



**3** Axial T2-weighted image (28/40) distal to Figure 2 showing retracted distal MCL fibers (arrow head) superficial to the intact pes anserinus tendons (long arrows).



**4** Sagittal fat suppressed proton density-weighted image (44/59) showing edematous impaction fracture of the posterior lateral femoral condyle (arrow).

MCL tears are not usually isolated. Aside from bone contusions, other injuries such as ACL tears and medial meniscal tears (O'Donoghue's triad) are often seen [5]. 73% of complete MCL tears are associated with other knee injuries, most commonly ACL tear [5]. Compared to the Lateral Collateral Ligament (LCL) injuries, the sensitivity, specificity, and accuracy of MRI for MCL injuries are less well established due to their nonsurgical nature, but they may be assumed to be similar to those of the LCL. High T1-weighted fatty tissue interposed between the layers of the MCL is a normal finding that may mimic an MCL tear.

#### Non operative treatment

MCL tear healing potential is directly related to size of the gap between the

torn ends. Optimal healing occurs when the ends are directly opposed. MCL fibers heal much better than the ACL [3]. Maturation of scar tissue occurs from 6 weeks to one year. The ligament reaches approximately 50% of its original strength at 12 months. Mature scar tissue is about 60% as strong as a normal MCL, but the total load necessary for failure can be about the same as that of an uninjured MCL, since the thickness of scar tissue is usually greater than that of the original ligament.

#### Operative treatment

Surgery is obviously tailored to the location of the tear. If there is femoral avulsion, the location of the reattachment is very important. Reattachment anterior to its original location may limit knee

flexion, whereas posterior reattachment may cause laxity. The knee should be held in 30 degrees flexion during reattachment.

Surgical repair or at least relocation of Stener-like MCL tears should be considered [4]. This consists of refixation to the tibial insertion site. The surgeon may restore normal tension by securing the retracted ligament to an area of roughed up bone, and secure with sutures or a staple.

#### References

- 1 Wheelless, CR (original text). Medial Collateral Ligament. Wheelless Textbook of Orthopedics Web site. [http://www.wheellessonline.com/ortho/medial\\_collateral\\_ligament](http://www.wheellessonline.com/ortho/medial_collateral_ligament). Updated August 30, 2011. Accessed November 4, 2011.
- 2 De Maeseneer M, et al. Sonography of the Medial and Lateral Tendons and Ligaments of the Knee: The Use of Bony Landmarks as an Easy Method for Identification. *AJR* 2002; 178(6): 1437-1444.
- 3 Phisitkul P, et al. MCL Injuries of the Knee: Current Concepts Review. *Iowa Orthopaedic Journal* 2006; 26:77-90.
- 4 Corten K, et al. Case Reports: A Stener-like Lesion of the Medial Collateral Ligament of the Knee. *Clin Orthop Relat Res* 2010; 468(1):289-293.
- 5 Freitas A, et al. Collateral Ligament Injury MRI. Medscape Reference Web site. <http://emedicine.medscape.com/article/401472-overview>. Updated May 25, 2011. Accessed November 7, 2011.
- 6 Stener B. Displacement of the ruptured ulnar collateral ligament of the metacarpo-phalangeal joint of the thumb: a clinical and anatomical study. *J Bone Joint Surg Br.* 1962;44:869-879.
- 7 Sanders TG, et al. Bone Contusion Patterns of the Knee at MR Imaging: Footprint of the Mechanism of Injury. *RadioGraphics* 2000; 20:S135-S151.

#### Contact

Charles P. Ho, Ph.D., M.D.  
Steadman Philippon Research Institute  
181 W. Meadow Dr. Suite 1000  
Vail, CO 81657  
USA  
[Karen.briggs@spravail.org](mailto:Karen.briggs@spravail.org)

# Case Report: Posterior Glenoid Labral Tear

Eric K. Fitzcharles, M.D.; Charles P. Ho, Ph.D., M.D.

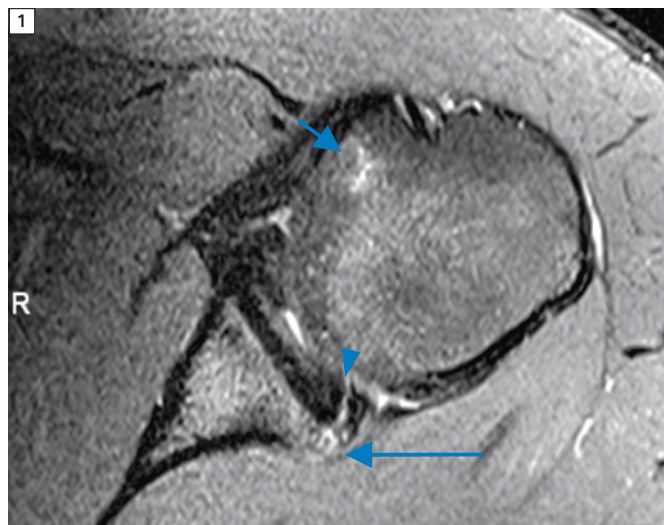
Steadman Philippon Research Institute, Vail, CO, USA

## History of the present illness

The patient plays running back on the football team, and he comes for complaints of left shoulder pain. He states that he was running in camp a few weeks ago where he was hit with the ball and felt like his arm pushed superiorly and inferiorly. Since that time, he has not played. He is having continued symptoms. The patient has a past history of right shoulder Latarjet procedure in 2007, and an arthroscopy performed a year before consisting of Bankart repair. The patient now states that he is unable to play and practice football and wishes to have this addressed. He describes his discomfort as pain and instability when playing. The patient states the pain is 2/10 at rest and 9/10 at its worst. The patient states that the pain does not wake him up from sleep. Rest alleviates his symptoms.

## Musculoskeletal examination

Examination of bilateral upper extremities shows full strength 5/5 muscle strength in his rotator cuff as well as biceps and triceps bilaterally. More specific exam of his left shoulder shows patient has pain with anterior apprehension test and posteriorly. He has no real feeling of apprehension as it does not feel like it is dislocating in the front. He has positive O'Brien's. He has negative Speed's and Yergason's. He has a mildly positive jerk test mostly with just discomfort. On load and shift, he has some discomfort when attempting to shift him posteriorly, however, no gross laxity is



**1** Axial fat suppressed proton density-weighted image (19/29) showing a tear through the posterior labrum (arrow head) which extends through the periosteum. There is mild edema of the anterior humeral head (medium arrow) suggesting contusion or possible small shallow reverse Hill Sachs lesion. There is irregularity and truncation of the posterior osseous glenoid with small ossicle (long arrow), suggestive of reverse bony Bankart lesion.

felt anteriorly. There is some mild subluxation posteriorly. X-rays showed no fracture or dislocation and good maintenance of joint space. The left shoulder was imaged using a 3T Siemens MAGNETOM Verio MRI scanner. Details of the technique are shown in Table 1. MRI images (Figures 1–4) show a posterior labral tear extending through the articular and capsular margins and periosteum, with possible small reverse bony Bankart lesion as well. There is osseous edema in the anterior humeral head suggesting contusion or possible small shallow reverse Hill-Sachs impaction lesion. The overall appearance suggests acute on chronic findings.

## Operative findings

The patient had a posterior labral tear with detachment with a flap and a loose

body within the joint. The remainder of the shoulder had some anterior labral fraying and some synovitis. Otherwise, there was no Hill-Sachs or reverse Hill-Sachs and no bone loss. Biceps and biceps anchor were intact.

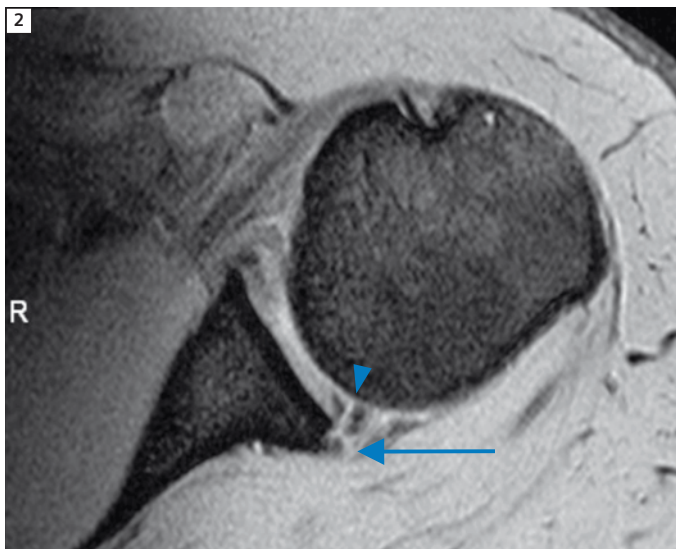
## Procedures performed

1. Left shoulder arthroscopy with extensive glenohumeral debridement.
2. Arthroscopic removal of loose body.
3. Arthroscopic posterior labral repair with capsular shift.

## Discussion

### Background

The shoulder is the most unstable joint in the animal kingdom, and has the greatest range of motion of any joint in the human body [1]. The humeral head and glenoid are by themselves inher-



**2** Axial T2-weighted gradient echo image (18/29) showing a tear through the posterior labrum which extends through the periosteum (arrow head). There is irregularity and truncation of the posterior osseous glenoid (long arrow) with small ossicle, suggestive of reverse bony Bankart lesion.

ently unstable, and require the labrum, capsule, ligaments and tendons to help stabilize the joint. Injury to any of these structures can increase the stress on the surrounding normal structures, causing pain and instability.

Glenohumeral joint instability extends over a spectrum of severity, ranging from dislocation to transient subluxation. Instability may occur in any direction, or it may be multidirectional. Posterior instability can result from repeated microtrauma. Abduction, flexion, and internal rotation (including throwing) may be the mechanism of injury. Most of these patients will respond to conservative therapy, which includes strengthening of the posterior stabilizing muscles [2].

Posterior dislocation may result from a fall on an outstretched hand, direct traumatic injury, or muscle contraction in the case of seizure. Acute dislocation may lead to instability, and surgery may be necessary. Acute posterior dislocation can be missed clinically, and lead to a later presentation of frozen shoulder. Anterior dislocation patients may develop Bankhart and Hill-Sachs lesions [3, 4]. The classic Bankart lesion is an anterior labral tear/detachment which extends through periosteum, and may involve the bony glenoid or just the labrum. The classic Hill-Sachs lesion is an impaction injury of the posterolateral humeral head, caused by contact of the

humerus against the anterior rim of the bony glenoid. Posterior dislocation patients, as discussed below, may suffer similar injuries, but in opposite locations due to opposite dislocation direction. This has given rise to lesions named 'reverse Bankhart' and 'reverse Hill-Sachs'.

### Clinical presentation

Symptoms of a labral tear depend on where the tear is located, but may include:

- Nonlocalized pain
- Catching sensation with movement
- Popping and clicking
- Pain with specific activities
- Pain with overhead activities or when the arm is held behind the back.
- Weakness
- Joint instability
- Pain with flexion of the biceps

Posterior labral injuries are much more common with football players than in the general population [5]. In addition, similar injuries occur in non-football players whose shoulders are likely subjected to a similar posteriorly directed force leading to posterior translation of the humeral head relative to the glenoid. Many posterior labral tears result from multiple episodes of microtrauma, and weight training such as bench pressing may be an important causative factor.

### Imaging

Non-contrast MRI has historically been considered less accurate than MR arthrography for depiction of small labroligamentous lesions associated with shoulder dislocation [6]. Early in development and experience of shoulder MRI and understanding of shoulder MRI anatomy on low to high field strength scanners, noncontrast MRI has been reported to have sensitivities of 67–86% and specificities of 44–95% in the diagnosis of glenoid labral tears, while MR arthrography has been reported to have sensitivities of 90–95% and specificities of 67–86%. However with increased understanding and experience with shoulder MRI anatomy and pathology, and improved MRI sequences and shoulder coils, current high field 1.5T and newer 3T noncontrast MRI techniques are highly accurate. MR arthrography, with its risk and discomfort, is no longer necessary for most shoulder MR imagers and patients.

### MRI findings

Using MRI, findings related to posterior instability are typically the reverse of those for anterior instability. Tearing or detachment of the posterior glenoid labrum is common [2]. Capsular detachment or stripping may also be seen, as evidenced by disruption or stretching/laxity of the normal, well defined continuous low signal capsule line connecting the glenoid and labral margin to the humeral neck. There may be bony impaction or fragmentation of the posterior glenoid rim and the anterior humeral head, which are the characteristic reverse Bankhart and reverse Hill-Sachs lesions. There may be a tear of the posterior band of the inferior glenohumeral ligament. There is also an association with teres minor tears (may tear along with the posterior band of the IGHL), and internal bodies in the glenohumeral joint.

There may also be associated rotator cuff injury. Glenoid erosive changes, sclerosis, or heterotopic bone formation may be seen chronically. There may be soft-tissue findings of associated edema, hematoma, or extravasated joint fluid.

The humeral head may be posteriorly subluxed in relation to the glenoid. In chronic cases, there may be bone loss and remodeling with retroversion of the glenoid, although there is a reported wide normal range of glenoid inclination from 25° retroversion to 8° anteversion. Age-related changes are frequently found in the glenoid labrum, and labral tears are not uncommon in cadavers and older patients. Senescent changes on MRI may be diffusely increased labral signal and fraying. Location, patient age, and clinical presentation should always be part of surgical decision-making. Paralabral cysts can be classified as synovial cysts, ganglion cysts, or pseudocysts [7]. They may be unilocular or multilocular, and are nearly always related to a nearby labral tear, although

the tear may not always be seen. Paralabral cysts extending into the suprascapular notch or spinoglenoid notch may cause entrapment of the suprascapular nerve, which may lead to supraspinatus and infraspinatus muscle denervation atrophy for more proximal entrapment (suprascapular notch lesions or proximal spinoglenoid notch lesions extending along the supraspinatus fossa of the scapula). Isolated infraspinatus atrophy may occur for more distal lesions (inferior aspect of spinoglenoid notch extending into the infraspinatus fossa of the scapula). Rarely, a large inferior cyst extending into the quadrilateral space may impinge on the axillary nerve and cause teres minor atrophy and deltoid atrophy. In the absence of pain, paralabral cysts are treated conservatively.

### Labral abnormalities associated with posterior shoulder joint instability

#### Bennett lesion

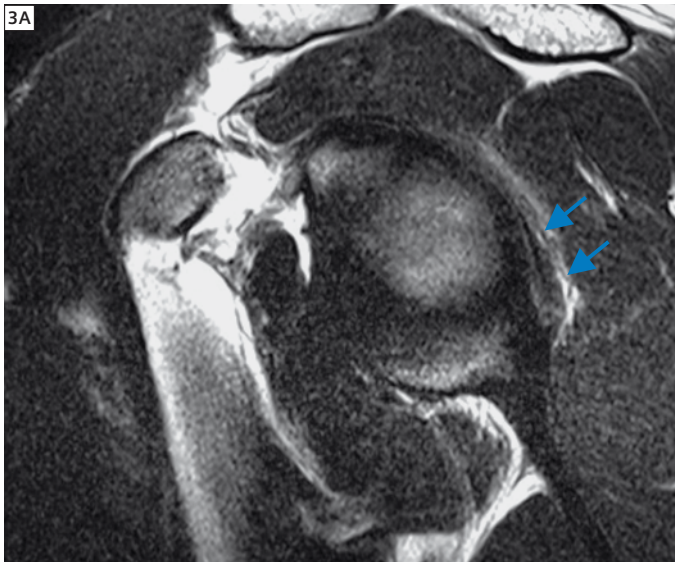
The Bennett lesion represents an enthesophyte arising from the posterior portion of the glenoid rim, which is commonly seen in baseball pitchers.

#### POLPSA lesion

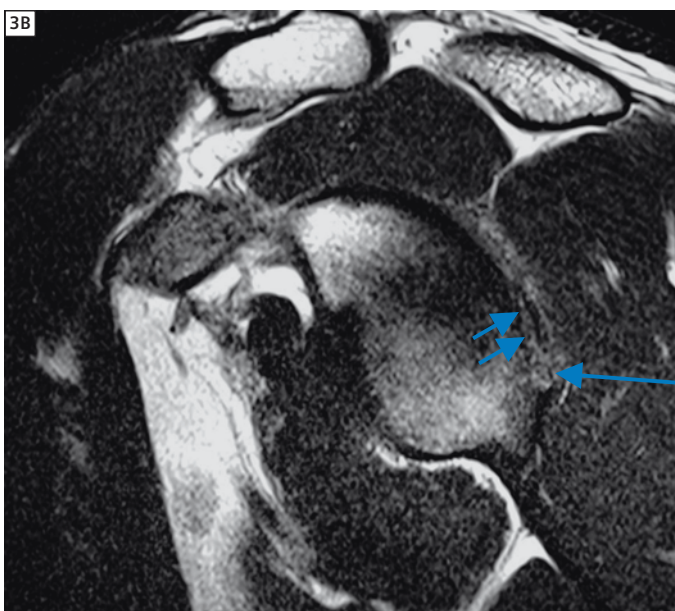
The posterior labrocapsular periosteal sleeve avulsion (POLPSA) lesion is the posterior analogue of the anterior labroligamentous periosteal sleeve avulsion (ALPSA). It is associated with posterior instability. Wherein the reverse Bankart lesion the periosteum is torn, the periosteum is stripped but intact in a POLPSA lesion.

**Table 1: MRI technique**

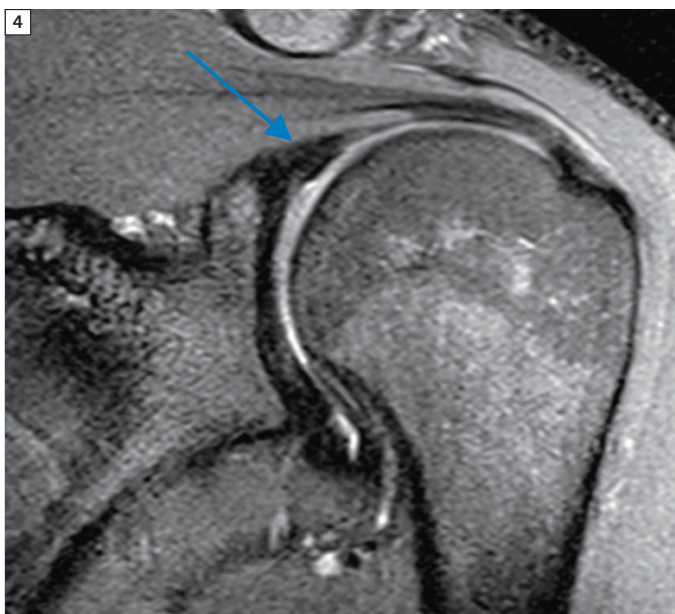
Weighting and planes	Field-of-view	TR	TE	Sequence	Slice thickness	Gap	Matrix size
T2-weighted axial	120	650	7.5	Gradient Echo	3 mm	0.3 mm	512 x 512
Proton Density-weighted axial fat suppressed	120	3350	46	Turbo Spin Echo fat suppressed	3 mm	0.3 mm	512 x 512
Proton Density-weighted sagittal	120	4000	93	Turbo Spin Echo	2 mm	0.3 mm	640 x 640
Proton Density-weighted sagittal fat suppressed	120	3000	46	Turbo Spin Echo fat suppressed	2 mm	0.3 mm	512 x 512
Proton Density-weighted coronal	120	2510	34	Turbo Spin Echo	3 mm	0.3 mm	768 x 768
Proton Density-weighted coronal fat suppressed	120	3000	46	Turbo Spin Echo fat suppressed	2 mm	0.3 mm	512 x 512



**3A** Sagittal T2-weighted image (20/25) showing a tear through the posterior labrum (short arrows).



**3B** Sagittal T2-weighted image (21/25) showing truncation of the posterior glenoid margin (short arrows), and adjacent capsulolabral avulsion (long arrow).



**4** Coronal fat suppressed proton density-weighted image (13/25) showing sparing of the superior labrum (arrow).

## Limitations of MRI

Variable labral shape can cause false diagnosis of labral tear. Glenohumeral ligaments can be confused with torn or detached labrum. Articular cartilage at the base of the labral attachment, can exhibit intermediate to high T2 signal, and occasionally be mistaken for labral tear or detachment.

## References

- 1 Medscape Reference: Glenoid Labrum Injury MRI. Author: Ali Nawaz Khan, MBBS, FRCS, FRCP, FRCR; Chief Editor: Felix S Chew, MD, MBA, EdM.
- 2 Medscape Reference: Shoulder Dislocation Imaging. Author: Gavin Yeh Tseng, MBBS, FRCR, FRANZCR; Chief Editor: Felix S Chew, MD, MBA, EdM.
- 3 Hill HA, Sachs MD. The grooved defect of the humeral head: a frequently unrecognized complication of dislocations of the shoulder joint. *Radiology* 1940; 35:690-700.
- 4 Bankart ASB. Recurrent or habitual dislocation of the shoulder-joint. *Br Med J* 1923; 2: 1132-3.
- 5 Increased Risk of Posterior Glenoid Labrum Tears in Football Players. Eva M. Escobedo et al. *AJR* January 2007 vol. 188 no. 1 193-197.
- 6 Chandnani VP, Yeager TD, DeBerardino T, et al. Glenoid labral tears: prospective evaluation with MRI imaging, MR arthrography, and CT arthrography. *AJR Am J Roentgenol.* Dec 1993;161(6):1229-35.
- 7 Paralabral cyst associated with posterior labral tear, Justin Q. Ly, MD and Douglas P. Beall, MD, *Applied Radiology*, Volume 32, Number 11, November 2003.

## Contact

Charles P. Ho, Ph.D., M.D.  
Steadman Philippon Research Institute  
181 W. Meadow Dr. Suite 1000  
Vail, CO 81657  
USA  
Karen.briggs@sprivail.org

# Musculoskeletal Advisory Board Provides Protocols for 1.5 and 3T MAGNETOM systems

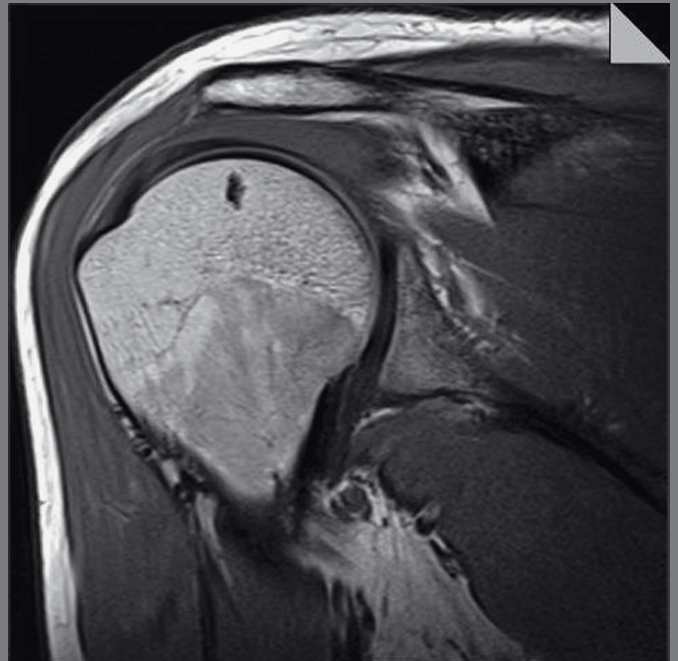
We have launched the MSK Advisory Board website, providing proven MSK protocols (.edx files) for download. To support Technologists there are also coil positioning videos and tips & tricks.

## Board members are:

- Christian Glaser, LMU Grosshadern, Germany
- Jürg Hodler, Balgrist University Hospital, Switzerland
- Young-Jo Kim, Harvard Medical School, Children's Hospital Boston, USA
- Tallal Charles Mamisch, Bern University, Switzerland
- Michael Recht, New York University, USA
- Siegfried Trattnig, AKH Wien, Austria
- Lawrence M. White, University of Toronto, Canada

Visit us at

[www.siemens.com/magnetom-world](http://www.siemens.com/magnetom-world)



# Myocardial T1-Mapping: Techniques and Clinical Applications

Juliano Lara Fernandes<sup>1</sup>; Ralph Strecker<sup>2</sup>; Andreas Greiser<sup>3</sup>; Jose Michel Kalaf<sup>1</sup>

<sup>1</sup>Radiologia Clinica de Campinas; University of Campinas, Brazil

<sup>2</sup>Healthcare MR, Siemens Ltda, Sao Paulo, Brazil

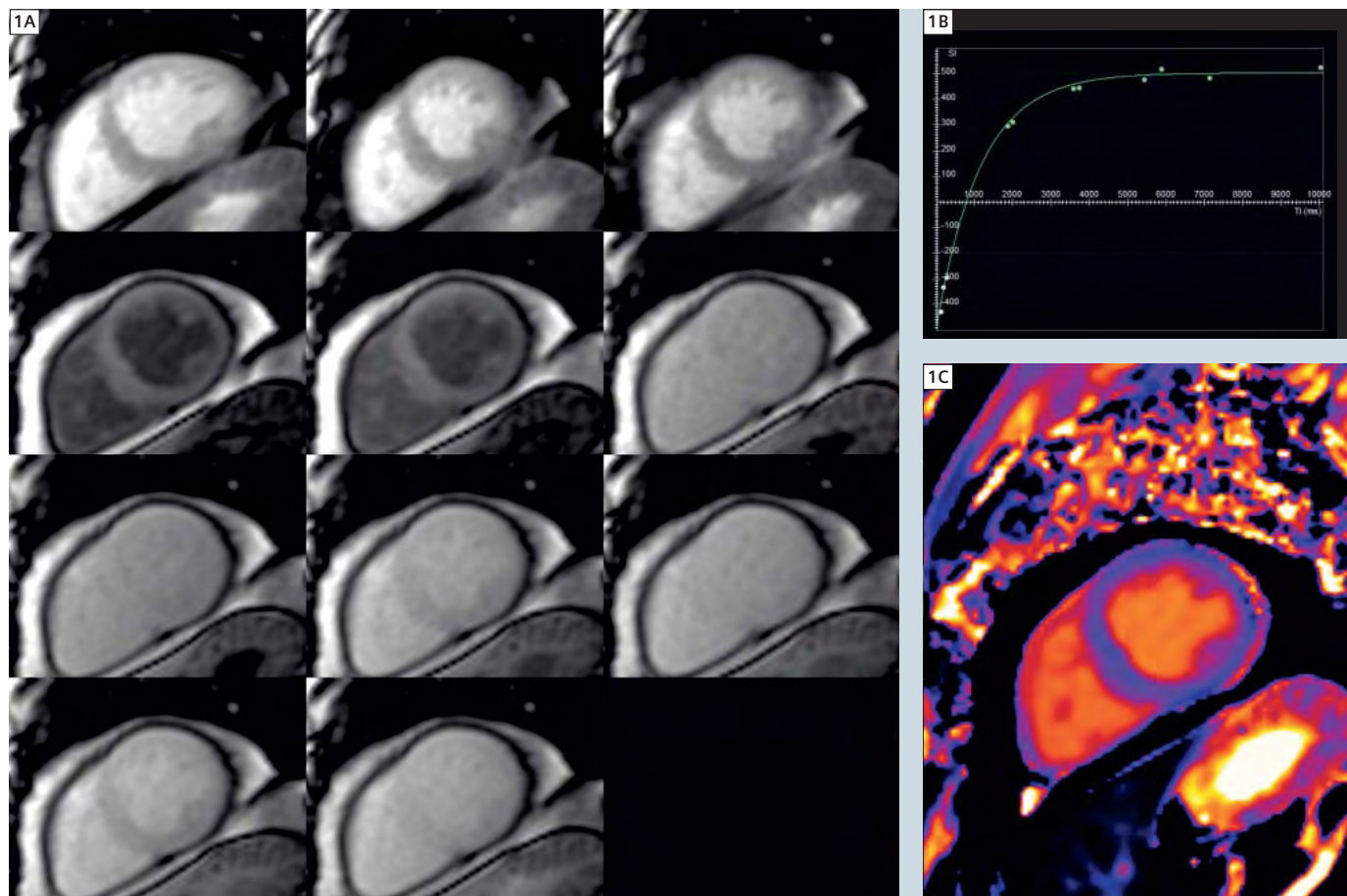
<sup>3</sup>MR Cardiology, Siemens Healthcare, Erlangen, Germany

## Introduction

Cardiovascular magnetic resonance (CMR) has been an increasingly used imaging modality which has experienced significant advancements in the last years [1]. One of the most used

techniques that have made CMR so important is late gadolinium enhancement (LGE) and the demonstration of localized areas of infarct and scar tissue [2–4]. However, despite being very sen-

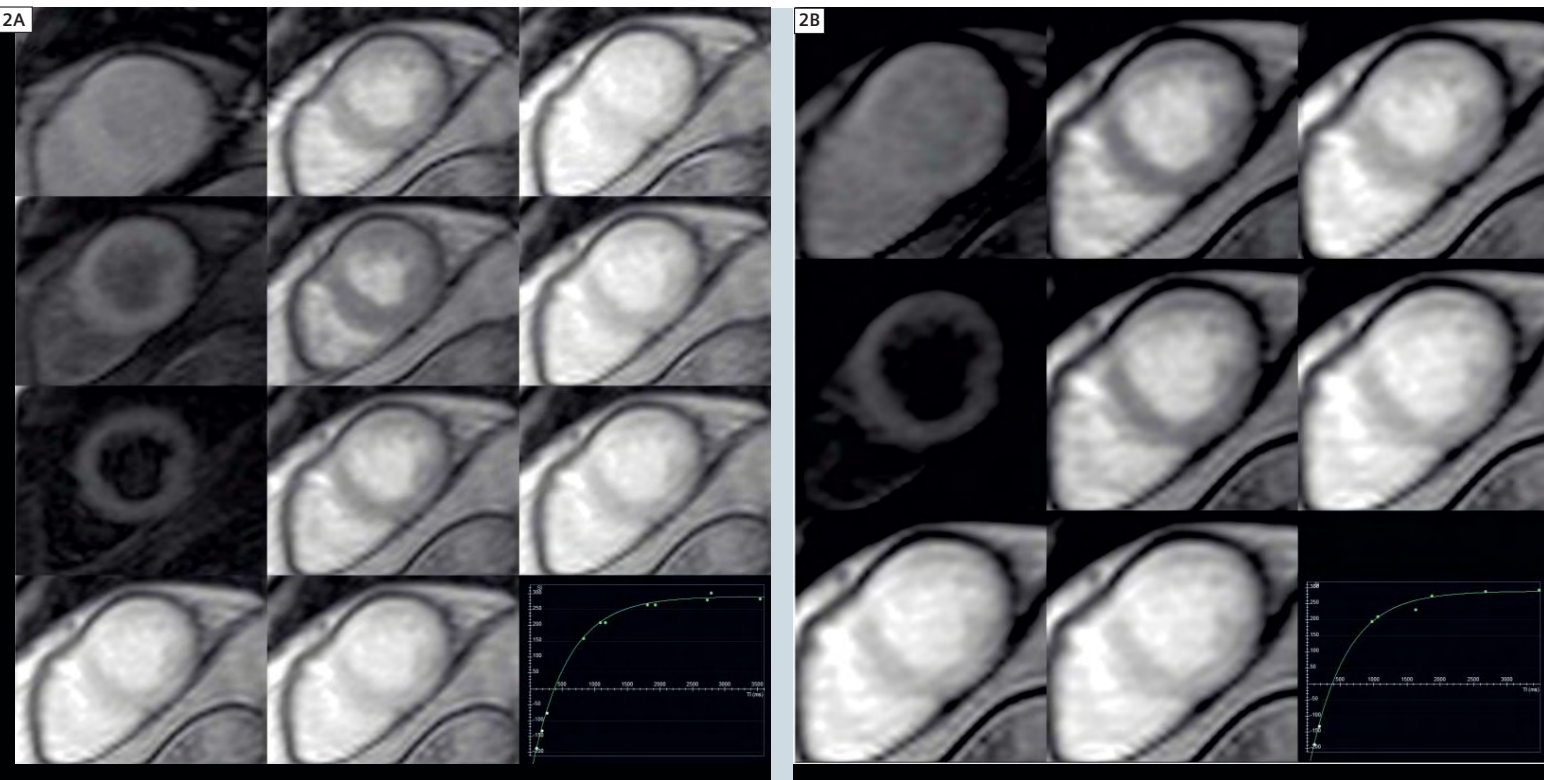
sitive to small areas of regional fibrosis, LGE techniques are mostly dependent on the comparison to supposedly normal reference areas of myocardium, thus not being able to depict more diffuse disease.



**1** MOLLI images (1A) with respective signal-time curves (1B) and reconstructed T1 map (1C) at 3T. The mean T1 time for this patient was 1152 ms (pre-contrast).

**Table 1: Comparison of the MOLLI sequences available for T1-mapping:**

Sequence	Original MOLLI T1 sequence [15]	Optimized MOLLI sequence [17]	Shortened MOLLI sequence [18]
Preparation	Non-selective inversion recovery	Non-selective inversion recovery	Non-selective inversion recovery
Bandwidth	1090 Hz/px	1090 Hz/px	1090 Hz/px
Flip angle	50°	35°	35°
Base matrix	240	192	192
Phase resolution	151	128	144
FOV x % phase	380 x 342	256 x 100	340 x 75
TI	100 ms	100 ms	100 ms
Slice thickness	8 mm	8 mm	8 mm
Acquisition window	191.1 ms	202 ms	206 ms
Trigger delay	300 ms	300 ms	500 ms
Inversions	3	3	3
Acquisition heartbeats	3,3,5	3,3,5	5,5,1
Recovery heartbeats	3,3,1	3,3,1	1,1,1
TI increment	100–150 ms	80 ms	80 ms
Scan time	17 heartbeats	17 heartbeats	9 heartbeats
Spatial resolution	2.26 x 1.58 x 8 mm	2.1 x 1.8 x 8 mm	1.8 x 1.8 x 8 mm



**2** MOLLI (2A) versus ShMOLLI (2B) in a single patient at 3T post-contrast. The calculated values for the 11 MOLLI images were 551 ms versus 544 ms for the 8 images of the shMOLLI set. The time to acquire the MOLLI images were 21 seconds versus 14 seconds for the shMOLLI sequence (with a patient heart rate of 61 bpm).

Myocardial interstitial fibrosis, with a diffuse increase in collagen content in myocardial volume, develops as a result of many different stimuli including pressure overload, volume overload, aging, oxidative stress and activation of the sympathetic and renin-angiotensin-aldosterone system [5]. Different from replacement fibrosis, where regional collagen deposits appear in areas of myocyte injury, LGE has a limited sensitivity for interstitial diffuse fibrosis [6]. Therefore, if one wants to image diffuse interstitial fibrosis within the myocardium other techniques might be more suitable. While echocardiogram backscatter and nuclear imaging techniques may be applied for that purpose [7, 8], myocardial tissue characterization is definitely an area where CMR plays a large role. While equilibrium contrast CMR and myocardial tagging have been shown to reflect diffuse myocardial fibrosis,

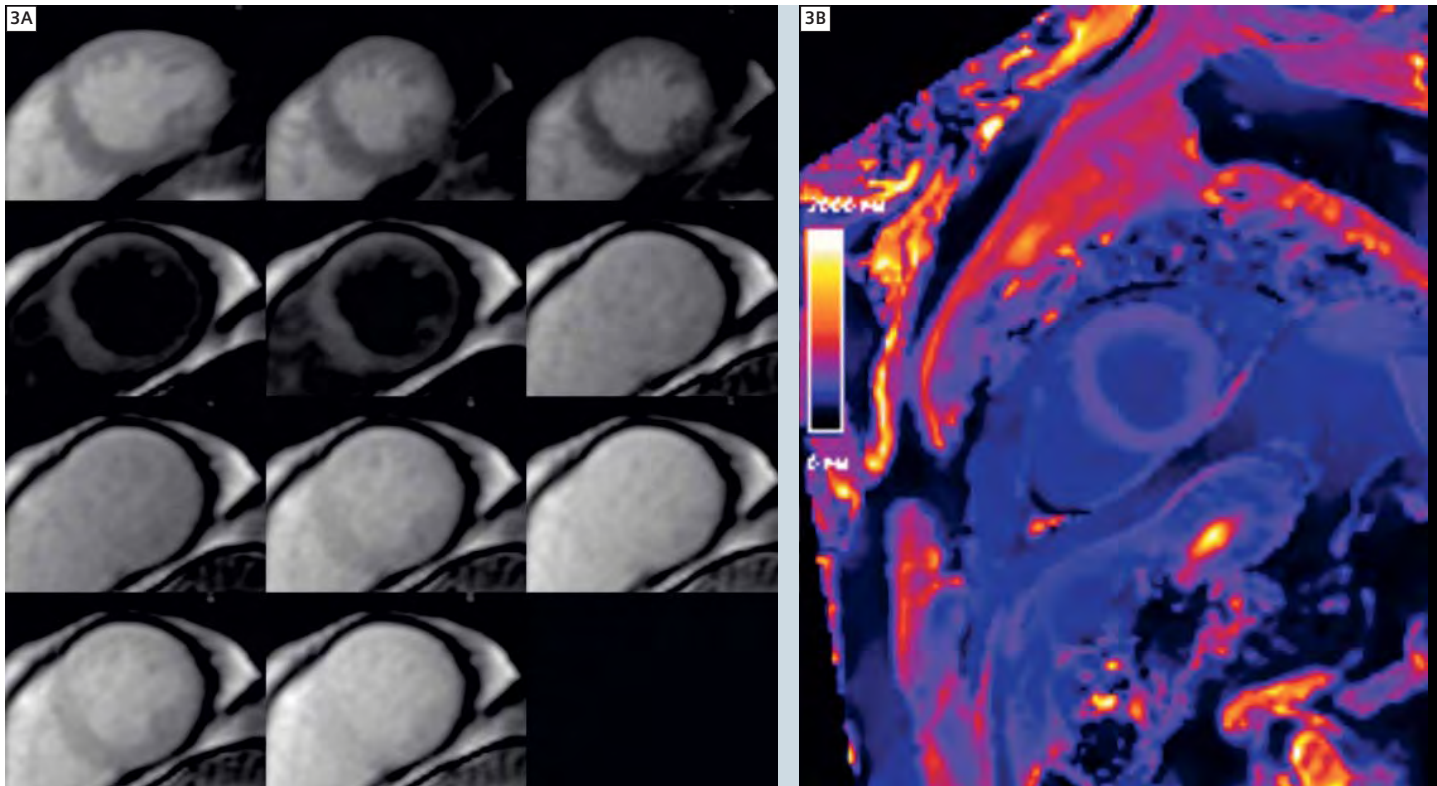
T1-mapping techniques have been most widely used. In the following, we describe the developments in T1-mapping as well as their possible current and future uses.

### T1-mapping

By directly quantifying T1 values for each voxel in the myocardium, a parametric map can be generated representing the T1 relaxation times of any region of the heart without the need to compare it to a normal reference standard before or after the use of a contrast agent. The first attempts to measure T1 times in the myocardium used the original Look-Locker sequence and were done using free breathing with acquisition times of over 1 minute per image [9, 10], not allowing for pixel-based-mapping but only for regions-of-interest analysis. Another implementation of T1-mapping used variable sampling of

the k-space in time (VAST), acquiring images in three to four breath-holds and correlating that data to invasive biopsy [11]. Other sequences have been used for quantification of T1 as well using inversion recovery TrueFISP [12, 13] or multishot saturation recovery images [14] but their reproducibility and accuracy have not been extensively validated.

The most widely used T1-mapping sequence is based on the Modified Look-Locker Inversion-recovery (MOLLI) technique. Described originally by Messroghli et al. [15] it consists of a single shot TrueFISP image with acquisitions over different inversion time readouts allowing for magnetization recovery of a few seconds after 3 to 5 readouts. The parameters for the original MOLLI sequence are described in Table 1. The advantages of this sequence over previous methods are its acquisition in only

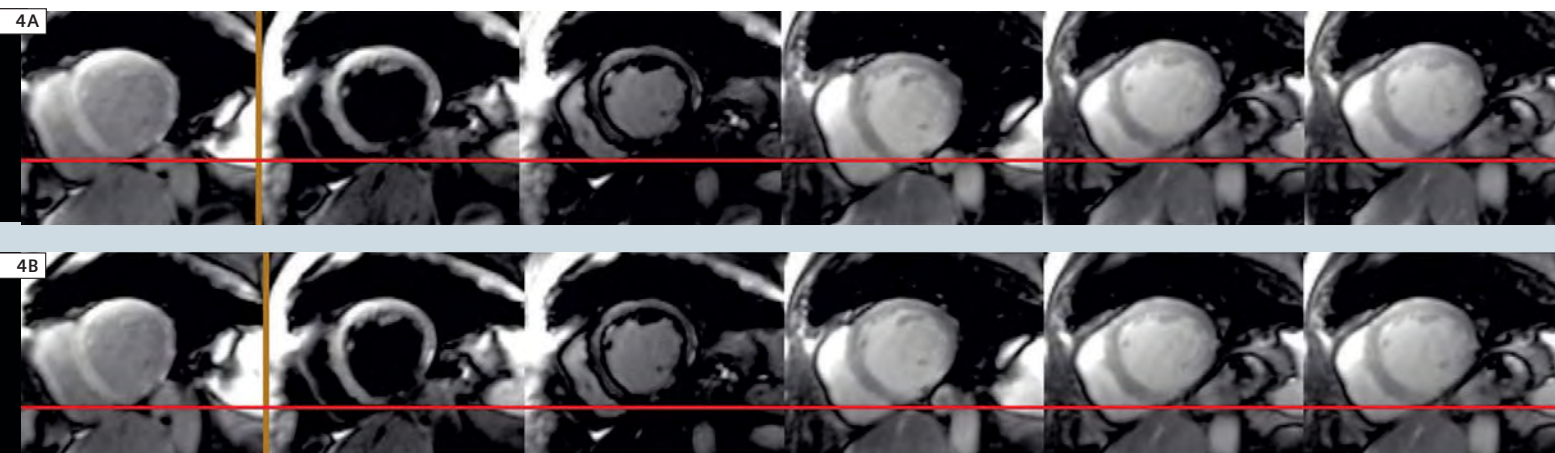


**3** An example of an automated T1-map generated on the fly with inline processing after acquisition of a MOLLI sequence at 3T. In (3A) the original images acquired and in (3B) the inline map. The T1 for this patient was calculated at 525 ms post-contrast.

one relatively short breath-hold, the higher spatial resolution ( $1.6 \times 2.3 \times 8$  mm) and increased dynamic signal. Reproducibility studies using this sequence have shown that the method is very accurate with a coefficient of variation of 5.4% [16] although an underestimation of 8% should be expected based on phantom data. An example of MOLLI images and its respective signal-time curves and map are shown in Figure 1. One disadvantage of this implementation of MOLLI is its dependence on heart rate, mostly true for T1 values less than 200 msec or greater than 750 msec. However, because the deviation is systematic, raw values can be corrected using the formula  $T1_{corrected} = T1_{raw} - (2.7 \times [\text{heart rate} - 70])$ , bringing the coefficient of variation down to 4.6% after applying the correction. An optimized MOLLI sequence was subsequently described

where heart rate correction might not be even necessary [17]. In the optimized sequence, the authors tested variations in readout flip angle, minimum inversion time, inversion time increments and number of pauses between each readout sequence. The conclusion from these experiments showed that a flip angle of  $35^\circ$ , a minimum inversion time of 100 msec, increments of 80 msec and three heart cycle pauses allowed for the most accurate measurement of myocardial T1 (Table 1). Because T1 assessment may be sensitive to motion artifacts and not all patients might be able to hold their breaths throughout all the necessary cardiac cycles used in MOLLI's sequence implementation, more recently a shortened version sequence (ShMOLLI) using only 9 heart beats was presented to account for those limitations [18]. Using incomplete recovery of the longitudinal magnetization that is

corrected directly in the scanner by conditional interpretation, ShMOLLI was directly compared to MOLLI in patients over a wide range of T1 times and heart rates both at 1.5 and 3T. The results showed that despite an increase in noise and slight increase in the coefficient of variation (especially at 1.5T), T1 times were not significantly different using ShMOLLI with the advantage of much shorter acquisition times ( $9.0 \pm 1.1$  sec versus  $17.6 \pm 2.9$  sec). An example of MOLLI and ShMOLLI images from the same patient is presented in Figure 2. Up to now, after acquiring images for T1-mapping, one had to analyze them using in-house developed software, dedicated commercial programs or open-source solutions [19], not always a simple and routine task, leading to difficulty in post-processing the data and generating T1 values. Recent advances have provided new inline processing



techniques that will generate the T1-maps automatically after image acquisition with MOLLI, without the need for further post-processing, accelerating the whole process. An example of such automated T1-map is presented in Figure 3. At the same time, inline application of motion correction permits more accurate pixel-wise maps, avoiding errors due to respiratory deviations. An example of an image with and without motion correction is presented in Figure 4.

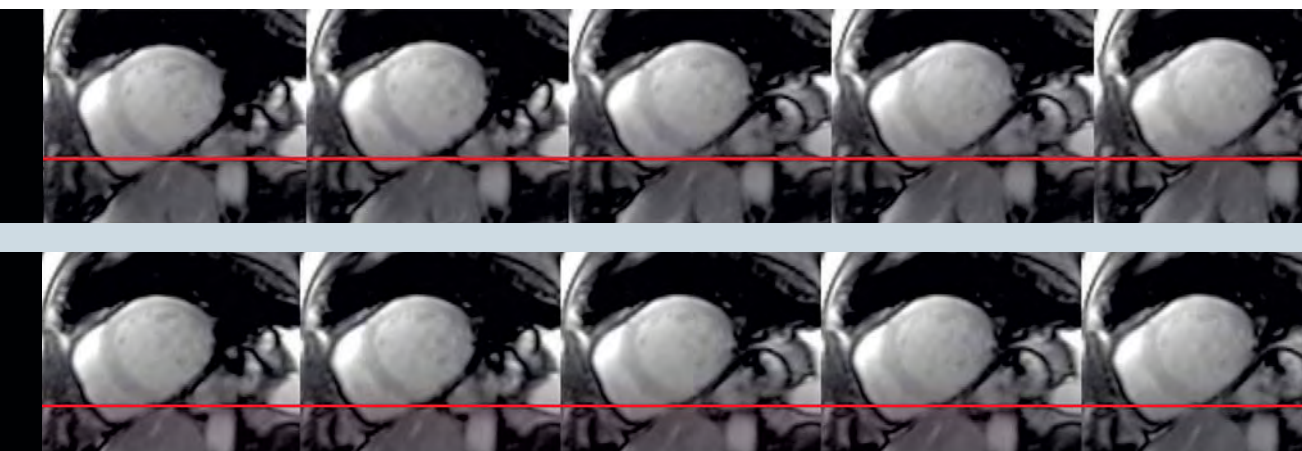
### Clinical applications

Potentially, T1-mapping can be used to assess any disease that affects the myocardium promoting diffuse fibrosis. However, because of its recent development, the technique has only been evaluated on a small number of patients although the clinical scenarios are varied. The first clinical description of direct T1-mapping in pathological situations was done in patients with acute myocardial infarction [20]. While the authors did not use the described MOLLI sequence, they did note that pre-contrast infarct areas had an  $18 \pm 7\%$  increase in T1 times compared to normal myocardium and that after contrast the same areas showed a  $27 \pm 4\%$  reduction compared to non-infarcted areas ( $P < 0.05$  for both). In chronic myocardial

infarction, where LGE has proven so useful, these changes were also observed although differences were not as pronounced as in the acute setting [21]. In amyloidosis, post-contrast T1 times were also detected to be shorter in the subendocardial regions compared to other myocardium areas [22]. The combination of both LGE identification and T1 times  $< 191$  msec in the subendocardium at 4 minutes provided a 97% concordance in diagnosis of cardiac amyloidosis and T1 values significantly correlated to markers of amyloid load such as left ventricular mass, wall thickness, interatrial thickness and diastolic function.

In valve disease, an attempt to show differences in T1 values in patients with chronic aortic regurgitation using MOLLI sequence did not find any changes in the overall group before or after contrast [23]. However, the authors did notice that differences were observed regionally in segments that demonstrated impaired wall motion in cine images. The small number of patients ( $n = 8$ ) in the study might have affected the conclusions and further evaluation of similar data might yield other conclusions. A more recent study showed that, using equilibrium contrast CMR, diffuse fibrosis measured in aortic stenosis patients provided significant correlations to

quantification on histology [24]. In heart failure, the use of T1-mapping has been more widely studied and directly correlated to histology evaluation [11]. In this paper, the authors evaluated patients with ischemic, idiopathic and restrictive cardiomyopathies showing that post-contrast T1 times at 1.5T were significantly shorter than controls even after exclusion of areas of LGE ( $429 \pm 22$  versus  $564 \pm 23$  msec,  $P < 0.0001$ ). We have investigated a similar group of patients on a 3T MAGNETOM Verio scanner and have found that both dilated and hypertrophic cardiomyopathy patients have lower post-contrast T1 times compared to controls, but non-infarcted areas from ischemic cardiomyopathy patients do not show significant differences (unpublished data). Examples of a myocardial T1-map at 3T from a patient with dilated cardiomyopathy and suspected hypertrophic cardiomyopathy are seen in Figure 5 and 6 respectively. Finally, in patients with both type 1 and 2 diabetes melitus, T1-mapping using CMR was able to show that these patients may have increased interstitial fibrosis compared to controls as T1 times were significantly shorter ( $425 \pm 72$  msec versus  $504 \pm 34$  msec,  $P < 0.001$ ) and correlated to global longitudinal strain by echocardiography, demonstrating impaired myocardial systolic function.



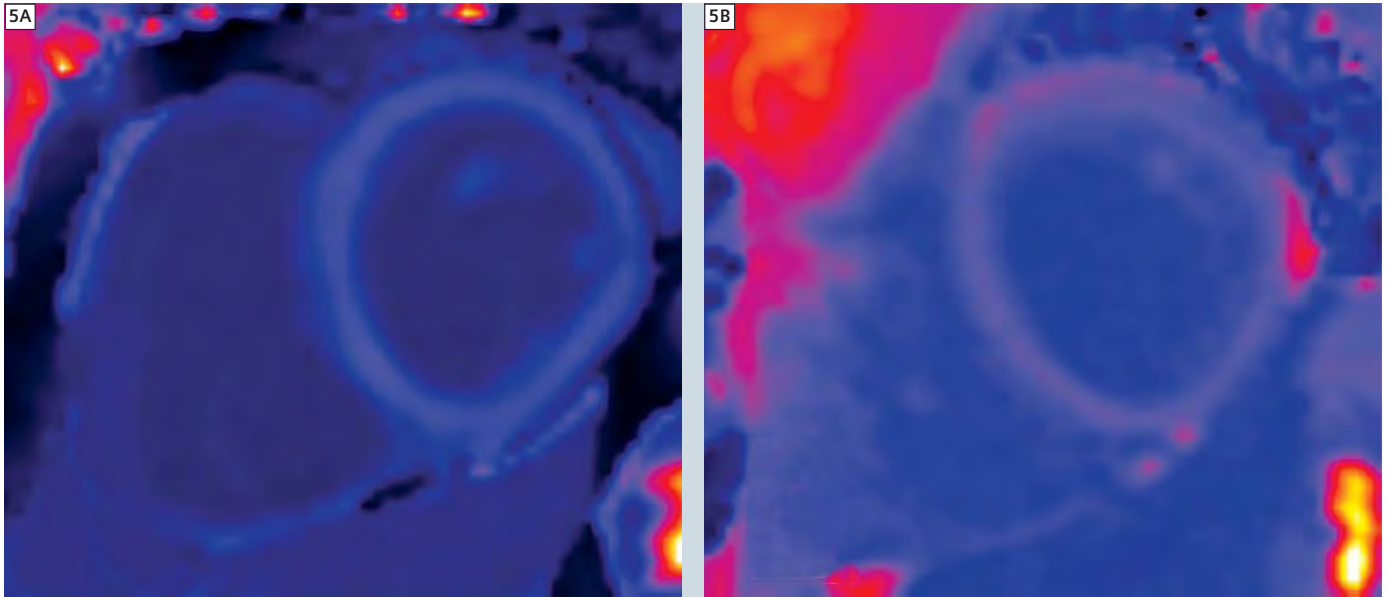
**4** Example of a MOLLI sequence obtained without (4A) and with (4B) motion correction. Notice the deviation from baseline of the left ventricle during the image acquisition cycle, fully corrected in (4B).

## Future directions

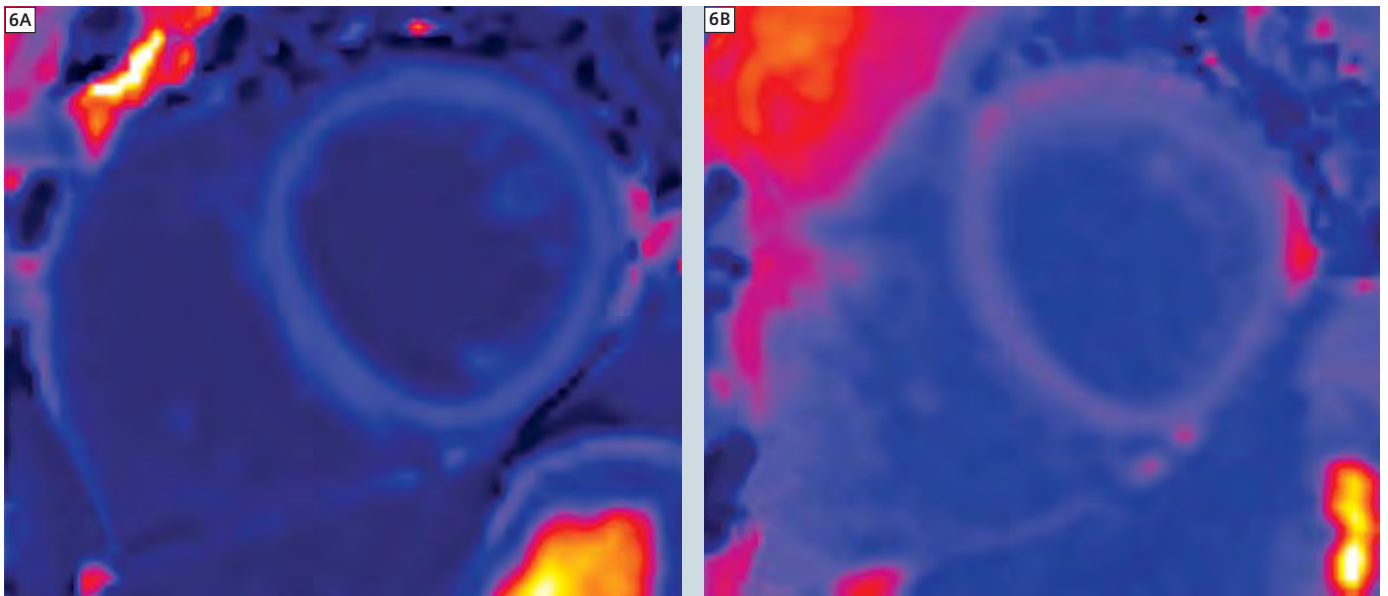
Certainly with the research of T1-mapping in different clinical scenarios the applicability of the method will increase substantially. In the meantime, more effort has been made to further standardize values across different patients and time points. As T1 time, especially after injection of contrast, depends on both physiologic and scan acquisitions, methods have been described to account for these factors, with normalization of T1 values [25]. More than that, standardization of normal values across a larger number of normal individuals is also necessary since most papers provide data on much reduced cohorts, mostly limited to single center data. In that regard, a large multicenter registry is already collecting data at 3T in patients from 20 to 80 years of age in Latin America [Fernandes JL et al. – [www.clinicaltrials.gov](http://www.clinicaltrials.gov) – NCT01030549]. Besides that, other techniques are under development that might allow T1 measurement with larger coverage of the heart using 3D methods [26]. Nevertheless, with the current techniques available there are already much more clinical applications to explore and certainly quantitative T1-mapping will become one of the key applications in CMR in the near future.

## References

- Fernandes JL, Pohost GM. Recent advances in cardiovascular magnetic resonance. *Rev Cardiovasc Med* 2011;12:e107-12.
- Kim RJ, Wu E, Rafael A, et al. The use of contrast-enhanced magnetic resonance imaging to identify reversible myocardial dysfunction. *N Engl J Med* 2000;343:1445-53.
- Assomull RG, Prasad SK, Lyne J, et al. Cardiovascular magnetic resonance, fibrosis, and prognosis in dilated cardiomyopathy. *J Am Coll Cardiol* 2006;48:1977-85.
- Ordovas KG, Higgins CB. Delayed contrast enhancement on MR images of myocardium: past, present, future. *Radiology* 2011;261:358-74.
- Jellis C, Martin J, Narula J, Marwick TH. Assessment of nonischemic myocardial fibrosis. *J Am Coll Cardiol* 2010;56:89-97.
- Mewton N, Liu CY, Croisille P, Bluemke D, Lima JA. Assessment of myocardial fibrosis with cardiovascular magnetic resonance. *J Am Coll Cardiol* 2011;57:891-903.
- Picano E, Pelosi G, Marzilli M, et al. In vivo quantitative ultrasonic evaluation of myocardial fibrosis in humans. *Circulation* 1990;81:58-64.
- van den Borne SW, Isobe S, Verjans JW, et al. Molecular imaging of interstitial alterations in remodeling myocardium after myocardial infarction. *J Am Coll Cardiol* 2008;52:2017-28.
- Flacke SJ, Fischer SE, Lorenz CH. Measurement of the gadopentetate dimeglumine partition coefficient in human myocardium in vivo: normal distribution and elevation in acute and chronic infarction. *Radiology* 2001;218:703-10.
- Brix G, Schad LR, Deimling M, Lorenz WJ. Fast and precise T1 imaging using a TOMROP sequence. *Magn Reson Imaging* 1990;8:351-6.
- Iles L, Pfluger H, Phrommintikul A, et al. Evaluation of diffuse myocardial fibrosis in heart failure with cardiac magnetic resonance contrast-enhanced T1 mapping. *J Am Coll Cardiol* 2008;52:1574-80.
- Schmitt P, Griswold MA, Jakob PM, et al. Inversion recovery TrueFISP: quantification of T(1), T(2), and spin density. *Magn Reson Med* 2004;51:661-7.
- Bokacheva L, Huang AJ, Chen Q, et al. Single breath-hold T1 measurement using low flip angle TrueFISP. *Magn Reson Med* 2006;55:1186-90.
- Wacker CM, Bock M, Hartlep AW, et al. Changes in myocardial oxygenation and perfusion under pharmacological stress with dipyridamole: assessment using T\*2 and T1 measurements. *Magn Reson Med* 1999;41:686-95.
- Messroghli DR, Radjenovic A, Kozerke S, Higgins DM, Sivananthan MU, Ridgway JP. Modified Look-Locker inversion recovery (MOLLI) for high-resolution T1 mapping of the heart. *Magn Reson Med* 2004;52:141-6.
- Messroghli DR, Plein S, Higgins DM, et al. Human myocardium: single-breath-hold MR T1 mapping with high spatial resolution--reproducibility study. *Radiology* 2006;238:1004-12.
- Messroghli DR, Greiser A, Frohlich M, Dietz R, Schulz-Menger J. Optimization and validation of a fully-integrated pulse sequence for modified look-locker inversion-recovery (MOLLI) T1 mapping of the heart. *J Magn Reson Imaging* 2007;26:1081-6.
- Piechnik SK, Ferreira VM, Dall'Armellina E, et al. Shortened Modified Look-Locker Inversion recovery (ShMOLLI) for clinical myocardial T1-mapping at 1.5 and 3 T within a 9 heartbeat breath-hold. *J Cardiovasc Magn Reson* 2010;12:69.
- Messroghli DR, Rudolph A, Abdel-Aty H, et al. An open-source software tool for the generation of relaxation time maps in magnetic resonance imaging. *BMC Med Imaging* 2010;10:16.
- Messroghli DR, Niendorf T, Schulz-Menger J, Dietz R, Friedrich MG. T1 mapping in patients with acute myocardial infarction. *J Cardiovasc Magn Reson* 2003;5:353-9.
- Messroghli DR, Walters K, Plein S, et al. Myocardial T1 mapping: application to patients with acute and chronic myocardial infarction. *Magn Reson Med* 2007;58:34-40.
- Maceira AM, Joshi J, Prasad SK, et al. Cardiovascular magnetic resonance in cardiac amyloidosis. *Circulation* 2005;111:186-93.
- Sparrow P, Messroghli DR, Reid S, Ridgway JP,



**5** T1-mapping at 3T after contrast of a patient with (5A) dilated cardiomyopathy (T1 of 507 ms) in comparison to (5B) a control patient (T1 of 615 ms).



**6** T1-mapping of a patient with (6A) suspected hypertrophic cardiomyopathy (T1 of 466 ms) in comparison to (6B) a control patient (with a T1 of 615 ms).

Bainbridge G, Sivananthan MU. Myocardial T1 mapping for detection of left ventricular myocardial fibrosis in chronic aortic regurgitation: pilot study. *AJR Am J Roentgenol* 2006;187:W630-5.

24 Flett AS, Hayward MP, Ashworth MT, et al. Equilibrium contrast cardiovascular magnetic resonance for the measurement of diffuse myocardial fibrosis: preliminary validation in humans. *Circulation* 2010;122:138-44.

25 Gai N, Turkbey EB, Nazarian S, et al. T1 mapping of the gadolinium-enhanced myocardium: adjustment for factors affecting interpatient comparison. *Magn Reson Med* 2011;65:1407-15.

26 Coolen BF, Geelen T, Paulis LE, Nauerth A, Nicolay K, Strijkers GJ. Three-dimensional T1 mapping of the mouse heart using variable flip angle steady-state MR imaging. *NMR Biomed* 2011;24:154-62.

#### Contact

Juliano L Fernandes  
R. Antonio Lapa 1032  
Campinas-SP – 13025-292  
Brazil  
Phone: +55-19-3579-2903  
Fax: +55-19-3252-2903  
jlaraf@fcm.unicamp.br

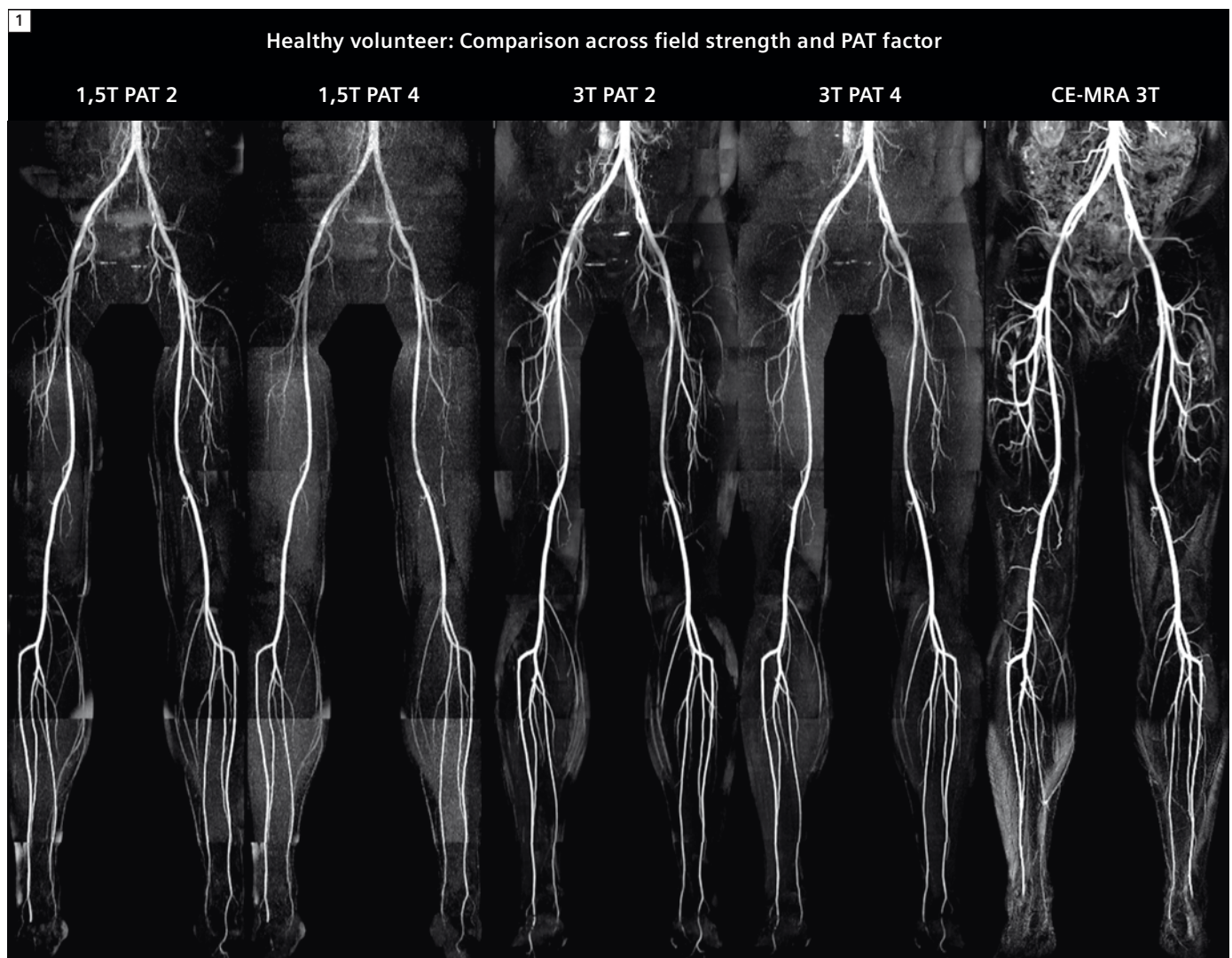
# High Acceleration Quiescent-Interval Single Shot Magnetic Resonance Angiography at 1.5 and 3T

Maria Carr R.T.R (CT)(MR)<sup>1</sup>; Christopher Glielmi, Ph.D.<sup>2</sup>; Robert R. Edelman, M.D.<sup>3</sup>; Michael Markl, Ph.D.<sup>1</sup>; James Carr, M.D.<sup>1</sup>; Jeremy Collins, M.D.<sup>1</sup>

<sup>1</sup>Northwestern Memorial Hospital and Northwestern University Feinberg School of Medicine, Chicago, IL, USA

<sup>2</sup>Cardiovascular MR R&D, Siemens Healthcare, Chicago, IL, USA

<sup>3</sup>NorthShore University HealthSystem, Evanston, IL, USA



**1** QISS maintains excellent image quality with PAT 4 acquisition. 3T imaging demonstrates higher SNR and potentially better results at high PAT factors. All protocols have high correlation to CE-MRA (right).

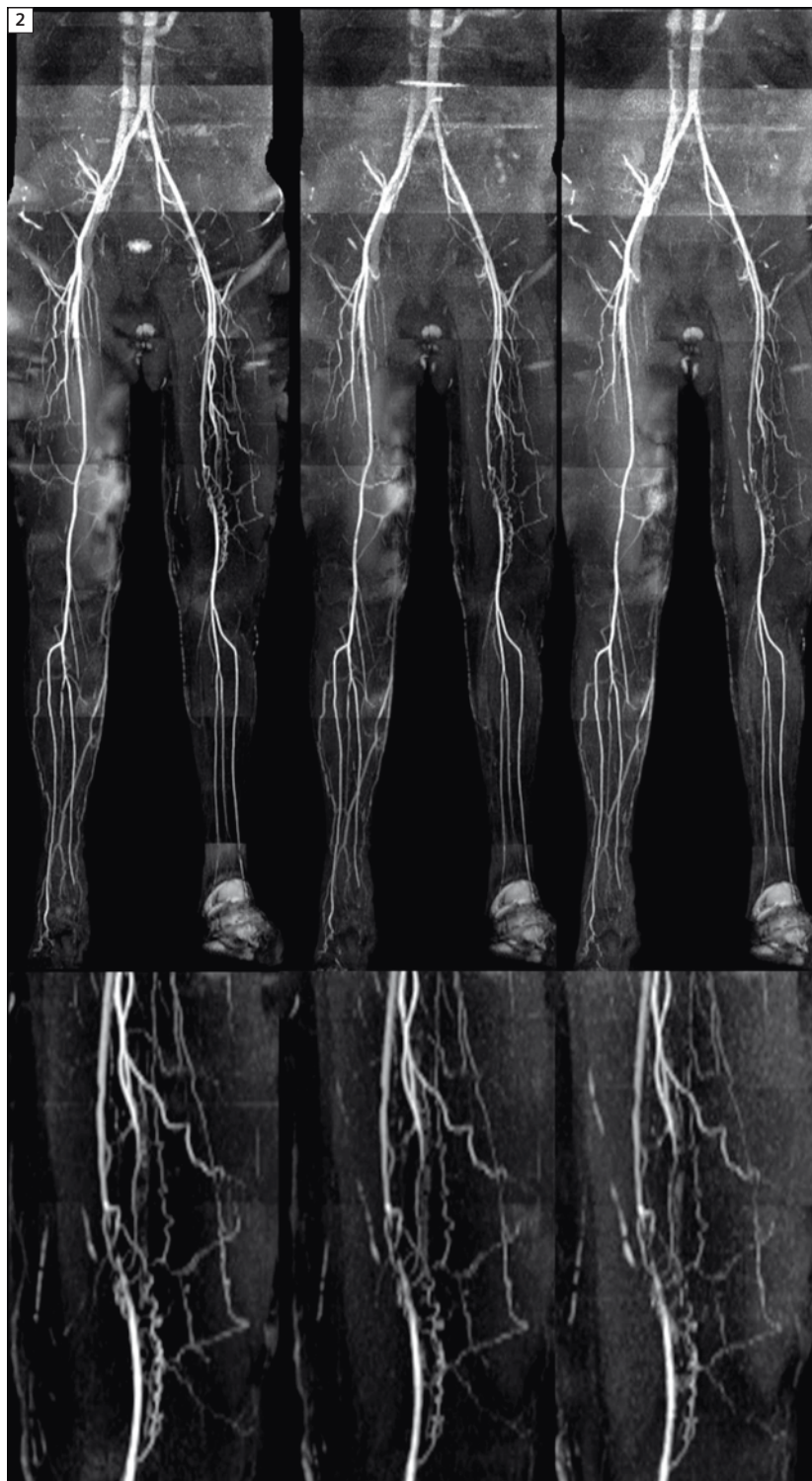
\*This product is still under development and not yet commercially available. Its future availability cannot be ensured.

## Background

Contrast-enhanced MR angiography (CE-MRA) is routinely used for the evaluation of peripheral arterial disease (PAD). However, due to the increased concern of nephrogenic systemic fibrosis (NSF) associated with gadolinium administration in patients with impaired renal function, there has been increased interest in the development of non-contrast MRA (NC-MRA) techniques. Quiescent-interval single-shot (QISS) imaging\* has recently been described as an NC-MRA technique for assessment of the lower extremity vasculature [1] with proven clinical utility at 1.5T [2, 3]. These studies have demonstrated that QISS is easy to use, does not require patient-specific imaging parameters, has minimal flow dependence and is less sensitive to motion than subtractive techniques. Increased SNR at 3T potentially provides improved image quality and enable higher parallel imaging acceleration (PAT) factors. Increasing the PAT factor can be critical to maintaining an acquisition rate of one slice per heartbeat in patients with fast heart rates. In order to evaluate these aspects of QISS NC-MRA, the purpose of our study was to determine

1. the effect of field strength on QISS image quality,
2. the potential to accelerate imaging at 3T using higher PAT factors and
3. to compare NC-MRA QISS at 3T to a conventional CE-MRA protocol.

In addition, the diagnostic quality of QISS at 3T in patients with PAD was evaluated.



**2** 3T QISS in a patient shows segmental occlusion in the adductor canal with reconstitution in the profunda femoral collateral for patient with low GFR (no CE-MRA reference). Standard PAT factor 2 (left), as well as higher PAT factors 3 (center) and 4 (right) clearly depict disease, enabling shorter single shot acquisition capabilities for patients with fast heart rates.

## Methods

QISS is a two-dimensional electrocardiographically gated single-shot balanced steady-state free precession acquisition of one axial slice per heartbeat. Image contrast is generated using in-plane saturation to suppress background tissue and a tracking saturation pulse to suppress venous signal prior to a quiescent inflow period. ECG gating ensures that the quiescent inflow period coincides with rapid systolic flow to maximize inflow of unsaturated spins into the imaging slice; since only a 2D slice is saturated, only minimal inflow is required. Images are acquired with a series of imaging stations, each with 70 slices around the magnet isocenter. Stations in the pelvis and abdomen typically use a series of breath-hold concatenations to minimize respiratory motion.

To validate QISS at 3T, twelve healthy volunteers (9 males age 22–49, 3 females age 26–43) were scanned at 1.5 and 3T within one week using a dedicated 36-channel peripheral vascular coil and an 18-channel body array coil (1.5T MAGNETOM Aera and 3T MAGNETOM Skyra, Siemens Healthcare, Erlangen, Germany). In addition, CE-MRA was performed at 3T (8.4–10 ml at 2 ml/sec, Ablavar, Lantheus Medical Imaging, N. Billerica, MA, USA). Additionally, 3 patients with lower extremity PAD were scanned using 3T QISS NC-MRA and CE-MRA as the reference standard if glomerular filtration rate (GFR) was sufficient. Imaging parameters are provided in Table 1. For each scan session, three QISS run-off scans were acquired in randomized order with GRAPPA PAT factors 2, 3 and 4. The total acquisition and shim time for each QISS NC-MRA run-off was approximately 10 minutes depending on the heart rate. Two blinded radiologists scored image quality for venous contamination, arterial conspicuity and arterial artifacts using a 4-point scale (0 = poor, 1 = fair, 2 = good, 3 = excellent) and inter-observer reliability was measured using the kappa statistic.

## Validation results

QISS image quality was consistent for both field strengths. 3T results were particularly robust, even with high PAT factors and showed higher signal-to-noise ratio (SNR) relative to 1.5T (representative volunteer in Fig. 1). Arterial conspicuity and artifact scores were comparable to CE-MRA, and slightly higher for 3T ( $2.8 \pm 0.1$ ) relative to 1.5T ( $2.5 \pm 0.2$ ). Venous suppression was superior at 1.5T; venous signal did not impact arterial assessment at 3T, however. QISS at 3T also had higher inter-observer agreement ( $\kappa = 0.759$ ) than at 1.5T ( $\kappa = 0.426$ ) for image quality scoring. Overall, QISS performed comparably to CE-MRA at both field strengths, even with a high PAT factor of 4 [4]. Despite the presence of respiratory or bowel motion in some volunteers, QISS with concatenated breath-holding performed consistently in the abdomen and pelvis. Moreover, one always has the option to repeat all or part of the data acquisition in case of technical difficulty or macroscopic patient motion - an option that is not afforded by CE-MRA.

## Clinical results

Based on impressive results in volunteers, several patients were scanned at 3T to demonstrate clinical utility. Initial results suggest that QISS is effective at 3T and has high correlation with CE-MRA.

### Clinical case 1

42-year-old male with longstanding history of type I diabetes complicated by renal failure presents with left diabetic foot requiring transmetatarsal amputation. He subsequently received a kidney transplant and now presents to vascular surgery clinic with non-healing wounds of the right 3<sup>rd</sup> and 4<sup>th</sup> toes. The patient's renal function is poor, with a Creatinine of 2.35 mg/dl and an eGFR of 31 ml/min/1.73 m<sup>2</sup>. The patient was referred for QISS NC-MRA at 3T to assess options for right lower extremity revascularization (Fig. 2). NC-MRA demonstrated segmen-

tal occlusion of the distal left superficial femoral artery at the adductor canal over a distance of approximately 3 cm with reconstitution via branches of the profunda femoris artery (Fig. 2). Small collateral vessels are clearly depicted for PAT factors 2, 3, and 4 (suitable for 738, 660 and 619 ms R-R intervals, respectively) suggesting that high PAT factors can be used to maintain acquisition of one slice per heartbeat for patients with high heart rates. The QISS NC-MRA images of the calves clearly depict the arterial run-off beyond the level of occlusion. No significant arterial stenoses were apparent in the right lower extremity and the patient was diagnosed with microvascular disease. The patient continued wound care, with plans for transmetatarsal amputation if conservative therapy was unsuccessful.

### Clinical case 2

64-year-old male with a history of hypertension, chronic back pain, and tobacco abuse presents with diminished exercise tolerance. The patient reports that these symptoms have been slowly progressive over two years such that he is only able to walk half a block, limited by fatigue and left leg weakness of the hip and buttock. Lower extremity arterial flow studies demonstrated an ankle brachial index of 0.69 with duplex findings suggestive of inflow disease. The patient was referred for CE-MRA at 1.5T and underwent QISS NC-MRA at 3T for research purposes (Fig. 3). CE-MRA with a single dose of gadobenate dimeglumine (Multihance, Bracco Diagnostics Inc., Princeton, NJ, USA) demonstrated long segment occlusion of the left external iliac artery, with reconstitution of the common femoral artery. There was no significant left lower extremity outflow disease; three-vessel runoff was noted to the left foot. QISS NC-MRA demonstrated similar findings, with segmental occlusion of the external iliac artery, with the common femoral artery reconstituted by the inferior epi-

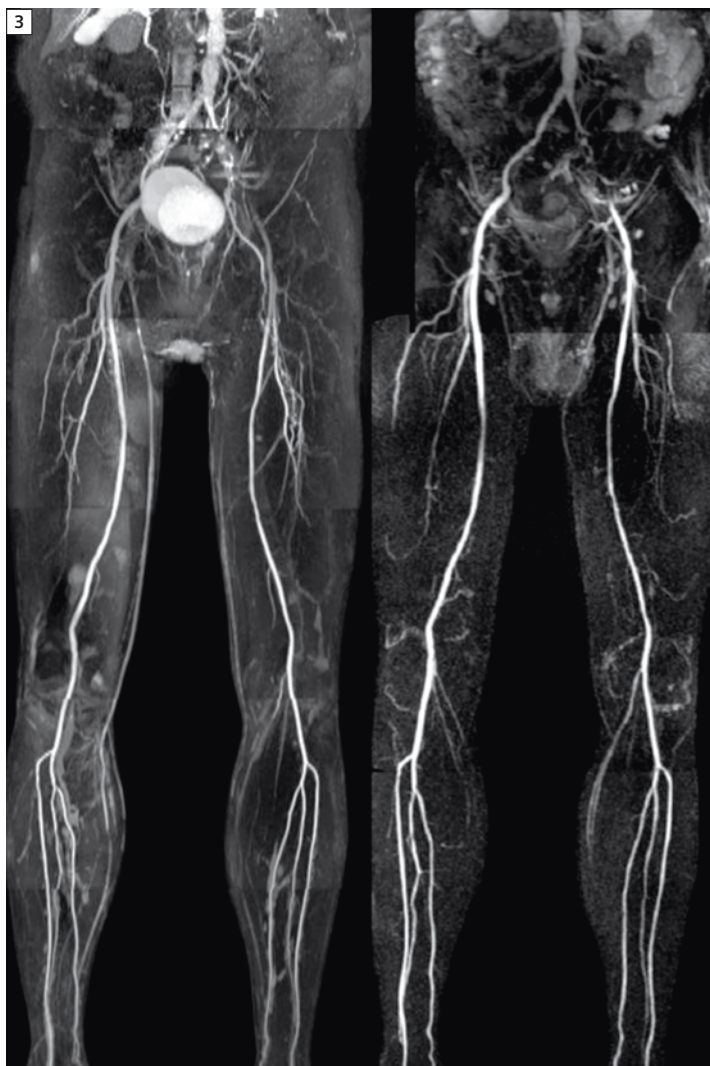
gastric and deep circumflex iliac arteries. The patient will undergo revascularization with left iliac stent placement at a later date.

### Clinical case 3

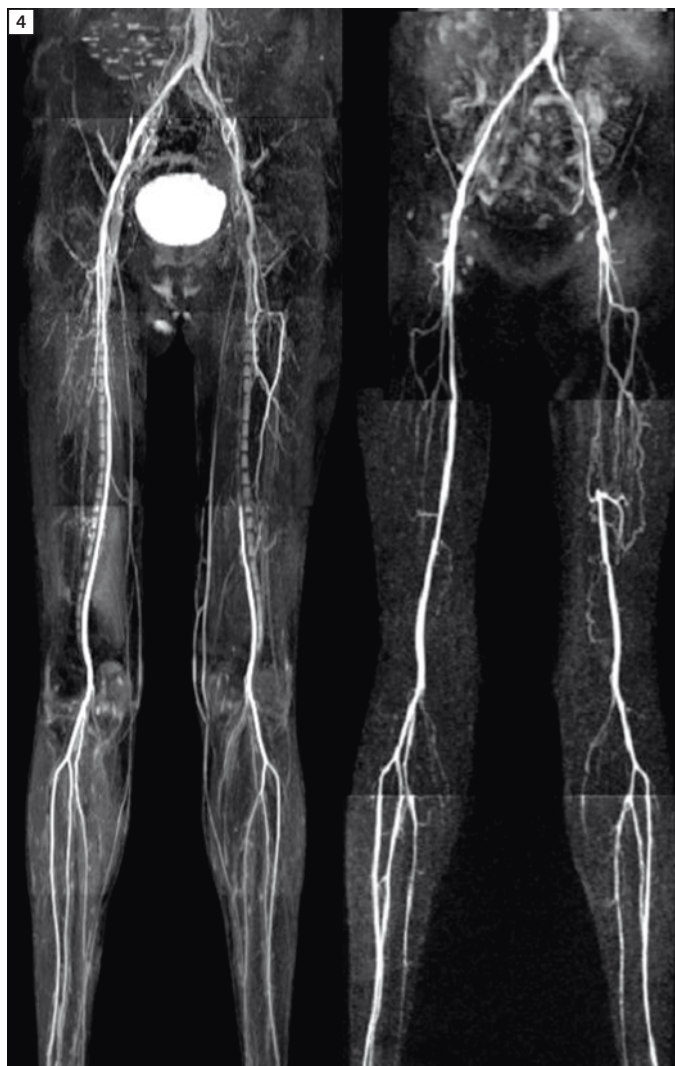
56-year-old female with a history of hypertension, type II diabetes, and lumbar radiculopathy presents with intermittent left lower extremity claudication gradually increasing in severity over the

course of a year, now limiting her walking to a half block. The patient describes increased sensitivity to her left foot and pain in the anterior left thigh, which keeps her awake at night. She notes improved pain with Vicodin. The patient was referred for CE-MRA and underwent QISS NC-MRA at 3T for research purposes (Fig. 4). CE-MRA was performed at 1.5T following a double-dose of gadopentetate dimeglumine (Magnevist, Bayer Healthcare

Pharmaceuticals, Inc, Wayne, NJ, USA) demonstrating long segment occlusion of the left mid to distal superficial femoral artery, with reconstitution of the popliteal artery via branches of the hypertrophied profunda femoris artery. These findings are well seen using QISS NC-MRA, which delineates the length of the occlusion and the run-off vessels without contrast media. Mild venous signal contamination is noted on QISS NC-



**3** Both QISS and CE-MRA depict long segment occlusion of the left external iliac artery, with reconstitution of the common femoral artery. QISS PAT 3 acquisition (left) maximizes SNR while still maintaining single shot acquisition every heartbeat.



**4** QISS and CE-MRA demonstrate long segment occlusion of the left mid to distal superficial femoral artery, with reconstitution of the popliteal artery via branches of the hypertrophied profunda femoris artery. For this patient, QISS PAT 4 acquisition (left) maintained single shot acquisition every heart beat.

MRA without impacting diagnostic yield of the maximum intensity projection (MIP) images. The patient underwent successful endovascular recanalization of the left superficial femoral artery with stent placement with resolution of her claudication symptoms.

## Conclusion

QISS NC-MRA is promising at 3T and demonstrates comparable image quality to CE-MRA in depicting the peripheral arteries in both volunteers and patients with PAD. Improved SNR at 3T enables higher PAT factors to reduce image acquisition time while maintaining image quality in patients with faster heart rates. While QISS at 1.5T has shown excellent clinical utility, our results suggest that imaging at 3T may provide further clinical benefit. QISS NC-MRA at 3T demonstrated arterial vessels with slightly greater conspicuity and lower arterial artifacts compared to QISS NC-MRA at 1.5T. Although venous signal contamination is greater at 3T, the increased arterial signal enables ready differentiation on MIP imaging and does not impact diagnostic utility. Volunteer and patient data demonstrate that the QISS acquisition can be accelerated up to four fold without significant image quality degradation, suitable for heart rates approaching 100 beats per minute. At both field strengths, the QISS technique is a valuable alternative to CE-MRA especially in patients with renal insufficiency.

**Table 1: Quiescent-interval single-shot (QISS) sequence details.**

QISS sequence details	
TR (ms) / TE (ms) / flip angle (deg.)	3.2/1.7/90
In-plane resolution	1 x 1 mm
Partial Fourier	5/8
Slice thickness	3 mm
Orientation	axial
No. of slices per group	70
No. of slice groups	7
Acquisition time / slice group	~55 s (heart rate dependent)
Parallel imaging	GRAPPA x 2–4
ECG gating	Yes
Inversion time	345 ms

## References

- 1 Edelman, R.R., et al., Quiescent-interval single-shot unenhanced magnetic resonance angiography of peripheral vascular disease: Technical considerations and clinical feasibility. *Magn Reson Med*, 2010. 63(4): p. 951–8.
- 2 Hodnett, P.A., et al., Evaluation of peripheral arterial disease with nonenhanced quiescent-interval single-shot MR angiography. *Radiology*, 2011. 260(1): p. 282–93.
- 3 Hodnett, P.A., et al., Peripheral Arterial Disease in a Symptomatic Diabetic Population: Prospective Comparison of Rapid Unenhanced MR Angiography (MRA) With Contrast-Enhanced MRA. *AJR* December 2011 197(6): p. 1466–73.
- 4 Glielmi, C., et al. High Acceleration Quiescent-Interval Single Shot Magnetic Resonance Angiography at 1.5 and 3T. *ISMRM* 2012, 3876.

## Contact

Maria Carr, RT (CT)(MR)  
CV Research Technologist  
Department of Radiology  
Northwestern University  
Feinberg School of Medicine  
737 N. Michigan Ave. Suite 1600  
Chicago, IL 60611  
USA  
Phone: +1 312-503-1417  
m-carr@northwestern.edu

# Pediatric MR Elastography of the Liver

Marilyn J. Siegel, M.D.<sup>1</sup>; Agus Priatna, Ph.D.<sup>2</sup>; Bradley D. Bolster, Jr., Ph.D.<sup>2</sup>; John J. Kotyk, Ph.D.<sup>1</sup>

<sup>1</sup>Mallinckrodt Institute of Radiology, Washington University School of Medicine, St Louis, MO, USA

<sup>2</sup>R&D Collaborations, Siemens Healthcare, USA

## Introduction

Hepatic cirrhosis is an increasing complication of cystic fibrosis (CF). Liver biopsy remains the gold standard for diagnosis and detection of CF, but unfortunately is prone to sampling errors. A non-invasive test that assesses the entire liver would be beneficial for both patient management and therapeutic trials. Hepatic stiffness measured with magnetic resonance elastography<sup>§</sup> (MRE) has shown potential as a surrogate for detecting liver disease and hepatic fibrosis [1–4]. MRE is quantifiable and can be used in patients with obesity or ascites. In conjunction with other MR scans, MRE can help differentiate fat from fibrosis. Application of MRE also spares the discomfort and risk associated with liver biopsy; it allows assessment of a large volume of the liver, decreasing sampling errors associated with sonography; and, it allows for multiple follow-up studies without risk of radiation exposure. MRE generates images depicting the relative stiffness of liver tissue by imaging the shear wave propagation generated by an external wave generator or active acoustic driver. The mechanical excitation is conducted to the patient in the magnet pneumatically, by means of a long hose terminated with a drum-like passive driver. The driver waveform is synchronized to motion encoding gradients in the MR imaging sequence to encode tissue displacement as phase in the reconstructed images. The strength of the wave propagation in the tissue is controlled by the amplitude of the driver



**1** The Resoundant acoustic driver system.



**2** MR Elastography setup.

\*MR scanning has not been established as safe for imaging fetuses and infants under two years of age. The responsible physician must evaluate the benefit of the MRI examination in comparison to other imaging procedures.

<sup>§</sup>Under development. Not for sale in the U.S.

waveform and the quality of the coupling between the passive driver and the liver.

In this study we use MRE and other MR techniques to simultaneously measure hepatic stiffness and steatosis in healthy pediatric\* subjects and CF patients with cirrhosis to assess the potential value of MRE for detection of chronic liver disease. Special emphasis was placed on evaluating the methods for use on pediatric subjects where smaller body habitus markedly increases the coupling between the driver and the patient's liver. For pediatric patients it is critical to adjust the amplitude or the strength of the wave generated by the driver for both patient comfort and size, while simultaneously providing good elastography data.

## Methods

The MRE data were collected on a conventional 1.5T MAGNETOM Avanto system using the MRE research application package. The MRE examination was added to a conventional MR examination of the upper abdomen and requires less than one minute of additional imaging time. After collecting T2-weighted localizer images, ten subjects with a mean age of 18.6 years (range 7–44 years) were studied. Four subjects were healthy and six of them had CF and cirrhosis documented by conventional MRI methods. Patients were imaged in the supine position with a passive pneumatic driver placed on the abdomen overlying the liver to generate mechanical waves.

MRE acquisitions were performed using a gradient-recalled echo based MR elastography sequence. A six element body matrix coil was placed anterior to the liver while six to nine elements of a spine matrix coil were positioned poste-

riorly. A transverse slice orientation was used with elastography motion encoding through each slice. Four acquisitions were performed per slice, each with a different phase offset between the driver and the scanner. GRAPPA parallel imaging was applied with an acceleration factor of 2, allowing data to be acquired in a single 20 second breath-hold per slice. Imaging parameters were: 256 x 64 acquisition matrix, TE/TR 22/50 ms, FOV 340 or 380 mm, slice thickness 5 mm, read bandwidth 260 Hz/pixel and flip angle 25°. A 60 Hz mechanical wave was generated by the active acoustic driver (Resoundant, Mayo Clinic, Rochester, MN, USA) shown in Figure 1. The applicator of the MRE device was placed over the anterior wall of the chest adjacent to the liver as shown schematically in Figure 2. The amplitude of the driver was adjusted for pediatric patients between 10%–20% of the maximum amplitude, as opposed to the 40%–60% amplitude that was used for adult patients.

The MR wave images were generated using an offline inversion algorithm (Mayo Clinic, Rochester, MN, USA), and used to calculate elastographic images (or elastograms) that depict liver stiffness. Mean elasticity values are reported in kilopascal (kPa) by manually placing regions of interest in four regions on each cross sectional image. All patients also had intrahepatic triglyceride (IHTG) content quantified with MR spectroscopy using a Double PRESS sequence (TE 1 = 23 ms, TE 2 = 53 ms). Statistical analyses were performed using non-paired t-tests.

## Results

MRE was successfully accomplished in all subjects. Representative wave and MRE images of the liver from subjects

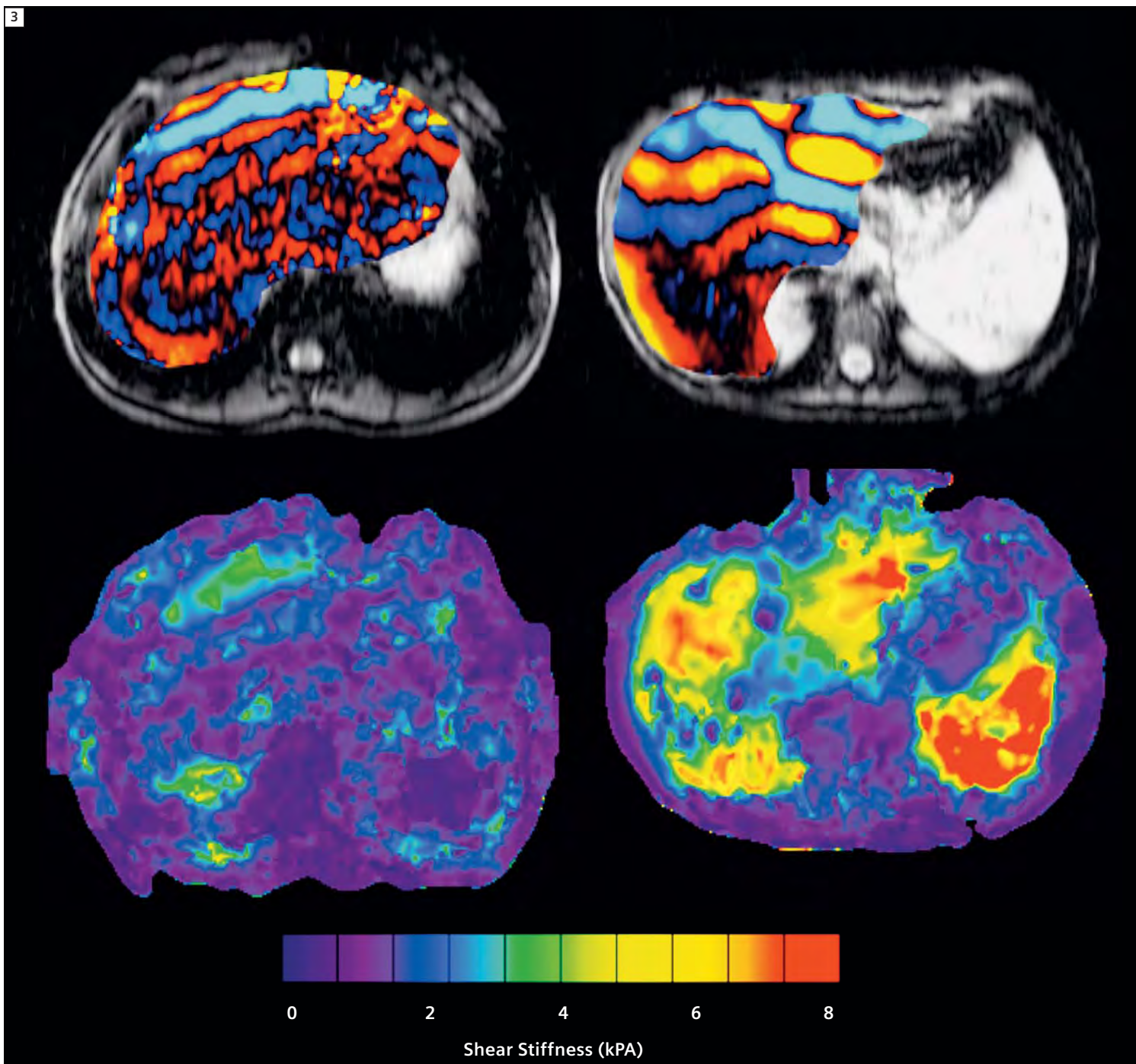
with or without cirrhosis are depicted in Figure 3. The mean hepatic shear stiffness was significantly higher in subjects with cirrhosis (mean 4.84 kPa, range 4.02–6.21 kPa) than those without cirrhosis (mean 2.99 kPa, range 2.70–3.38 kPa) ( $P = 0.0026$ ). Receiver operator characteristic analysis identified a cutoff of > 3.38 kPa as both 100% sensitive and specific for discriminating cirrhosis in this patient population.

We adjusted driver amplitude downwards roughly based on the body weight of the pediatric patients in order to avoid image artifacts due to excessive vibration amplitude. Driver amplitudes between 10%–20% provided good quality MRE data in patients ranging from 15 to 35 kg in weight. Figure 4 shows a representative case of elastograms acquired with low driver amplitudes on a 10-year-old patient. As seen in this figure, the elastograms show similar quality for both 10% and 15% amplitude. To determine whether steatosis influenced detection of cirrhosis in CF liver disease, the IHTG content was assessed and found to be normal in four (mean 2.3%, range 1.12%–3%) and increased in six subjects (mean 6.6%, range 4.97%–8.25%) and was no different in patients with or without cirrhosis ( $P = 0.27$ ).

## Discussion and conclusions

MRE can show increased liver stiffness in patients with liver disease and can be used to identify hepatic cirrhosis. Use of MRE may lead to a new quantitative method for evaluating cirrhosis in patients with CF and other chronic liver diseases. This technique has the advantages of being non-invasive, allowing assessment of a large liver area, and allowing for multiple follow up studies without risk of radiation exposure.

3



**3** Representative wave images and elastograms in a healthy subject (left column) and a CF patient with cirrhosis (right column). In the healthy subject, the wave image (top left) shows short wavelengths consistent with normally soft liver, and the elastogram (bottom left) reveals stiffness values ranging from 0 to 3 kPa, mean 2.1 kPa. In the CF patient, the wave image (top right) shows shear waves with longer wave lengths and the elastogram (bottom right) depicts stiffness values of 4–8 kPa, mean value of 7.2 kPa.

In this study we have shown that MRE is safe and feasible when applied to a pediatric population and that it can identify increased liver stiffness in CF patients with hepatic cirrhosis. To avoid excessive signal loss due to phase dispersion, the driver amplitudes used for pediatric subjects were well below those that are used for typical adults and yet we were able to obtain good quality elastograms and wave images. Since the vibrations were well tolerated in the pediatric population, these findings provide a good starting point for future pediatric examinations.

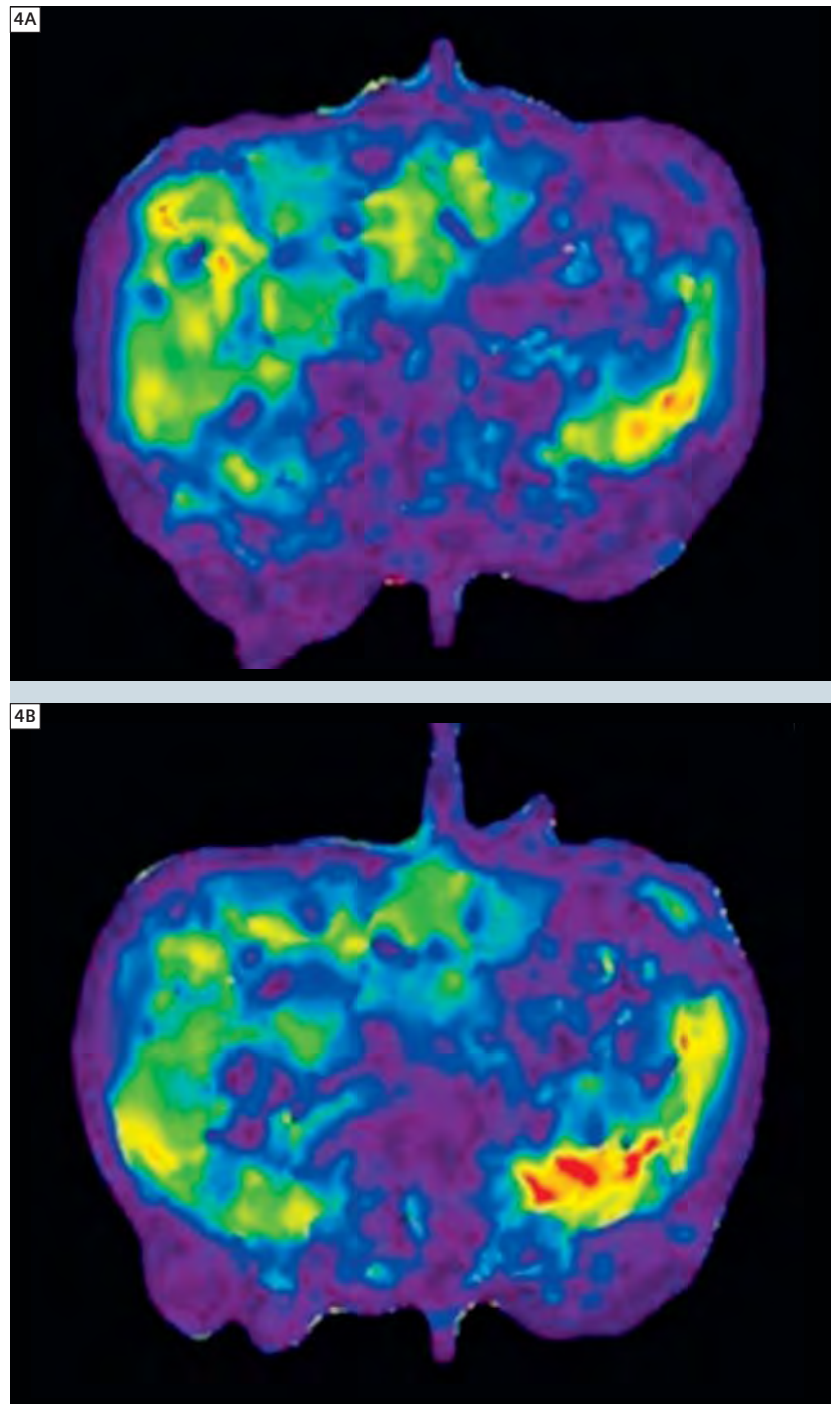
We have demonstrated that a shear stiffness cutoff value of 3.38 kPa separates healthy patients from those with cirrhosis. Our results are similar to those in adults showing that a shear stiffness cutoff value of 2.93 kPa discriminates between healthy patients and those with chronic liver disease [1]. We also show that the presence of hepatic steatosis had no apparent effect on the liver stiffness measurements.

#### References

- 1 Yin M, Talwalkar JA, Glaser KJ, et al. Assessment of hepatic fibrosis with magnetic resonance elastography. *Clin Gastroenterol Hepatol* 2007; 5:1207-1213.
- 2 Taouli B, Ehman R, Reeder S. Advanced MRI Methods for Assessment of Chronic Liver Disease. *American Journal of Radiology* 2009; 193:14-27.
- 3 Talwalkar JA, Yin M, Fidler JL, et al. Magnetic Resonance Imaging of Hepatic Fibrosis: Emerging Clinical Applications. *Hepatology* 2008; 47: 332-342.
- 4 Hines CDG, Bley TA, Lindstrom MJ. Repeatability of Magnetic Resonance Elastography for Quantification of Hepatic Stiffness. *Journal of Magnetic Resonance Imaging* 2010; 7325-730.

#### Contact

Marilyn J. Siegel, M.D.  
Professor of Radiology and Pediatrics  
Mallinckrodt Institute of Radiology  
510 South Kingshighway Blvd.  
St. Louis, MO 63110  
USA  
Phone: +1 314-454-6229  
Fax: +1 314-454-2868  
siegelm@mir.wustl.edu



**4** Elastograms acquired on a 10-year-old patient with (4A) a 10% amplitude, and (4B) a 15% amplitude.

# MR Biomarkers of Gestational Age in the Human Fetus

Judy R. James<sup>1</sup>; Majid A. Khan<sup>1</sup>; David A. Joyner<sup>1</sup>; David P. Gordy<sup>1</sup>; Razvan Buciuc<sup>1</sup>; James A. Bofill<sup>2</sup>; Kenneth W. Liechty<sup>2</sup>; Manohar S. Roda<sup>1</sup>

<sup>1</sup>Department of Radiology, University of Mississippi Medical Center, Jackson, MS, USA

<sup>2</sup>University Center for Fetal Medicine, University of Mississippi Medical Center, Jackson, MS, USA

## Abstract

Fetal biometry measurements using ultrasound have been the standard for assessment of fetal development and gestational age, however, no similar standards exist for fetal\* MR imaging (MRI). Rapid high-resolution MRI evaluation of 110 fetuses with a gestational age =  $27 \pm 9$  weeks was performed and the bi-parietal-diameter (BPD), occipital-frontal-diameter (OFD), head-circumfer-

ence (HC), femur-length (FL), humerus-length (HL), and abdominal-circumference (AC) were determined and correlated with the ultrasound measurement. The results demonstrate an excellent correlation with ultrasound with insignificant differences between reported biometrics and gestational age. All of the MR biometric measurements correlated well with the ultrasound measurements

(slope =  $0.97 \pm 0.03$  and an  $R^2 = 0.91 \pm 0.03$ ). Gestational ages computed from the MR biometrics, also correlated well with the ultrasound ages (slope =  $0.97 \pm 0.04$ ;  $R^2 = 0.90 \pm 0.02$ ). There was no significant difference between the biometrics (p-value =  $0.13 \pm 0.07$ ) and the gestational ages (p-value =  $0.58 \pm 0.25$ ) obtained from either of the imaging modalities. The mean gestational age

**Table 1: Fetal MR imaging sequences and parameters:**

	T2 HASTE	TrueFISP	3D VIBE (In/Out phase)	FLASH	DWI
Sequence type	HASTE	TrueFISP	VIBE	GRE	EPI
Breath-hold	Yes	Yes	No	Yes	No
Concatenations	2	2	1	1	1
FOV (mm)	290	350	320	350	300
Slices (brain/body)	20/32	30/37	22/36	25/30	30/30
Slice thickness (mm)	5	4	5	7	5
Slice gap (mm)	0/0	0.6	0	1.4	1
TR (ms)	1200	4	8	113	5000
TE (ms)	85	2	4	4.6	85
Averages	1	1	1	1	2
PAT	Off	Off	2	Off	2
Flip angle	180	70	10	25	–
Fat suppression	No	No	Yes	No	Yes
Base resolution	256	256	256	256	156
Phase resolution	216	220	192	180	156
Receiver bandwidth	195	558	320	260	1282
Acquisition time (sec)	46	45	13	40	22

\*MR scanning has not been established as safe for imaging fetuses and infants under two years of age. The responsible physician must evaluate the benefit of the MRI examination in comparison to other imaging procedures.

obtained from MR was in excellent correlation with the ultrasound mean gestational age (slope = 0.99,  $R^2 = 0.92$ , p-value = 0.52). In addition, MRI was able to provide more anatomical and structural information regarding complex fetal anomalies. MR biometry can be used as an appropriate modality to accurately assess fetal gestational age, fetal development, and fetal growth proportions.

## Introduction

Assessment of fetal biometry is of vital importance in prenatal diagnosis and is an established way of assuring appropriate brain development. Ultrasound is considered to be a screening modality of choice for biometric assessment and is performed in great numbers everyday on very large populations of pregnant women and has established biometric reference standards in various cohorts of human fetuses. MRI, in contrast, is a complementary tool and is usually performed following detection of abnormalities with ultrasound, especially in cases where sonographic findings are equivocal. There have been significant advances in fetal MR imaging, with the advent of multiple new MR imaging techniques resulting in the increased utilization of MRI for fetal evaluation, especially in known cases of congenital fetal anomalies [1–3]. In addition, MR imaging

provides greater detail, improved spatial resolution and soft-tissue contrast than routine ultrasound imaging. Hence, it is now more feasible to determine normal biometric data for fetuses from just a few MRI sequences.

The use of MRI as an adjunct to ultrasound in fetal imaging is becoming widespread in clinical practice and in the literature. Fast MR imaging sequences have been helpful in eliminating fetal motion artifacts while providing superior resolution and anatomic detail of the fetal brain [4–9]. A potential advantage of the improved high contrast resolution is to accurately acquire and measure fetal biometric values, which can be used as a screening tool to identify fetuses that fall outside the normal range of measurements and thus are at increased risk of morphologic abnormalities.

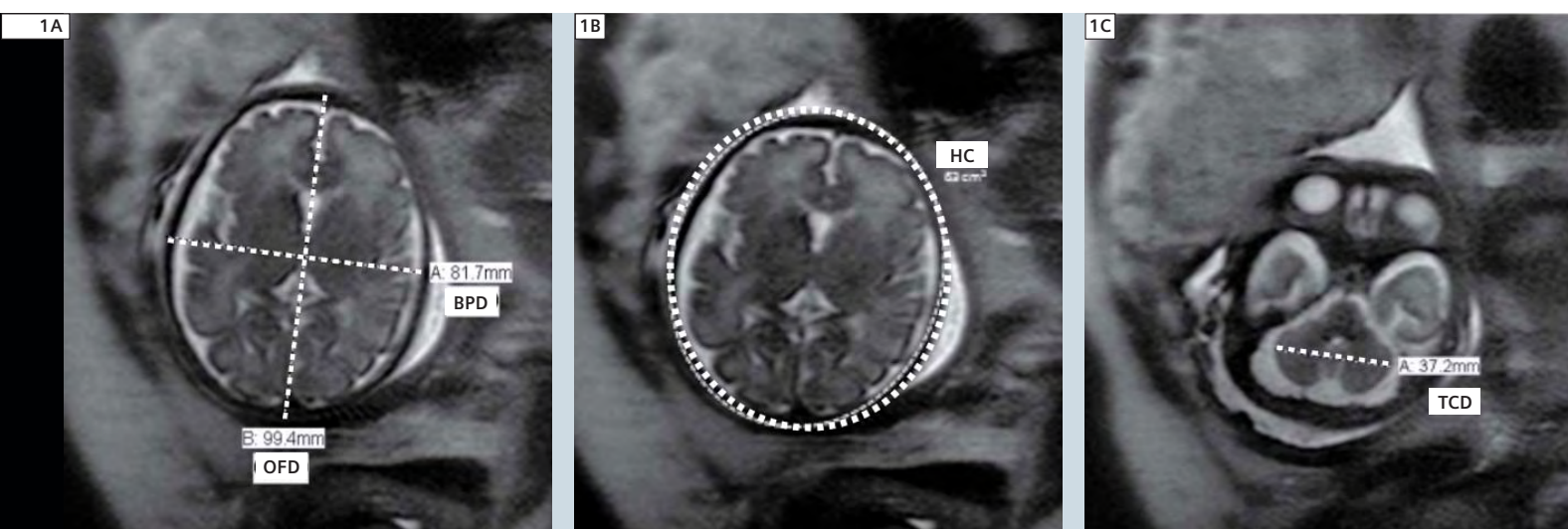
Comparisons of MRI and ultrasound in the measurement of fetal biometric values and organ size have been shown in some reports with limited number of fetuses [10–11]. As expected, a good agreement between the two methods exists with a slight advantage to MRI in certain cases, such as fetal weight estimation and measurement of the posterior fossa [12]. Since we already obtain ultrasound and MR whole-body images of high-risk fetuses, a decision was made to analyze MR fetal biometry mea-

surements of fetal head, abdomen, and extremities from a large cohort of MR fetal images and compare to ultrasound values. Our aim was to perform multi-parameter assessment of bi-parietal diameter (BPD), occipital frontal diameter (OFD), head circumference (HC), femur length (FL), humerus length (HL) and abdominal circumference (AC) and the gestational ages determined from these measurements and correlate these findings with ultrasound. We hope that the findings from this study could add a crucial dimension to fast imaging MRI for reliable normal fetal biometric evaluation.

## Methods

### a) Study population

A retrospective review of the MRI database for fetal MRI examinations was performed. Once the study protocol was reviewed and approved by the institutional review board (*University of Mississippi Medical Center, Jackson, MS, USA*), a retrospective measurement analysis for fetal biometrics of high-risk fetal MR images ( $n = 110$ , gestational age =  $27 \pm 9$  weeks) was done with images acquired using conventional MR techniques. Pregnant women with high-risk fetuses were referred for an MRI scan by the ultrasound, obstetric, maternal fetal medicine or pediatric surgery departments. An ultrasound report was avail-



**1** MR images showing multi-parameter assessment of gestational age with fetal head measurements: **(1A)** bi-parietal diameter (BPD) and occipital frontal diameter (OFD), **(1B)** trans-cerebellar diameter (TCD) and **(1C)** head circumference (HC).

able for each fetus with the respective reported fetal biometrics and corresponding gestational ages.

The inclusion criteria were:

- Fetal ultrasound reports with all fetal biometrics (BPD, OFD, HC, FL, HL and AC), except TCD, should be included in the chart.
- Fetal ultrasound report must have estimated gestational ages from each biometrics (except OFD) reported in the chart.
- Fetal ultrasound report must have the average composite gestational age reported.
- Ultrasound and MRI scans of the fetus must have been done on the same day or within  $\pm 3$  days for correlation purposes.
- Absence of movement artifacts which would render the measurements inaccurate.
- Absence of significant intracranial abnormalities and/or absence of significant body abnormalities which may affect head or abdominal size and measurements.
- Absence of skeletal dysplasia.

MRI examinations for these high-risk fetuses were performed because of increased risk and/or positive family history of cranial pathology (including suspicion of infectious fetopathy, suspicion of cerebral abnormality, absent septum pellucidum, giant cisterna magna, Dandy Walker variants, cerebral biometry at the lower limit of the normal on ultrasound), cleft lip and/or palate, spina bifida, club foot, polyhydramnios, suspected esophageal or duodenal atresia, lung lesions like sequestration, CCAM, maternal disease (with possible consequences for fetal cerebral development), congenital heart defects, incidental mass lesions detected on ultrasound like lymphangioma, teratoma and placental abnormalities. The cases with intracranial abnormalities causing hydrocephalus from aqueductal stenosis, Arnold Chiari malformation, intracranial hemorrhage, obstructive mass lesions and microcephaly, which may and/or would affect head size and measurements, were excluded. The cases with signifi-

cant body wall and diaphragmatic abnormalities like gastroschisis, omphalocele, diaphragmatic hernias, ectopia vesicae, which may affect abdominal size and measurements were also excluded. The cases with severe oligohydramnios were excluded, due to difficulty in obtaining the measurements.

#### **b) Non-contrast image acquisition on MR scanner**

Fetal MRI was performed on 1.5T MR scanners (MAGNETOM Espree and MAGNETOM Symphony a Tim System, Siemens Healthcare, Erlangen, Germany) with optimized fetal MR protocols to image fetuses and pregnant women in an effective and timely manner. The subjects were positioned supine with the coil placed on their torso. The coil was positioned in such a way that the liver was in the centre of the coil. No respiratory or cardiac gating was used. Proton images were acquired with the 6-channel Body Matrix coil anterior coupled with 6 channels of the Spine Matrix coil posterior for a total of a 12-channel array.

Fast imaging MR sequences such as Half-fourier-Acquisition-Single-shot-Turbo-spin-Echo (HASTE), True-Fast-Imaging-with-Steady-state-Precession (TrueFISP), Fast-Low-Angle-Shot (FLASH), Volumetric-Interpolated-Breath-hold-Examination (VIBE), T1 Gradient-Recalled-Echo (GRE) and Diffusion-Weighted (DW) images were included in the fetal MR scans. Imaging parameters used for these sequences are reported in Table 1. These sequences were used to acquire high-resolution whole-body images of the fetus in different orientations (sagittal, coronal and axial planes). The fetal images were then sent to a reporting database for review by radiologists.

#### **c) Fetal biometric measurements**

Two expert radiologists (M.K. and M.R.) in neuro imaging and body imaging reviewed all the fetal MR images and performed the biometric measurements independently. The appropriate and specific planes and slices for reporting the fetal head, abdomen, and extremity measurements were chosen from the MR images presented to them.

#### **■ Head measurements**

BPD, HC, OFD and TCD were measured as part of the head measurements, shown in Figure 1. The BPD and OFD were measured on a transverse axial section of the fetal head which included the falx cerebri anteriorly and posteriorly, the cavum septum pellucidum anteriorly in the midline and the thalami.

The BPD was measured from the outer edge of the nearer parietal bone to the inner edge of the more distant parietal bone in relation the anterior abdominal wall so as to match with the ultrasound technique. The OFD was measured perpendicular to the BPD from the outer edge to the outer edge of the bones.

The longest transverse width of the cerebellum, either on axial or coronal plane, was measured in the posterior fossa views to obtain TCD measurement.

#### **■ Abdomen measurements**

The abdominal circumference was measured at the level of the liver and stomach of the fetus, including the left portal vein at the umbilical region, shown in Figure 2A. This measurement was used in the assessment of gestational age and fetal growth, particularly in the second half of the pregnancy to demonstrate normal fetal proportions.

#### **■ Extremities measurements**

The long bones were measured along their true longest axis. The visualization of femoral or humeral shaft and the visualization of both cartilaginous ends indicated that the image plane was on the longest axis and is the optimal measurement plane, shown in Figures 2B and C. The calipers were placed along the diaphyseal shaft excluding the epiphysis.

Both the radiologists were completely blinded to the ultrasound measurements and gestational ages reported from the ultrasound scan for each of these fetuses. Once the MRI measurements were reported, corresponding gestational ages were tabulated from the same reference charts as used in ultrasound.

#### **d) Statistical correlation**

MR fetal biometrics reported by the radiologists was correlated using linear squares regression (slope,  $R^2$ ) analysis and Pearson's bivariate parametric corre-

lations coefficients,  $R$ , ( $p$ -value ( $P_{\text{Pearson}}$ )  $\leq 0.05$  level) with the ultrasound measurements. Student's  $t$ -test was performed to determine any significant differences between the biometric measurements and gestational ages obtained from the two imaging modalities ( $p$ -value ( $P_{t\text{-test}}$ )  $< 0.05$ ). All statistical analyses were done in Microsoft Excel® or IBM SPSS Statistics 19.

## Results

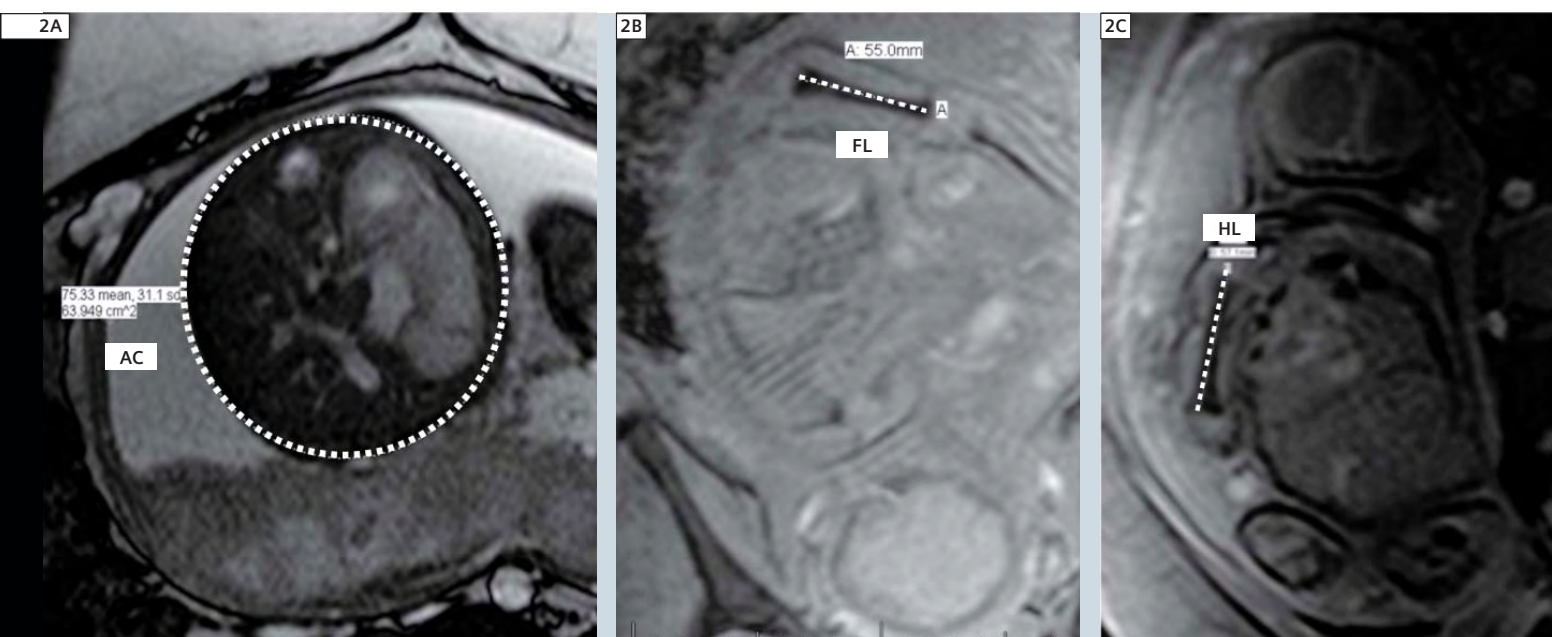
Results showed an excellent correlation with insignificant differences between ultrasound and MRI reported biometrics and gestational ages. All the MR biometric measurements correlated well with the ultrasound measurements (slope =  $0.97 \pm 0.03$  and an  $R^2 = 0.91 \pm 0.03$ ) as shown in Figure 3. Gestational ages computed from the MR biometrics, also correlated well with the ultrasound ages (slope =  $0.97 \pm 0.04$ ;  $R^2 = 0.91 \pm 0.02$ ) as shown in Figure 4. There was no significant difference between the biometrics ( $P_{t\text{-test}} = 0.13 \pm 0.07$ ) and the gestational ages ( $P_{t\text{-test}} = 0.58 \pm 0.25$ ) obtained from both the imaging modalities. Mean gestational age from MR was in excellent correlation with ultrasound mean

gestational age (slope = 0.99,  $R = 0.96$ ,  $P_{\text{Pearson}} < 0.01$ ,  $P_{t\text{-test}} = 0.52$ ) as shown in Figure 5.

A strong correlation was also observed for each of the fetal head and body biometric measurements and gestational ages between MRI with ultrasound. This was also confirmed to be significant by Pearson's parametric correlations done at 0.01 levels. For HC, measurement and age correlation between the two imaging modalities was with a slope = 0.99 and 0.99,  $R = 0.97$  and  $0.96$ ,  $P_{\text{Pearson}} < 0.01$  for both and  $P_{t\text{-test}} = 0.34$  and  $0.32$ . For BPD, measurement and age correlation was with a slope = 0.95 and 0.96,  $R = 0.95$  and  $0.98$ ,  $P_{\text{Pearson}} < 0.01$  for both, and  $P_{t\text{-test}} = 0.38$  and  $0.34$ . For OFD, the measurement correlation was with a slope = 0.95,  $R = 0.9$ ,  $P_{\text{Pearson}} < 0.01$  and  $P_{t\text{-test}} = 0.34$ . Gestational age estimated from OFD was not reported in the ultrasound report for comparison purposes with MRI. For AC, measurement and age correlation was with a slope = 1.02 and 0.98,  $R = 0.96$  and  $0.96$ ,  $P_{\text{Pearson}} < 0.01$  and  $P_{t\text{-test}} = 0.51$  and  $0.46$ . For FL, measurement and age correlation was with a slope = 0.95 and 1.00,  $R = 0.91$  and  $0.91$ ,  $P_{\text{Pearson}} < 0.01$  for both and  $P_{t\text{-test}} =$

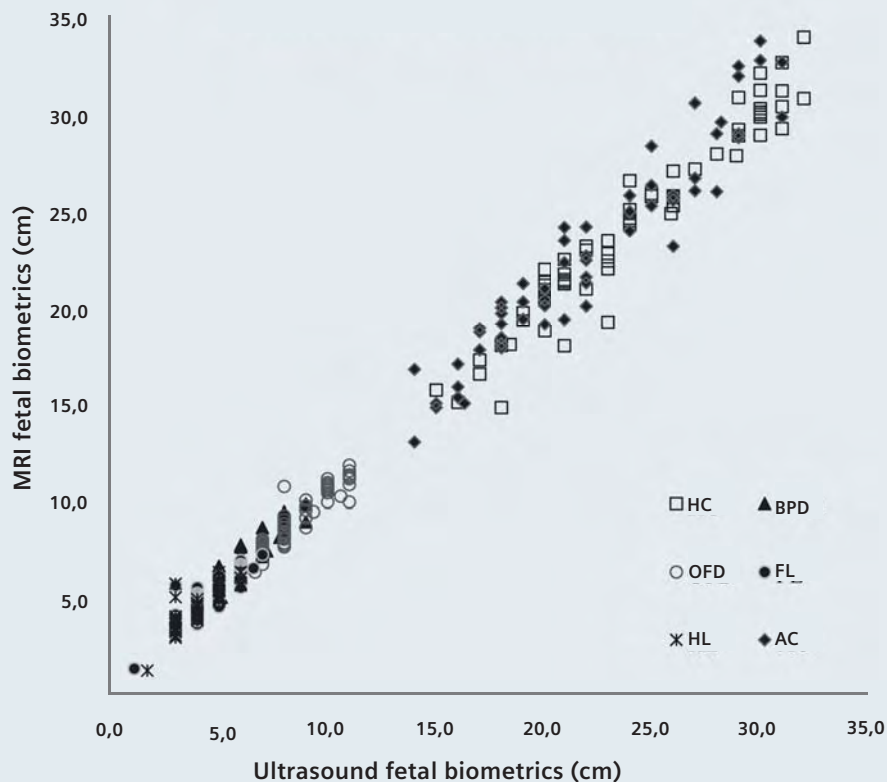
0.50 and 0.44. For HL, measurement and age correlation was with a slope = 0.99 and 1.0,  $R = 0.86$  and  $0.88$ ,  $P_{\text{Pearson}} < 0.01$  for both and  $P_{t\text{-test}} = 0.43$  and  $0.40$ .

The analysis from various biometric measurements from MRI vs. the respective MR gestational ages yielded very interesting results. It was observed that some head and body measurements increased in a linear fashion with gestational age but some of the fetal biometric measurements increased more rapidly than others as gestational age increased as exposed by the slope of the correlation charts. HC and AC measurements had an almost perfect linear increase with age (slope = 1.02 and 0.91,  $R^2 = 0.97$  and  $0.93$  respectively) where as BPD had a slope = 3.61 ( $R^2 = 0.98$ ), OFD had a slope = 2.91 ( $R^2 = 0.91$ ), FL had a slope = 4.07 ( $R^2 = 0.97$ ) and HL had a slope = 4.71 ( $R^2 = 0.95$ ). Results also showed that HL and FL developed at a much faster rate than other measurements with gestational age. This was in concordance with the ultrasound measurement correlations with their respective gestational ages. In addition to using MRI for deriving accu-



**2** MR images showing multi-parameter assessment of gestational age with fetal body measurements: (2A) abdominal circumference (AC), (2B) femur length (FL) and (2C) humerus length (HL).

### Biometrics correlation chart



**3** Biometric correlation chart showing strong correlation (slope =  $0.98 \pm 0.03$  and  $R^2 = 0.91 \pm 0.03$ ) between measurements obtained from MRI and ultrasound.

rate fetal biometrics, MRI was also able to provide additional information regarding the fetal anomalies.

### Discussion

In this study, non-invasive MRI has been used to perform fetal biometry measurements and to determine gestational ages based on the measurements from a reasonably large cohort of patients with a large gestational age range ( $n = 110$ , gestational age =  $27 \pm 9$  weeks) with high accuracy and good correlation with ultrasound measurements throughout the gestational age range. In this project, various biometric measurements were performed in the fetal images and compared to ultrasound to establish the reliability and accuracy of MRI in providing biometric values as well as gestational ages. Biometric measurements were derived from MRI and ultrasound for BPD, OFD, HC, FL, HL and AC and additional values such as TCD obtained from MR images. TCD is not routinely

reported on ultrasound in our institution. Biometrics was done on high-risk fetuses without any significant intracranial abnormalities which could affect the head measurements and/or without any significant body abnormalities which could affect the body measurements. Fetal biometry and gestational age determination using ultrasound is considered the gold standard and is appropriate for screening purposes. This has resulted in various accurate fetal growth charts [13] that are used for age determination and validation of MRI measurements since there have been no charts developed yet based on MRI measurements. But, MRI of the fetuses is gaining widespread acceptance due to its improved spatial resolution and soft-tissue contrast as compared to ultrasound [14–15]. But in current clinical practice, MRI is still not the foremost choice of modality for screening fetuses for normality or abnormalities. Ultrasound is definitely the primary

choice for fetal imaging. Ultrasound being widely available, easy to use and less expensive than other imaging modalities makes it a convenient modality of choice for fetal imaging. Ultrasound imaging does give a clear image of the soft tissues but is not capable of identifying all fetal anomalies as on an MRI scan due to the lack of spatial resolution and visual clarity. Ultrasound images are highly dependent on the operator and are interpreter dependent, too. The ultrasound images are also highly influenced by fetal positioning, for instance if the fetal head is low in the pelvis, it is highly challenging to acquire clear ultrasound images. Additionally, fetal ultrasound can often be suboptimal due to beam limitations enforced by maternal body habitus. However, the peripheral skeletal evaluation is better on ultrasound due to real time cine imaging.

MRI is normally a complementary technique to ultrasound for evaluation of fetus and fetal anomalies. MRI visualization of the fetus is not limited by fetal position and provides a superior soft-tissue contrast, spatial resolution and has superior abilities to distinguish internal structures such as gray and white matter in the brain, neck, spine, lungs, mediastinum, liver, kidneys and wall of the abdomen. Multiple views obtained using MRI with an adjustable FOV allows for visualization of the whole fetus in relation to the gravid uterus. MRI also makes it possible to acquire true cerebral and abdomen biometric measurements rather than measurements of the skull vault [16].

One of the limitations MRI faces is its relatively high motion sensitivity. Fetal motion causes artifacts that deteriorate image quality and can render the scan non-diagnostic for measurement purposes. Due to the selection of fast imaging sequences, we were nevertheless able to produce images with high quality and high signal-to-noise ratio (SNR) within 15–20 s. The fast imaging sequences used for the study included breath-hold T2 HASTE, steady-state – free-precession TrueFISP, 3D VIBE, and DW images in all 3 planes – axial, coro-

nal and sagittal. All sequences had relatively low SAR characteristics. To enhance SNR and the speed of the scans, an iPAT factor of 2 (GRAPPA 2) was enabled. The FOV was adjusted to the body part of interest. For example, FOV was reduced in the case of the fetal brain such that reading would be similar to that in adults. Sufficient phase oversampling was provided to avoid phase wrap artifacts from the mother's body. Breath-hold times were carefully calibrated to avoid any breathing artifacts while maintaining a scan time of ~ 20 s per breath-hold.

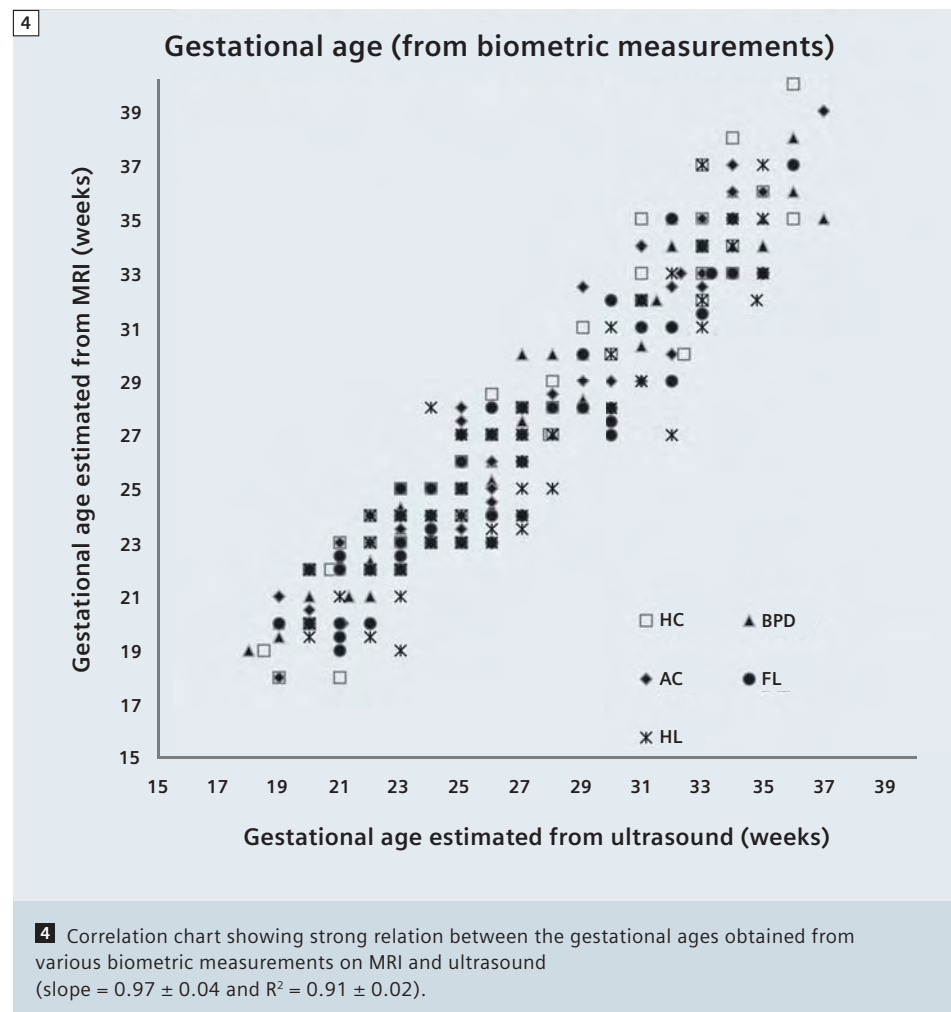
The radiologists chose the appropriate sequence for evaluation and measurement of the head and various body parts. It was noted that most of the head measurements were done by drawing appropriate regions-of-interest (ROI) on the axial or coronal T2 HASTE images where as the head and the abdominal circumferences were done on the axial TrueFISP images due to high SNR and high T1/T2 contrast enabling visualization of the structures more clearly. FL and HL measurements were mostly done on sagittal T1-weighted GRE sequences such as 3D FLASH or VIBE due to enhanced contrast of bones versus surrounding tissues. DWI and apparent diffusion coefficient computed maps also helped visualize the bones very clearly due to hypointense signal.

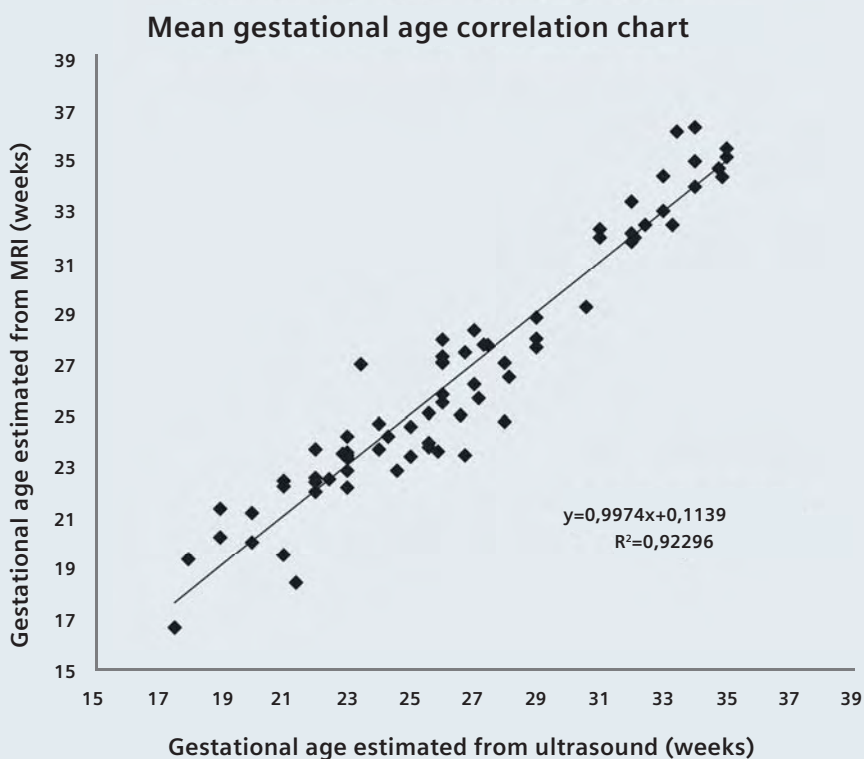
Correlation charts between head and body MRI and ultrasound biometric measurements and gestational ages (starting from 18 weeks) showed that there was a strong correlation between the two modalities for the biometrics examined, though HL and FL showed a slightly lower correlation ( $R^2 = 0.86$ ) compared to others. Reports exist that document no measure of the HL and FL from fetal MRI due to signal void of the bony cortex on MRI [7, 17]. The orientation of the femur is much less predictable than those of the head and abdomen. This leads to time consuming post-processing technique and less accurate results. Despite these challenges, our results correlated well. The ultrasound surely has the added advantage in evaluating peripheral skeletal evalua-

tion due to real time cine imaging. TCD is a stable gestational age independent parameter for early detection of fetal growth abnormalities. TCD measurements from MRI could not be compared since the ultrasound reports did not specify the respective measurements. Similarly, the gestational age based on OFD was not reported in the ultrasound for comparison with MRI. It was also very interesting to note that not all the head and body biometric measurements developed in a linear pattern with increasing GA. Some of the structures increased in size more rapidly than others as gestational age went up, as observed from the slopes of the correlation charts. HC and AC measurements had a near perfect linear increase with GA where as BPD, OFD and FL and HL measurements increased at much faster rate than HC and AC. Among all

the parameters, HL and FL had the maximum rate of growth than other measurements.

One of our major limitations in this study was the lack of follow-up of the new borns to ascertain that they were normal. This would be of particular interest if there was no abnormality detected during pregnancy on ultrasound or with MRI. The sample size was also relatively small with only 110 subjects. Intra-rater reliability of the measurements and inter-observer error were not quantified. However, both the ultrasound maternal-fetal medicine physicians/technologists and the MRI operators/radiologist were highly experienced in obtaining fetal scans/ biometric values and most likely provided accurate and reliable data.





**5** Average fetal gestational age obtained from ultrasound and MRI shows a strong correlation as indicated by the slope.

## Conclusion

Fetal\* MRI is a very useful diagnostic tool to evaluate fetal anomalies and could be a great adjunct to ultrasound for determining the fetal biometrics and gestational ages. A multi-parameter assessment of fetal gestational ages was possible with rapid high-resolution MRI techniques. An excellent correlation was observed with insignificant differences between ultrasound and MRI reported biometrics. In addition, MRI was able to provide more information regarding determination of other biometric measurements, such as trans-cerebellar diameter, and can also be very useful as a problem solving tool in assessing complex congenital anomalies. Our future goal is to include new MR biomarkers to demonstrate normal fetal growth proportions and to be able to predict fetal anomalies from biometric deviations at various gestational ages. Developments in MRI technology such as DWI and tensor imaging will further expand the role of fetal MRI to functionally map the developing brain and make it an indispensable tool in prenatal medicine.

## Acknowledgement

The authors would like to thank the technologists of University of Mississippi Medical Center for providing valuable feedback in protocol optimization and image acquisitions. The authors would like to specially thank Aaron Flammang, (Siemens Corporate Research, CAMI, Baltimore, MD, USA), for his valuable input and assistance in preparing this manuscript.

### Contact

Manohar S. Roda, M.D.  
Radiology  
University of Mississippi Medical Center  
2500 North State Street  
Jackson, MS 39216  
USA  
Phone: +1 (601) 815-5615  
Fax: +1 (601) 984-4986  
mroda@umc.edu

Judy Rose James, Ph.D.  
Radiology  
University of Mississippi Medical Center  
2500 North State Street  
Jackson, MS 39216  
USA  
Phone: +1 (601) 984-2585  
Fax: +1 (601) 984-4986  
jjames2@umc.edu

## References

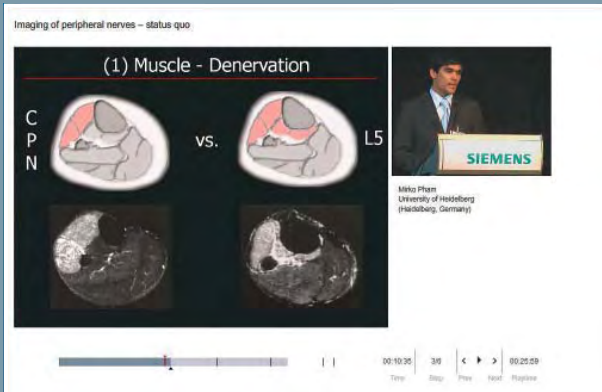
- 1 L. De Catte, et al., "Prenatal Neurologic Anomalies: Sonographic Diagnosis and Treatment," *Paediatr Drugs*, Jan 13 2012.
- 2 J. de Laveaucoupet, et al., "[What is the impact of fetal magnetic resonance imaging (MRI) on prenatal diagnosis of cerebral anomalies.]," *Med Wieku Rozwoj*, vol. 15, pp. 376-384, 2011.
- 3 A. C. Engels, "[Fetal surgery: prenatal treatment of congenital abnormalities]," *Kinderkrankenschwester*, vol. 30, pp. 409-13, Oct 2011.
- 4 O. A. Glenn and A. J. Barkovich, "Magnetic resonance imaging of the fetal brain and spine: an increasingly important tool in prenatal diagnosis, part 1," *AJNR Am J Neuroradiol*, vol. 27, pp. 1604-11, Sep 2006.
- 5 O. A. Glenn and J. Barkovich, "Magnetic resonance imaging of the fetal brain and spine: an increasingly important tool in prenatal diagnosis: part 2," *AJNR Am J Neuroradiol*, vol. 27, pp. 1807-14, Oct 2006.
- 6 R. Chung, et al., "The current state and future of fetal imaging," *Clin Perinatol*, vol. 36, pp. 685-99, Sep 2009.
- 7 C. Garel, "The role of MRI in the evaluation of the fetal brain with an emphasis on biometry, gyration and parenchyma," *Pediatr Radiol*, vol. 34, pp. 694-9, Sep 2004.
- 8 C. Garel, et al., "The fetal cerebellum: development and common malformations," *J Child Neurol*, vol. 26, pp. 1483-92, Dec 2011.
- 9 A. J. Barkovich, "MR imaging of the neonatal brain," *Neuroimaging Clin N Am*, vol. 16, pp. 117-35, viii-ix, Feb 2006.
- 10 K. R. Duncan, et al., "A comparison of fetal organ measurements by echo-planar magnetic resonance imaging and ultrasound," *BJOG*, vol. 112, pp. 43-9, Jan 2005.
- 11 C. Garel and C. Alverti, "Coronal measurement of the fetal lateral ventricles: comparison between ultrasonography and magnetic resonance imaging," *Ultrasound Obstet Gynecol*, vol. 27, pp. 23-7, Jan 2006.
- 12 M. V. Zaretsky, et al., "Comparison of magnetic resonance imaging to ultrasound in the estimation of birth weight at term," *Am J Obstet Gynecol*, vol. 189, pp. 1017-20, Oct 2003.
- 13 F. P. Hadlock, et al., "Estimation of fetal weight with the use of head, body, and femur measurements—a prospective study," *Am J Obstet Gynecol*, vol. 151, pp. 333-7, Feb 1 1985.
- 14 F. V. Coakley, et al., "Fetal MRI: a developing technique for the developing patient," *AJR Am J Roentgenol*, vol. 182, pp. 243-52, Jan 2004.
- 15 D. M. Twickler, et al., "Second-opinion magnetic resonance imaging for suspected fetal central nervous system abnormalities," *Am J Obstet Gynecol*, vol. 188, pp. 492-6, Feb 2003.
- 16 B. Tilea, et al., "Cerebral biometry in fetal magnetic resonance imaging: new reference data," *Ultrasound Obstet Gynecol*, vol. 33, pp. 173-81, Feb 2009.
- 17 M. R. Hatab, et al., "Comparison of fetal biometric values with sonographic and 3D reconstruction MRI in term gestations," *AJR Am J Roentgenol*, vol. 191, pp. 340-5, Aug 2008.

\*MR scanning has not been established as safe for imaging fetuses and infants under two years of age. The responsible physician must evaluate the benefit of the MRI examination in comparison to other imaging procedures.

# Relevant clinical information at your fingertips

From technology to clinical applications, you will find all the latest news on Siemens MR at

[www.siemens.com/magnetom-world](http://www.siemens.com/magnetom-world)



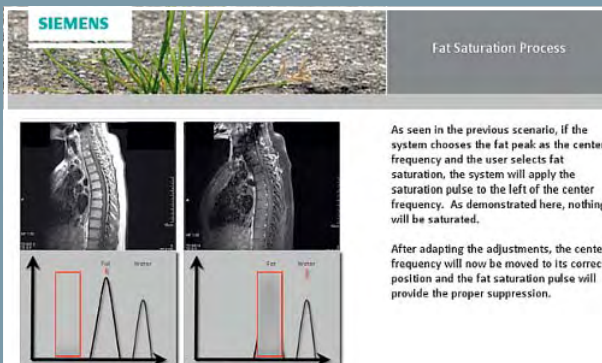
Don't miss the talks of international experts on Magnetic Resonance Imaging.

Go to  
Education > e-trainings & Presentations



The centerpiece of the MAGNETOM World Internet platform consists of our users' clinical results. Here you will find case reports and clinical methods.

Go to  
Clinical Corner > Case Studies



Just a mouse click away you will find application videos and useful tips allowing you to optimize your daily MR examinations.

Go to  
Clinical Corner > Application Tips

For the whole range of clinical MR information visit us at

[www.siemens.com/magnetom-world](http://www.siemens.com/magnetom-world)

# 3D Fetal Reconstruction from MR Imaging

Heron Werner<sup>1,3</sup>; Maene Marcondes<sup>1,3</sup>; Marcio Bernardes<sup>1,2</sup>; Thomas M. Doring<sup>1,2,3</sup>; Pedro Daltro<sup>1,3</sup>; Emerson Gasparetto<sup>1,3</sup>; Taísa Gasparetto<sup>1,3</sup>; Romeu Cortes Domingues<sup>1,2</sup>

<sup>1</sup>*Clínica de Diagnóstico por Imagem (CDPI, DASA), Rio de Janeiro, Brazil*

<sup>2</sup>*Clínica Multiimagem (MI, DASA), Rio de Janeiro, Brazil*

<sup>3</sup>*Department of Radiology, Universidade Federal do Rio de Janeiro (UFRJ), Brazil*

## Objective

The aim of this study is to illustrate and to demonstrate fetal\* abnormalities by the reconstruction of three-dimensional (3D) images obtained from magnetic resonance imaging (MRI), correlating such morphological alterations with postnatal findings.

## Introduction

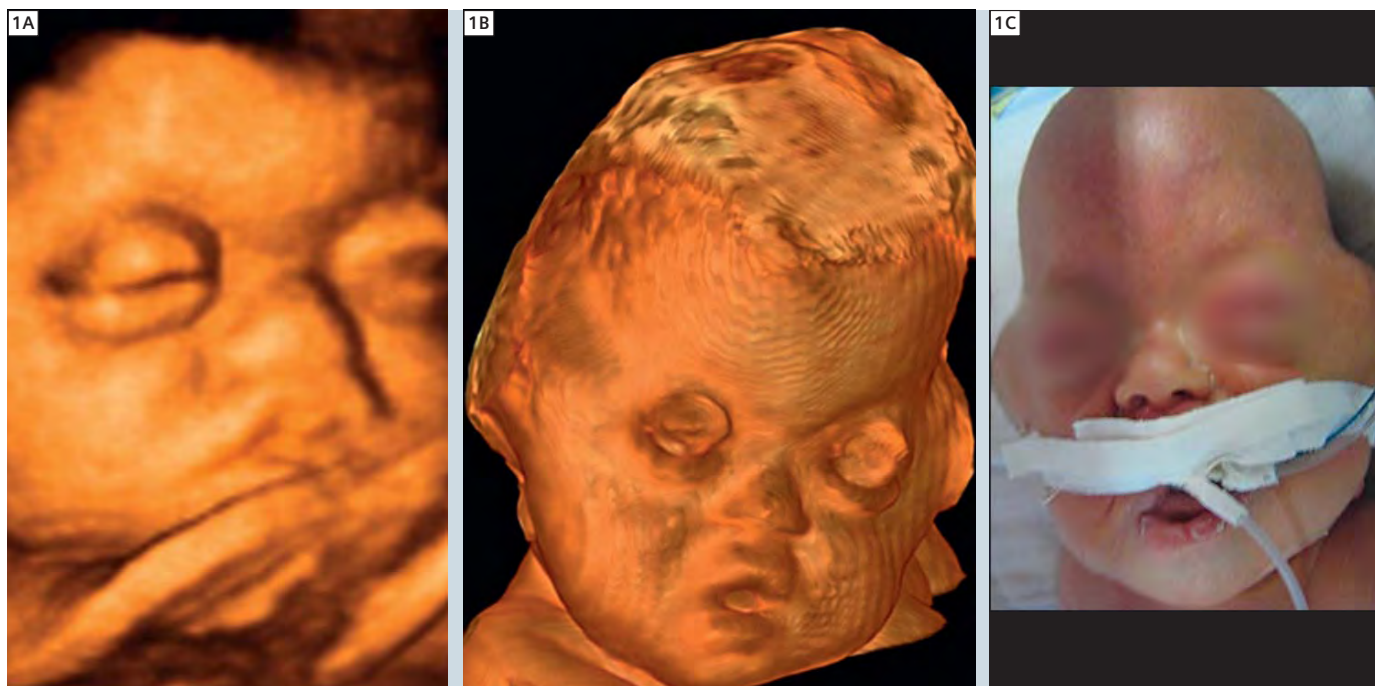
Technological advances in image processing have contributed a great deal to medicine, being particularly useful in

the diagnosis of fetal anomalies [1]. The main techniques used in the acquisition of images for gestational studies are ultrasound (US) and MRI. US is the primary image modality. It allows us to obtain immediate and reliable information for clinical advice and treatment [2, 3]. MRI is a non-invasive method that offers high-resolution fetal images with excellent contrast, enabling the visualization of internal tissues [4]. When US has dubious results, MRI is often used

because it provides information about fetal abnormalities in conditions where US can not provide images of high quality [5, 6]. With the advent of fast sequences, software dedicated to 3D reconstruction has enabled us to study more complex anatomical fetal alterations [1, 4, 7–9].

## Methods

From February 2009 to June 2011, 42 fetuses between 16 and 38 weeks



**1** 30-year-old, 36 weeks of gestation. Craniiosynostosis. (1A) reconstruction through US. (1B) Reconstruction through MR (1C) Picture of the newborn.

\*MR scanning has not been established as safe for imaging fetuses and infants under two years of age. The responsible physician must evaluate the benefit of the MRI examination in comparison to other imaging procedures.

(average of 27.2 weeks), and including four twins, were selected from assessed cases in the city of Rio de Janeiro, Brazil. All pregnant women had previously undergone US in the second trimester and were then referred for MRI examination due to suspicion of fetal abnormalities. The case studies are listed in Table 1, according to the diagnosis and gestational age. The findings from the related 3D reconstruction of images obtained from MRI were compared and related

to the postnatal diagnoses (Table 2). MRI was performed using a 1.5T MAGNETOM Avanto (Siemens, Erlangen, Germany). The protocol used was a T2-weighted TrueFISP sequence in the sagittal plane (trufi, TR/TE 3.02/1.34, voxel size 1.6 x 1.6 x 1.6 mm<sup>3</sup>, FA 70°, PAT 2, acquisition time 0.26 s). The entire examination time did not exceed 40 minutes. All tests were started without administration of sedatives. In 18 cases, the examination was interrupted because of maternal anxiety and/or

severe fetal movements.

Benzodiazepine was administered orally at a dose of 10 milligrams. About 20 minutes later, the sequences were repeated and good quality images could be obtained. The 3D reconstruction of the structure of interest was manually made from a 3D TrueFISP sequence using an interactive pen tablet (*syngo* Multimodality 2009B, Siemens, Germany), which requires an average of 30 minutes to be completed. The ethical issues associated with this study were carefully considered.

## Results

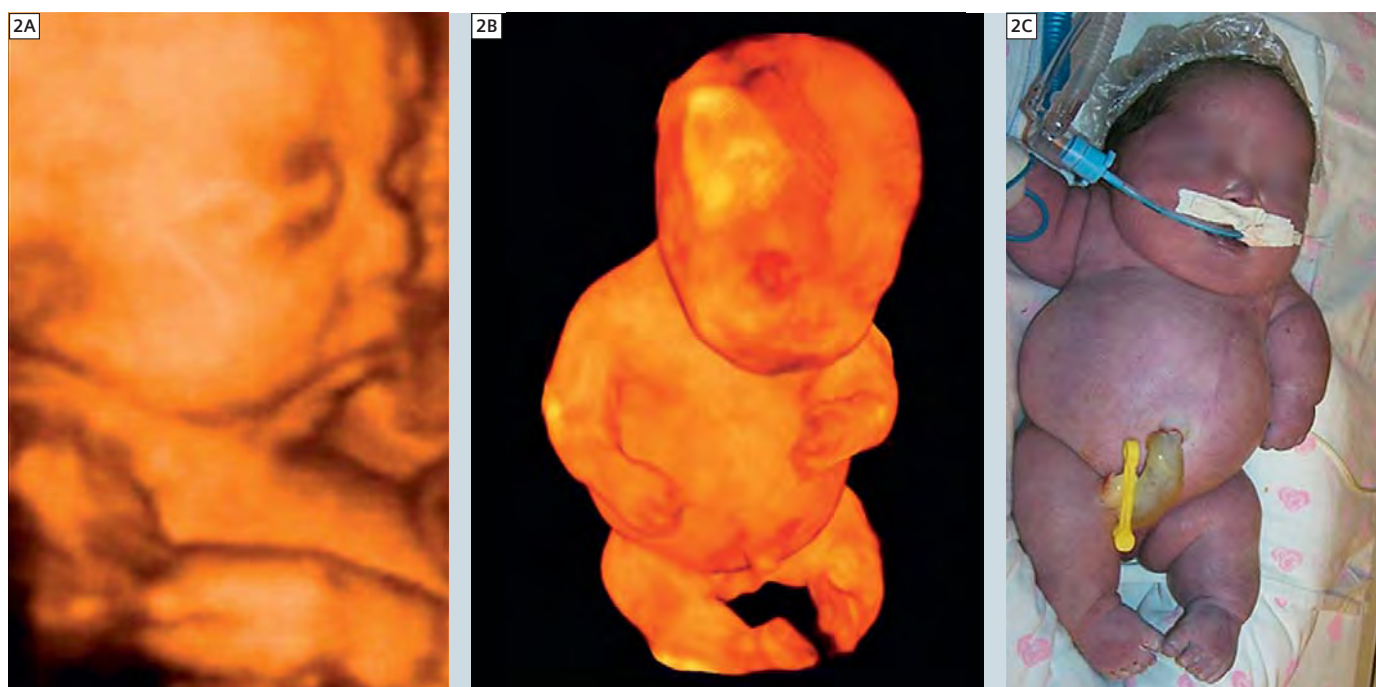
In the study population, 38 cases were evaluated pre and postnatally (Tables 1 and 2). 3D MRI reconstruction corroborated the alterations previously detected by US.

In case 37, the 3D view of a 36 week fetus obtained by MRI was similar to the postnatal image (Fig. 1). In case 36, the 3D reconstruction by MRI of a fetus with skeletal dysplasia showed the alterations

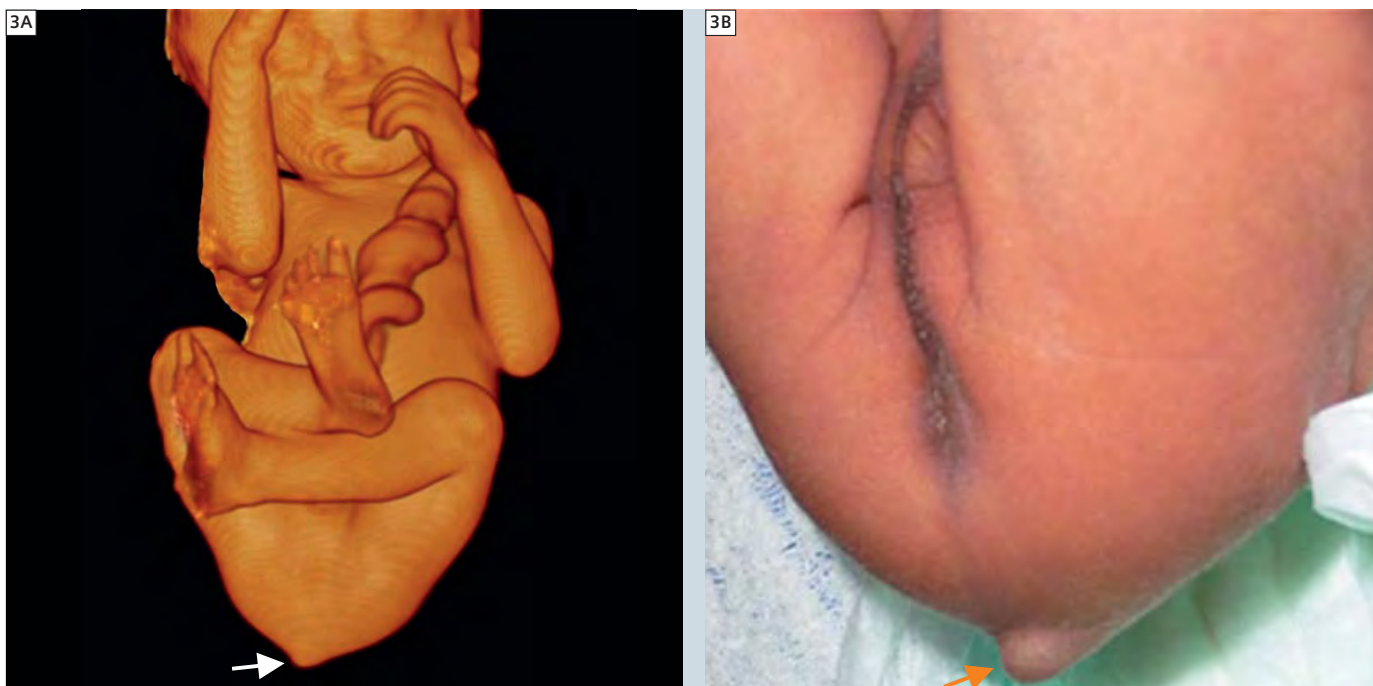
previously identified by US: shortening of long bones and hypoplastic thorax. However, this technique has a greater visual field, allowing, as a result, the evaluation of the fetus as a whole (Fig. 2). In case 26, the detection of the vestigial tail was possible only in the 3D MRI (Fig. 3).

## Discussion

US still has some limitations, such as the influence of fetal movements, the volume of amniotic fluid and the visual field for orientation. Hellinger and Epelman [10] enumerated potential benefits of using 3D MRI in fetuses, such as the possibility of improving the visualization and communication of key findings (treatment planning and counseling of parents), to improve the analysis and interpretation of examinations, to reduce the number of fast 2D sequences, and to shorten examination time. Kubik-Huch et al. [8] suggested that the use of 3D images reconstructed from MRI can increase life expectancy in the diagnosis



**2** 30-year-old, 35 weeks of gestation. Skeletal dysplasia. **(2A)** Reconstruction through US. **(2B)** Reconstruction through MR. Note facial profile hypoplastic thorax and shortening of long bones. **(2C)** Picture of the newborn.



**3** 26-year-old, 29 weeks of gestation. Syndromic aspects of facial alterations and vestigial tail. **(3A)** Reconstructions through MR. **(3B)** Picture of the newborn. Note vestigial tail (arrows).

of fetal anomalies of the morphology in the prenatal period in cases of intra-uterine growth restriction and pre-operative simulation of fetal surgery. This result may be promising to increase the applicability of the method.

The multiplanar capability of MRI can help determine the origin and extent of the abnormality. MRI is not limited to fetal position or maternal body type as in US, particularly in the third trimester.

However, oligodramnios, fetal position and artifacts produced by fetal movements have proved to be limitations in the image processing of 3D reconstruction from MRI. In some cases of severe fetal movements, there was the need for maternal sedation in order to reduce artifacts during the acquisition of volumetric sequence. Although MRI provides valuable information in cases of suspected complex fetal anomalies or where US

results might be misleading or incomplete, it should not replace US in the routine screening of the fetus or in the diagnosis of any fetal anomalies.

## Conclusion

The study of fetal malformation through 3D reconstructions by MRI should be used as a complementary tool since it adds valuable information to the educational training of specialists as well as to the emotional control of parents.

## References

- 1 Frates M, Kumar AJ, Benson CB, Ward VL, Tempany CM. Fetal anomalies: comparison of MR imaging and US for diagnosis. *Radiology* 2004; 232: 398-404.
- 2 Benacerraf BR, Benson CB, Abuhamad AZ, Copel JA, Abramowicz JS, Devore GR, Doubilet PM, Lee W, Lev-Toaff AS, Merz E, Nelson TR, O'Neill MJ, Parsons AK, Platt LD, Pretorius DH, Timor-Tritsch IE. Three- and 4-dimensional ultrasound in obstetrics and gynecology: proceedings of the American Institute of Ultrasound in Medicine Consensus Conference. *J Ultrasound Med* 2005; 24: 1587-1597.
- 3 Merz E. Current 3D/4D ultrasound technology in prenatal diagnosis. *Eur Clinics Obstet Gynaecol* 2005; 1: 184-193.
- 4 Werner H, Dos Santos JRL; Fontes R, Daltro P, Gasparetto E, Marchiori E, Campbell S. Additive manufacturing models of fetuses built from three-dimensional ultrasound, magnetic resonance imaging and computed tomography scan data. *Ultrasound Obstet Gynecol* 2010; 36: 355-361.
- 5 Brugger PC, Stühr F, Lindner C, Prayer D. Methods of fetal MR: beyond T2-weighted imaging. *Eur J Radiol* 2006; 57: 172-181.
- 6 Prayer D, Brugger PC, Kasprian G, Witzani L, Helmer H, Dietrich W, Eppel W, Langer M. MRI of fetal acquired brain lesions. *Eur J Radiol* 2006; 57: 233-249.
- 7 Campadelli P, Casiraghi E, Lombardi G, Serrao G. 3D volume reconstruction and biometric analysis of fetal brain from MR images. In *Computational Intelligence Methods for Bioinformatics and Biostatistics*, Masulli F, Tagliaferri R, Verkhivker GM (eds). Springer-Verlag: Berlin and Heidelberg, 2009; 188-197.
- 8 Kubik-Huch RA, Wildermuth S, Cettuzzi L, Rake A, Seifert B, Chaoui R, Marincek B. Fetus and uteroplacental unit: fast MR imaging with three-dimensional reconstruction and volumetry-feasibility study. *Radiology* 2001; 219: 567-573.
- 9 Rubesova E, Vance CJ, Ringertz HG, Barth RA. Three-dimensional MRI volumetric measurements of the normal fetal colon. *AJR Am J Roentgenol* 2009; 192: 761-765.
- 10 Hellinger JC, Epelman M. Fetal MRI in the third Dimension. *Applied Radiology* 2010; 39: 8-22.

## Contact

Heron Werner  
Clínica de Diagnóstico por Imagem  
Rio de Janeiro  
Brazil  
heron.werner@gmail.com

**Table 1: Summary of the 38 cases with abnormalities: diagnostic correlation and gestational age.**

Case studies*	Gestational age at examination (weeks)	Diagnoses
1	16	Acrania
2	20	Gastroschisis
3 (#)	20	Monochorionic- diamniotic twin pregnancy (acardiac fetus) (#)
4	22	Skeletal dysplasia (shortening of long bones and thoracic hypoplasia)
5	22	Occipital encephalocele, cervical and dorsal meningocele
6	23	Parietal encephalocele
7	24	Isolated hypoplasia of the tibia and fibula
8	24	Chiari II malformation
9	24	Patau syndrome (Trisomy 13)
10	25	Occipital parietal prominence
11	25	Omphalocele and allantoic cyst
12	25	Isolated forearm amputation
13	26	Chiari II malformation
14	26	Chiari II malformation
15	26	Beckwith-Wiedemann syndrome
16	26	Chiari II malformation associated with clubfeet
17	26	Edwards syndrome (Trisomy18)
18	27	Omphalocele
19	27	Cervical lymphangioma
20	27	Chiari II malformation
21(#)	27	Monochorionic- diamniotic twin pregnancy (Gastroschisis in one fetus) (#)
22 (§)	27	Imperfect twinning (conjoined abdominal and/or thoracic cavities) (§)
23	28	Edwards syndrome (Trisomy18)
24	28	Chiari II malformation
25	28	Umbilical cord insertion in the fetal abdomen cyst
26	29	Cryptic chromosomal abnormality (apparent translocation 7;15)
27	29	Sacroccygeal teratoma type III and clubfeet
28	29	Intrauterine growth restriction
29 (§)	30	Imperfect twinning (thoraco-omphalopagus) associated with clubfeet (§)
30	30	Cervical lymphangioma
31	31	Ulnar hypoplasia, radial agenesis and clubhands
32	31	Skeletal dysplasia (hyperlordosis, clubhands and clubfeet)
33	32	Gastroschisis
34	33	Skeletal dysplasia (shortening of long bones and thoracic hypoplasia)
35	35	Cervical lymphangioma
36	35	Skeletal dysplasia (shortening of long bones and thoracic hypoplasia)
37	36	Craniosynostosis
38	38	Cervical teratoma

\*Thirty-eight cases are shown: cases 22 and 29 (§) included four fetuses with thoraco-omphalopagus and cases 3 and 21 (#) included twin pregnancy with one twin affected.

**Table 2: Abnormalities detected in the 3D reconstruction of MRI alongside their postnatal confirmation.**

Regions	Malformations	Identified abnormalities through 3D MRI	Posnatal confirmation
<b>Skull and Face</b>	Acrania	1	1
	Microcephaly	4	4
	Brachycephaly	1	1
	Increased longitudinal and lateral skull (skull in "clover")	1	1
	Encephalocele	3	3
	Prominence of the forehead / occipital parietal prominence	2	2
	Microphthalmia	1	1
	Exophthalmos	2	2
	Hypotelorism	2	2
	Hypertelorism	3	3
	Nasal hypoplasia (saddle nose)	7	7
	Cebocephalia	1	1
	Cleft lip	2	2
	Macroglossia	1	1
	Micrognathia	2	2
	Low-set ears	6	6
<b>Neck and Thorax</b>	Tumor	4	4
	Hypoplastic	3	3
	Merged (imperfect twinning)	2	2
	shapeless mass of tissue (acardiac fetus)	1	1
<b>Abdomen</b>	Omphalocele	3	3
	Gastroschisis	3	3
	Merged (imperfect twinning)	2	2
	Umbilical cord insertion in the fetal abdomen cyst	2	2
<b>Spine and Extremities</b>	Spina bifida	7	7
	Hyperlordosis (concavity)	1	1
	Shortening of long bones	7	7
	Isolated forearm amputation	1	1
	Clubfeet	4	4
	Clubhands	2	2
	Sacroccygeal tumor	1	1
	Vestigial tail	1	1
<b>Total</b>		<b>83</b>	<b>83</b>

# Listen to the talks on 7T imaging that we have captured during the last Ultra High Field User Meeting



**Robin Heidemann**  
Max Planck Inst. (Leipzig, Germany)

**Physics of ultra high field**



**Zang-Hee Cho**  
NRI, Gachon Medical School (Incheon, Korea)

**Pre-Clinical and Clinical 7T Studies**



**Sebastian Schmitter**  
University of Minnesota (Minneapolis, United States)

**7T TOF Angiography**



**Siegfried Trattnig**  
Medical University of Vienna (Vienna, Austria)

**MSK at 7T**



**Armin M. Nagel**  
DKFZ (Heidelberg, Germany)

**Low Gamma Imaging at 7T**



**Michael Bock**  
DKFZ (Heidelberg, Germany)

**Neuro Oncology Imaging**



**Rainer Goebel**  
Brain Imaging Center (Maastricht, Netherlands)

**Neuroscience at 7T and beyond**



**Oliver Speck**  
IfN, Univ. Magdeburg (Magdeburg, Germany)

**Flow Visualization in Cranial Vessels**



**Thoralf Niendorf**  
Berlin Ultrahigh Field Facility (Berlin, Germany)

**Exploring Cardiovascular Diseases**



**Peter van Gelderen**  
National Institutes of Health (Bethesda, United States)

**T2 Imaging,  $B_0$  and  $B_1$  Shimming**

Visit us at [www.siemens.com/magnetom-world](http://www.siemens.com/magnetom-world)

Go to **International Version > Education > e-trainings & Presentations**

# Cerebral TOF Angiography at 7T: Pushing the Limits to Reap the Benefits of Ultra-High Field Imaging

Sebastian Schmitter<sup>1</sup>; Xiaoping Wu<sup>1</sup>; Josef Pfeuffer<sup>2</sup>; Michael Hamm<sup>2</sup>; Kâmil Uğurbil<sup>1</sup>; Pierre-François Van de Moortele<sup>1</sup>

<sup>1</sup>University of Minnesota, Center for Magnetic Resonance Research, Minneapolis, MN, USA

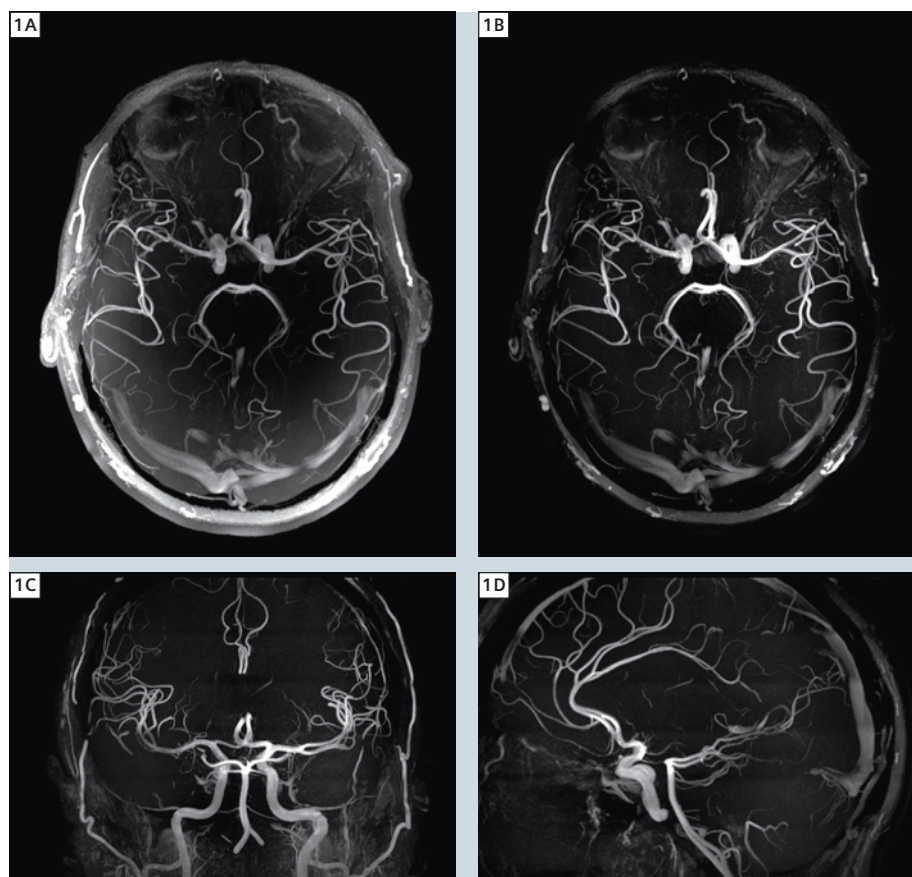
<sup>2</sup>MR Application Development, Siemens Healthcare, Erlangen, Germany

## Background

Time-of-flight (TOF) imaging is clinically the most commonly used non-contrast enhanced MR angiography (MRA) technique [1]. In 3D-TOF a slab selective 3D steady state gradient echo sequence with a TR much shorter than the T1

relaxation time of static tissue, usually in the order of 20-60 ms, is used in combination with a sufficiently large flip angle of typically 20°–40°. Under this steady-state regime, signal from static 'background' tissue is strongly reduced while fully relaxed blood flowing into the excita-

tion slab provides strong MR signal, resulting in a positive, suitable vessel contrast. Since the initial demonstration at 1.5T that TOF angiograms could be obtained in a single gradient echo acquisition, without image subtraction [2], allowing for detecting occlusions and aneurisms in the human brain, multiple sequence developments have greatly improved contrast and image quality in cerebral TOF MRA. As a relatively large volume coverage is sought with high spatial resolution, a multiple overlapping thin slab approach [3] has become a standard in order to limit, within each imaging slab, the progressive attenuation of blood signal which inevitably occurs with short TR repeated excitations. Substantial contrast enhancement between unwanted static background signal and blood signal is obtained with magnetization transfer (MT) contrast pulses, yielding a significant suppression of static tissue signal [4] with only a minor impact on blood signal. Cerebral TOF imaging also has the capability to selectively visualize arterial blood vessels, which can be achieved by positioning a travelling saturation slab above the imaging slab to saturate signal from venous blood flowing in head-foot direction. Alternatively, the same approach can be used to selectively visualize venous signal by positioning the saturation slab below the imaging slab.



**1** Maximum intensity projections (40 mm thickness) of a whole brain, multi-slab 3D-TOF data set at 7T using a non-optimized protocol, with a resolution of  $0.34 \times 0.34 \times 0.4 \text{ mm}^3$ . Neither VERSE transformation, saturation pulse nor MT pulses were enabled. The importance of removing the receive RF coil profile from TOF images can be appreciated by comparing Fig. 1A (receive profile not removed) with Fig. 1B–D (receive profile removed).

## High field benefits

An important characteristic of TOF imaging sequences is that they directly benefit from using MR scanners operating at higher magnetic field. This positive

## Data acquisition

Measurements were performed at the Center for Magnetic Resonance Research, Minneapolis, on two whole body 7 Tesla scanners (Siemens Healthcare, Erlangen, Germany), each being equipped with a 16-channel  $B_1^+$  shimming unit with 16 x 1 kW RFamps (CPC, Hauppauge, USA). One of the two scanners was a prototype 16-channel pTX Siemens system equipped with its own 16 x 1 kW RFamps capable of generating 16 independent RF pulse shapes to feed the 16-channel transceiver coil used in this study. Prior to TOF acquisition, second order  $B_0$  shimming was performed and flip angle maps were acquired [32] to adjust RF frequency and RF voltage references. TOF images were acquired using 3 different parameter sets:

**1)** For contrast optimization based on VERSE excitation, VERSE saturation and sparse MT pulses, the following

parameters were used: FOV 220 x 172 x 78 mm<sup>3</sup>, resolution (0.5 mm)<sup>3</sup>, 4 slabs with 24 mm thickness each, 25% overlap,  $\alpha = 24^\circ$ , TR / TE = 33 ms / 3 ms.

**2)** For  $B_1^+$  shimming and pTX, the following parameters were altered: FOV 220 x 172 x 60 mm<sup>3</sup>, 3 slabs of 24 mm thickness,  $\alpha = 23^\circ$ , TR / TE = 25 ms / 3 ms (25 / 3.6 ms for pTX). In all  $B_1^+$  shimming acquisitions, venous saturation RF pulses were applied with CP-mode phase setting, but no MT pulses were used. In pTX acquisitions, only excitation pulses were used (neither saturation nor MT pulses).

**3)** Additionally to these (0.5 mm)<sup>3</sup> resolution protocols, a non optimized (0.34 mm)<sup>3</sup> resolution TOF data set was acquired without VERSE, without saturation pulses and without MT pulses for comparison. All reported SAR values were measured by the console and are given in percent of the SAR limit ( $SAR_{max}$ ) defined by the regulatory guidelines.

impact results from higher signal-to-noise ratio (SNR) [5] and from longer T1 relaxation constant in cerebral tissues [6] yielding further static tissue steady-state saturation, thus higher contrast between vessel and background signal. These field dependent advantages, already demonstrated in clinical practice when moving from 1.5T to 3T [7], provide the opportunity to further enable smaller vessels conspicuity and vascular defects detection when moving up to 7T\* [8–10]. However, serious challenges need to be addressed before the full benefit of imaging at ultra high field (UHF) can be realized, especially with regards to SAR limits and  $B_1$  inhomogeneity.

## Challenges and limits at UHF

### SAR

The specific absorption rate (SAR) often is a challenging constraint at UHF because achieving a given excitation flip angle at higher Larmor frequency requires a substantial increase in RF power for a fixed combination of RF pulse shape and RF pulse duration, with increased SAR. This SAR increase makes it impossible, at 7T, to apply as-is some efficient approaches utilized at 1.5T to improve TOF angiogram quality, such as saturation and MT pulses that require high levels of RF power [8, 11–13]; running at 7T a standard TOF protocol based on 3T parameters, including both

these pulses, would yield more than 300% of the maximum SAR limits ( $SAR_{max}$ ). It should be noted that, even at 3T, MT pulses are not always applied because, in some TOF protocols, the combination of relatively high excitation flip angle, short TR and saturation pulses may already reach the maximum SAR limits.

### $B_1^+$ field inhomogeneity

At 7T, where RF wavelength is in the order of human head dimensions, complex transmit  $B_1$  ( $B_1^+$ ) field interferences occur through the brain, resulting in strongly inhomogeneous RF excitation [14]. The typical pattern obtained with a volume coverage transmit head coil consists of strong  $B_1^+$  field amplitude in the center of the brain and much weaker amplitude in the periphery [15]. For TOF imaging this spatial pattern tends to result in stronger angiographic contrast in the brain center and suboptimal contrast in the periphery, which can be deleterious especially for vessels in the periphery, and for smaller vessels with slow flow taking their origin in central parts of the brain.

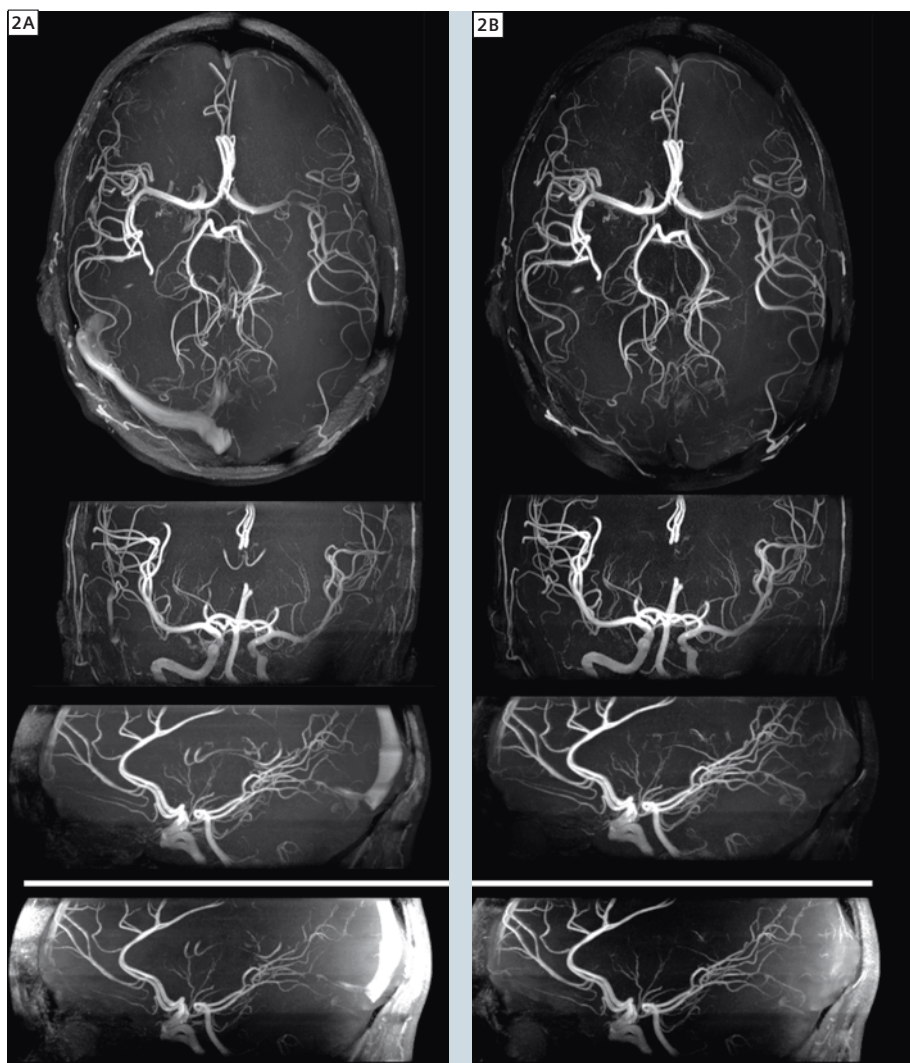
### $\Delta B_0$ , $T_2^*$ and chemical shift

Additional to SAR and  $B_1^+$  inhomogeneity issues, imaging at very high field also requires dealing with increased suscepti-

## TOF image processing

To better estimate the impact of each RF management component on TOF angiograms, the RF coil receive (RX) profile was estimated and removed from all native TOF images unless otherwise stated. To estimate the RX profile, for each session a single slice small tip angle GRE image was divided by the flip angle map and spatially smoothed. The resulting dataset was then approximated by a 2D polynomial function to obtain a continuous function and the TOF dataset was divided by this function. After RX profile reduction, maximum intensity projections (MIP) were generated with 50 mm thickness, unless otherwise stated.

\*The product is still under development and not yet commercially available. Its future availability cannot be ensured.



**2** Comparison of MIP images generated from TOF images acquired: **(2A)** without VERSE, without venous saturation and without MT pulses, and **(2B)** with VERSE applied on excitation pulse and venous saturation pulse, together with MT pulse applied prior to the center-most 10% of the k-space lines. Gray scale windowing was deliberately adjusted toward a higher visibility of background signal to better appreciate the impact of using these RF pulse strategies. The two bottom rows only differ in their post-processing status: the receive profile of the RF coils was not removed in the lowest row for comparison purpose.

bly induced  $\Delta B_0$ , increased fat/water chemical shift and shorter  $T_2^*$  relaxation constants. As will be seen, these additional challenges have a direct impact on methods aiming at mitigating  $B_1$  heterogeneity and reducing SAR, although they can, sometimes, be used as an advantage.

### Solutions for reducing SAR while optimizing TOF contrast

#### VERSE: SAR reduction for excitation and saturation pulses

A common approach at UHF to reduce

RF power consists of extending RF pulse duration while reducing RF amplitude, resulting in final SAR proportional to the inverse of the RF pulse duration. This approach however can only be applied up to a certain degree, since unwanted  $T_2$  relaxation effects may occur during excessively long RF excitation and an increase in minimum TE may yield undesired  $T_2^*$  weight, especially at UHF where  $T_2$  and  $T_2^*$  relaxation constants are shorter [16]. A well known, similar and more efficient approach is the vari-

able rate selective excitation (VERSE) [17], which enjoys a regain of interest with the fast development of 7T human scanners. Here, based on the quadratic dependence of RF power on RF pulse amplitude, only segments of the pulse with an amplitude exceeding a pre-defined threshold are stretched in time to keep RF amplitude below this threshold, allowing for significant RF power and SAR reduction with very limited increase in pulse duration. Further, RF pulse segments with RF amplitude below the threshold may be compressed to keep the RF pulse duration strictly unchanged.

We implemented the VERSE transformation for both, TOF excitation and venous saturation pulses, setting the excitation amplitude threshold to 50%, and the saturation amplitude threshold to 25% or 30%, of the peak amplitude of the initial excitation and saturation RF pulses, respectively. Because the VERSE transformation intrinsically lowers the bandwidth of some RF segments, the resulting profile is more susceptible to chemical shift and susceptibility induced  $\Delta B_0$  variations [10]. However, applying VERSE on the selective venous saturation RF pulse can have beneficial side effects in the context of a large chemical shift ( $\sim 1$  kHz) between fat and water protons at 7T: with the VERSE venous saturation profile centered on the chosen venous saturation slab for water protons, the corresponding fat proton profile gets shifted in space along the slice selective direction. This shift can be adjusted to coincide with the TOF imaging slab, strongly attenuating fat signal in angiograms [18].

#### Sparse MT pulses: reducing SAR while preserving contrast enhancement

MT pulses are well known for their high demand in RF power, which even at lower field sometimes forbids their inclusion in imaging protocols. In order to drastically reduce MT induced SAR, we implemented a sparse utilization of MT pulses, applying them only prior to the acquisition of k-space lines close to the k-space center. At lower field this approach already proved to be an effec-

tive tradeoff between power reduction and contrast enhancement [19, 20]. Here, at 7T, we applied MT pulses to the centermost 10% of the acquired k-space lines, allowing for substantial gain in vessel to tissue contrast while limiting SAR increase to only about 20%.

### **B<sub>1</sub><sup>+</sup> shimming: addressing heterogeneous transmit B<sub>1</sub> profile**

Transmit B<sub>1</sub> (B<sub>1</sub><sup>+</sup>) shimming (or RF shimming) is an effective method to spatially modify the B<sub>1</sub><sup>+</sup> field amplitude (thus the excitation flip angle profile) by modulating the amplitude and/or phase of the RF input for each channel of a multi-element transmit coil [21]. In the present study, we used a 16-channel transceiver coil similar to [22], powered by 16 x 1 kW amplifiers with a B<sub>1</sub> shimming unit capable of channel-wise RF amplitude and phase modulation (in this work we only adjusted RF phase, not RF magnitude). When B<sub>1</sub> shimming was not used, RF phases were set in a 'circularly polarized-like' (CP-like) mode, to approximate a volume head coil profile (bright center, weak periphery). When applying B<sub>1</sub> shimming, we calculated a set of RF

phases generating a much more homogeneous excitation profile by minimizing, in regions-of-interest (ROIs) drawn on 7 axial slices, the coefficient of variation (CV) of |B<sub>1</sub><sup>+</sup>|, where  $CV = \text{std}(|B_1^+|) / \text{mean}(|B_1^+|)$ , to the cost however of a lower RF efficiency with a reduced B<sub>1</sub> Multi-Channel Interference Index (see definition in B<sub>1</sub> shimming text box).

### **Parallel transmit spoke RF pulses: shaping further the excitation profile**

A noticeable advantage of 'parallel transmit' (pTX) methods [23, 24] over B<sub>1</sub> shimming is the capability to further shape the final *excitation pattern* rather than just altering a static *transmit B<sub>1</sub> profile*. This is typically achieved by combining, in different ways depending on the chosen pTX approach, dynamic modulations of spatial encoding gradients together with independent RF pulse shapes one each transmit RF channel. The so-called 'selective pTX spoke RF pulse design' consists of applying several slice or slab selective pTX sub-pulses separated by spatial encoding gradient blips. Although the *same pulse shape* is typically used for all channels and all

sub-pulses, a *different magnitude and phase* is applied for each transmit channel during each sub-pulse [25, 26].

Another advantage of pTX methods is that ΔB<sub>0</sub> maps can often be included in RF pulse calculations to avoid corresponding deviations of the excitation profile.

In order to demonstrate the use of 16-channel pTX spoke RF pulses for improving contrast homogeneity in cerebral TOF at 7T, we implemented this approach on a prototype 7T human system equipped with 16 independent transmit channels (Siemens Healthcare, Erlangen, Germany). We utilized a 3-axial slab TOF protocol and we designed, for each of these slabs, a 2-spoke pTX RF pulse, based on 16 complex B<sub>1</sub><sup>+</sup> maps and a ΔB<sub>0</sub> map measured in 3 different axial slices (top, center and bottom slices of the slab). The pTX RF pulse optimization was performed based on the magnitude least squares method [27] using the spatial domain formalism [28]. For comparison, a single spoke acquisition (thus with a single B<sub>1</sub> shimming setting) was obtained using a CP-like B<sub>1</sub> setting.

## **B<sub>1</sub><sup>+</sup> shimming: methods**

We used a 16-channel stripline transceiver coil similar to [22] powered by 16 x 1 kW amplifiers in combination with a remotely operated phase/gain control unit capable of altering the phase and amplitude of the low voltage input of each RF amplifier (CPC, Hauppauge, USA). In this work, we only adjusted the phase  $\varphi_k$  (not the magnitude) of each transmit (TX) channel k (with k:1→16). The 16 complex, spatial B<sub>1</sub><sup>+</sup> profiles needed for B<sub>1</sub><sup>+</sup> shimming optimization were acquired using a hybrid approach [31]. Firstly, an absolute 3D |B<sub>1</sub><sup>+</sup>| map was acquired using the actual flip angle (AFI) mapping technique [32] with all channels transmitting together. Secondly, 16 relative B<sub>1</sub><sup>+</sup> maps were acquired in the small flip angle regime in 7 axial gradient echo 2D images. By combining both datasets, complex B<sub>1</sub><sup>+</sup> maps were obtained for each of the 16 individual channels. When applying a set of transmit B<sub>1</sub> phases, the final complex B<sub>1</sub><sup>+</sup> field of the 16-channel transmit coil is a linear superposition of the 16 complex spatial profiles B<sub>1,k</sub><sup>+</sup>

$$\text{(with } k:1 \rightarrow 16): B_1^+(r) = a \sum_{k=1}^N B_{1,k}^+(r) \cdot e^{i\varphi_k} \quad \text{where } r \text{ represents}$$

the spatial position [14]. B<sub>1</sub><sup>+</sup> shimming phases were calculated to minimize the coefficient of variation of B<sub>1</sub><sup>+</sup> through ROIs drawn on the axial slices. For each set of transmit B<sub>1</sub> phases, the resulting B<sub>1</sub><sup>+</sup> efficiency was quantified with a B<sub>1</sub> Multi-Channel Interference (B<sub>1</sub>MCI) Index obtained by dividing the magnitude of the sum (MOS) of the complex B<sub>1,k</sub><sup>+</sup> field by the sum of the magnitude (SOM) of the same B<sub>1,k</sub><sup>+</sup> fields [14, 21, 30]. By definition, the B<sub>1</sub>MCI Index takes values between 0 (fully destructive interferences) and 1 (fully constructive interferences):

$$B_1 \text{ MCI Index} = \frac{\left| \sum_{k=1}^N B_{1,k}^+(r) \cdot e^{i\varphi_k} \right|}{\sum_{k=1}^N |B_{1,k}^+(r)|} = \text{MOS/SOM}.$$

Overall, global SAR values are approximately proportional to the inverse of the squared B<sub>1</sub>MCI Index. All computations were using nonlinear optimization tools in Matlab (The Mathworks, USA).

### pTX 2-spoke RF pulse design: methods

Parallel transmission (pTX) was performed with the 16-channel prototype 7T system. We designed 2-spoke slab selective RF pulses aiming at achieving uniform excitation flip angle through the ROIs drawn on 2D gradient echo axial images. Different transmit  $B_1$  settings were applied during each of the two sub-pulses which were separated by a brief gradient encoding blip [25]. During the optimization routine, a complex weighting factor (amplitude and phase) was calculated for each channel and each spoke, based on the spoke location in k-space, on the 16 complex  $B_1^+$  profiles and on  $B_0$  maps for each slice. For each of the three slabs in pTX TOF, three slices (top, center and bottom) were used for optimizing the flip angle inside ROIs drawn on the latter. The optimization was performed using the magnitude least squares method [27] using 2 spokes of 1.5 ms duration each. For comparison a single spoke acquisition using a CP-like phase setting was also acquired.

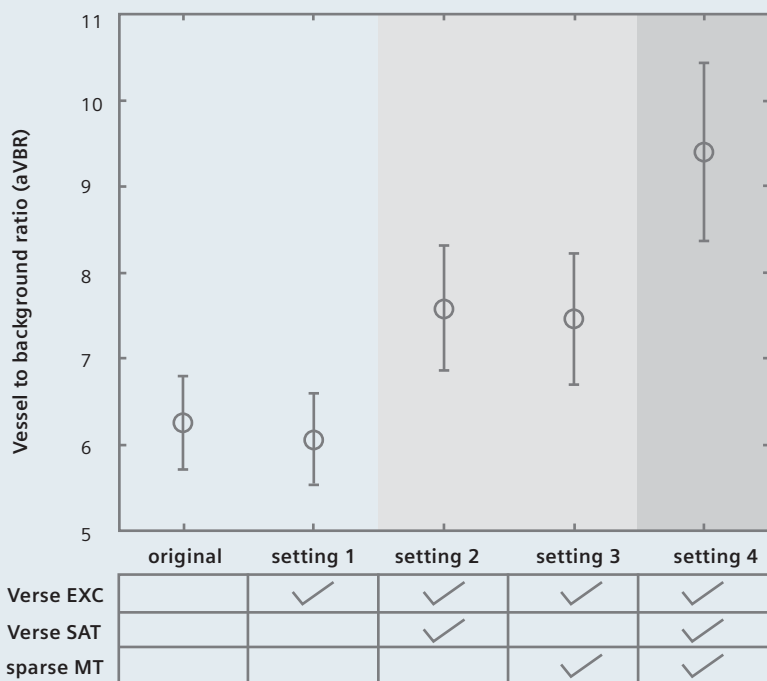
### Results

Some of the main potential strengths and limitations of TOF angiography at UHF are illustrated in Fig. 1, showing a  $0.34 \times 0.34 \times 0.4 \text{ mm}^3$  resolution 3D-TOF acquired at 7 Tesla. The non-corrected axial thick maximum intensity projection (MIP) view shown in Fig. 1A is a reminder of the large apparent signal amplitude variation, in the form of a positive centrifugal gradient, which results from the root sum of square of the sensitivity profiles with a coil array. After removing this receive  $B_1$  profile, in Figs. 1B–D, a fairly sharp vessel to tissue contrast can be appreciated, together with intrinsically high SNR in some small vessels, both effects being indicative of direct imaging benefits at higher fields. Some limitations, however, can also be readily identified. Indeed, because of SAR limitations, neither saturation nor MT pulses could be used in this standard TOF protocol, which resulted in strong venous blood signal (see for example the large posterior draining veins) as well as limited background signal suppression, and non-saturated subcutaneous fat signal. Another confounding factor, which may be less evidently identified at first sight, is the fact that a stronger angiographic contrast is obtained in the center of the brain, with, in average, more limited small vessel conspicuity in the periphery. In order to facilitate the comparison of methodological components developed to address these issues in our study, all TOF experiments shown in the present report (except for Fig. 1) were acquired at the same isotropic resolution of  $0.5 \times 0.5 \times 0.5 \text{ mm}^3$ .

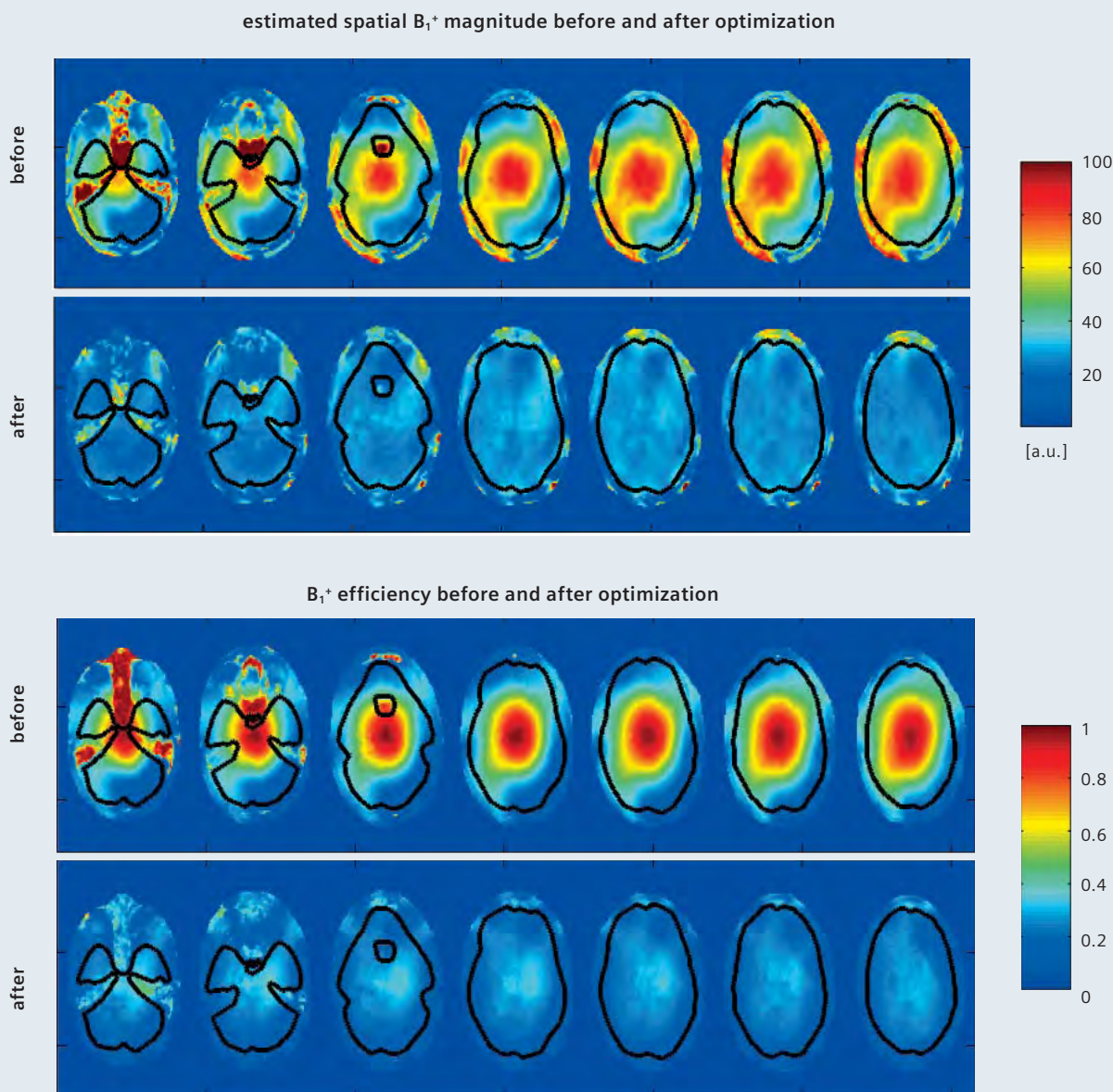
### VERSE and sparse MT pulses

Figure 2 demonstrates the dramatic gains in vessel to tissue contrast that can be obtained when including VERSE venous saturation pulse and sparse MT pulses in the TOF protocol, as shown in Fig. 2B, to be compared with Fig. 2A where neither standard saturation nor standard MT pulses could have been

3



**3** TOF contrast improvement obtained by applying saturation (SAT) and MT RF pulses, quantified by measuring the arterial vessel to background signal ratio (aVBR) in 5 subjects. The bottom grid indicates which RF strategies were applied in each case. As expected, no noticeable difference was observed when only applying VERSE to the excitation pulse, whereas clear contrast gain was obtained with either VERSE saturation or sparse MT pulses. Note the synergy observed when both latter pulses are used.



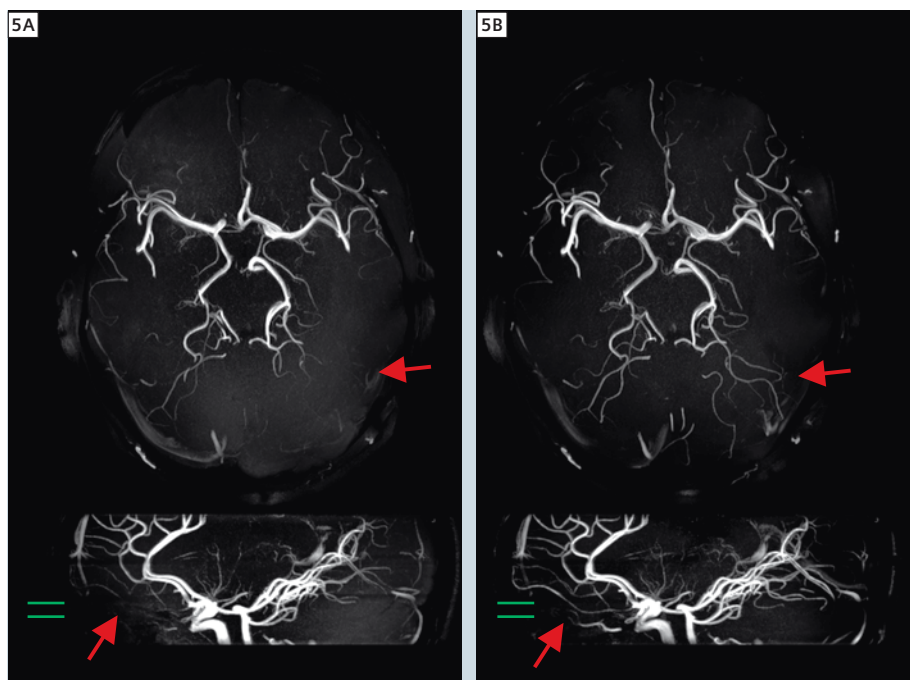
**4 Top two rows:** Estimated spatial  $B_1^+$  maps obtained before  $B_1$  shimming, applying a set of CP-like transmit phases (before), and after  $B_1$  shimming with a set of  $B_1$  transmit phases computed to achieve a more homogeneous  $|B_1^+|$  pattern (after). **Bottom two rows:** Corresponding  $B_1$  Multi-Channel Interference index maps, showing  $B_1^+$  efficiency with CP-like transmit phases (before) and with  $B_1$  shimming (after).

included due to SAR limits. Note that the gray scale in these images has been deliberately adjusted to exaggerate the visibility of residual background signal to help identifying the discussed effects. Beside the evident suppression of venous blood signal and a strong attenuation of residual background signal, helping better visualizing smaller vessels, it can be seen that the selective saturation pulse also provides, within the imaging slab, a significant reduction, up to 90%, of the subcutaneous fat signal. This effect, obtained by exploiting the large water/fat chemical shift, is especially beneficial when generating maxi-

mum intensity projections. Noticeably, the improvement in TOF contrast, expressed as the arterial vessel to background signal ratio (aVBR), does not result solely from sparse MT pulses, it also results from MT effects induced by VERSE saturation pulses [29]. This synergy is summarized for 5 subjects in Fig. 3: either VERSE saturation or sparse MT pulse increases the contrast by about 20%, whereas applying both pulses improves the contrast by about 50%. On the other hand, as expected, applying the VERSE transformation on the excitation pulse does not affect the contrast. Importantly, the optimized protocol

(with VERSE excitation, VERSE saturation and sparse MT pulses) only generates 69% of  $SAR_{MAX}$ , whereas applying standard excitation, saturation and MT pulses would generate about 320% of  $SAR_{MAX}$ .

Despite of these substantial improvements in angiogram quality, one can notice that TOF contrast still is inhomogeneous in Fig. 2B with, in average, a stronger contrast with brighter vessels in the center of the brain, and a reduced visibility of smaller vessels in the periphery, especially in the anterior and posterior poles of the brain. These effects are a direct consequence of the inhomoge-



**5** 15 mm thin axial and 50 mm thick sagittal MIP images from multi-slab 3D TOF data sets acquired with different  $B_1^+$  phase settings during the excitation RF pulse: **(5A)** CP-like transmitter phase setting (no  $B_1$  shimming) and **(5B)** after  $B_1$  shimming with a set of  $B_1$  transmit phases computed to achieve a more homogeneous  $|B_1^+|$ . In both cases, saturation RF pulses were applied using a CP-like transmit phase setting. MT was not used in any of the two data sets. The green bars in the sagittal MIP images indicate the position of the axial MIP location.

neous CP-like transmit  $B_1$  field profile, and must be distinguished from the receive  $B_1$  profile bias which, for comparison and demonstration purpose, has not been removed from the images shown in the lowest row of Fig. 2. In the next two sections, we will demonstrate the potential of applying recently developed multi channel methods to address  $B_1$  inhomogeneity issues in TOF at 7T.

### $B_1$ shimming

A remarkable improvement in  $|B_1^+|$  homogeneity was achieved with  $B_1$  shimming, as demonstrated in Fig. 4 where the two upper rows show, in 7 axial slices, the flip angle maps measured before (CP-like mode) and after (homogeneous  $|B_1^+|$ )  $B_1$  shimming (only pixels in the ROIs are considered), with the coefficient of variation of  $|B_1^+|$  dropping from 35% to 14%. One can appreciate in Fig. 5 the impact of using a homogeneous (Fig. 5B, after

$B_1$  shimming) rather than an inhomogeneous (Fig. 5A, CP-like mode before  $B_1$  shimming) excitation profile with the TOF sequence. When examining reconstructions of an axial *thin* MIP (a *thin* MIP was chosen to help focusing on a few vessels within a slab) and of a sagittal MIP (the green marks indicate the axial thin MIP range), one can identify, with the homogeneous excitation, a fairly rich network of smaller vessels in the periphery, and possibly smaller vessels with slower flow in the center, that were poorly or not visualized when the excitation profile was stronger in the center and weaker in the periphery. (Note that, in Fig. 5, VERSE saturation was applied using a CP-like mode  $B_1$  profile, and no MT pulse was used). These fairly spectacular and promising results, however, were obtained at the cost of a significant loss in RF efficiency, a well known phenomenon with  $B_1$  shimming in large ROIs at 7T due to large destructive interferences between

complex  $B_1^+$  fields [14]. The source of this reduction in effective final  $|B_1^+|$ , despite unchanged input RF power, can be appreciated by looking at the corresponding  $B_1$  Multi-channel Interference ( $B_1$ MCI) index maps. This index is the ratio of the effectively achieved  $|B_1^+|$  (magnitude of the sum of the 16 complex  $B_1^+$  maps) over the sum of the magnitude of the 16  $|B_1^+|$  maps and, by definition, ranges between 0% (fully destructive  $B_1$  interference) and 100% (fully constructive  $B_1$  interference) [14, 30]. In Fig. 4, the lower two rows show the  $B_1$ MCI index maps before and after  $B_1$  shimming, with an average value dropping from 46% in CP-like mode (with local values of about 90% in the center and below 30% in the periphery) down to 23% after  $B_1$  shimming. As a consequence, in order to achieve a given nominal flip angle in the center of the brain, assuming unchanged pulse duration, the voltage of the excitation RF pulse has to be increased more than two fold, which means a more than four fold increase in RF power as well as in SAR. This emphasizes the fact that applying VERSE on the excitation pulse may become critical, when applying a homogeneous  $B_1^+$  shimming solution, in order to not exceed  $SAR_{MAX}$ .

### pTX spoke RF pulses

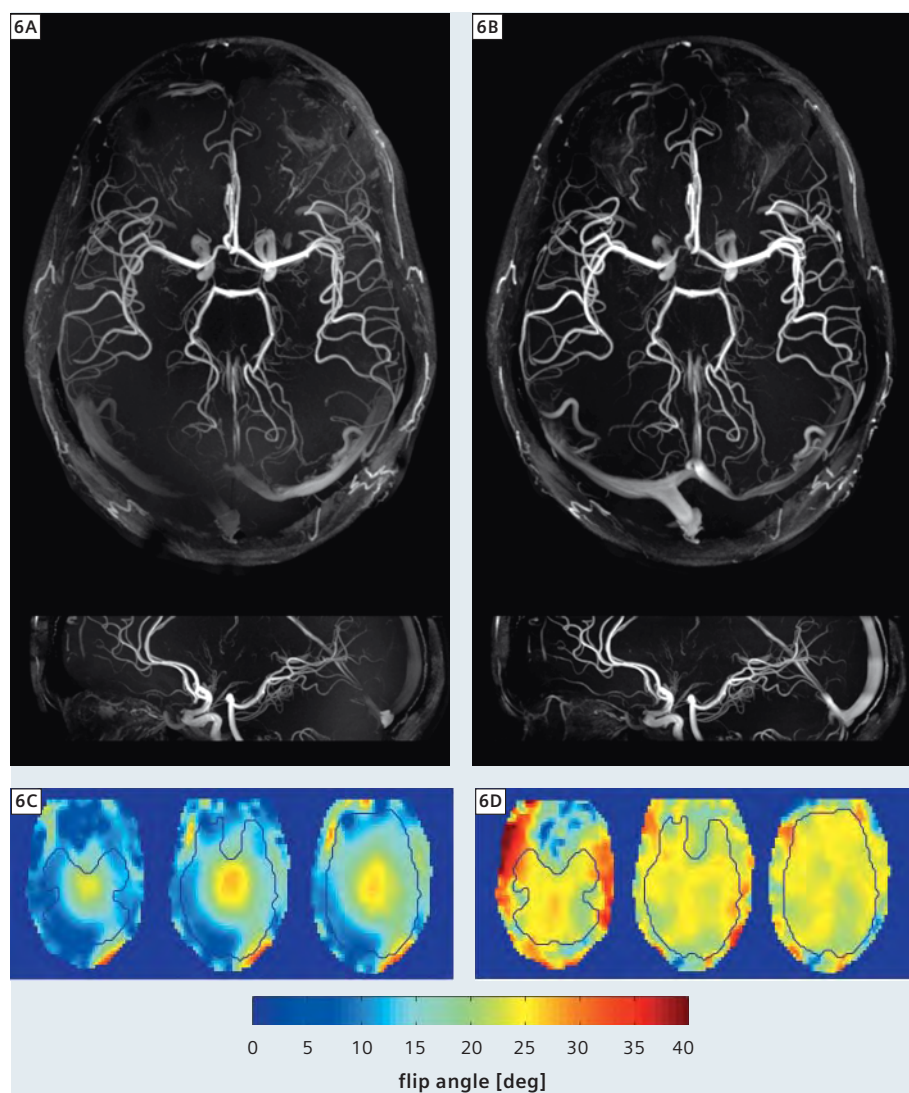
As can be seen in Fig. 6D, showing flip angle maps measured in the center slice of each of the three axial slabs, excellent excitation flip angle homogeneity was achieved with a 2-spoke pTX RF pulse within the ROIs used for RF computation. For comparison (Fig. 6C), flip angle maps are also shown using a single spoke, with CP-like mode  $B_1$  shimming, with a traditional bright center and weak periphery pattern. This is a direct illustration of very satisfactory results that can be obtained with pTX RF pulse design, where the target is defined as the final *excitation flip angle profile*, different  $|B_1^+|$  profiles being applied in each sub-pulse (whereas in static  $B_1$  shimming the target is restricted to a single static  $|B_1^+|$  profile). A substantial impact of these pTX 2-spoke RF pulses on TOF angiograms

can be seen on axial and sagittal MIP reconstructions (Figs. 6A, B), with a remarkably more uniform signal magnitude through vessels, especially in the periphery (see the anterior and posterior poles on the sagittal view). Even though in this initial implementation neither saturation pulse nor MT pulses were enabled in our pTX TOF sequence (thus, venous and fat signal were not suppressed), a much more homogeneous overall background signal suppression was readily achieved, resulting from the more uniform excitation pattern through each slab. It is important to emphasize that the design of the pTX RF pulses explicitly includes  $\Delta B_0$  maps measured at the beginning of the scanning session and can counteract deleterious effects of the latter. Based on these very promising pTX results, future work will be pursued to further constraints RF pulse design towards lower SAR and to introduce, in the pTX version of the TOF sequence, saturation and MT RF pulses.

## Discussion

Thanks to higher SNR and longer  $T_1$  relaxation constants, TOF angiography can greatly benefit from ultra high field MR scanners, offering the potential for higher spatial resolution imaging, stronger contrast between static tissue and vessels, which ultimately may result in significantly improving diagnosis performances.

It is well known that imaging at UHF is hampered by serious obstacles, such as high SAR level and excitation profile distortion, which are especially challenging with imaging modalities, such as TOF MRA, that are intrinsically both highly sensitive to RF excitation inhomogeneity and highly demanding in RF power. We initially found that great contrast-enhancement provided by saturation and MT pulses could not be used at 7T because  $SAR_{MAX}$  would be exceeded. However, high SAR levels induced by sequence components demanding high RF power can be greatly reduced by using, when possible, VERSE pulse transformation (excitation, saturation pulses) or sparse application of preparation pulses (MT), while preserving, or even



**6 Top two rows:** Multi-slab 3D-TOF acquired with standard RF excitation pulse with CP-like transmit  $B_1$  phases (6A) and with a pTX 2-spoke excitation RF pulse design (6B). Note the clear improvement in angiographic contrast in (6B), with increased conspicuity of multiple small vessels and more homogeneous vessel signal brightness through the slice. Note that neither saturation pulse nor MT pulse were enabled in the pTX version of the TOF sequence.

**Bottom row:** Corresponding measured flip angle maps with CP-like transmit  $B_1$  phase (6C) and using pTX 2-spoke excitation RF pulse (6D). Note the clear gain in  $B_1$  homogeneity within the ROIs (black line) when applying the 2-spoke RF pulse.

increasing, vessel to background contrast in cerebral TOF at 7T. Furthermore, recent advances in RF engineering and corresponding MR methods, especially multi-transmit technology, allow for dramatically improving the uniformity of either transmit  $B_1$  profile ( $B_1$  shimming) or excitation flip angle profile (pTX). These are significant improvements that may dramatically reduce or eliminate the risk of overlook-

ing clinical lesions on UHF images due to local defects or strong heterogeneity in transmit  $B_1$  distribution, especially in the periphery of the brain.

## Conclusion

Imaging at UHF holds promises for higher spatial resolution and higher contrast TOF MRA, with the potential of clinically relevant improved diagnosis performance.

Although serious and well known challenges at UHF include increased SAR and image contrast inhomogeneity, our results indicate that sequence optimization and recent multi-transmit technology provide the means to efficiently address these handicaps, paving the road towards gaining actual clinical benefits from UHF TOF MRA. These positive results have to be read in the context of a growing number of studies from multiple groups working at 7T [8, 9, 11–13], including ours [10], that demonstrate clinically relevant findings in MR neuro-imaging at 7T.

Speed (fast  $B_1$  calibration/computation within the time window of a clinical scan), SAR control, robustness and integration of these methods within a standard clinical interface will be critical to a successful implementation of these technological advances in the clinical world.

#### References

- 1 M Miyazaki, VS Lee. Nonenhanced MR Angiography. *Radiology* 2008;248:20–43.
- 2 GT Gullberg, FW Wehrli, A Shimakawa, MA Simons. MR Vascular Imaging with a Fast Gradient Refocusing Pulse Sequence and Reformatted Images From Transaxial Sections. *Radiology* 1987;165:241–246.
- 3 D Parker, C Yuan, D Blatter. MR Angiography by Multiple Thin Slab 3D Acquisition. *Magn Reson Med* 1991;17:434–451.
- 4 RR Edelman, SS Ahn, D Chien, W Li, A Goldmann, M Mantello, J Kramer, J Kleefield. Improved Time-of-Flight MR Angiography of the Brain with Magnetization Transfer Contrast. *Radiology* 1992;184:395–399.
- 5 K Ugurbil, G Adriany, P Andersen, W Chen, M Garwood, R Gruetter, P Henry, S Kim, H Lieu, I Tkac, T Vaughan, P Van de Moortele, E Yacoub, X Zhu. Ultrahigh Field Magnetic Resonance Imaging and Spectroscopy. *Magn Reson Imaging* 2003;21:1263–1281.
- 6 WD Rooney, G Johnson, X Li, ER Cohen, S-G Kim, K Ugurbil, CS Springer. Magnetic Field and Tissue Dependencies of Human Brain Longitudinal  $1H_2O$  Relaxation in Vivo. *Magn Reson Med* 2007;57:308–318.
- 7 O Al-Kwif, DJ Emery, AH Wilman. Vessel Contrast at Three Tesla in Time-of-Flight Magnetic Resonance Angiography of the Intracranial and Carotid Arteries. *Magn Reson Imaging* 2002;20:181–187.
- 8 C-K Kang, C-W Park, J-Y Han, S-H Kim, C-A Park, K-N Kim, S-M Hong, Y-B Kim, KH Lee, Z-H Cho. Imaging and Analysis of Lenticulostriate Arteries Using 7.0-Tesla Magnetic Resonance Angiography. *Magn Reson Med* 2009;61:136–144.
- 9 C von Morze, D Xu, DD Purcell, CP Hess, P Mukherjee, D Saloner, DAC Kelley, DB Vigneron. Intracranial Time-of-Flight MR Angiography at 7T with Comparison to 3T. *Magn Reson Imaging* 2007;26:900–904.
- 10 S Schmitter, M Bock, S Johst, EJ Auerbach, K Ugurbil, P-F van de Moortele. Contrast Enhancement in TOF Cerebral Angiography at 7 T Using Saturation and MT Pulses Under SAR Constraints: Impact of VERSE and Sparse Pulses. *Magn Reson Med* 2011.
- 11 S Maderwald, SC Ladd, ER Gizewski, O Kraff, JM Theysohn, K Wicklow, C Moenninghoff, I Wanke, ME Ladd, HH Quick. To TOF or Not to TOF: Strategies for Non-Contrast-Enhanced Intracranial MRA at 7 T. *MAGMA* 2008;21:159–167.
- 12 JJM Zwanenburg, J Hendrikse, T Takahara, F Visser, PR Luijten. MR Angiography of the Cerebral Perforating Arteries with Magnetization Prepared Anatomical Reference at 7 T: Comparison with Time-of-Flight. *Magn Reson Imaging* 2008;28:1519–1526.
- 13 JT Heverhagen, E Bourekas, S Sammet, MV Knopp, P Schmalbrock. Time-of-Flight Magnetic Resonance Angiography at 7 Tesla. *Invest Radiol* 2008;43:568–573.
- 14 P-F van de Moortele, C Akgun, G Adriany, S Moeller, J Ritter, CM Collins, MB Smith, JT Vaughan, K Ugurbil. B(1) Destructive Interferences and Spatial Phase Patterns at 7 T with a Head Transceiver Array Coil. *Magn Reson Med* 2005;54:1503–1518.
- 15 JT Vaughan, M Garwood, CM Collins, W Liu, L DelaBarre, G Adriany, P Andersen, H Merkle, R Goebel, MB Smith, K Ugurbil. 7T vs. 4T: RF Power, Homogeneity, and Signal-to-Noise Comparison in Head Images. *Magn Reson Med* 2001;46:24–30.
- 16 N Boulant. T1 and T2 Effects During Radio-Frequency Pulses in Spoiled Gradient Echo Sequences. *Magn Reson Imaging* 2009;197:213–218.
- 17 S Conolly, D Nishimura, A Macovski, G Glover. Variable-Rate Selective Excitation. *Magn Reson Imaging* 1988;78:440–477.
- 18 M Doyle, T Matsuda, GM Pohost. SLIP, a Lipid Suppression Technique to Improve Image Contrast in Inflow Angiography. *Magn Reson Med* 1991;21:71–81.
- 19 C Lin, MA Bernstein, GF Gibbs, J Huston. Reduction of RF Power for Magnetization Transfer with Optimized Application of RF Pulses in K-Space. *Magn Reson Med* 2003;50:114–121.
- 20 DL Parker, HR Buswell, KC Goodrich, AL Alexander, N Keck, JS Tsuruda. The Application of Magnetization Transfer to MR Angiography with Reduced Total Power. *Magn Reson Med* 1995;34:283–286.
- 21 GJ Metzger, C Snyder, C Akgun, T Vaughan, K Ugurbil, P-F van de Moortele. Local  $B_1^+$  Shimming for Prostate Imaging with Transceiver Arrays at 7T Based on Subject-Dependent Transmit Phase Measurements. *Magn Reson Med* 2008;59:396–409.
- 22 G Adriany, P-F van de Moortele, J Ritter, S Moeller, EJ Auerbach, C Akgun, CJ Snyder, T Vaughan, K Ugurbil. A Geometrically Adjustable 16-Channel Transmit/Receive Transmission Line Array for Improved RF Efficiency and Parallel Imaging Performance at 7 Tesla. *Magn Reson Med* 2008;59:590–597.
- 23 U Katscher, P Bornert, C Leussler, JS van den Brink. Transmit SENSE. *Magn Reson Med* 2003;49:144–150.
- 24 Y Zhu. Parallel Excitation with an Array of Transmit Coils. *Magn Reson Med* 2004;51:775–784.
- 25 K Setsompop, V Alagappan, BA Gagoski, A Potthast, F Hebrank, U Fontius, F Schmitt, LL Wald, E Adalsteinsson. Broadband Slab Selection with  $B_1^+$  Mitigation at 7T via Parallel Spectral-Spatial Excitation. *Magn Reson Med* 2009;61:493–500.
- 26 K Setsompop, V Alagappan, B Gagoski, T Witzel, J Polimeni, A Potthast, F Hebrank, U Fontius, F Schmitt, LL Wald, E Adalsteinsson. Slice-Selective RF Pulses for in Vivo  $B_1^+$  Inhomogeneity Mitigation at 7 Tesla Using Parallel RF Excitation with a 16-Element Coil. *Magn Reson Med* 2008;60:1422–1432.
- 27 K Setsompop, LL Wald, V Alagappan, BA Gagoski, E Adalsteinsson. Magnitude Least Squares Optimization for Parallel Radio Frequency Excitation Design Demonstrated at 7 Tesla with Eight Channels. *Magn Reson Med* 2008;59:908–915.
- 28 W Grissom, C-Y Yip, Z Zhang, VA Stenger, JA Fessler, DC Noll. Spatial Domain Method for the Design of RF Pulses in Multicoil Parallel Excitation. *Magn Reson Med* 2006;56:620–629.
- 29 M Miyazaki, F Kojima, N Ichinose, Y Onozato, H Igarashi. A Novel Saturation Transfer Contrast Method for 3D Time-of-Flight Magnetic Resonance Angiography: a Slice-Selective Off-Resonance Sinc Pulse (SORS) Technique. *Magn Reson Med* 1994;32:52–59.
- 30 J Ellermann, U Goerke, P Morgan, K Ugurbil, J Tian, S Schmitter, T Vaughan, PF Van de Moortele. Simultaneous Bilateral Hip Joint Imaging at 7 Tesla Using Fast Transmit B(1) Shimming Methods and Multichannel Transmission – a Feasibility Study. *NMR Biomed.* 2012.
- 31 P-F. Van de Moortele, C. Snyder, L. DelaBarre, G. Adriany, J.T Vaughan, K. Ugurbil, Calibration tools for RF Shim at Very High Field with Multiple Element RF Coils: from Ultra Fast Local Relative Phase to Absolute Magnitude  $B_1^+$  Mapping. ISMRM 15th Annual meeting, 2007.
- 32 V.L. Yarnykh. Actual flip angle imaging in the pulsed steady state: a method for rapid three-dimensional mapping of the transmitted radiofrequency field. *Magn Reson Med* 2007;57(1):192–200.

#### Contact

Pierre-François Van de Moortele,  
M.D., Ph.D.  
Center for Magnetic Resonance  
Research (CMRR)  
University of Minnesota Medical School  
2021 6th St. SE  
Minneapolis, MN 55455  
USA  
Phone: +1 612-626-2001  
Fax: +1 612-626-2004  
pfvdm@cmrr.umn.edu

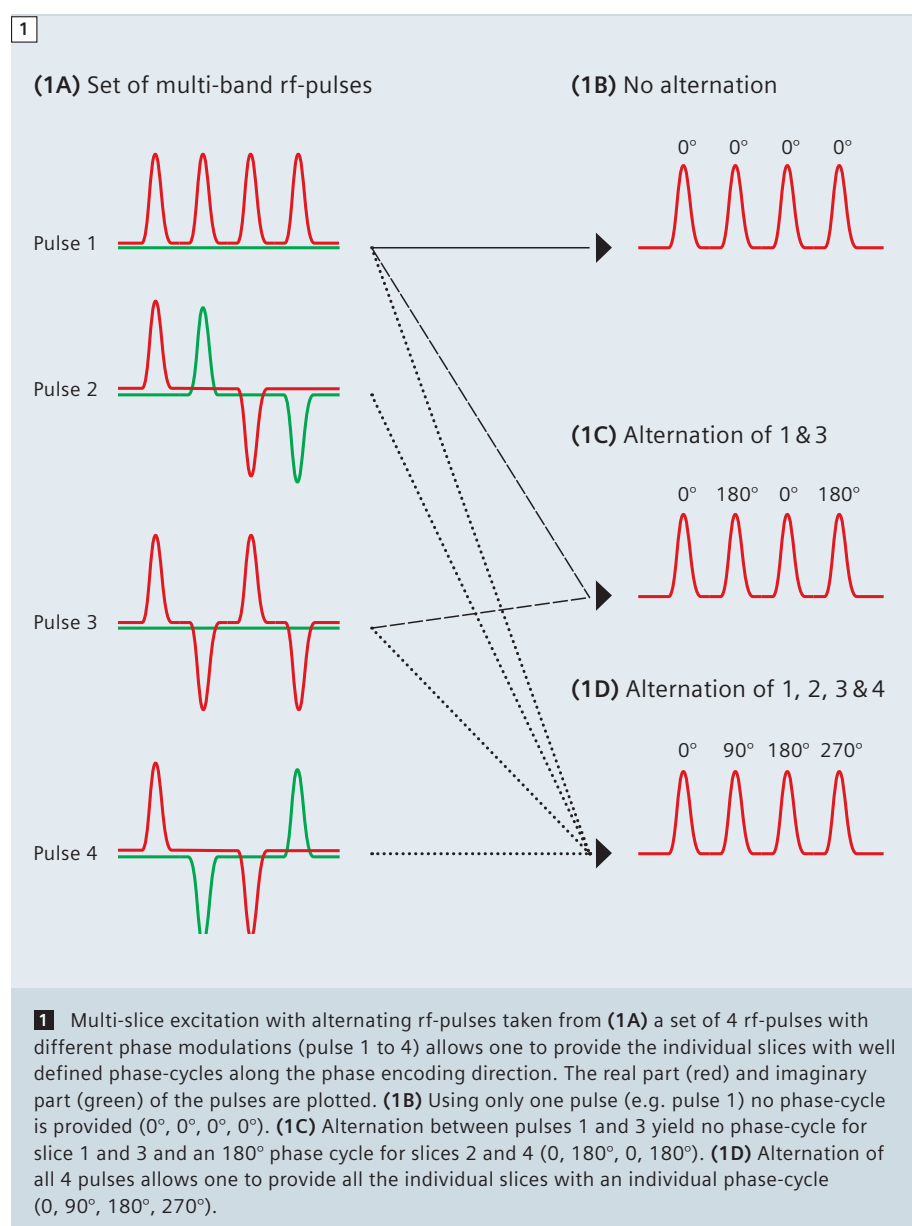
# Controlled Aliasing in Parallel Imaging Results in Higher Acceleration (CAIPIRINHA)

Felix Breuer<sup>1</sup>; Martin Blaimer<sup>1</sup>; Mark Griswold<sup>2</sup>; Peter Jakob<sup>1,3</sup>

<sup>1</sup>Research Center, Magnetic Resonance Bavaria e.V (MRB), Würzburg, Germany

<sup>2</sup>Case Center for Imaging Research, Case Western Reserve University and University Hospitals, Cleveland, OH, USA

<sup>3</sup>Dept. of Experimental Physics 5, University of Würzburg, Würzburg, Germany

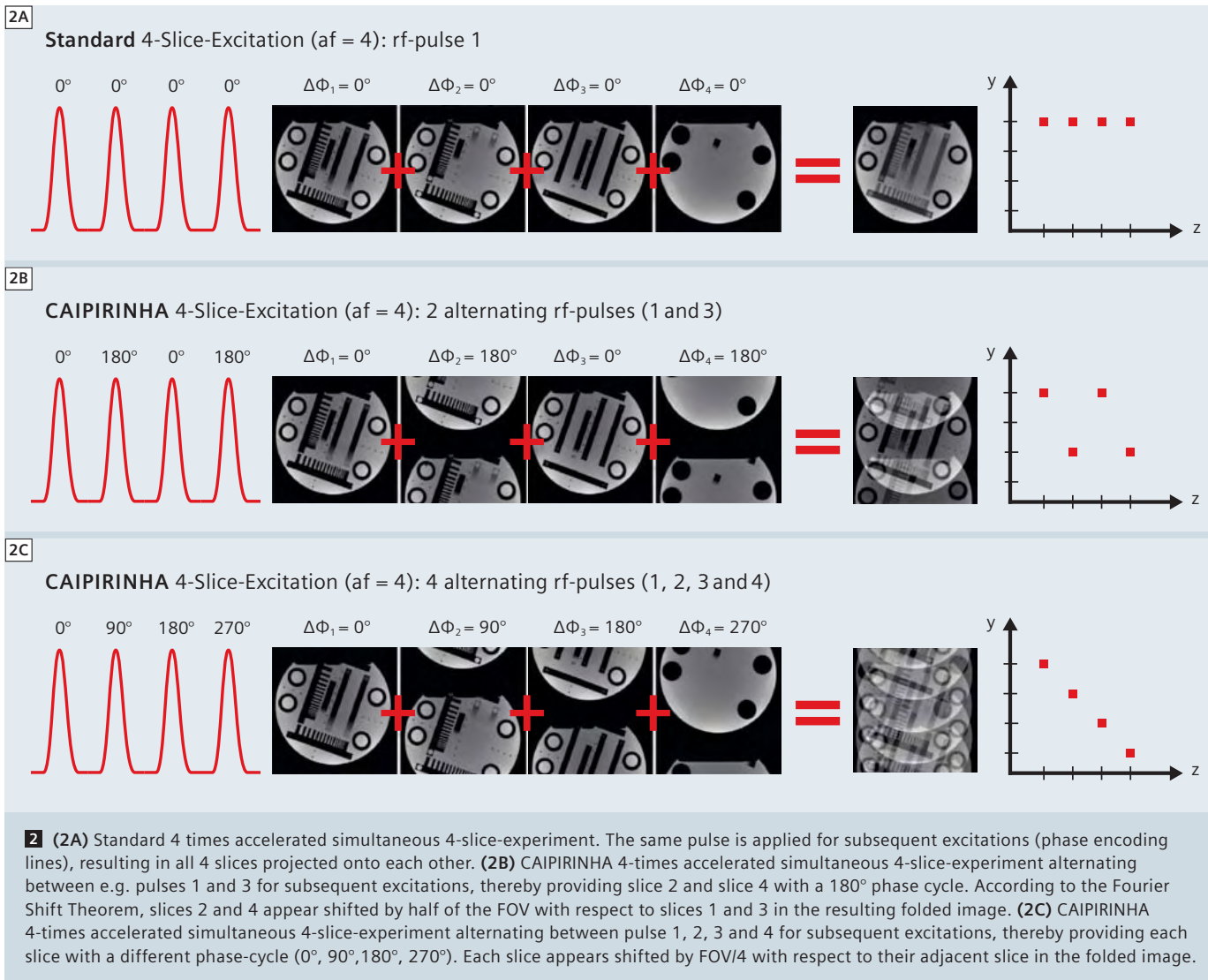


## Introduction

Image acquisition time is one of the most important considerations for clinical magnetic resonance imaging (MRI). The development of multi-coil receiver hardware as well as dedicated parallel MRI (pMRI) reconstruction methods such as SENSE [1] and GRAPPA [2] allowed for significant decrease of acquisition times in almost all clinical applications. Thus, today, pMRI plays a substantial role in everyday clinical routine.

pMRI operates by reducing the amount of data necessary to form an image. In the Cartesian case, this is usually accomplished by uniformly undersampling the k-space (e.g. skipping every other phase-encoding line) resulting in so-called 'aliasing artifacts' in the image domain. pMRI reconstruction methods seek to compensate the lack of spatial encoding by taking into account the spatial sensitivity information, provided by a multi-coil receiver array. Unfortunately, the pMRI concept is intrinsically associated with a signal-to-noise (SNR) loss compared to a fully encoded image. The SNR is

**a)** reduced by the square root of the acceleration factor, simply due to the fact that less data is acquired, and **b)** by the so-called g-factor, depending strongly on the encoding capabilities of the underlying receiver array. Thus, pMRI is often limited to applications with sufficiently high base SNR, such as volumetric imaging methods. With the newest generation of MR scanners

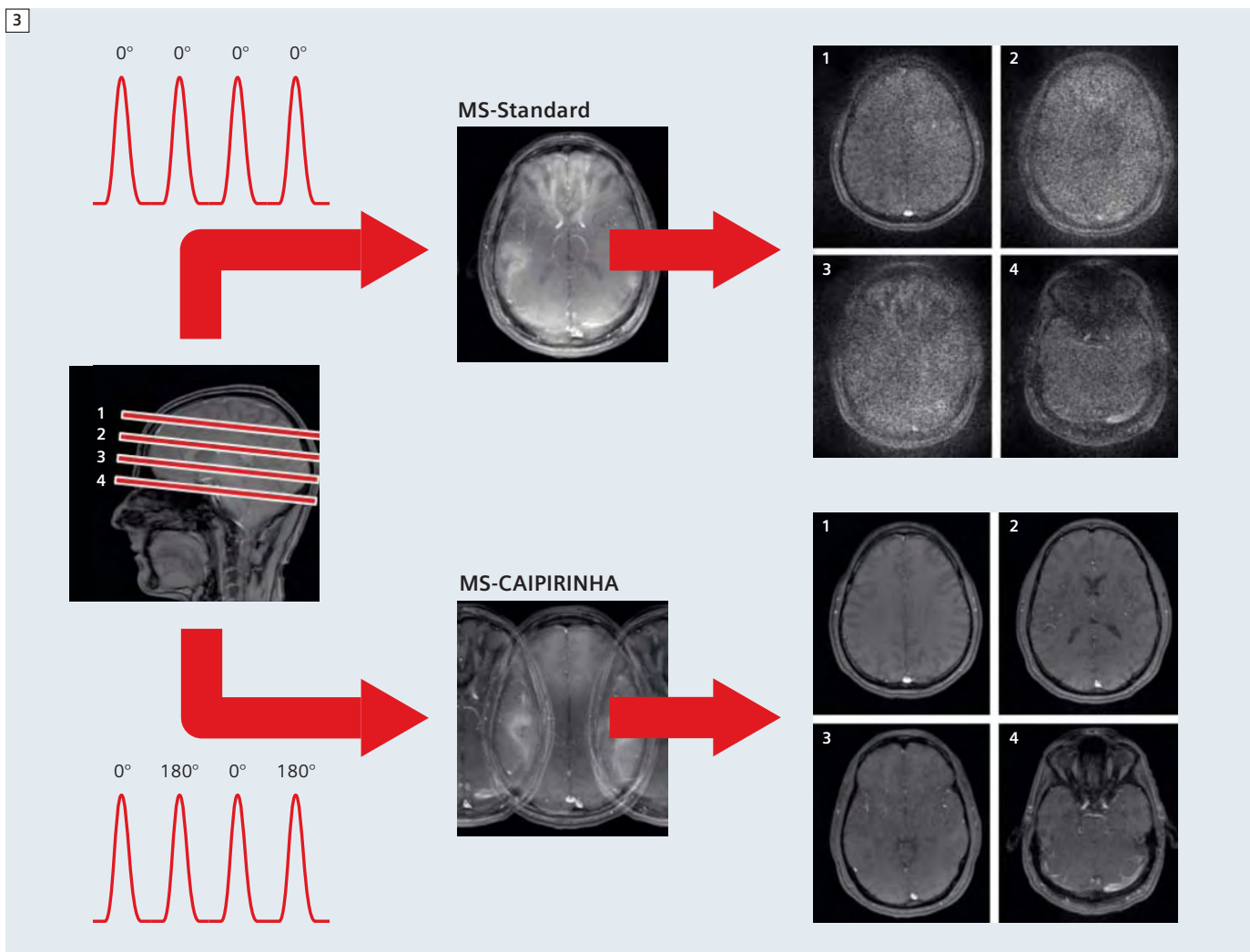


providing up to 128 independent receiver channels, further scan time reductions are potentially achievable. However, in conventional 2D clinical imaging, parallel imaging today is still restricted to relatively moderate scan time reductions (acceleration factors of 2 to 3) due to intrinsic limitations in the coil sensitivity variations along one phase encoding direction (1D parallel imaging). In 3D and simultaneous multi-slice imaging, parallel encoding can be carried out in two encoding directions (2D parallel imaging), thereby employing the sensitivity variations in both directions, as has been demonstrated in, for example, 2D SENSE [3] and MS SENSE [4]. This concept has been shown

to significantly improve the reconstruction conditions, allowing for higher accelerations of the acquisition (>3). However, both techniques require sufficient sensitivity variations in two encoding directions for successful image reconstruction and therefore strongly depend on the underlying coil geometry. As mentioned above, spatial encoding with a receiver array is associated with a certain noise amplification known as 'g-factor noise'. Quantitative g-factor estimation methods have been derived for SENSE [1] and GRAPPA reconstructions [5] and serve as a quality metric for pMRI reconstructions. One important approach to reduce this g-factor noise for a given application is the optimiza-

tion of the receiver array geometry (e.g. number of coils, coil arrangement) towards the application at hand. However, hardware limitations, the diversity of patient weight and size, the need for flexibility regarding a wider range of applications, as well as sequence or protocol specific considerations, hamper the viability.

The **CAIPIRINHA** concept (**C**ontrolled **A**liasing **I**n **P**arallel **I**maging **R**esults **I**N **H**igher **A**cceleration) allows one to partially overcome these requirements and limitations by modifying the aliasing conditions in a well defined manner. This is done already during the data acquisition by modifying the rf-excitation or gradient encoding scheme in



**3** In vivo brain example: 4 x accelerated simultaneous 4-slice experiment using no phase cycling (MS-Standard) results in superimposition of all the slices directly on top of each other. Due to the lack of sufficient sensitivity variations along the slice direction strong noise amplifications can be observed after GRAPPA reconstruction. Using MS-CAIPIRINHA, employing 2 alternating multi-band rf-pulses, slices 2 and 4 appear shifted with respect to slices 1 and 3 in the folded image. In this way sensitivity variations in the phase encoding direction (LR) can be used in addition to the sensitivity variations available in the slice direction. The concept results in significantly improved image quality after GRAPPA reconstruction. Imaging parameters: 3T MAGNETOM Skyra, TE 3.4 ms, TR 100 ms, FA 50°, FOV 178 x 220 mm<sup>2</sup>, matrix 208 x 320, slice thickness 4 mm, distance factor 300 %.

order to use the coil encoding power of the underlying receiver array to full capacity. The concept has been successfully applied so far to simultaneous multi-slice imaging (MS-CAIPIRINHA) [6] and 3D imaging where data reduction can be carried out in two phase-encoding directions (2D-CAIPIRINHA) [7]. In addition, both strategies can be extended to the third remaining direction, namely the read-out direction, by utilizing e.g. zig-zag shaped read-out trajectories [8]. The following provides a

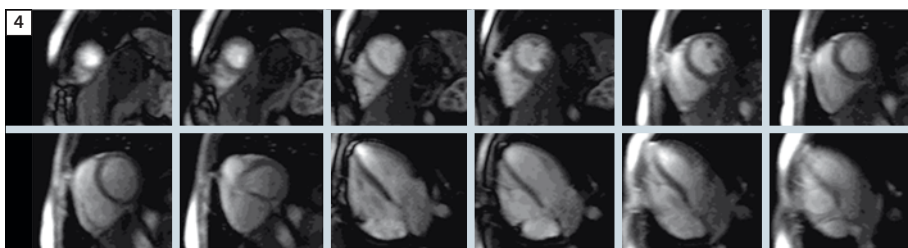
brief overview of MS-CAIPIRINHA and 2D-CAIPIRINHA.

### Improving parallel imaging performance with CAIPIRINHA

#### MS-CAIPIRINHA

Simultaneous multi-slice imaging offers an SNR benefit over standard single-slice imaging and comprises rf-excitations with specialized multi-band pulses as displayed in Figure 1. After multi-band excitation the received signals will accrue from all the slices (bands) and

thus are subject to the subsequent gradient encoding sequence. Simply replacing the standard single-slice excitation pulse with a multi-slice pulse in an MR imaging sequence will therefore result in an image with all the simultaneously excited slices projected onto each other (Fig. 2A). As mentioned above, the parallel imaging concept provides an elegant way to separate multiple image signals which are aliased into one image pixel. Thus, sufficient sensitivity variations of the underlying receiver array



**4** In vivo cardiac example: The MS-CAIPIRINHA approach enables the acquisition of up to 6 slices per cardiac cycle. Here, 12 slices are acquired within 2 cardiac cycles (8 slices in short axis view and 4 in the long axis). Imaging parameters: 1.5T MAGNETOM Avanto, 32-channel cardiac array (Rapid Biomedical, Würzburg, Germany); Sequence: SR-TrueFISP, CAIPIRINHA phase cycle +90°/-90°; FOV 320 x 260 mm<sup>2</sup>, matrix 128 x 77, resolution 2.5 x 3.4 mm<sup>2</sup>, slice thickness 10 mm, distance factor (two-slice pulse) of short/long axis: 200%/100%; partial Fourier 6/8, measurements: 20, TR 2.8 ms, TI 120 ms, TE 1.4 ms, FA 50°, reconstruction algorithm GRAPPA (R=3). Images courtesy of Daniel Stäb.

along the slice direction will then allow for separation of the slices using adapted standard pMRI reconstruction algorithms [4, 9]. However, in cases where the sensitivity variations along the slice direction are not sufficient e.g. as a result of small slice distances or suboptimal coil geometry, the pMRI reconstruction will fail and result in large noise amplification. Sensitivity variations, potentially available along the other spatial directions, here the phase-encoding direction, are not employed.

It has been demonstrated that increasing the field-of-view (FOV) by the number of simultaneously excited slices allows the individual slices to be shifted with respect to each other in an extended FOV (along the phase-encoding) [10, 11] such that the slices show no superposition. A similar concept is Hadamard aided rf-encoding [12]. The required shifts mentioned above can be accomplished by employing dedicated alternating multi-band rf-pulses providing the individual bands with well-defined phase-cycles along the phase-encoding direction (e.g. using the set of rf-pulses displayed in Fig. 1). Due to the volumetric excitation this approach offers a benefit in SNR efficiency of square root of the number of simultaneously excited slices compared to single slice acquisitions, however at the cost of increased pulse energy deposition. Using this concept in combination with image acceleration (fewer phase-encod-

ing steps) superimposed slices with individual shifts along the phase-encoding direction can be realized by employing alternation of rf-pulses taken e.g. from the set of pulses given in Fig. 1. A four-slice excitation at an acceleration of  $af = 4$  using only rf-pulse 1 yields a superposition of 4 image pixels originating from all the 4 slices at the same location in the phase-encoding direction (Fig. 2A). Employing an alternation of rf-pulses (e.g. pulse 1 and pulse 3, or pulses 1, 2, 3 and 4) the individual slices can be shifted with respect to each other in the FOV (Figs. 2B, C). In this way, as demonstrated in the corresponding  $z_y$ -plots, aliased pixels may now originate from both different slices and different locations in the phase-encoding direction in a well defined manner (MS-CAIPIRINHA), thereby allowing the pMRI reconstruction to take advantage of sensitivity variations in the slice and the phase encoding direction.

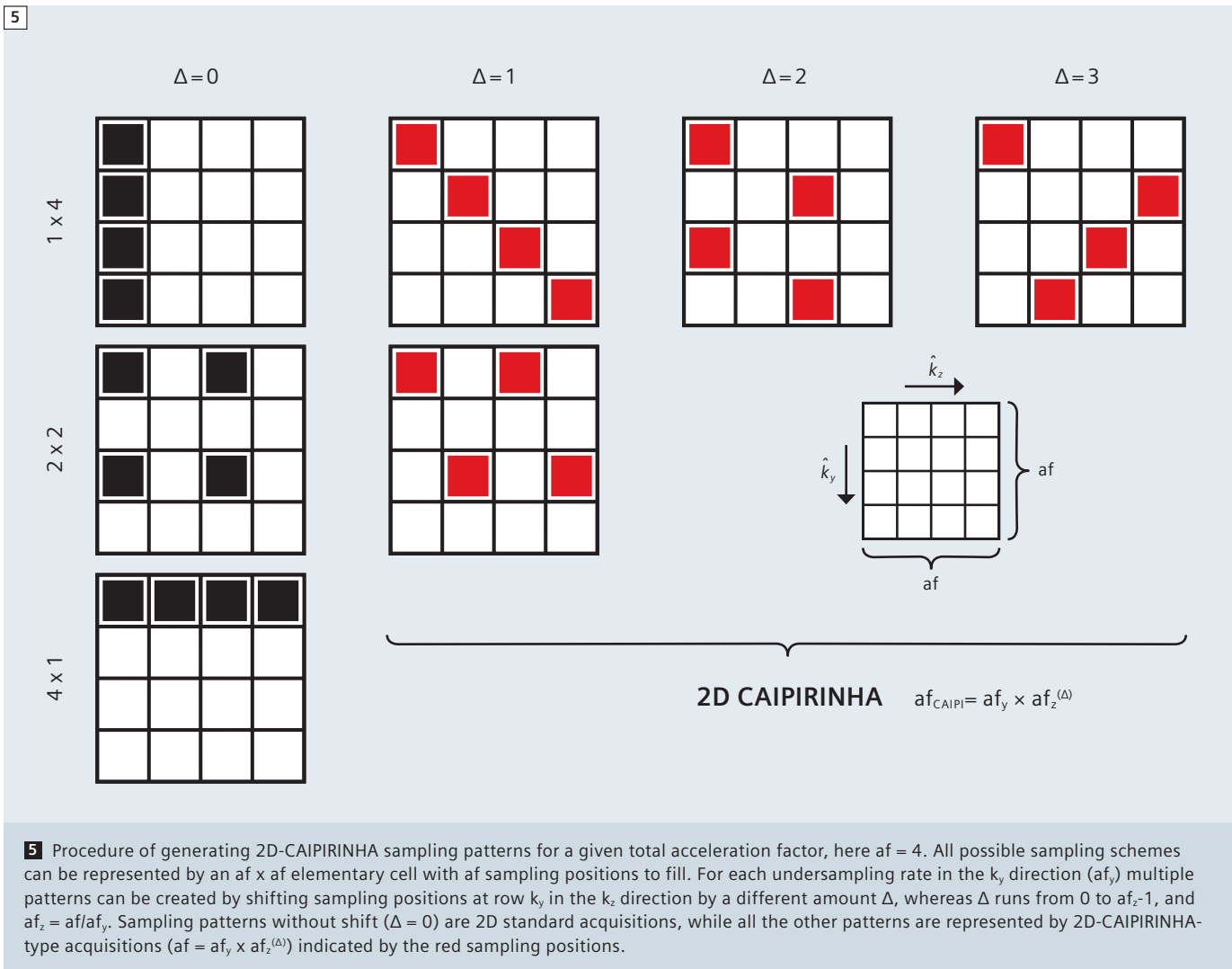
The benefit of MS-CAIPIRINHA is demonstrated in vivo employing a 4 times accelerated simultaneous 4-slice experiment: Figure 3 shows 4 slices in a volunteer's brain (slice positions are indicated in the sagittal brain image), which are excited simultaneously using specialized multi-band rf-pulses taken from the set of pulses given in Figure 1A. In the case of non-alternating rf-pulses [4] (MS-Standard), each slice is subject to the same phase cycle along the phase-encoding direction (LR). The slices appear projected directly on top of each

other, thereby allowing the pMRI reconstruction (here GRAPPA-SENSE hybrid [9]) only to use sensitivity variations available in the slice direction. Due to the relatively small slice distances, the relatively high acceleration factor ( $af = 4$ ) and the limited sensitivity variations provided by the coil array in the slice-direction, the reconstruction results in large noise amplifications and thus unacceptable image quality. However, using a MS-CAIPIRINHA acquisition in combination with an adapted GRAPPA reconstruction, the folded image pixels can now be separated almost without any noise amplification. In this example, an MS-CAIPIRINHA scheme as depicted in Figure 2B has been employed. Alternation of pulses 1 and 3 provides slices 2 and 4 with a 180° phase-cycle along the phase encoding direction causing these slices to appear shifted by FOV/2 with respect to the slices 1 and 3 which had no phase modulation. Thus, in this case, MS-CAIPIRINHA allowed the acquisition of 4 slices in the same time normally required or a single slice without losing SNR.

In addition, the applicability of MS-CAIPIRINHA to cardiac perfusion imaging is demonstrated in Figure 4. A two-slice CAIPIRINHA saturation recovery TrueFISP sequence has been employed using a total acceleration of  $af = 3$ . This allows for the acquisition of 12 slices (8 slices in the short axis view and 4 in the long axis) in only two cardiac cycles. A repetition of the sequence during contrast agent uptake has the potential for cardiac perfusion imaging with significantly increased spatial coverage in high temporal resolution [13].

## 2D-CAIPIRINHA

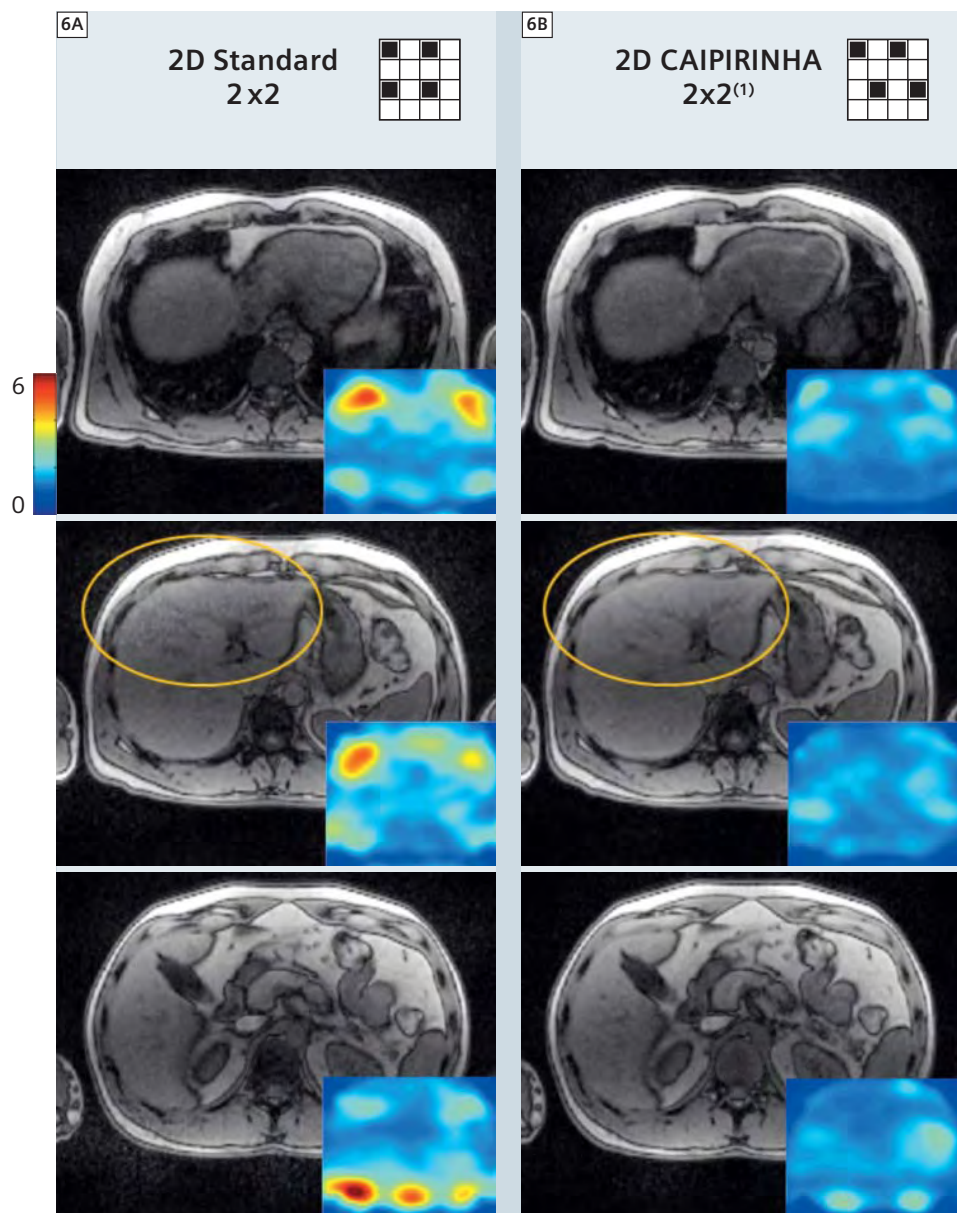
In contrast to conventional 2D imaging where only one phase-encoding direction is available for scan-time reduction (1D pMRI), 3D volumetric imaging with a second phase encoding direction offers the potential to choose the direction in which undersampling is performed, or even to split the acceleration between the two phase-encoding directions (2D pMRI). Given a receiver array geometry providing sensitivity variations in both phase encoding directions, this



strategy has shown the potential to allow for higher total image accelerations compared to undersampling schemes restricted to only one direction [4, 5]. However, since the sensitivity variations available for the pMRI reconstruction depend not only on the coil geometry but also on the image position and orientation, the choice of the FOVs and encoding directions as well as the object position, size and shape, the right choice of the undersampling rate for the individual phase-encoding directions is not easily predictable and remains a challenging task. Thus, in many applications the reconstructed images suffer from severe residual artifacts or strong noise amplifications, depending on the choices made by the operator. Again, the CAIPIRINHA concept has

shown to partially overcome these limitations. It has been realized that, besides the standard rectangular sampling patterns with undersampling using simple integer reductions, many other patterns are conceivable where the sampling positions are shifted from their original positions in the 2D phase encoding scheme. Here we restrict ourselves to sampling positions on so-called 'sheared grids' which form periodic lattices [14] resulting in exactly  $af$  superimposed image pixels at an acceleration factor of  $af$  as it is the case in all standard rectangular patterns. The procedure of generating the available 2D-CAIPIRINHA patterns is schematically displayed in Figure 5 for a total image acceleration of  $af = 4$ . The sampling schemes can be represented by an  $af \times af$  elementary cell with

$af$  sampling positions to fill. For each undersampling rate in the  $k_y$  direction ( $af_y$ ) multiple patterns can be created by shifting sampling positions at row  $k_y$  in the  $k_z$  direction by a different amount  $d$ , whereas  $d$  runs from 0 to  $af_z - 1$ , and  $af_z = af/af_y$ . Sampling patterns without shift ( $d = 0$ ) are 2D standard acquisitions, while all the other patterns are represented by 2D-CAIPIRINHA-type acquisitions. This concept can also be used for prime number accelerations ( $af = 2, 3, 5 \dots$ ) where standard accelerations only allow undersampling in one of the phase encoding directions. The required shifts in  $k$ -space can simply be realized by applying additional gradient offsets to the phase encoding gradient tables. These 2D-CAIPIRINHA sampling patterns, analogous to the phase-cycles in simultaneous



**6** In vivo liver example; volunteer: Compared are GRAPPA reconstructions (3 example slices) derived from two different reduction schemes (**6A**) Standard 2x2 and (**6B**) 2D-CAIPIRINHA 2x2<sup>(1)</sup>. In addition, the corresponding GRAPPA g-factor maps are displayed. In the indicated region the SNR benefit of 2D-CAIPIRINHA can be appreciated.  
**Imaging details:** 1.5T MAGNETOM Avanto, 6-channel body matrix coil and 6-channel spine matrix coil; VIBE af = 4, extra reference scan matrix 32 x 24 x 24. FOV 400 x 312.5 mm<sup>2</sup>, matrix 320 x 170 x 50 GRAPPA, total acquisition time 9 s breath-hold.

multi-slice imaging, modify the appearance of aliasing in 2D parallel imaging compared to conventional rectangular reduction schemes and have the potential to relax the requirements of integer reductions to great extent. This is demonstrated in more detail in the original publication [7]. By shifting the sampling

positions in a well-directed manner, aliasing can be shifted in such a way that sensitivity variations provided by the underlying receiver array are employed more efficiently. In some cases the amount of aliasing can even be reduced. These modified aliasing conditions may then result in a further

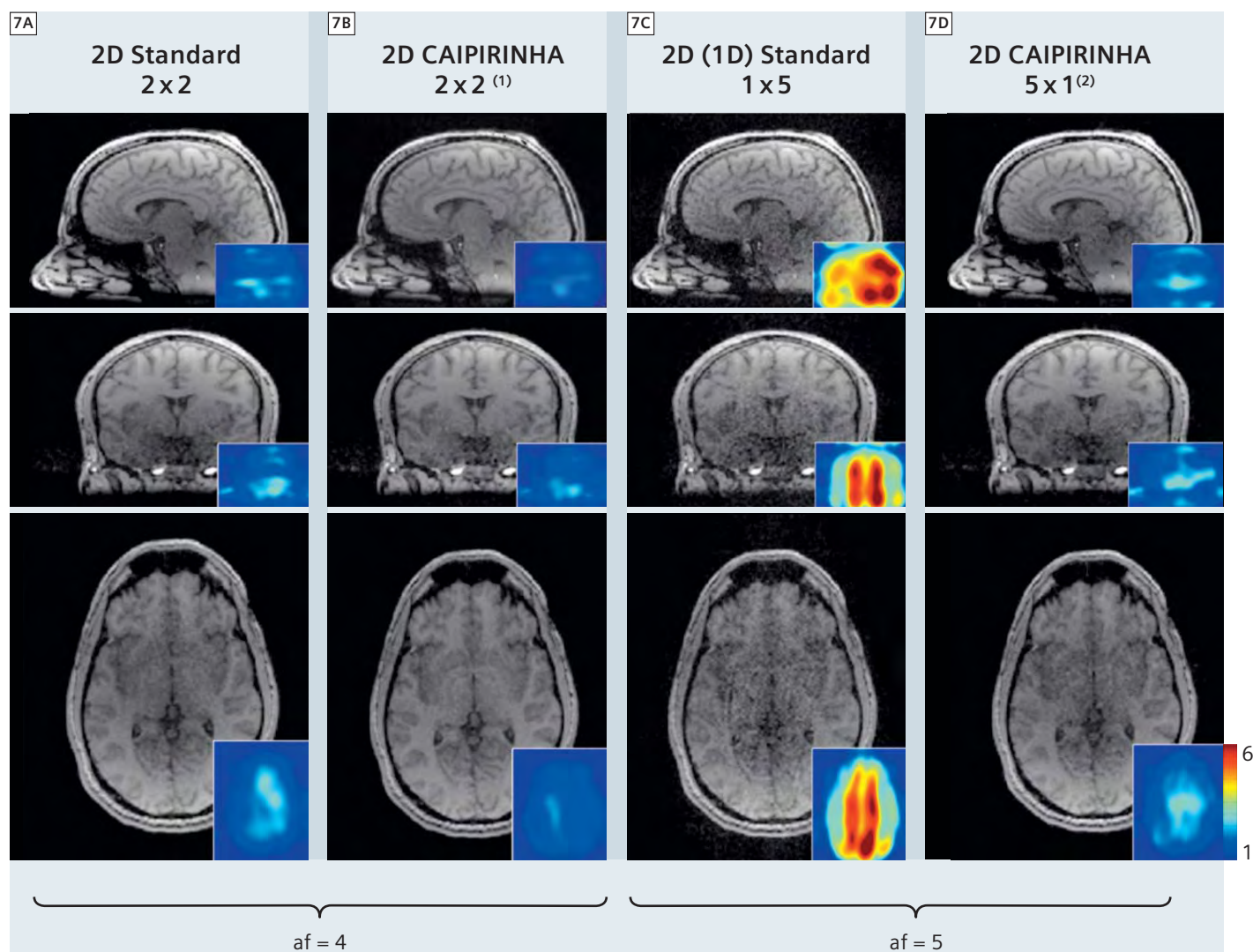
improvement in parallel imaging reconstruction conditions and therefore in better image quality. Recently, this concept has also been extended to more generalized sampling schemes which are not restricted to sheared grids [15]. In order to demonstrate the benefit of 2D-CAIPIRINHA in vivo, two subsequent accelerated (af = 4) abdominal 9 s breath-hold VIBE experiments have been carried out on a volunteer. In Figure 6 GRAPPA reconstructions from three out of 50 slices from

**a)** a standard 2x2 and  
**b)** a 2D-CAIPIRINHA 2x2<sup>(1)</sup> acquisition are displayed. In addition, the corresponding g-factor maps of the GRAPPA reconstructions are displayed as a quantitative measure of image quality. As indicated by the lower g-factor values in the 2D-CAIPIRINHA reconstructions the improved image quality can clearly be observed, even on a visual scale (see region indicated by the orange circle).

Furthermore, the improvements in image quality associated with 2D-CAIPIRINHA are demonstrated taking four different T1-weighted 3D FLASH experiments of a volunteer's brain with different acceleration factors and acquisition schemes (Fig. 7). The acquisitions compared are

- a)** standard 2x2,
- b)** 2D-CAIPIRINHA 2x2<sup>(1)</sup>,
- c)** 2D-CAIPIRINHA 1x5<sup>(2)</sup> and
- d)** standard 5x1 scheme.

Displayed are the central sections of the reconstructed 3D image data in the sagittal, coronal and axial view in addition to the corresponding quantitative g-factor maps. Comparing reconstruction results from af = 4 (7A) and (7B) the improvement of 2D-CAIPIRINHA can clearly be appreciated. Comparing results from af = 5 (7C) and (7D) the gain in SNR is even more obvious. In this case the parallel imaging performance of 2D-CAIPIRINHA 1x5<sup>(2)</sup> (7C) compares pretty well with the standard af = 4 (2x2) acquisition employed in (7A). While the 2D-CAIPIRINHA patterns in general appear to be more tolerant against user influence and suboptimal patient positioning, the automatic



**7** In vivo 3D FLASH brain imaging using different acceleration schemes: (7A) Standard 2x2 (7B) 2D-CAIPIRINHA 2x2<sup>(1)</sup> (7C) Standard 5x1 (7D) 2D-CAIPIRINHA 1x5<sup>(2)</sup>. Displayed are central slices in the sagittal, coronal and axial view. In addition the corresponding GRAPPA g-factor maps are shown.

**Imaging details:** 3T MAGNETOM Skyra, 20-channel head neck matrix coil, 3D FLASH, GRAPPA with extra reference scan, matrix 32 x 32 x 32, TE / TR 4.3 ms / 16 ms, FA 35°, FOV 256 x 208 x 204 mm<sup>3</sup>, matrix 256 x 168 x 144; partial Fourier factor 7/8, total scan time 1 min 40 s (af = 4) and 1 min 16 s (af = 5).

extraction of the optimal pattern for the given imaging setup remains a challenging task and has not been sufficiently answered.

## Conclusion

In all current parallel imaging techniques, aliasing artifacts resulting from an undersampled acquisition are removed by a specialized pMRI image reconstruction algorithm. The CAIPIRINHA concept aims at modifying the

appearance of the aliasing artifacts already during the acquisition to improve the following parallel image reconstruction procedure. Specifically, this concept has been successfully applied to simultaneous multi-slice imaging (MS-CAIPIRINHA) and 3D imaging (2D-CAIPIRINHA).

### MS-CAIPIRINHA

Aliasing in simultaneous multi-slice acquisitions can be modified already during the acquisition by employing

alternating rf-pulses for subsequent phase encoding lines, thereby allowing the imprint of the individual slices with individual phase-cycles causing the slices to appear shifted with respect to each other thereby improving the reconstruction process minimizing g-factor related noise enhancements. Thus, a CAIPIRINHA-type 4 slice excitation with low g-factor values (close to 1) allows the acquisition of 4 slices in the same time usually required for 1 slice without

loss of SNR. Recently, the MS-CAIPIRINHA concept has been also successfully applied to more advanced acquisition schemes such as SSFP [13] EPI [16] and radial [17] simultaneous multi-slice imaging.

However, it is important to note that multi-slice excitations are associated with significantly increased energy deposition, currently limiting the method to a moderate number of simultaneously excited slices, and/or to low flip angles. However, recently, a promising concept for reducing the rf power of multi-band pulses has been introduced [18]. Thus, MS-CAIPIRINHA is expected to become a powerful strategy in the near future allowing to significantly accelerate many clinical protocols in almost preserved image quality.

#### 2D-CAIPIRINHA

In conventional pMRI accelerated 3D imaging, data reduction is performed in two spatial dimensions simultaneously

by integer-valued undersampling in each phase encoding direction. Though sensitivity variations can be exploited in two spatial dimensions, this sampling strategy provides suboptimal encoding performance. The 2D-CAIPIRINHA strategy similar to MS-CAIPIRINHA modifies aliasing in a controlled manner already during the data acquisition. This is accomplished by shifting sampling positions in the two dimensional phase encoding scheme with respect to each other. In this way, at certain image acceleration values, an optimal sampling pattern can be found which minimizes signal overlap and at the same time allows one to efficiently take advantage of all the sensitivity variations provided by the coil array in the 2D phase encoding plane. Thus, 2D-CAIPIRINHA provides optimal reconstruction performance given a certain coil configuration and object shape, and therefore results in optimal image reconstruction quality.

## Acknowledgments

The authors thank Daniel Neumann from the Research Center Magnetic Resonance Bavaria (MRB), Würzburg, Germany and Daniel Stäb from the Institute for Diagnostic Radiology, University Hospital Würzburg, Germany for providing material.

In addition, the authors are extremely grateful for receiving continuing support from the colleagues from Siemens Healthcare, especially Stephan Kannengiesser, Dominik Nickel, Berthold Kiefer, Mathias Nittka, Vladimir Jellus and Randall Kroeker.

#### References

- Pruessmann KP, Weiger M, Scheidegger B, Boesiger P. SENSE: sensitivity encoding for fast MRI. *Magn Reson Med* 1999; 42:952-962.
- Griswold MA, Jakob PM, Heidemann RM, Nittka M, Jellus V, Wang J, Kiefer B, Haase A. Generalized Autocalibrating Partially Parallel Acquisitions (GRAPPA). *Magn Reson Med* 2002; 47:1202-1210.
- Weiger M, Pruessmann KP, Boesiger P. 2D SENSE for faster 3D MRI. *MAGMA*. 2002 Mar; 14(1):10-9.
- Larkman DJ, Hajnal JV, Herlihy AH, Coutts GA, Young IR, Ehnholm G. Use of multicoil arrays for separation of signal from multiple slices simultaneously excited. *J Magn Reson Imaging*. 2001 Feb; 13(2):313-7.
- Breuer FA, Kannengiesser SA, Blaimer M, Seiberlich N, Jakob PM, Griswold MA. General formulation for quantitative G-factor calculation in GRAPPA reconstructions. *Magn Reson Med*. 2009 Sep;62(3):739-46.
- Breuer FA, Blaimer M, Heidemann RM, Mueller MF, Griswold MA, Jakob PM. Controlled Aliasing in Parallel Imaging Results in Higher Acceleration (CAIPIRINHA) for Multislice Imaging. *Magn Reson Med* 2005; 53:684-691.
- Breuer FA, Blaimer M, Mueller MF, Seiberlich N, Heidemann RM, Griswold MA, Jakob PM. Controlled aliasing in volumetric parallel imaging (2D CAIPIRINHA). *Magn Reson Med*. 2006 Mar;55(3):549-56.
- Breuer FA, Moriguchi H, Seiberlich N, Blaimer M, Jakob PM, Duerk JL, Griswold MA. Zigzag sampling for improved parallel imaging. *Magn Reson Med*. 2008 Aug;60(2):474-8.
- Blaimer M, Breuer FA, Seiberlich N, Mueller MF, Heidemann RM, Jellus V, Wiggins G, Wald LL, Griswold MA, Jakob PM. Accelerated volumetric MRI with a SENSE/GRAPPA combination. *J Magn Reson Imaging*. 2006 Aug;24(2):444-50.
- Muller S. Simultaneous multislice imaging (SIMUSIM) for improved cardiac imaging. *Magn Reson Med*. 1989 Apr;10(1):145-55.
- Glover GH. Phase-offset multiplanar (POMP) volume imaging: a new technique. *J Magn Reson Imaging*. 1991 Jul-Aug; 1(4):457-61.
- Souza SP, Szumowski J, Dumoulin CL, Plewes DP, Glover G. SIMA: simultaneous multislice acquisition of MR images by Hadamard-encoded excitation. *J Comput Assist Tomogr*. 1988 Nov-Dec;12(6):1026-30.
- Stäb D, Ritter CO, Breuer FA, Weng AM, Hahn D, Köstler H. CAIPIRINHA accelerated SSFP imaging. *Magn Reson Med*. 2011 Jan;65(1):157-64.
- Willis NP and Bresler Y. Optimal scan design for time varying tomographic imaging {II}: Efficient design and experimental validation. *IEEE Trans. Image Processing*, 1995 May; 4: 654-666.
- Wu B, Millane RP, Watts R, Bones PJ. Improved matrix inversion in image plane parallel MRI. *Magn Reson Imaging*. 2009 Sep;27(7):942-53.
- Setsompop K, Gagoski BA, Polimeni JR, Witzel T, Wedeen VJ, Wald LL. Blipped-controlled aliasing in parallel imaging for simultaneous multislice Echo Planar Imaging with reduced g-factor penalty. *Magn Reson Med*. 2011 Aug 19.
- Yutzy SR, Seiberlich N, Duerk JL, Griswold MA. Improvements in multislice parallel imaging using radial CAIPIRINHA. *Magn Reson Med*. 2011 Jun;65(6):1630-7.
- Norris DG, Koopmans PJ, Boyacıoğlu R, Barth M. Power independent of number of slices radiofrequency pulses for low-power simultaneous multislice excitation. *Magn Reson Med*. 2011 Nov;66(5):1234-40.

#### Contact

Dr. Felix Breuer  
Research Center  
Magnetic Resonance Bavaria e.V (MRB)  
Am Hubland  
97074 Würzburg  
Germany  
Phone: +49 (0) 931 318 3060  
Fax: +49 (0) 931 318 4680  
breuer@mr-bavaria.de

# Siemens Healthcare Publications

Our publications offer the latest information and background for every healthcare field. From the hospital director to the radiological assistant – here, you can quickly find information relevant to your needs.



## Medical Solutions

Innovations and trends in healthcare. The magazine is designed especially for members of hospital management, administration personnel, and heads of medical departments.



## eNews

Register for the global Siemens Healthcare News-letter at [www.siemens.com/healthcare-eNews](http://www.siemens.com/healthcare-eNews) to receive monthly updates on topics that interest you.



## AXIOM Innovations

Everything from the worlds of interventional radiology, cardiology, fluoroscopy, and radiography. This semi-annual magazine is primarily designed for physicians, physicists, researchers, and medical technical personnel.



## MAGNETOM Flash

Everything from the world of magnetic resonance imaging. The magazine presents case reports, technology, product news, and how-to articles. It is primarily designed for physicians, physicists, and medical technical personnel.



## SOMATOM Sessions

Everything from the world of computed tomography. With its innovations, clinical applications, and visions, this semiannual magazine is primarily designed for physicians, physicists, researchers, and medical technical personnel.



## Imaging Life

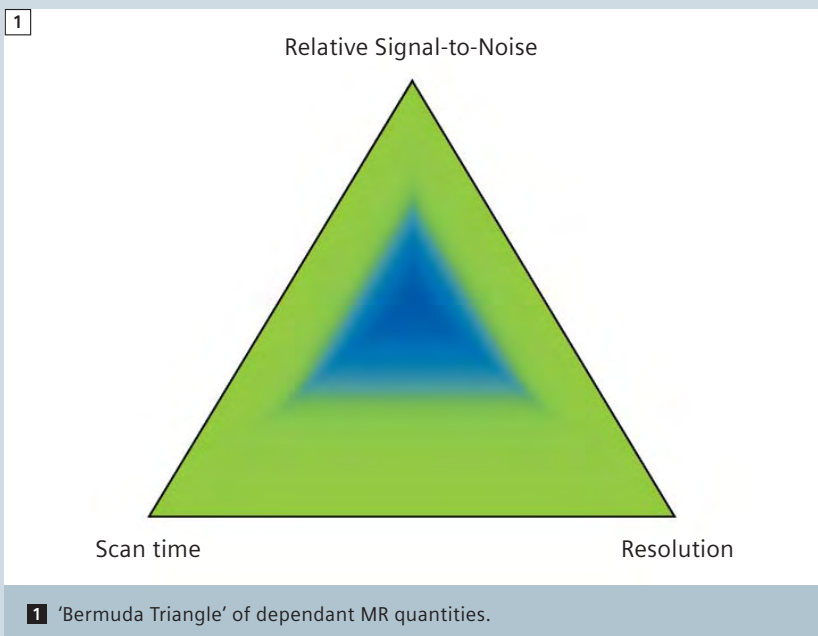
Everything from the world of molecular imaging innovations. This bi-annual magazine presents clinical case reports, customer experiences, and product news and is primarily designed for physicians, hospital management and researches.

For current and past issues and to order the magazines, please visit [www.siemens.com/healthcare-magazine](http://www.siemens.com/healthcare-magazine).

# The Signal-to-Noise Indicator or How to Navigate the 'Bermuda Triangle'

Joachim Graessner, Dipl. Ing.

Siemens Healthcare, Hamburg, Germany



We observe quite often that people feel uneasy with the interpretation of the numbers the signal-to-noise (S/N) indicator shows on the *syngo* program-card. "May I change the protocol although the SNR indicator shows a value of 0.3?" "Why does oversampling improve S/N? The larger FOV only covers more air." Such questions and many more will be answered in this article. We will take away the mystery of parameter changes and explain their mutual dependencies (Fig. 1).

## What is signal-to-noise?

The total MR-signal is a mixture of the signal from the pure MR experiment plus thermal noise and other sources of noise. A measure of quality for a medical image is the ratio of the signal-intensity in the object divided by the signal-inten-

sity of the noise (SNR) typically measured in the air outside the body.

## Why is the SNR relative?

The SNR indicator of a saved protocol always shows the value 1.00 or 100%. Changing certain MR parameters changes this indicator value but only relative to the initially stored version of this protocol. After saving the performed parameter changes the SNR indicator switches back to the value of 1.00. Do not use this value for comparisons between different protocols!

## Which parameters influence the SNR indicator?

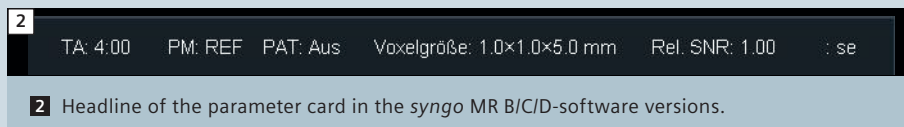
There are several parameters which alter the signal S. Or, looking at the equation, the signal S is proportional to certain parameters.

$$S_{2D} \sim 1/\sqrt{\text{BW}} \cdot \Delta x \cdot \Delta y \cdot \Delta z \cdot \sqrt{\text{AC} \cdot N_{pe}}$$

$$S_{3D} \sim 1/\sqrt{\text{BW}} \cdot \Delta x \cdot \Delta y \cdot \Delta z \cdot \sqrt{\text{AC} \cdot N_{pe} \cdot N_{3D}}$$

- BW – bandwidth in Hz/pixel
- $\Delta x$  – inplane resolution in x-direction:  $\text{FOV}_x / N_{re}$
- $\Delta y$  – inplane resolution in y-direction:  $\text{FOV}_y / N_{pe}$
- $\Delta z$  – Slice thickness or partition thickness in 3D case: slab-thickness/  $N_{3D}$
- AC – Averages: number of excitations per same encoding step
- $N_{re}$  – Base matrix size in read direction
- $N_{pe}$  – Number of phase encoding steps
- $N_{3D}$  – Number of phase encoding steps in 3D direction or Z-direction

For our problem we are only looking for dependencies with respect to resolution, i.e. voxel size, total number of acquired echoes (number of phase encoding steps), number of averages (number of excitations) and readout-properties such as bandwidth per pixel. Parameters determining contrast like TE, TR, TI and flip angle as well as the sequence type, field strength and coil type do not play any role for the SNR indicator (Fig. 2).



## What does the resolution indicator show?

In *syngo* MR A/B/C software versions you get with mouse-over on the resolution field a display of values down to an accuracy of 1/100 mm. In the *syngo* MR D-version you additionally get a display of the measured and the calculated resolution (Fig. 3).

Example:

$$1.00 \times 1.00 \times 1.00 \text{ mm} = \Delta x * \Delta y * \Delta z$$

## What does the scan time indicator show?

The measurement time (TA) depends on the product of TR time, number of averages AC, number of phase encodings, and number of 3D encodings and may be divided by the Turbo factor TF, EPI factor and time saving factors from sampling strategies like iPAT and Halffourier.

$$TA_{2D} = [(TR * AC * N_{pe}) / (TF * PAT_{2D})] + \text{Prep} + \text{Intro}$$

$$TA_{3D} = [(TR * AC * N_{pe} * N_{3D}) / (TF * PAT_{2D} * PAT_{3D})] + \text{Prep} + \text{Intro}$$

- Prep – preparation pulses at the beginning of a sequence to bring the magnetization into steady state. This takes a few seconds.
- Intro – 3 gradient knockings at the beginning of a protocol to warn the patient; can be switched off for breath-hold series on the sequence card.

## What do these values tell me?

Fortunately the MR software does all these calculations for you. When changing parameters of a given protocol which already delivered decent image quality you get an idea of how the scan time, the resolution and the relative SNR change compared to the initial protocol setup. A protocol with a lot of reserve in SNR can still deliver good image quality, even with an SNR indicator on 0.1. But

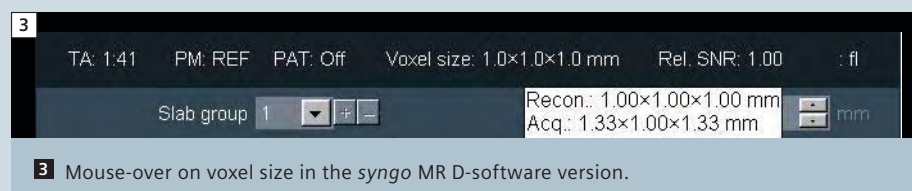
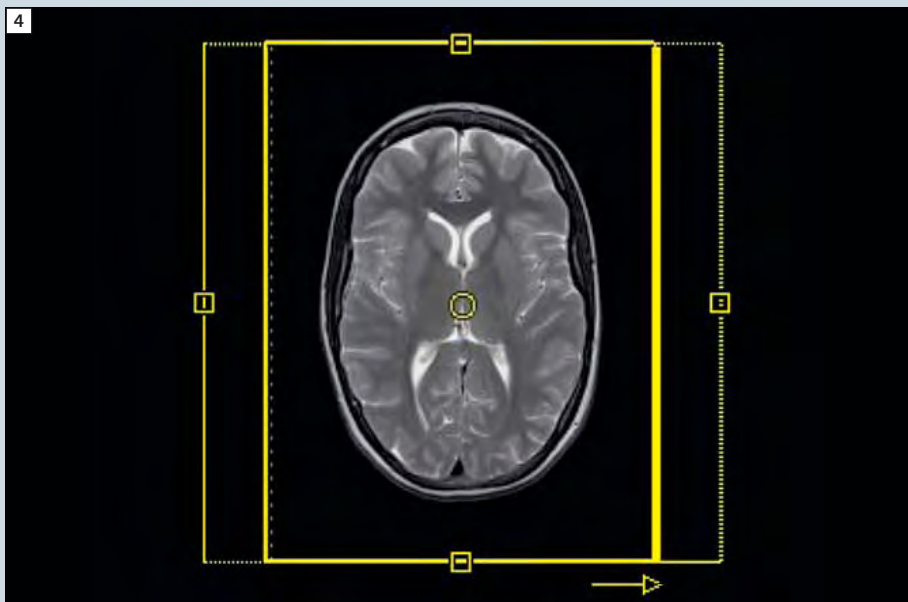


**Table 1: Changing the number of phase encoding steps and averages affects scan time TA, pixel size and relative SNR.**

FOV (mm)	Matrix $N_{pe} \times N_{re}$	AC	TA a.u.	Pixel size (mm <sup>2</sup> )	Rel. SNR a.u.	Explanation
512	256 x 256	2	1	2 x 2	4.00	4 times the pixel size
256	128 x 128	2	0.5	2 x 2	$2.83 = (4 / \sqrt{2}) = 2 * \sqrt{2}$	4 times the pixel size and 2 times less $N_{pe}$
256	128 x 256	2	0.5	2 x 1	$1.41 = (2 / \sqrt{2}) = \sqrt{2}$	twice the pixel size, but 2 times less $N_{pe}$
256	256 x 256	4	2	1 x 1	$1.41 = \sqrt{2}$	twice the number of ACs
256	256 x 256	2	1	1 x 1	1.00	start protocol (reference)
256	256 x 256	1	0.5	1 x 1	$0.71 = (1 / \sqrt{2})$	half the number of ACs
256	256 x 512	2	1	1 x 0.5	0.5	half the pixel size
256	512 x 512	2	2	0.5 x 0.5	$0.35 = (0.25 * \sqrt{2})$	quarter pixel size, but 2 times more $N_{pe}$
128	256 x 256	2	1	0.5 x 0.5	0.25	quarter pixel size



4 33% phase oversampling applied on a 75% phase FOV.

Table 2: How MR parameters affect TA, resolution and SNR.

Parameter		Measurement time TA	Resolution	SNR
Matrix	↑	↑	↑	↓
Fields-of-view (FOV)	↑	—	↓	↑
Slice thickness	↑	—	↓	↑
Bandwidth per pixel	↑	$(\downarrow)^*$	—	↓
Averages AC	↑	↑	—	↑
Phase oversampling	↑	↑	—	↑
Rectangular FOV	↓	↓	—	↓
iPAT factor	↑	↓	—	↓
Partial Fourier factor	↑	↓	—	↓

\* only if TR can be shortened

when you already pushed resolution and scan time to a level where the images start to get noisy, a further change with a resulting SNR of 0.9 could result in an unacceptable quality. As said, the SNR indicator shows a relative quantity. It depends on the starting conditions. You will always have to sacrifice one or two items when optimizing the third one.

Better resolution in less scan time with higher SNR is impossible unless you change the measurement conditions like field strength or type of RF coil.

Table 1 gives an example:

- Bandwidth and slice thickness are assumed constant
- No iPAT and quadratic FOV
- Pixel size x slice thickness = Voxel size

Obviously the factor square root of two ( $\sqrt{2}$ ) plays an important role when diminishing or enlarging certain MR parameters by a factor of two. Only alterations of the slice thickness change the SNR indicator linearly. All other parameters go with the square root of the change factor up or down.

### Why does phase oversampling improve the S/N?

Oversampling in phase direction acquires more encoding steps and thus increases SNR. Each independently-sampled phase encoding step adds a portion to the total SNR. Each echo contains information about the whole image; there are no echoes which collect data in the air.

Figure 4 shows a special case with 75% phase FOV combined with 33% phase oversampling (PhOS). Compared to 100% phase FOV with no PhOS you have the same SNR, scan time and resolution. The same is true for a setup with 100% PhOS and half the number of ACs or instead iPAT = 2.

### Why does the SNR not increase with more reference lines in GRAPPA mode?

Because the number of reference lines are not included in the formula. The

**Table 3: Parameters for SNR discovery protocols.**

	SE 2D	TSE 2D	GRE 3D	GRE 2D
Sequence name	tse	tse	gre	gre
Dimension	2D	2D	3D	2D
FOV read	256	256	256	256
FOV phase	100%	100%	100%	100%
Base resolution	256	256	256	256
Phase resolution	100%	100%	100%	100%
Slice thickness	5 mm	5 mm	1 mm	5 mm
TR	467 ms	3050 ms	5.5 ms	235 ms
TE	12 ms	107 ms	2.35 ms	5 ms
AC	2	2	2	2
iPAT	none	none	none	none
Bandwidth	130	130	390	260
Slice/Slices per slab	5	10	64	5
Flipangle	90	180	25	70
Turbo factor	1	9	n.a.	n.a.
Introduction	deselect	deselect	deselect	deselect
Coil	8/12/16-	channel	head	coil
TA	4:00 min	3:00 min	3:00 min	2:00 min
Resolution	1.0x1.0x5.0	1.0x1.0x5.0	1.0x1.0x1.0	1.0x1.0x5.0
Rel. SNR	1.00	1.00	1.00	1.00

same is true for interpolation. But the SNR actually benefits in most sequences from the additionally sampled number of reference lines using the 'integrated' mode.

### Why does allowed partial Fourier not change scan time in a TSE sequence?

Partial Fourier in a TSE sequence only shortens the echo train length. This gives you the opportunity to shorten TR

and gain some scan time if appropriate for the contrast.

### Is there a rule of thumb for changes in the SNR indicator?

A red arrow in Table 2 indicates for both directions a drawback compared to our positive expectations of shorter scan times, better resolution and SNR. There is always at least one red arrow accompanying a black arrow.

### How can I get a feeling for the amount of change in the SNR indicator?

Generate a protocol with the parameters shown in Table 3, save it and then play around with the MR parameters and discover their influence on SNR, TA and resolution. The TRs were chosen that way to get round scan times, which will have slight deviations when changing the number of averages AC. These few seconds are due to the preparation phase at

**Table 4: Influence of the voxel size on total volume and SNR.**

SVS voxel size (mm <sup>3</sup> )	approx. UI values (mm <sup>3</sup> )	Volume (cm <sup>3</sup> )	Rel. SNR a.u.
20x20x20	20x20x20	8	1.00
18.1x18.1x18.1	18x18x18	6	0.75
15.9x15.9x15.9	16x16x16	4	0.5
12.6x12.6x12.6	13x13x13	2	0.25
10x10x10	10x10x10	1	0.125
7.9x7.9x7.9	8x8x8	0.5	0.063
6.3x6.3x6.3	6x6x6	0.25	0.031
5x5x5	5x5x5	0.125	0.016

the very beginning of a protocol which is played out only once.

### Is there anything different with spectroscopy protocols?

In single voxel spectroscopy (SVS) you have to be aware of the fact that a slight decrease in the side length of a single voxel will result in a large change to the measured volume, i.e. dramatic decrease in SNR, which can rarely be compensated by an increase of averages (Table 4). CSI protocols can deliver much smaller voxels than SVS due to higher number of encoding steps in two or three dimensions. But this has to be paid for by longer scan times and a more global shim situation.

→ Visit [www.siemens.com/magnetom-world](http://www.siemens.com/magnetom-world) to download training files in .edx format. Training files are available for software versions syngo MR D11D, syngo MR B15 and syngo MR B17.



#### References

*Recommended literature for the curious reader in the order of increasing physical depth:*

- 1 "Magnets, Spins and Resonances"; Siemens 2003.
- 2 "Magnets, Flow and Artifacts"; Siemens 2004.
- 3 "The Physics of Clinical MR Taught Through Images"; Runge, Nitz, Schmeets; Thieme 2008.
- 4 "Questions & Answers in MRI"; Elster, Burdette; Mosby 2001.

- 5 "MRI the Basics": Hashemi, Bradley, Lisanti; LWW 2010.

- 6 "MRI from Picture to Proton": McRobbie, Moore, Graves, Prince; Cambridge 2007.

*Especially recommended for the German speaking community:*

- 7 „Praxiskurs MRT“: Nitz, Runge; Thieme 2011.
- 8 „MRT-Guide für MTRA/RT“: Nitz; Thieme 2012.

#### Contact

Joachim Graessner, Dipl.Ing.  
Siemens AG Healthcare  
GER H IM BM MR  
Lindenplatz 2  
20099 Hamburg  
Germany  
[joachim.graessner@siemens.com](mailto:joachim.graessner@siemens.com)

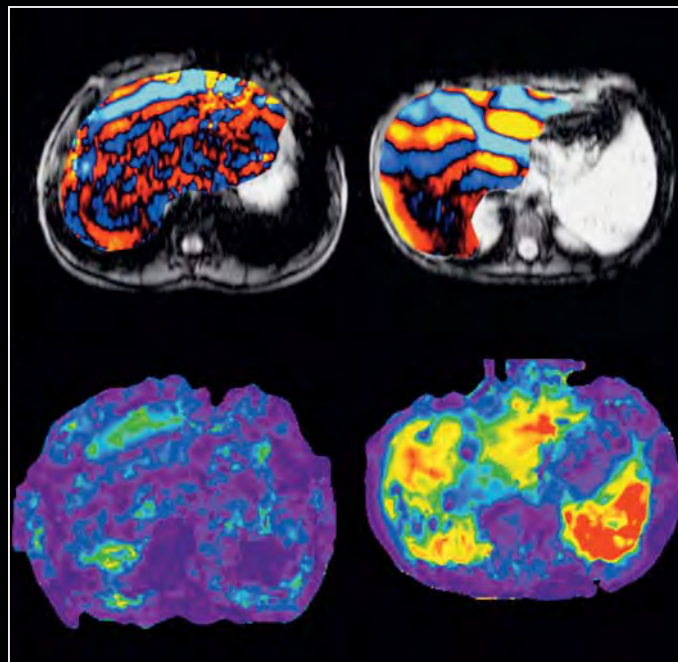
# Try them on your system

Trial licenses for some of the applications featured in this issue of MAGNETOM Flash are available free of charge for a period of 90 days. For further details, product overviews, image galleries, step-by-step videos, case studies and general requirements please visit us online\* at

[www.siemens.com/discoverMR](http://www.siemens.com/discoverMR).

\*Direct link for US customers:  
[www.siemens.com/WebShop](http://www.siemens.com/WebShop)

\*Direct link for UK customers:  
[www.siemens.com.uk/mrwebshop](http://www.siemens.com.uk/mrwebshop)



MR Elastography, page 108.

MAGNETOM Flash – Imprint  
© 2012 by Siemens AG, Berlin and Munich,  
All Rights Reserved

Publisher:  
**Siemens AG**  
Medical Solutions  
Business Unit Magnetic Resonance,  
Karl-Schall-Straße 6, D-91052 Erlangen,  
Germany

Editor-in-Chief: Dr. Matthias Lichy, M.D.  
([matthias.lichy@siemens.com](mailto:matthias.lichy@siemens.com))

Associate Editor: Antje Hellwich  
([antje.hellwich@siemens.com](mailto:antje.hellwich@siemens.com))

Editorial Board: Christiane Bernhardt;  
Peter Kreisler, Ph.D.; Wellesley Were;  
Milind Dhamankar, M.D.; Michelle Kessler;  
Gary McNeal; Sunil Kumar, M.D.

Production: Norbert Moser, Siemens AG,  
Medical Solutions

Layout: independent Medien-Design  
Widenmayerstrasse 16, D-80538 Munich

Printer: Mediahaus Biering GmbH,  
Freisinger Landstr. 21, 80939 Munich, Germany

**MAGNETOM Flash is also available  
on the internet:**

[www.siemens.com/magnetom-world](http://www.siemens.com/magnetom-world)

Note in accordance with § 33 Para.1 of the German Federal Data Protection Law: Despatch is made using an address file which is maintained with the aid of an automated data processing system.

MAGNETOM Flash with a total circulation of 35,000 copies is sent free of charge to Siemens MR customers, qualified physicians, technologists, physicists and radiology departments throughout the world. It includes reports in the English language on magnetic resonance: diagnostic and therapeutic methods and their application as well as results and experience gained with corresponding systems and solutions. It introduces from case to case new principles and procedures and discusses their clinical potential.

The statements and views of the authors in the individual contributions do not necessarily reflect the opinion of the publisher.

The information presented in these articles and case reports is for illustration only and is not intended to be relied upon by the reader for instruction as to the practice of medicine. Any health care practitioner reading this information is reminded that they must use their own learning, training and expertise in dealing with their individual patients. This material does not substitute for that duty and is not intended by Siemens Medical Solutions to be used for any purpose in that regard. The drugs and doses mentioned

herein are consistent with the approval labeling for uses and/or indications of the drug. The treating physician bears the sole responsibility for the diagnosis and treatment of patients, including drugs and doses prescribed in connection with such use. The Operating Instructions must always be strictly followed when operating the MR system. The sources for the technical data are the corresponding data sheets. Results may vary. Partial reproduction in printed form of individual contributions is permitted, provided the customary bibliographical data such as author's name and title of the contribution as well as year, issue number and pages of MAGNETOM Flash are named, but the editors request that two copies be sent to them. The written consent of the authors and publisher is required for the complete reprinting of an article.

We welcome your questions and comments about the editorial content of MAGNETOM Flash. Please contact us at [magnetomworld.med@siemens.com](mailto:magnetomworld.med@siemens.com). Manuscripts as well as suggestions, proposals and information are always welcome; they are carefully examined and submitted to the editorial board for attention. MAGNETOM Flash is not responsible for loss, damage, or any other injury to unsolicited manuscripts or other materials. We reserve the right to edit for clarity, accuracy, and space. Include your name, address, and phone number and send to the editors, address above.

# MAGNETOM Flash

The Magazine of MR

Issue Number 1/2012  
ISMRM Edition  
Not for distribution in the US.

SIEMENS

## Clinical

Clinical Experience with  
MR-PET Acquisition  
Page 6

MR Elastography  
Page 20

Understanding  
the Whiplash Condition  
at 3T  
Page 44

Myocardial T1-Mapping  
Page 96

## Technology

Cerebral TOF  
Angiography at 7T  
Page 126

CAIPIRINHA  
Page 135

## How I do it

The SNR Indicator  
Page 144



Please enter your business address

Institution

Department

Function

Title

Name

Street

Postal Code

City

State

Country

MR system used

Please include me in your mailing list for the  
following Siemens Healthcare customer magazine(s):

☐ Medical Solutions

☐ MAGNETOM Flash

☐ SOMATOM Sessions

☐ AXIOM Innovations

Stay up to date with the latest information  
Register for:

E-mail

Please print clearly!

☐ Yes, I consent to the above information being used  
for future contact regarding product updates and other  
important news from Siemens.

☐ unsubscribe from info service

# MAGNETOM Flash



Siemens AG  
Medical Solutions  
Magnetic Resonance  
Antje Hellwich - Marketing  
P.O. Box 32 60  
D-91050 Erlangen  
Germany



→ Visit [www.siemens.com/magnetom-world](http://www.siemens.com/magnetom-world)  
for case reports,  
clinical methods,  
application tips,  
talks and much more  
clinical information.

**SUBSCRIBE NOW!**

– and get your free copy of future  
MAGNETOM Flash! Interesting information from  
the world of magnetic resonance – gratis to your  
desk. Send us this postcard, or subscribe online at  
[www.siemens.com/MAGNETOM-World](http://www.siemens.com/MAGNETOM-World)

## Global Siemens Headquarters

Siemens AG  
Wittelsbacherplatz 2  
80333 Muenchen  
Germany

## Global Siemens Healthcare Headquarters

Siemens AG  
Healthcare Sector  
Henkestrasse 127  
91052 Erlangen  
Germany  
Phone: +49 9131 84-0  
[www.siemens.com/healthcare](http://www.siemens.com/healthcare)

[www.siemens.com/healthcare-magazine](http://www.siemens.com/healthcare-magazine)

Order No. A91MR-1000-86C-7600 | Printed in Germany | CC 104 041230. | © 04.12, Siemens AG

On account of certain regional limitations of sales rights and service availability, we cannot guarantee that all products included in this brochure are available through the Siemens sales organization worldwide. Availability and packaging may vary by country and is subject to change without prior notice. Some/All of the features and products described herein may not be available in the United States.

The information in this document contains general technical descriptions of specifications and options as well as standard and optional features which do not always have to be present in individual cases.

Siemens reserves the right to modify the design, packaging, specifications and options described herein without prior notice.  
Please contact your local Siemens sales representative for the most current information.

Note: Any technical data contained in this document may vary within defined tolerances. Original images always lose a certain amount of detail when reproduced.

## Global Business Unit

Siemens AG  
Medical Solutions  
Magnetic Resonance  
Henkestr. 127  
DE-91052 Erlangen  
Germany  
Phone: +49 9131 84-0  
[www.siemens.com/healthcare](http://www.siemens.com/healthcare)

## Local Contact Information

### Asia

Siemens Pte Ltd  
The Siemens Center  
60 MacPherson Road  
Singapore 348615  
Phone: +65 6490-8096

### Canada

Siemens Canada Limited  
Medical Solutions  
2185 Derry Road West  
Mississauga ON L5N 7A6  
Canada  
Phone: +1 905 819-5800

### Europe/Africa/Middle East

Siemens AG  
Medical Solutions  
Henkestr. 127  
91052 Erlangen  
Germany  
Phone: +49 9131 84-0

### Latin America

Siemens S.A.  
Medical Solutions  
Avenida de Pte. Julio A. Roca No 516,  
Piso 7  
C1067ABN Buenos Aires  
Argentina  
Phone: +54 11 4340-8400

### USA

Siemens Medical Solutions U.S.A., Inc.  
51 Valley Stream Parkway  
Malvern, PA 19355-1406  
USA  
Phone: +1-888-826-9702